# In-Line Extrusion Monitoring and Product Quality

by

Forouzandeh Farahani Alavi

A thesis submitted in conformity with the requirements for the degree of
Doctor of Philosophy
Graduate Department of Chemical Engineering and Applied Chemistry
University of Toronto

# In-Line Extrusion Monitoring and Product Quality

Doctor of Philosophy 2010
Forouzandeh Farahani Alavi
Department of Chemical Engineering and Applied Chemistry
University of Toronto

## Abstract

Defects in polyethylene film are often caused by contaminant particles in the polymer melt. In this research, particle properties obtainable from in-line melt monitoring, combined with processing information, are used to predict film defect properties.

"Model" particles (solid and hollow glass microspheres, aluminum powder, ceramic microspheres, glass fibers, wood particles, and cross-linked polyethylene) were injected into low-density polyethylene extruder feed. Defects resulted when the polyethylene containing particles was extruded through a film die and stretched by a take-up roller as it cooled to form films 57 to 241μm in thickness.

Two off-line analysis methods were further developed and applied to the defects: polarized light imaging and interferometric imaging. Polarized light showed residual stresses in the film caused by the particle as well as properties of the embedded particle. Interferometry enabled measures of the film distortion, notably defect volume. From the images, only three attributes were required for mathematical modeling: particle area, defect area, and defect volume. These attributes yielded two "primary defect properties": average defect height and magnification (of particle area). For all spherical particles, empirical correlations of these properties were obtained for each of the two major types of defects that

emerged: high average height and low average height defects. Analysis of data for non-spherical particles was limited to showing how, in some cases, their data differed from the spherical particle correlations.

To help explain empirical correlations of the primary defect properties with film thickness, a simple model was proposed and found to be supported by the high average height defect data: the "constant defect volume per unit particle area" model. It assumes that the product of average defect height and magnification is a constant for all film thicknesses.

A numerical example illustrates how the methodology developed in this work can be used as a starting point for predicting film defect properties in industrial systems. A limitation is that each prediction yields two pairs of primary defect property values, one pair for each defect type. If it is necessary to identify the dominant type, then measurement of a length dimension of sufficient defects in the film is required.

## Acknowledgements

I would like to express my deep appreciation to my supervisor, Professor Stephen T. Balke, for his continuous guidance and support in this project. His help and encouragement were invaluable. Also, I learned many important life lessons from him, most notably, to believe in myself and to be determined.

I am most grateful to my co-supervisor, Dr. Saed Sayad, for his very valuable advice, support, and insight throughout the course of this project. Most of all, I thank him for introducing me to the world of data mining and for patiently teaching me about it.

I wish to express my gratitude to the members of my Ph.D. committee, Professor Mark T. Kortschot and Professor David C. S. Kuhn, for their exceptionally valuable advice and very insightful comments. I thank the Department of Chemical Engineering and Applied Chemistry at the University of Toronto for giving me the opportunity to pursue this degree and for providing financial support.

It is also a pleasure to thank my fellow group members, Amar Virdi and Shou Yan, for their friendship and generous assistance in setting up of equipment. In addition, I would like to thank Lianne Ing and Keivan Torabi for helping me learn various technical aspects in the early stages of this project. I also acknowledge Ivan Gutierrez for providing much needed assistance in conducting many of the extruder runs in this work.

I owe my deepest gratitude to my parents for their love and for all the sacrifices that they made to support my education. I would like to express my heartfelt thanks to my husband, Morad Kamkar, for his true friendship and for supporting and encouraging me. Finally, I would like to thank my son, Kian, for bringing so much love and happiness to my life!

# Table of Contents

# List of Tables

# List of Figures

# List of Appendices

# Nomenclature

| | |
|---|---|
| A | Area of an image object [$\mu m^2$] |
| $d_{roll}$ | Diameter of the take-up roll [cm] |
| $L_{roll}$ | Length of the take-up roll [cm] |
| C | Specific heat [cal $g^{-1}$ °$C^{-1}$] |
| D | Average diameter of an image object [μm] |
| DR | Draw ratio (Eqn. 2-1) |
| F | Tensile force applied to the filmstrip by the take-up roll [N] |
| G | Polymer mass flow rate [$kgh^{-1}$] |
| H | Average defect height [μm] (Eqn. 2-15) |
| $H_{max}$ | Maximum defect height [μm] |
| h(x) | Film thickness at distance x from the die in the machine direction [μm] |
| $h_{die}$ | Thickness of the discharge opening at the film die [cm] |
| $h_{film}$ | Thickness of the final film sample [μm] |
| $h_{roll}$ | Thickness of the film at the chill roll [μm] |
| k | Thermal conductivity [cal $s^{-1}$ $m^{-1}$ °$C^{-1}$] |
| L | Length of the drawing zone [cm] |
| M | Magnification (Eqn. 2-14) |
| P | Perimeter of an image object [μm] |
| Q | Polymer volume flow rate ($cm^3s^{-1}$) |
| RPM | Revolutions per minute of the extruder screw |
| $RPM_{roll}$ | RPM of the take-up roll |
| Run | Identifies the extruder run number during which each defect was generated. |

| | |
|---|---|
| $T(x)$ | Film temperature at distance x from the die in the machine direction [°C] |
| $T_1$, $T_2$, $T_3$ | Set temperature for each of three extruder zones [°C] |
| $T_{air}$ | Air temperature in the vicinity of the film die and the take-up roll [°C] |
| $T_{die}$ | Set temperature for the die zone [°C] |
| $T_{roll}$ | Temperature of the cooling water circulating in the take-up roll [°C] |
| $u(x)$ | Velocity of the film at distance x from the die in the machine direction [$cms^{-1}$] |
| $u_{die}$ | Velocity of the polymer exiting the film die [$cms^{-1}$] |
| $u_{roll}$ | Velocity of the take-up roll [$cms^{-1}$] |
| $V$ | Volume of an object [$\mu m^3$] |
| $v$ | Strained volume per unit area of particle [$\mu m^3$] |
| $w(x)$ | Width of the film at distance x from the die in the machine direction [cm] |
| $w_{film}$ | Width of the final film sample [cm] |
| $w_{die}$ | Width of the discharge opening at the film die [cm] |
| x, y, z | Distance in the machine, transverse, and out-of-plane directions, respectively [cm]. |

## Greek Letters

| | |
|---|---|
| $\alpha$ | Thermal expansion coefficient [$°C^{-1}$] |
| $\varepsilon$ | Strain |
| $\eta$ | Polymer viscosity [$gcm^{-1}s^{-1}$] |
| $\rho$ | Density [$gcm^{-3}$] |
| $\sigma$ | Stress [$Nm^{-2}$] |

## Subscripts for Image Objects

| | |
|---|---|
| DI | Defect property obtained from an interferometric image |
| DP | Defect property obtained from a polarized light image |
| P | particle property obtained from a polarized light image |

# 1 INTRODUCTION

The topic of this thesis is plastic film defects that generally occur during film manufacturing. These defects often spoil the aesthetics and even the intended use of the film. Plastic film is produced by long screw pumps known as extruders. Defects in manufactured film are normally associated with contaminant particles in the polymer melt being extruded. They may originate from the polymer feed or may be created during the extrusion process. Industrial attempts to prevent such defects involve ways of first detecting them and then diagnosing their origin. Traditionally, visual inspection of film followed by trial and error procedures to eradicate them have been commonplace.

More recently, automated in-line web imaging inspection methods have been used for detection. Such automated methods allow the line to be shut down before large amounts of inferior film are produced. However, often film is produced by combining the output of several different extruders to form a multi-layer film. Thus, automated film inspection often cannot reveal which extruder is the source of the contaminant particles. A complementary approach to automated examination of the film being extruded is automated imaging of the polymer melt in the extruder. Such polymer melt inspection can potentially be more useful for locating the source of particles causing the defects since the monitoring station can be located on each of several extruders whose output is combined to form multi-layer film.

Extensive work has been done at the University of Toronto in development of a melt-imaging monitor. (Desa 1995, Desa *et al.* 1995, Mehra 1995, Vujnovic 1996) A new

"camera microscope" termed the "Scanning Particle Monitor" was developed and shown to be capable of detecting particles as small as 10 μm at any point across the diameter of an extruder at a monitoring station just previous to the die. (Ing *et al.* 2001, Ing *et al.* 2002) Recently advanced machine learning software has been combined with image processing software to enable a computer to determine which of the hundreds of images produced was showing a particle and which was not. (Torabi 2004, Torabi *et al.* 2005, Yan 2007, Yan *et al.* 2009, Yan *et al.* 2009a)

Initially it was thought that all visible particles produced visible defects in the final film. However, it was soon learned that was not the case. Even polymers, which appear completely transparent to the unaided eye, are generally filled with particles originating from un-dissolved, intentionally added, additives. These additives include antioxidants, ultraviolet light stabilizers, etc. In more recent work (Ing *et al.* 2002, Torabi 2004), particles considered to be worth detecting ("contaminant particles") were those judged by a human observer examining the image to be likely to cause a defect. Generally comparatively large, dark particles were those identified. This unsatisfactory situation provided the motivation for this thesis.

- **Hypothesis:**

The hypothesis of this research is as follows:

"In-line image monitoring of the polymer melt during plastics extrusion can be used to associate the properties of observed particles, along with processing variables to the presence and properties of film defects."

- **Objectives:**

The objectives defined to test this hypothesis are:

1. **To equip an extruder with a film die and to conduct image monitoring of extrusion runs during addition of "model" particles.** Film extrusion is widely practiced. However, no previous studies where defects were intentionally created using particles have been published.

2. **To measure off-line the size, shape and other properties of film defects corresponding to properties of particles observed in the melt during in-line image monitoring.** Selection of suitable methods for characterizing the defects must fit the type of defects being produced and the requirements of mathematical modeling (the third objective). Furthermore, the methods are to produce images of the defects for the needed information to be obtained.

3. **To develop a mathematical model, that will relate in-line particle properties, extrusion conditions, and film properties to defect properties.** Initially this objective was to simply mean predicting whether or not a defect would be produced from a particular particle. However, early observations showed that there were different types of defects being produced and that some defects would likely be less objectionable, depending upon the application or even less visible, depending upon the human observer, than others. If "families" of defects could be identified (perhaps by an automated "clustering" method) then a classification model could be developed to predict

the family of a new defect. Alternatively, perhaps specific quantitative properties of defects could be predicted from fitting particle and processing data using a regression method. A model that contained knowledge of the physical phenomena involved in cluster formation would be most desirable. However, it was anticipated that the situation was very complex and likely only an empirical model that satisfactorily interpolated over the range of the data would be able to be developed.

In the next section, the literature relevant to this work is summarized. There it will be seen that the novelty of the work meant that the published literature was not of great assistance. Towards the end of the literature review section a new mechanistic model is proposed. The model is a very simple one and is based upon the idea that all particles are surrounded by a defect volume. The defect volume per unit of particle area is hypothesized to be a constant but it can be stretched to present a larger defect area than the area of the original particle. Subsequent sections show how a database including the only processing variable (take-up roller speed which was synonymous with film thickness), particle properties, and defect properties was constructed. Use of this database to obtain correlations and to test the model is then described. Guidelines for using the work to monitor film quality are then provided.

# 2 LITERATURE REVIEW AND THEORETICAL DEVELOPMENT

This section examines the published literature most relevant to this work and shows the development of a new theoretical model directed at helping to predict characteristics of defects. The section is divided into three main topics, each corresponding to one of the objectives of this work: the extrusion of plastic film containing purposefully induced defects, characterization of these film defects, and mathematical modeling to predict them.

## 2.1 The Extrusion of Plastic Film Containing Defects

The first step in accomplishing the first objective was to set up a process for producing plastic film. There are two widely used processes for film manufacturing and both use an extruder: film blowing and film casting.

In film blowing, polymer is extruded from an annular die and then is stretched over a mandrel of air trapped inside the blown film bubble. The molten polymer film is cooled by radiation and by forced convective cooling from external air rings in addition to the internal air rings. Blown films are typically biaxially oriented. (Figure 2-1(a)) (Campbell and Kanai 1999, Peacock 2000)

In the second process, film casting, the polymer is extruded from a flat die. The molten polymer film is rapidly stretched in the machine direction by the motion of a chill roll, which also cools the filmstrip. The product is a film that is highly oriented in the machine direction.

(Figure 2-1(b)) (Campbell and Kanai 1999) In general, film casting gives higher productivity and greater film thickness uniformity than does film blowing. Faster quenching rates encountered in chill roll film casting results in lower crystallinity and greater clarity. (Peacock 2000) These advantages and its simpler, less expensive design made chill roll film casting the natural choice for this research.

### 2.1.1 Plastic Film Defects

Defects in plastic film are the main concern in this work. Due to their thin and usually transparent nature, the quality of plastic film is very sensitive to foreign particles in the polymer melt. A visual defect transmits light differently from the rest of the material in the film and spoils the appearance, as well as possibly the functioning of the film. (Rauwendaal 2002)

Types of defects vary from one manufacturing field to another depending on the materials, processing conditions, and processing steps. Generally, defect appearance depends on its source and processing conditions. Defects appear in different forms such as holes, black specks, bubbles, areas with different surface texture, lumps, discolorations, and scratches (Sweeting 1968, Simonds *et al.* 1952)

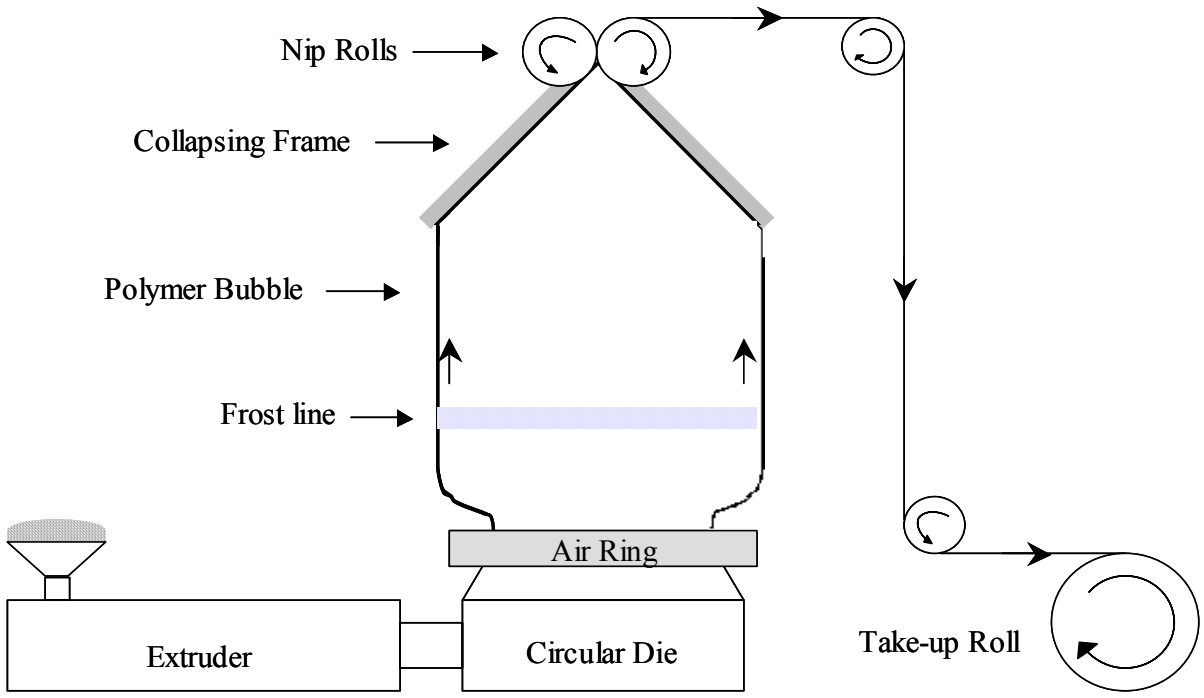


**(a)**

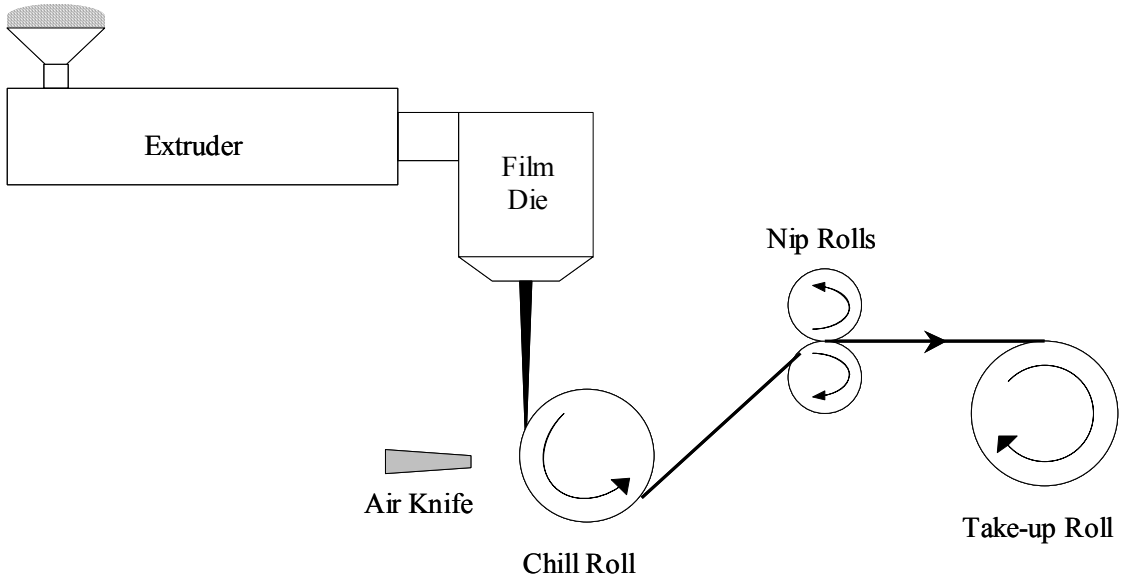


**(b)**

**Figure 2-1:** Principal components of **(a)** Film blowing equipment, **(b)** Chill roll casting equipment.

In film manufacturing, some defects are caused by problems in the manufacturing line or malfunctioning parts. For example, any scratches or sharp points on the film die, rollers, or winders will result in a film defect. Any non-uniformity in extrusion flow rate and roller or winder pulling rate will result in film thickness and width variations. In most cases, it is possible to readily determine the source of these types of defects and resolve the problem. (Sweeting 1968, Simonds *et al.* 1952)

More difficult to resolve, and the main concern of this thesis, are defects originating from particles in the melt. Dirt, gels, and degraded polymer pieces in the melt can generate a defect in the film. These particles are either present in the raw material fed to the extruder or are created during extrusion. Gels are one of the most common visual defects and come from a number of sources: un-melted or partially melted bits of higher molecular weight material, cross-linked material by overheating, additives with poor thermal stability, and catalyst residue. Based on the appearance of gels, physical properties of the carrier resin, extrusion operating conditions and additive properties, it is sometimes possible to find out why gels are created and how to avoid them. (Rauwendaal 2002, Sweeting 1968)

Traditionally, plastic film quality is investigated by off-line measurement of different film properties. Among these, visual quality control is conducted by placing a piece of film sample against the light and counting the number of visible defects or defects in a predefined size range in a specified area. This number is then compared with established standards for overall appearance quality.

The off-line approach is time consuming and does not provide real-time feedback to prevent defect generation. It can only monitor a small part of the product. In addition, personal judgment and opinion may be involved leading to variability in results. As will be seen in the next section, over the years, fast and reliable automated real-time film inspection systems have been developed.

### 2.1.2 Monitoring for Film Defects: In-Line Web Inspection

The increasing demand for better product quality, higher production rate, and lower production cost requires product quality monitors faster and more reliable than the off-line approach. The real-time in-line monitoring systems eliminate the need for laboratory measurements and therefore are much faster than off-line approaches. With these systems, it is possible to monitor the production line continuously and to create a database of defect information, which can be used for further analysis and data mining.

Machine vision and industrial inspection has become a very important step in improving product quality and gaining costumer confidence. A significant amount of work has been conducted to develop real-time web inspection systems in manufacturing of products such as polymer films, sheets, and tubes; paper; metal sheets and films; and textiles.

There are several examples of such inspection systems in the plastic processing industry. Bobberts and Van Allen (1995) developed an in-line film quality control system called the “Film Quality Analyzer” (FQA). In this system, light is transmitted through the plastic film and a charge coupled device (CCD) camera placed above the production line

captures images of the moving film. Image processing software detects contaminants based on the intensity value of each pixel and a preset threshold value.

Pratt and Warner (2000) reported a machine vision system, which can be used for the detection of defects in glass ribbon and plastic sheets. This system uses multiple line scan CCD cameras and LED light sources located at opposite sides of the web. This setup can detect and characterize defects both along and across the web.

To study the quality of resin or master batch in plastic compounding, Dominey and Goeckel (2003) described a technique for producing sample film on a continuous basis and analyzing the film in real time. This system utilized a line scan camera and a high frequency fluorescent light source. All defect images were recorded and processed using image processing software. Defects were classified and counted based on their size and intensity.

Advanced web inspection systems named “SmartView” were developed by Cognex Corporation in 2003. (Cognex Corp. 2009). These systems detect, identify, and visualize defects on the surface of products that are manufactured in a continuous fashion. SmartView Plastics is capable of inspecting millions of square meters of plastic film and sheet every day. Specially designed cameras, lens assemblies, and lighting systems provide real time, high-resolution image acquisition. Similar systems were also developed by Dr. Schenk GmbH (Konig 2009), and Wintriss Engineering Corp. (Hardin 2004).

An alternative to monitoring film defects is monitoring particles responsible for those defects. This is the alternative that motivated this thesis research and is the topic of the next section.

### 2.1.3 Monitoring for Film Defects: Particles in the Polymer Melt

In addition to improving our ability to diagnose the origin of particles in an extrusion system (especially in a co-extrusion system) the properties of particles and their motion in the melt provide potentially useful information for a variety of purposes (e.g. characterizing melt mixing). However, as mentioned earlier, the need to relate particle properties (together with processing conditions) to the production of film defects created the motivation for this research.

A fundamental problem is that polymer being extruded generally does contain particles most of which are intentionally added for a variety of reasons. The following is a list of reasons for adding special particles to polymers (Wypych 1999, Murphy 1996):

- To make plastic processing easier (e.g. Processing Aids, Antistatic Agents, Lubricants)
- To prevent degradation (e.g. Antioxidants, Heat Stabilizers, Light Stabilizers)
- To improve mechanical and/or chemical properties of the final product (e.g. flame retardants, impact modifiers, reinforcements, fillers)
- To change or enhance the appearance of the final product (e.g. pigments, fragrances)
- To lower the cost of production (e.g. fillers, extenders)

In polymer composites, particles or fibers are incorporated with polymer resins in different ways to create new materials with significantly improved properties. Properties of the resulting composite depend on the properties of its individual components, their size and shape distributions, and orientation.

The most widely used mineral fillers (or reinforcements) are calcium carbonate, talc, clay, silica, mica, and glass. (Utracki 1982) Other materials such as rubber, ceramic, and metal particles are also used as fillers. Some of the important properties of fillers that affect the properties of the final composite material are density, particle size, particle shape, hardness, thermal expansion coefficient, melting temperature, and surface tension.

Addition of filler particles and fibers to polymers in molding and extrusion applications is common. However, in clear film manufacturing, only very low concentrations of filler can be added to the polymer if clarity is to be retained.

The in-line melt monitoring research at the University of Toronto, serving as a precursor to this work, was begun by Desa (1995). Desa *et al.* (1995) focused on monitoring the quality of recycled plastic waste during extrusion. The main goal was to detect particles and microgels inside the melt. The developed system was able to detect particles near the extruder wall, however image quality was poor. Mehra (1995) and Vujnovic (1996) also used a similar system to monitor contaminants during extrusion.

Based on the results of this previous work and with the advances made in the lighting and CCD camera technology, a new and powerful in-line melt monitoring system was developed by Ing *et al.* (2001, 2002) This system is capable of scanning through the melt channel, hence called the Scanning Particle Monitor (SPM). The SPM can monitor low concentrations of dispersed phases across a translucent polymer melt. This system provides quantitative information on particle properties, velocity and concentration profiles. A schematic diagram of the SPM and its components is shown in Figure 2-2.

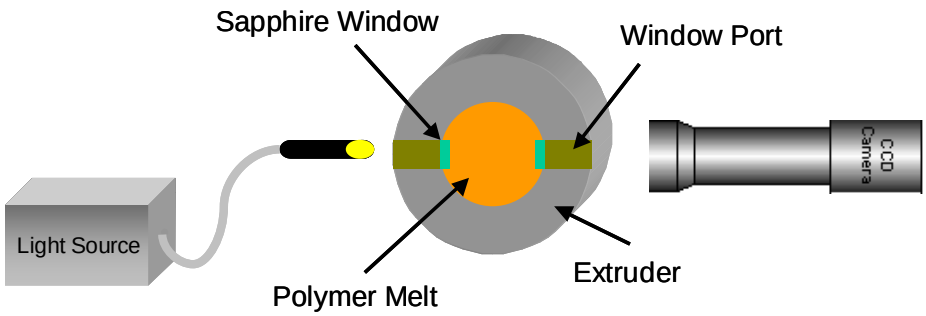


**Figure 2-2:** Schematic diagram of the Scanning Particle Monitor (SPM) and its components

Torabi (2004) developed software for in-line interpretation of the images acquired by the SPM. In this software, adaptive machine learning based on a Bayesian model is used to automatically determine whether or not a contaminant particle is present and to determine the size of the particles. (Torabi *et al.* 2005) Image quality plays an important role in determining the success of the image interpretation step. Yan (2007) developed automated methods for improving image quality based on adaptive machine learning methods and incorporated them into Torabi's work. (Yan *et al.* 2009, Yan *et al.* 2009a)

### 2.1.4 The Film Casting Process

In the film casting process, molten polymer is extruded through a film die, which has a very thin, rectangular opening. The molten film is then stretched in air by a take-up roller system and cooled on a chill roll. A schematic diagram of chill roll film casting is shown in Figure 2-3. Depending on the take-up roller speed and the length of the air gap, polymer solidification can occur at contact with the chill roll or before it. (Lamberti and Titomanlio 2005) The distance between the die exit and the solidification point is called the drawing zone. Draw ratio (DR) is defined as the ratio of the chill roll velocity ($u_{roll}$) to the velocity of the molten film at the die opening ($u_{die}$). (Dobroth and Erwin 1986)

$$DR = \frac{u_{roll}}{u_{die}} \tag{2-1}$$

Polymer processing in the extruder and the film die is dominated by shear flow deformation. As the viscoelastic polymer melt exits the die, it swells to relieve the elastic shear stresses accumulated in the die. (Dobroth and Erwin 1986, Yamada 1999) This is known as “Extrudate Swell”.

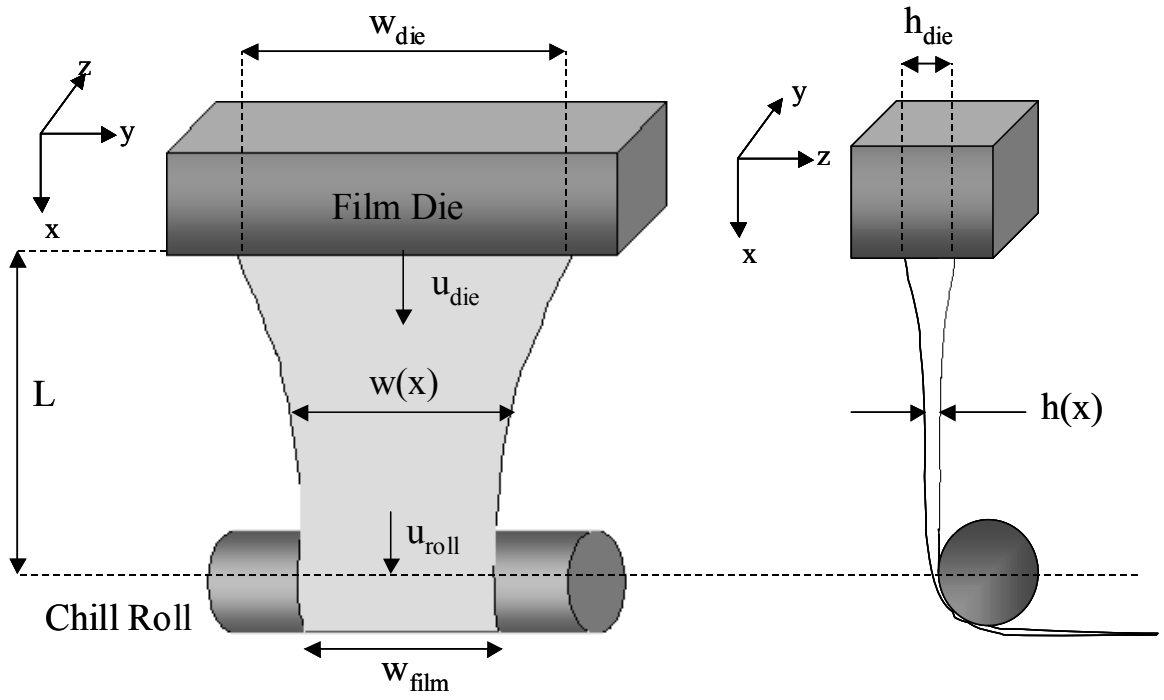


**Figure 2-3:** Schematic diagram of chill roll film casting **(Left)** Front view **(Right)** Side view

Since the polymer melt is an incompressible fluid, as the filmstrip is stretched in the machine direction, its thickness and width are both reduced. Thickness and width reductions are functions of draw ratio and length of the drawing zone. (Lamberti *et al.* 2001) The reduction in film width is known as the "neck-in" phenomenon. Shrinkage is defined as the ratio of the die opening width ($w_{die}$) to the width of the final film ($w_{film}$).

After the polymer exits the die, it undergoes shear free elongational flow as the material is stretched and oriented in the machine direction. In the drawing zone, the elongational viscosity is the dominant deformation mode. (Campbell and Kanai 1999) Dobroth and Erwin (1986) proposed a simple model for polymer flow in the drawing zone. According to this model, near the edge of the web, the streamlines are free to converge and thus form a thicker film. However, at the center, the polymer is constrained by the polymer

closer to the edge and the streamlines are essentially parallel. Thus, at the center, the polymer elongates in plane stress while the two edge regions elongate in uniaxial stress. Based on the stress strain conditions in each region, the following equations were derived to relate the film thickness at the chill roll ($h_{roll}$) to the initial film thickness ($h_{die}$).

$$\left( DR = \frac{h_{die}}{h_{roll}} \right)_{Center}$$

$$\left( \sqrt{DR} = \frac{h_{die}}{h_{roll}} \right)_{Edge} \qquad (2\text{-}2)$$

Edge stress effects are formed because of the differences between stress and strain conditions at the center and at the edge of the film. Dobroth and Erwin (1986) theoretically showed that the edge stress effect is the predominant cause of thick regions formed at the film edge known as “edge beads”. The width of the edge bead is directly dependent on the length of the drawing zone. Its thickness can be up to five times the thickness of the central part of the film. The edge beads create problems in winding, storing, and further processing of the film product. Therefore, the edge beads are usually trimmed, then recycled or scrapped.

Ito *et al.* (2003) experimentally studied the two-dimensional flow behavior of molten polymer film in the drawing zone by a particle tracking method and confirmed the Dobroth-Erwin’s theoretical model (Dobroth and Erwin 1986). In addition, they showed that the film thickness profile (both in center and at the edge of the film) in the machine direction could be fitted by an exponential model, similar to that for a Newtonian fluid.

$$h(x) = h_{die} \exp(-\beta_1 x) \qquad (2\text{-}3)$$

where x is the distance from the die in the machine direction, h(x) is the film thickness at distance x from the die, $h_{die}$ is the thickness of the discharge opening of the film die, and $\beta_1$ is a quantity related to planar extension rate at the die and initial polymer velocity.

Understanding the film casting process and polymer behavior in the drawing zone is necessary in predicting the film properties and improving the film quality. As will be described in the most pertinent examples cited below, a number of studies were conducted with a focus on mathematical simulation of the film casting process.

Yamada (1999) developed a mathematical model for vertical film casting of polyolefins. This model was used to predict film velocity, temperature, thickness, deformation rate, and take-up stress as a function of distance from the die in the machine direction (x). The results showed that in the drawing zone, the film velocity (u(x)) increased exponentially with increasing x, and this resulted in a rapid decrease in film thickness (h(x)). The film temperature (T(x)) appeared to decrease gradually and in a linear fashion with increasing x. Strain rate increased with distance from the die but its rate decreased gradually close to the die. Stress rate increased exponentially because of the increase in strain rate and film viscosity. Increasing the take-up roller speed resulted in an increase in the rate of change of film velocity, stress, and strain.

Smith (1997) developed finite element models for simulating one-dimensional and two-dimensional non-isothermal film casting from a viscous polymer. In each case, governing mechanical and heat transfer equations and boundary conditions were derived.

Profiles of important film properties such as velocity, width, thickness, and temperature were investigated under different processing and material conditions. It was shown that when the filmstrip contacted the chill roll, the geometry of the film remained unchanged. Therefore, Smith concluded that a model of the film casting process did not have to include the chill roll section. Comparison with the experimental data showed that the temperature of the film in the air gap was well fitted by a linear model. In addition, as the heat transfer coefficient increased, the temperature decreased more rapidly and resulted in a faster increase in the viscosity. This reduced neck-in and increased the portion of the film width with uniform thickness.

Silagy *et al.* (1999) reported an isothermal, Newtonian, time dependent, two-dimensional membrane model for film casting. The Newtonian hypothesis is relevant for poorly elastic polymers such as some linear low-density polyethylene samples. The focus of this study was on neck-in effect, edge bead effect, draw resonance, and film breakage at high take-up speeds. It was shown that an increase in the length of the air gap improved the stability of the process. d'Halewyu *et al.* (1990) also simulated the film casting process with a focus on neck-in and edge bead phenomena.

Lamberti *et al.* (2001) developed a model to predict width and temperature distribution in the drawing direction for an isotactic polypropylene resin. The process of stretching in air was modeled assuming steady state, incompressible flow, and constant temperature on each cross section. It was also assumed that film cross section stayed rectangular during stretching and that velocity in the draw direction was only a function of

distance from the die. In the drawing zone, the width and thickness of the molten film decreased as a function of the draw ratio and stretching distance. In addition, it was shown that the final film width decreased as the take-up velocity or extrusion flow rate increased. This model was also used to study crystallization and heat transfer in the drawing zone.

For the same polymer, Lamberti *et al.* (2002) investigated temperature distribution in the drawing zone. Temperature was experimentally measured as a function of flow rate and distance from the die with a narrow-band IR pyrometer. The measured temperature values and the predicted values by the model developed by Lamberti *et al.* (2001) showed relatively good agreement. The temperature estimation for the area adjacent to the die was not satisfactory. In addition, the experimental temperature data showed a plateau below the freezing line while the model predicted further temperature decrease for this region. One explanation could be that the heat released by the crystallization process balanced out the heat lost by the film.

Lamberti and Titomanlio (2005) modified the previous model by describing a new heat exchange coefficient which accounted for natural and forced convection, radiating exchange between film and surrounding air and film die. The comparison between the predicted temperature values by the new model with the experimental data showed a better prediction of the temperature distribution in the drawing zone.

In addition to the simulation work, a few studies were conducted with a focus on obtaining experimental data. This data is useful for investigating the film behavior in the drawing zone and for verification of the film casting models.

Canning *et al.* (2001) conducted film casting experiments with a low-density polyethylene resin. Experimental data on the rheological properties of the polymer melt, the film tension, the velocity profile, the width profile, the thickness profile of the solid film, and the edge bead effect were obtained. The profile of the film properties was similar to the modeling results discussed in this section. However, the film tension was found to be higher than previously estimated. The presence of a central region with plane stress elongation and thick edge regions with uniaxial stress elongation was confirmed. It was also shown that by increasing the draw ratio, the central region of the film expanded toward the edge and neck-in was reduced. In another study, Canning and Co (2000) compared the flow behavior of three polymers in film casting experiments.

Seyfzadeh *et al.* (2005) conducted film casting experiments with a commercial polyethylene terephthalate (PET) resin. Thermal and rheological properties of the polymer were investigated. In addition, velocity and temperature of the filmstrip was measured at different locations in the drawing zone by laser Doppler velocimetry method and an IR pyrometer, respectively. Experimental velocity and temperature profiles in the machine and transverse directions at different distances from the die were obtained. Similar to the simulated results, the velocity profile in the transverse direction showed an approximately flat profile in the central region of the film with lower velocities at the edge regions. The

velocity profile along the machine direction showed an overall increasing trend. The temperature profile in the machine direction decreased with distance from the die, the rate of change depended on other processing attributes such as draw ratio.

In another study, Aniunoh and Harrison (2006) investigated polypropylene film formation in the air gap in film casting experiments with process variables such as draw ratio and die temperature. The temperature, velocity and width profiles and centerline strain rate at different locations in the air gap were produced. Some of the observations for this polymer are listed below:

- Increasing the length of the drawing zone at constant draw ratio increased the degree of neck-in. Increasing draw ratio increased neck-in due to conservation of mass.
- Increasing the draw ratio (by either increasing the chill roll speed at constant polymer flow rate or by increasing the flow rate at constant chill roll speed) increased neck-in and decreased film thickness. This resulted in faster cooling at the central region of the film by conduction. Therefore, centerline film temperature at the chill roll decreased by increasing draw ratio.
- Velocity profiles showed higher velocities in the central part of the film and lower velocities at the film edges. This is due to the mechanism of the neck-in and edge bead phenomena.
- At centerline, the velocity increased with increasing distance from the die due to extensional flows in the web. The rate of velocity change increased by increasing draw ratio.

- Temperature profile in the transverse direction starts out as flat right after the die exit. Gradually, by increasing distance from the die, a u-shaped profile is developed with lower temperatures in the central region and higher temperatures at the edge regions. (~ 10°C difference)
- At low draw ratios, the centerline strain rate increased in the region close to the die. Then, began to decrease in the region close to the chill roll. This could be due to lower film temperatures close to the chill roll, which results in higher viscosity and higher resistance to flow. However, at higher draw ratios, strain rate continued to increase with increasing distance from the die. It is possible that the increase in tension applied to the film by increasing the draw ratio overcame the increase in resistance to flow.

In this work, defects in the polymer film are the focus. Characterization of such defects is the subject of the next section.

## 2.2 Characterization of Polymer Film Defects

The second objective of this work is to measure off-line the size, shape and other properties of film defects corresponding to properties of particles observed in the melt during in-line image monitoring. Initial experimentation revealed that simple visible light microscopy often provided very indistinct images. As will be seen below, some defect characterization studies have utilized polarized light. Also, since the defects often deformed the surface of the film it was thought that interferometry might provide useful information. Thus, polarized light imaging and interferometry were closely examined and, as will be seen

later, provided the needed off-line characterization methods for the defects. These two topics will now be examined in turn.

### 2.2.1 Off-Line Film Monitoring Using Polarized Light

An unpolarized wave such as that emitted by a light bulb is made up of waves with randomly directed electric fields. When the electric field is restricted to vibrate in only one or two directions, the light is said to be polarized. Originally unpolarized light can be transformed into polarized light by different methods including reflection and scattering. The simplest way is to send the light through a polarizing sheet (or a polarizer). A polarizing sheet is made by embedding long-chain molecules in a flexible plastic sheet and then stretching the sheet to align the molecules parallel to each other. The polarizing axis of the polarizer is perpendicular to the alignment direction of the long molecules. Only radiation parallel to the polarizing axis passes through the polarizer. (Hecht 1984, Halliday *et al.* 1993) The main ways of utilizing polarized light to provide images of film defects are examined in this section.

If two polarizers are placed in the path of a light beam, the amount of light that passes through is equal to the intensity of the incident beam multiplied by the cosine of the angle between their polarizing axes (Malus's Law). Crossed polarizers are two polarizer filters with perpendicular polarizing axes, therefore no light passes through them. The first filter is usually called a polarizer and the second one is called an analyzer. If a third polarizing filter is placed in between the crossed polarizers, it will rotate the plane of polarization of light coming from the polarizer. As a result, some of the light will pass through the analyzer.

If a birefringent material (such as anisotropic crystals or oriented polymer samples) is placed between crossed polarizers, linearly polarized rays are generated. After exiting the sample, these waves are out of phase and recombine with constructive and destructive interference when they pass through the analyzer. (Hecht 1984,Oldenbourg 1996)

In 1816, Sir David Brewster discovered that normally transparent isotropic substances could be made anisotropic by the application of mechanical stress. The phenomenon is known as mechanical birefringence, photoelasticity or stress birefringence. Under compression or tension, the material behaves as a uniaxial crystal with its effective optic axis in the direction of the stress. The level of birefringence is proportional to the stress. (Hecht 1984, Ryu *et al.* 1998) Photoelasticity is widely used in design engineering to study the stresses in both transparent and opaque mechanical structures. For an opaque object, a scale model of the part is made out of epoxy or polyester resins.

Unwanted residual stress in plastic parts can be introduced by poor design or poor processing conditions. Residual stress can cause distortion, cracks, deterioration of optical performance, and changes in mechanical properties. Therefore, reliable and practical stress testing methods are needed. (Redner and Hoffman 1997, 1999)

When a sample under stress is placed in between crossed polarizers, a color pattern and black fringes are observed in the image. These indicate a retardation and rotation in the polarized plane of the incident polarized light on the sample. Interference colors are related to the birefringence and thickness of the sample. (Hecht 1984)

Polariscopes are simple, bench top instruments that can reveal stress patterns in transparent samples qualitatively. Each color band of the fringe indicates a degree of stress in the sample. In addition, stress birefringence can be quantified using a compensator as described in ASTM D4093. Currently, computer based methods are developed to measure stress from birefringence patterns very quickly. The result is a non-destructive test that can be easily modified for on-line applications. (Redner and Hoffman 1997, 1999, Feingold 2005)

Of particular interest in this work are previous attempts to study or detect defects in products. Many applications in biology, materials science, crystallography, and mining rely on transmitted or reflected polarized light to detect defects or specific anisotropic items. A few examples are discussed here.

Plastic bags for pharmaceutical packaging are manufactured using separate sheets of semi-translucent plastic that are brought together and heat sealed along the edges. The quality of the bag is highly affected by the quality of the seal. Crossed polarized light is used to inspect the bags and look for uniformity in the resulting joint. Amount of light transmitted is related to the seal strength. Therefore, defects can be quantitatively detected and characterized by image thresholding and count analysis. (National Instruments Corp. 2006)

Angioplasty balloons are critical devices for treating blockages. Because of the critical nature of angioplasty, the balloon catheter must have excellent performance characteristics, and defects that may impair its mechanical properties must be eliminated.

However, microscopic defects can be formed during manufacturing. Tcharkhtchi and Anderson (2002) used a number of methods including optical microscopy with polarized light to detect and characterize elliptical defects on balloon surface.

Hackett Jr. (2004) reported using crossed polarized light for qualitatively inspecting film quality in medical device packaging. In this field, applications that can benefit from crossed polarized light are: inspection of film components of a package after transportation; non-destructive inspection of packages made from transparent film; and incoming inspection of films.

When a film is punctured or cut, it is stressed in an area larger than the actual puncture or cut. Based on visual characteristics of defects revealed by the polarized light and knowledge of processing steps, it is possible to find the sources of defects. For example, after close observation of different defects and processing stages, it was concluded that a selected defect was created during film manufacturing and not during transportation. Other applications are in detecting pinholes, impact of sharp objects on film, and even fingerprints. In general, when polarized light is used, defects have a much higher contrast with the background. This improves the probability that the human or machine inspector would actually detect them.

Kody and Martin (1996) studied the stress whitening of polymer composites during surface deformation. This phenomenon can severely affect product appearance and quality for applications such as automobile interior components. They developed a technique to

characterize the surface deformation of polypropylene-talc composites caused by scratching. Samples were first deformed in a controlled manner. The deformed area was analyzed with reflected polarized light in an optical microscope equipped with an image analysis system. Incident linear polarized light was reflected off the surface and the scattered light was collected after passing through the analyzer. Measuring the light scattered from the sample as a function of incident light polarization and sample orientation provided information about deformation properties. This was used to evaluate and improve the performance of these materials in surface-sensitive applications.

It can be seen from the above review that polarized light does have the potential for providing information-rich images of defects. The obvious problem is that the observed image is affected by quite a variety of factors. Thus, in addition to polarized light imaging, it was desired to include a second imaging method. This method is optical interferometry and is summarized below.

### 2.2.2 Off-Line Film Monitoring Using Optical Interferometry

When the molten film is stretched while gradually cooling, because of its incompressible characteristics and also because of a mismatch between particle and matrix mechanical properties, an asperity (positive change in surface profile) occurs on the top film surface. The height and area of this asperity depend on the size of the particle, film thickness, the original position of the particle in film thickness direction, and the load. (Gerlach and Dunne 1994, Gerlach *et al.* 1996) Although no previously published work using interferometry for polymer film defect characterization was found, it does appear that the

asperity characteristics of a defect should be able to be characterized by interferometry. The following paragraphs briefly describe why this should be so.

Interferometry is based on interference of two or more waves resulting in a new wave pattern. Properties of the resulting waveform depend on frequency, amplitude of starting waves, and their phase difference. When phase difference is 0, waves are in phase and their combination results in a constructive interference. When phase difference is 180°, a destructive interference occurs.

Interferometers are optical devices that can be used to measure lengths or changes in length with great accuracy by means of interference fringes. There are many different types of interferometers; a well-known example is Michelson interferometer as illustrated in Figure 2-4.

As shown in Figure 2-4, an interferometer consists of a half-silvered mirror (also called a beam splitter) that splits the light beam coming from a single source into two separate beams. Each beam travels towards a mirror and is reflected at the mirror then proceeds to the detector. After traveling paths of different lengths, these beams are recombined and interfere to form a fringe pattern. The optical path length difference for the two beams when they recombine is $2D_2 - 2D_1$. Anything that changes this path difference changes the phase between these two waves and therefore changes the fringe pattern. Distances can be accurately expressed in terms of wavelength of light by counting the

number of fringes through which the fringe pattern shifts as a result of a path length change. (Halliday *et al.* 1993, Olszak *et al.* 2001)

During the measurement, the reference arm of the microscope containing the interferometric objective moves vertically to scan the sample surface at different heights. Fringe contrast at a single sample point is at maximum when the point is in focus. The measurement starts at above focus and the system scans through focus as the camera captures frames of interference data at evenly spaced intervals. As the reference arm moves downward the interference signal for each point on the surface is recorded. Finally, the vertical position corresponding to the peak of the interference signal is extracted for each point on the surface. (Veeco Instruments Corp. 1999)

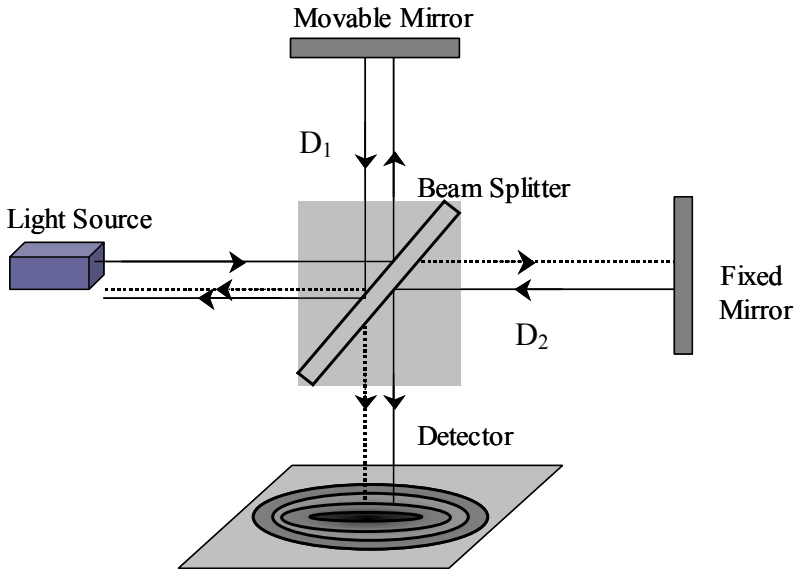


**Figure 2-4:** Schematic diagram of a Michelson interferometer

### 2.2.3 Image Processing

In this work both polarized light and interferometry methods provide images. Thus, in both cases, image processing is necessary. Although today image processing is relatively easily accomplished because software to accomplish it is readily available, there are an incredible variety of options associated with how an image is converted to information and what measures are used to express this information.

Digital images are in fact matrices where each matrix element represents the value of a pixel on the image. In gray scale images, the value of each pixel or its brightness varies from 0 for black to 255 for white. Color images in red, green, blue (RGB) color space have three values for each pixel representing the brightness of each color channel.

Pixel values can have different meanings depending on the type of the image. In light intensity images, pixel brightness represents the intensity of light reflected or transmitted by that point on the object. This pixel value is dependent on variables such as light source intensity, surface orientation, color, texture, density, and thickness. (Russ 1999)

Range images such as the images acquired by optical interferometers contain distance information. In other words, pixel brightness of a range image shows the elevation of each point on the surface. (Russ 1999) The original distance values are normalized between 0 and 255 to create a gray scale (or a pseudo color) image.

Aspects of image processing particularly important in this work are image segmentation and feature extraction. Image segmentation is the separation of objects of interest from the background. After image segmentation, feature extraction is the method used to obtain the desired information about the object.

The main characteristics of interest concern size, shape and color (or grayscale brightness value) of the object. For each of these, there are multiple quantities that can be obtained depending upon the image processing software used. Furthermore, three-dimensional quantities can also be obtained from range images or calculations using the two-dimensional image information along with shape assumptions, etc. The defect on an image is often composed of two main portions: the particle causing the defect and the distorted film. The intention in this work was to obtain information on both portions from the off-line images so that the particle causing the defect could be unambiguously identified.

## 2.3 Mathematical Modeling

The third objective is to develop a mathematical model, which will relate in-line particle properties, extrusion conditions, and film properties to defect properties. Thus, the model needs to be developed with the available data in mind. In this work almost all of the data (with the exception of film thickness and take-up roller speed) is obtained from polarized light and interferometric images. As described in the previous section, image processing converts images into data. The quality of this data is also very important to the modeling.

Image processing is renowned for providing many measures of objects visible in an image. Selecting the measures that are most useful to the development of a model is vital. This image object "feature selection" or "attribute selection" as part of exploratory data analysis is examined in Section 2.3.1. Regarding the actual mathematical modeling itself, data mining methods are needed. Data mining is the field that encompasses methods of model development that can deal with large quantities of data. In this case there are three main types of data mining methods potentially involved: clustering, classification, and regression.

Clustering refers to methods of identifying "families" or "groups" of defects evident from the data. The specific combination of measured properties of defects along with the range of their values needed to define the groups must be determined. There are many empirical methods available to do such "clustering" into groups. Clustering methods can be used with different combinations of attributes from the database in an exploratory way to see what groups can be defined from the data.

Once clustering is done then a classification model can be developed. A classification model relates specific a priori information (e.g. film thickness, particle size) with the appropriate "family" or "group" of defects identified by clustering. Once developed, a classification model is thus used for a categorical prediction.

The third major data mining method is regression. Regression aims at developing an equation that relates specific properties of a defect (e.g. defect area) to information available a priori. A developed regression model predicts quantitative defect property values.

These three data mining methods are briefly examined in Sections 2.3.2 and 2.3.3. Many entire books are available on these methods. Also, regression methods in particular are now the subject of undergraduate engineering courses. So, in Sections 2.3.2 and 2.3.3, only the most pertinent information is provided along strong reliance on the appropriate references.

For many industrial situations, especially in the financial area for example, data mining is applied very empirically. The main reason for that is that there is generally no useful theory to guide the model development. Also, the resulting models often perform very well, even when used for extrapolating beyond the range of the data used to develop the model. In Chemical Engineering, "mechanistic" models are usually the objective. The work attempts to identify dominant mechanisms and model them in a semi-empirical way by finding the values of unknown "parameters" in the model. "Purely empirical" modeling is sometimes done but such models are often considered not reliable for extrapolation beyond the range of the data used to develop the model.

In this work it was generally anticipated that very likely only a "purely empirical" model would be able to be developed. The main reason for this is the complexity of the physical situation coupled with the inability to measure, or perhaps to even identify, all of the

important variables. This is shown in Section 2.3.2 where previous modeling attempts relevant to this work are summarized. Finally, despite the complexity, a very simple new mechanistic model was developed and is summarized in Section 2.3.4. This model will be tested in this work.

### 2.3.1 Selection of Particle and Defect Attributes

Typical image processing software provides a very large number of features, many of which measure nearly the same characteristic with a concomitant large amount of redundant information. Simply proceeding with mathematical modeling using all of the variables would likely give useless results. The following criteria were developed in this work to assist attribute selection to find the most useful measures of particles and defects from the images obtained:

- **Relevance**

  An attribute needs to assist in the description of the defect allowing for limitations of the data collected. For example, values of color co-ordinates for a dataset (such as the one employed here) consisting of only grayscale images would be irrelevant for this study but not for a future study employing colored images. Testing for relevance can often be done by such simple reasoning. Inclusion of irrelevant attributes to the clustering can add noise (reproducibility) and bias (accuracy) problems in predictions.

- **Reproducibility**

  Random variability in the values of an attribute originating from uncontrollable factors can ruin the utility of an attribute. Variability originating from different types

of defects (i.e. defects whose images appear different) is highly desirable. Variability, which is random noise, conceals this desirable variability. Evaluation of variability is required to distinguish between the two sources.

- **Redundancy**

  When one attribute communicates exactly the same type of information as another about a defect then one of the attributes is redundant. A test for this is if the value of one attribute can immediately be predicted when the corresponding value of another attribute is known then one of the attributes is redundant.

  For example, one of the reported attributes ("Per-Area") is equal to the ratio of the object area to the overall image area. However, the image area is a constant for the data of this study, making "Per-Area" a redundant attribute synonymous with object area. If redundant attributes are not removed from the database then the effect is similar to entering that attribute value twice: that attribute is given double weighting. If many redundant attributes are permitted they can overwhelm the clustering and provide very unreliable results.

- **Sensitivity**

  This is the case where an attribute is relevant to describing defect type but does not vary significantly when different appearing defect images are examined. Classification requires attributes whose values can be used to distinguish one type of defect from another. Examination of variability of the attribute values for defect images that appear very different compared to the reproducibility of the attribute

values on defects that appear very similar can serve to assist sensitivity. As for irrelevant attributes, allowing insensitive attributes to enter the modeling can cause problems especially when reproducibility or accuracy of these attributes influences results.

- **Accuracy**

  In obtaining a useful understanding of a system, often, the degree to which the value of an attribute is "true" can be less important than the degree to which the value is "consistent". However, if an attribute value, for example an area value, is consistently computed biased towards say a lower value than is correct then the attribute may be fine for the database of the thesis but may cause problems when attempts to extend the model to new defect types are tried. Consistency tests employing ideal shapes of particles and comparing different attribute values can reveal inaccuracy.

Methods termed "exploratory methods" in data mining can be used to assist attribute selection. The first step in exploring the data is to study the descriptive statistics and the distribution of each attribute. The relationship between multiple attributes can be investigated by methods such as correlation matrices and scatter plot matrices. (Witten and Frank 2000, Kantardzic 2003) This combined with the definition of the property measured by each attribute provides valuable insight into the relationship between attributes.

In the literature, attribute selection is often closely coupled to the mathematical modeling work. For example, different sets of attributes are selected, often based upon unstated criteria, and tested in a clustering algorithm. The selected attributes are those that accomplish the best clustering. Therefore, the work in the literature associated with attribute selection will be examined together with the work on clustering and classification modeling in the next section.

### 2.3.2 Clustering and Classification Modeling of Defects

Hierarchical clustering can provide information about the natural clusters in a dataset and approximate number of them. Algorithms for this clustering method are divided into two categories: divisible algorithms (start from the entire dataset and partition it into smaller subsets.), and agglomerative algorithms (start with each instance as a cluster and merge the clusters based on similarity between them.). (Kantardzic 2003)

There are many similarity measures (depending on the type of attributes) that can be used to investigate the similarity between different instances. Amongst the most commonly used are: Euclidean distance, city block distance, Pearson correlation, and Minkowski distance. (Kantardzic 2003)

Classification models assign a new defect to a particular cluster (or, synonymously, “group” or “class”). An important objective of defect inspection and classification is the early detection and identification of manufacturing process problems. While defect detection

is critical for ensuring product quality, defect classification provides the information necessary to correct process problems. (Chou *et al.* 1997)

In classification learning (or supervised learning), the goal is to predict the class of a new case based on a set of instances with known outcome or class values. Classifiers use different algorithms to split the data into different sections based on the class attribute value and to develop rule sets. These rule sets (in the form of decision tables, decision trees, etc.) can be used to predict the class of a new instance. (Witten and Frank 2000)

One area where defect clustering and classification modeling has been investigated is in paper manufacturing. The presence of defects on paper surface can significantly affect paper quality and lower its value. Defects can be due to a number of reasons depending on the manufacturing processes and the machinery involved. Many paper inspection systems have been developed over the years to detect product defects. In most cases, the main objective is to find the association between different defect types and defect causes to fix the problem.

Kunttu *et al.* (2003) reported a clustering method for grayscale paper defect images generated by an inspection system. First, gray scale paper defects were segmented from the background using a segmentation algorithm developed in the same research group. From the segmentation results, the defect boundary was obtained. Two groups of defect properties, gray level and shape features were used for defect characterization and later for classification. Some representative sample images were manually selected to form a training

set which was hierarchically clustered. The rest of the defect images were clustered using these results and the k Nearest Neighbor (KNN) method. Euclidean distance was used to find the distance between attribute values.

Gray level distribution of paper defect images can be represented by first order statistical measures such as a histogram or by second order measures such as a correlogram or co-occurrence matrices. A histogram is commonly used due to its low computational cost. In this study, gray level histogram of only the segmented paper defect was selected as one of the defect features. Defect histograms were compared using the histogram intersection method. (Swain and Ballard 1991)

Shape is an important characteristic of an object. The goal of shape recognition is to find a description, which contains sufficient information to distinguish between differently shaped objects. (Iivarinen *et al.* 1998) Manual inspection of the paper defects revealed three major groups of defects based on their shape: circular, elongated, and complex. Three shape descriptors selected for defect characterization were compactness ($(\text{Perimeter})^2/\text{Area}$), ratio between major and minor axes, and convexity ($(\text{Perimeter})_{\text{convex hull}}/\text{Perimeter}$). (Appendix 4-II) The first level of hierarchical clustering in this dataset was based on defect shape and the second level was based on defect gray level. Root causes of different defect types were known beforehand. Therefore, from the defect images captured during production and the final clustering results, the cause of each defect can be tracked down.

Similarly, an adaptive texture and shape based defect classification method was proposed by Iivarinen *et al.* (1998), Iivarinen and Rauhamaa (1998), Iivarinen *et al.* (2000), and Iivarinen (2001). In this work, grayscale images of paper defects were acquired by an in-line inspection system. Defects were segmented from the background using a special segmentation algorithm. A set of morphological filters was applied to smooth the contour. The shape of the defect boundary was characterized by five shape descriptors. The internal structure of the defect was characterized by its gray level histogram and a set of texture features calculated from the co-occurrence matrix. Texture features included mean, energy, contrast, and entropy of the co-occurrence matrix. Each feature group was used to classify the defects; the results were then combined for final classification.

Automatic inspection of defects on printed circuit boards (PCBs) in semiconductor industry has also received considerable attention. Blaignan *et al.* (1995) presented a visual detection and classification method for solder joint defects on PCBs. Once a faulty solder joint is detected, it is important to find out what type of flaw it is in order to determine the cause of it and to correct the problem. The shape of the solder joint was observed to be the major difference between flawless and defective joints. Defect patterns were related to the curvature of the solder joint contour. The criteria for defect detection were nature of the contour curve (open, closed) and number of sign changes of the contour curve.

An automated defect classification system for detecting and classifying defects on semiconductor chips at various manufacturing steps was reported by Chou *et al.* (1997) This system was deployed in the IBM Burlington 16M DRAM manufacturing line. Measured

defect features included: size features (area and perimeter of convex hull bounding curve), shape features (roundness and elongation), color measurements (first and second moments of the red, green, and blue color values), composition features, location features, and color contrast between the defect and its surrounding area.

Laitinen *et al.* (1990) developed a system capable of detecting and classifying defects in copper alloy strips, which was installed for evaluation in a production line in a rolling mill. A special illumination setup was designed to help distinguish between 2D and 3D defects. With this setup, slightly sloped parts of 3D defects appeared brighter than the background while 2D defects appeared darker than the background. Grayscale images were pre-processed by applying dilation and erosion filters. The defect segmentation algorithm was morphology based dynamic thresholding and background subtraction method. Segmented defects were characterized by size, shape, local contrast, and orientation features. In the next step, defects were classified based on the measured defect features and using a tree classifier algorithm.

Zhang *et al.* (2006) reported an automatic method for classifying defects on the product surface after grinding and polishing. Grinding and polishing are standard operations in material processing to improve the dimensional accuracy and surface quality of the product. In this research, a number of feature extraction methods were examined. These methods included: shape features, Laws filter bank, Discrete Cosine Transformation (DCT) filter bank, Gabor filter bank, and statistical features based on co-occurrence matrix. Defect classification results based on each set of features were compared. It was shown that

combining the Gabor filter features and statistical parameters had the highest right classification rate.

van Helvoirt *et al.* (2005) studied the optical disk defects by a normalized mirror signal. By time-series mapping, this signal is mapped to a set of descriptive signal features that form the input for the clustering phase. The input data was clustered by an agglomerative hierarchical clustering algorithm (Ward Linkage) and Euclidean distance; results were illustrated in a dendrogram plot. Based on this plot and the distance between clusters, six defect classes were selected. To obtain a single representative for each class, a $15^{th}$ order least-squares polynomial was fit to the signals grouped in each cluster. A new defect is classified based on the Euclidean distance between its feature vector and those of the six defined classes. The class should yield the smallest distance value.

### 2.3.3 Regression Modeling of Defects

Regression is the fitting of equations to data. In general, in the published film defect literature, when lines need to be fit for mathematical modeling of defects there is little or no information on the details of the method of fitting used. In this work, more attention is paid to these details with the objective of better defining the effects of random error on the results. Both linear and non-linear regression methods are used. Both obtain the best fit to the data by minimizing the sum of squares of the distance from the experimental value on the ordinate axis to the value on the line. That is the sum of squares of the error (SSE) is minimized often using the reciprocal of the error variance of the y value ($\sigma^2$) as a weighting factor to emphasize the most precise data:

$$SSE = \sum_{i=1}^{n} \frac{1}{\sigma_i^2} \left( y_{i,\exp} - y_{i,line} \right)^2 \tag{2-4}$$

where $y_{i,exp}$ is the experimental y value and $y_{i,line}$ is the predicted y value by the fitted line. When the equation of the line is linear in all of the unknown coefficients then linear regression is used. When it is non-linear in any of them then non-linear regression is used.

Often in this work a regression line through the origin is found to be the best fit:

$$y_i = b_2 x_i \tag{2-5}$$

Applying the error propagation equation:

$$\text{var}(y_i) = \left( \frac{\partial y_i}{\partial b_2} \right)^2 \text{var}(b_2) = x_i^2 \, \text{var}(b_2) = x_i^2 s_{b_2}^2 \tag{2-6}$$

where $s_{b2}$ is the standard error of the slope.

So, the prediction limits for the predicted value of y on the line at a significance level of α are:

$$y_i^{\pm} = b_2 x_i \pm t_{1-(\alpha/2),n-1} \sqrt{\text{var}(y_i)} \tag{2-7}$$

$$y_i^{\pm} = b_2 x_i \pm t_{1-(\alpha/2),n-1} s_{b_2} x_i \tag{2-8}$$

$$y_i^{\pm} = (b_2 \pm t_{1-(\alpha/2),n-1} s_{b_2}) x_i \tag{2-9}$$

Eqn. (2-9) describes the two lines corresponding to the upper and lower confidence limits for the slope. The difference between these limits is known as the confidence interval about the mean response at a specific x value. The meaning at a significance level of 5% is as follows:

If the experiments were repeated, a new fitted line obtained and the 95% confidence interval about this line computed and then this procedure was repeated again and again for 1000 such lines, about 950 of those intervals would contain the mean value of y at a specific value of x as predicted by the "true" straight line model and about 50 would not. It's an effort to account for the fact that only a few data points are being used each time to obtain the estimates of the coefficients. It is a way of estimating what the predicted value of y would be if a very large number of data points were used to obtain the coefficient values.

Another commonly used quantity to provide an estimate of the "average" scatter of data about the fitted line is the "standard error of the estimate". It is defined as:

$$s_{y/x} = \sqrt{\frac{\sum_{i=1}^{n} (y_{i,\exp} - y_{i,line})^2}{n-p}} \tag{2-10}$$

where $y_{i,exp}$ is the experimental y value and $y_{i,line}$ is the predicted y value by the fitted line, n is the number of observations, and p is the number of coefficients.

Estimation of the prediction limits for a new value of y then requires Equation (2-11):

$$y_i^{\pm} = b_2 x_i \pm t_{1-(\alpha/2),n-1} \sqrt{\frac{s_{y/x}^2}{m} + s_{b_2}^2 x_i^2} \tag{2-11}$$

where m is the number of replicate measures of y at a particular value of x. As m becomes very large, Eqn. (2-11) approaches Eqn. (2-9) (Lavagnini and Magno 2007)

Eqn. (2-11) says that if there are 1000 replicate sets of data and each set is fit with a straight line through the origin and the limits provided by Eqn. (2-11) are calculated each time, then at a significance level of 5%, 950 of these limits will include a new y value at a specific value of x that is the average of m measurements and about 50 will not. This quantity is termed the $100(1-\alpha)\%$ prediction interval on a future observation of y at a specific value of x.

The standard error of the estimate is also an estimate of the error standard deviation of the experimental y values. In this work that fact is used to provide weighting factors in specific fits. A plot of residuals, the difference between the experimental value of y and the value of y on the fitted line versus the value of x, is often used to provide a visual estimate of the value of the fitted line to the data. In some parts of the work the two parameters in an exponential equation are obtained by a weighted least squares fit in accordance with Eqn. (2-4). It is possible to define prediction intervals and confidence intervals for such equations. However, the uncertainty in these boundaries is quite high because a continuous variation of weighting factors with the x value needs to be defined. In those cases only the standard error of the estimate and a plot of the fitted line to the data accompanied by a plot of residuals is provided.

Finally, another commonly used measure of the degree of fit of a line to data is the multiple correlation coefficient squared ($R^2$). It is given by:

$$R^2 = 1 - \frac{\sum_{i=1}^{n} (y_{i,line} - y_{i,\exp})^2}{\sum_{i=1}^{n} (y_{i,\exp} - y_{mean})^2} \quad (2\text{-}12)$$

$R^2$ is the fraction of the total sum of squares of the y values accommodated by the fit. However, this equation is only used if the fitted line has a non-zero intercept. For a line passing through the origin, $R^2$ is given by:

$$R^2 = 1 - \frac{\sum_{i=1}^{n} (y_{i,line} - y_{i,\exp})^2}{\sum_{i=1}^{n} y_{i,\exp}^2} \quad (2\text{-}13)$$

The value of $R^2$ based on Eqn. (2-13) represents the fraction of the total sum of squares of the y values from zero and accommodated by the fit.

### 2.3.4 Mechanistic Modeling

The presence of filler or contaminant particles in polymer films has the potential to create defects that could affect aesthetic or mechanical properties of the film. To understand and model the defect formation process, it is important to learn how particles influence the surrounding polymer matrix. In mechanistic modeling the objective is to identify dominant mechanisms and to explain them by reference to physical causes. This section presents a summary of published literature and mechanistic models on the influence of foreign particles on a polymer matrix during different processes.

Gerlach *et al.* (1996) developed a model to investigate the influence of filler particles on surface geometry in polyethylene terephthalate (PET) uniaxially drawn film. During the

processing of this film, surface friction between successive film layers can cause quality problems in the high speed winding process. Variable contact over the roll length makes the process unreliable and can permanently distort the film product. To reduce the friction, particles are embedded in the molten polymer near the surfaces. It has been confirmed that the friction and the film optical properties are influenced by the particle geometry, their positions, and the particle volume fraction. In this paper the influence of rigid, spherical particles on surface characteristics of PET film during manufacturing was studied. This was achieved by modeling the process of stretching of particle-filled PET using a non-linear finite element solver.

Gerlach *et al.* (1994) developed and implemented a large strain elastic viscoplastic constitutive model for particle-filled PET film. Particles act as stress raisers leading to localized high strain regions. Due to the highly non-linear strain-stress behavior of PET, the stresses near the particle rapidly become large, leading to matrix deformation such as voiding and debonding. Localized stresses lead to localized polymer chain alignment, crystallite formation, and strain hardening. This creates an inhomogeneous microstructure and results in a mismatch between the plastic strains imposed on different components in the system. In the model, the residual type stress distribution due to the inhomogeneous deformation is modeled by introducing an internal variable called “back stress”. This model was used to investigate stress distribution around the filler particles in PET films.

To draw the film, a load is applied on the particle/ polymer matrix system and the model is considerably stretched in the direction parallel with the applied force. However, due

to the incompressible characteristics of the material, this stretching results in a reduction of the film thickness. Presence of the particle reinforces the polymer matrix locally; as a result an asperity on the free surface close to the particle is formed. The surface deformation may be characterized by the maximum asperity height and a measure of length over which the asperity occurs. The height of the deformed area and stresses near the particle decrease rapidly around the particle and reach the matrix values. (Assuming that there is no particle-particle interaction.) (Gerlach *et al.* 1996)

Gerlach *et al.* (1996) showed that the asperity height increased rapidly with increasing particle diameter and more gradually with decreasing depth. The asperity length increased with increasing particle diameter or length. Since particles lead to large gradients in stress and strain local to the particle, an increase in particle diameter or a decrease in particle depth is likely to increase the influence of the particle on the top boundary. Positioning the particles deeper in the film extends the zone of influence and increases the asperity length. (Gerlach *et al.* 1996)

In heterogeneous polymer systems, such as the particulate filled composites, stress distribution around the particles determines micromechanical deformations and as a result macroscopic properties. Basic micromechanical deformations in polymers are shear deformation and crazing, which may be accompanied by particle debonding. Other studies have shown that the initiation of shear deformation and crazing depends on the local stress distribution around the particle, which is affected by thermal stresses. In general, three main

factors determine the stress distribution and possible deformation mechanisms: stress concentration, thermal stresses, and matrix-particle interaction. (Voros and Pukanszky 1995)

Voros and Pukanszky (1995) developed a model based on an interlayer with continuously changing properties to describe stress-strain behavior of filled polymers. In this model, it was assumed that an interphase spontaneously formed around the inclusions in particulate filled composites.

One of the major causes of stress around an inclusion is the mismatch between matrix and inclusion thermal properties. This can be a dominant factor in stress development in film casting. Harris (1978) proposed a simple model to calculate the residual stresses in polyester/glass composites that arise upon cooling. Brassell and Wischmann (1974) studied epoxy-urethane polymer filled with $Al_2O_3$ particles and determined mechanical and thermal expansion properties of this composite at ambient and liquid nitrogen temperatures. The authors provide a good background on the thermal expansion theory and coefficient estimation.

Depending on the thermal expansion coefficient of the filler particle ($\alpha_f$) and the polymer matrix ($\alpha_m$), a positive ($\alpha_f > \alpha_m$) or a negative ($\alpha_m > \alpha_f$) mismatch between filler and matrix exists. Generally, in polymer composites, the filler has a much higher modulus and a much lower thermal expansion coefficient, which creates a negative mismatch. As the composite is cooled, stresses develop around the filler particle due to the mismatch between the thermal expansion coefficients. For a negative mismatch, upon cooling, the polymer

matrix contracts or shrinks more than the filler particle. Therefore, the particle is subjected to radial compressive stresses, which act as a mechanical bond between the particle and the matrix. As a result, chemical bonding is unnecessary for load transfer. Some of the parameters used in this model depended on particle shape and size. (Brassell and Wischmann 1974)

### 2.3.5 Development of a Theoretical Model: Constant Defect Volume Per Unit Particle Area Model

The literature cited in the previous section shows that many factors will influence the generation and appearance of a film defect. The new model developed in this section focuses upon two characteristics of defects that appear particularly important to film quality: the degree to which the area of a particle is magnified by the defect as defined by the magnification as well as by the average defect height. These two characteristics are henceforward referred to as "primary defect properties". Magnification (M) is equal to the area of the defect divided by the area of the particle that caused the defect. (Eqn. 2-14) Average defect height (H) is equal to the ratio of defect volume to defect area. (Eqn. 2-15)

$$M = \frac{A_{DP}}{A_P} \tag{2-14}$$

$$H = \frac{V_{DI}}{A_{DP}} \tag{2-15}$$

where $A_{DP}$ and $A_P$ are the area of the defect and the embedded particle obtained from polarized light imaging, respectively. $V_{DI}$ is the volume of the defect obtained by interferometry.

The product of magnification and average defect height is the volume of the defect per unit particle area. This model assumes that this product is constant for all defects produced at one particular set of processing conditions. In this work it means that film thickness is constant and that all particles are the same shape.

$$HM = \frac{V_{DI}}{A_P} = constant \tag{2-16}$$

The volume of a defect is considered synonymous with the volume of a strained region of polymer surrounding the embedded particle.

Defect area is a two dimensional, overhead (area) view of this strained volume for each particle. As the film is stretched, the degree to which this viewed area increases depends upon deformation of the strained volume associated with a particle. When the strained volume is subjected to stress, the extent to which it deforms depends upon the magnitude of the stress applied, the time allowed for deformation of the volume and the resistance of the polymer surrounding the strained volume. The viscosity is a function of the polymer, the temperature and the rate of elongation.

To appreciate the influential variables involved in defect formation, a model of the film casting process can be examined. The work of Yamada (1999) provides a particularly useful model. The strain rate and stress tensors ($\|d\|$ and $\|\sigma\|$) derived by Yamada (1999) for an arbitrary point at distance x from the die in the drawing zone in film casting process are shown in Eqns. (2-17) and (2-18).

$$\|d\| = \begin{Vmatrix} d_{xx} & 0 & 0 \\ 0 & d_{yy} & 0 \\ 0 & 0 & d_{zz} \end{Vmatrix} = \frac{Q}{wh} \begin{Vmatrix} -\left\{\frac{1}{w}\frac{dw}{dx} + \frac{1}{h}\frac{dh}{dx}\right\} & 0 & 0 \\ 0 & \left\{\frac{1}{w}\frac{dw}{dx}\right\} & 0 \\ 0 & 0 & \left\{\frac{1}{h}\frac{dh}{dx}\right\} \end{Vmatrix} \tag{2-17}$$

$$\|\sigma\| = \begin{Vmatrix} \sigma_{xx} & 0 & 0 \\ 0 & \sigma_{yy} & 0 \\ 0 & 0 & \sigma_{zz} \end{Vmatrix} = \begin{Vmatrix} -\frac{2Q\eta}{wh}\left(\frac{1}{w}\frac{dw}{dx} + \frac{2}{h}\frac{dh}{dx}\right) & 0 & 0 \\ 0 & -\frac{2Q\eta}{wh}\left(\frac{1}{w}\frac{dw}{dx} - \frac{1}{h}\frac{dh}{dx}\right) & 0 \\ 0 & 0 & 0 \end{Vmatrix} \tag{2-18}$$

where Q is the polymer volumetric flow rate, w (same as w(x)) is the film width at distance x from the die, h (same as h(x)) is the film thickness at distance x from the die, and η is viscosity of the polymer.

Gravitational, drag, and friction forces are considered negligible compared with the viscosity related force. In addition, the neck-in and edge bead effects are assumed to be negligible. ($\frac{dw}{dx} = 0$) As a result, at steady state, the tension applied to the film by the rotating take-up roller (F) is balanced by the force within the film in the machine direction at a distance x from the die according to:

$$F = \sigma_{xx} wh = -2Q\eta \frac{2}{h}\frac{dh}{dx} \tag{2-19}$$

Based on Yamada's experimental data and Eqn. (2-3), the film thickness is expected to decrease exponentially from the extruder die to the film take-up roller:

$$h = \beta_o \exp(-\beta_1 x) \tag{2-20}$$

$$\frac{d \ln h}{dx} = -\beta_1$$

$$\frac{1}{h}\frac{dh}{dx} = -\beta_1$$

Then, Eqn. (2-19) becomes:

$$F = 4Q\eta\beta_1 \tag{2-21}$$

Eqn. (2-21) shows that the force on the strained volume is a product of the polymer volumetric flow rate (Q, a constant), the viscosity ($\eta$) and $\beta_1$, a quantity related to planar extension rate at the die and initial polymer velocity. (Eqn. 2-20) At high roller speed, film thickness will be lower and the initial planar extension rate greater. Thus $\beta_1$ increases for extruder runs providing lower film thicknesses. Viscosity is affected by both the rate of elongation and temperature.

There are two temperature gradients of interest: the gradient extending from the film/roller interface to the film/air interface and the gradient from the extruder die to some point beyond the first contact point of the film with the roller. Much of the literature indicates that the former gradient is not significant: film temperature is constant with film depth. So, assuming no variation of temperature with film depth and considering only the second mentioned gradient, the important aspect is that a thicker film would cool more slowly than a thick film.

The Yamada model deals only with a homogeneous film: no particles are present. A particle is essentially a spot of infinite viscosity. This spoils the force balance because it creates a point that will not deform. The particle will be carried by the surrounding polymer while the strained volume will deform around it. So, Yamada's work is limited to providing an indication of the important variables for defect formation via Eqn. (2-20). Of course it also does not include any particle properties that may participate in defect formation.

Interpretation of experimental data necessitates that plots of magnification (M) versus polymer thickness ($h_{film}$) be fit by an equation. The following equation is proposed:

$$M = b_o \exp(b_1 h_{film}) \tag{2-22}$$

where $b_0$ and $b_1$ are constants.

A first reason for this exponential equation form is based upon Equation (2-21) showing that viscosity is a very important variable. Viscosity generally varies exponentially with temperature: lower viscosities (contributing less resistance to deformation) corresponding to higher temperatures. As mentioned above, thicker films would be expected to be hotter for longer times than thinner films. With all conditions relevant to heat transfer being equal except the final film thickness then the time required for the film to cool sufficiently to stop all deformation would be proportional to the film thickness (i.e. the film mass). Also, roller speed is slower for thick films than for thin films. So the former will have more time to cool. Thus, if viscosity is the dominant variable, then the resistance to deformation would decrease exponentially (as temperature increased linearly, proportional to final film thickness) with increasing final film thickness. The defect volume would then

experience exponentially larger deformations and defect areas for thick films than for thin films. This rationalization is certainly an oversimplification. For example, it assumes that the variation of $\beta_1$ with film thickness does not affect the situation. Also, as the glass transition of the polymer is approached the exponential relationship of viscosity and temperature is no longer valid.

A second, more straightforward, reason is that the exponential form provides simple, necessary, complementary expressions for average defect height and magnification. Since it is assumed that the total strained volume per unit area of particle is a constant, then it would be expected that the average height of a defect generated by a particular particle would decrease sufficiently to accommodate the increase in defect area. In addition, the residual plot of the exponential model showed slightly lower residuals compared to those of other tested models (linear, logarithmic, polynomial, and power law models). If we assume an exponential form for the variation of average defect height with film thickness:

$$H = a_0 \exp(a_1 h_{film}) \tag{2-23}$$

where $a_0$ and $a_1$ are constants, then the product of average defect height (H) and magnification (M) is given by:

$$HM = a_0 b_0 \exp((a_1 + b_1) h_{film}) \tag{2-24}$$

This product represents the volume of the defect per unit particle area. If the data shows that $a_1$=-$b_1$ then HM is a constant ($a_0 b_0$).

## 2.4 Overview

The above sections have reviewed the previously published literature pertaining to the objectives of this work. Regarding the first objective, the formation of polyethylene film using chill roll casting is a well-known industrial process. However, although film defects are an extremely important industrial concern, intentionally forming defects in the film by injection of particles is novel. Characterizing particle and defect properties, the second objective of the work, employed two well known analytical methods: polarized light imaging and interferometry. Although polarized light imaging has been used for film defects, the exact design of off-line equipment needed to be deduced. No mention of using interferometry to characterize film defects appears in the published literature.

Furthermore, although in-line images of the particles in the melt were available, it is recognized that assigning the image of a defect obtained off-line to the corresponding particle image obtained in-line was not possible. It is proposed that since the particle is embedded in the defect, the image of the particle in the defect can be used to obtain the particle properties for purposes of investigating the relationship between particle and defect properties. Then the defect properties for that particular particle can be obtained from the remainder of the image. Once the relationship is known from this investigation then, in practice, the particle properties would be obtained from in-line melt monitoring and the defect properties predicted.

The third objective, mathematical modeling appears to be the most significant challenge of all. Selecting the correct particle and defect measures to use in the modeling

("attribute selection") was a major task because of the large number of such measures and their inter-correlation. However, in published work related to film defects, often attributes are selected based upon the demands of complex flow models for film casting and flow around particles. Alternatively, sometimes those selected are the attributes that were empirically found to provide the most effective clustering and classification results for very different systems than are to be utilized in this work. Powerful data mining empirical approaches (notably clustering and classification) are now readily applied with commercial software. Linear and non-linear regression methods are commonly used in Chemical Engineering but their use is barely mentioned in the published literature with regards to defect modeling.

In this work, special attention was paid to the details of regression to better define the effects of random error. The complexity of the film casting/defect creation process implies that only an empirical model will be possible. However, a simple, new mechanistic model "the Constant Defect Volume Per Unit Particle Area" model for describing the relationship between film thickness, particle area, defect area and average defect height (where the latter two are termed "primary defect properties") was developed in Section 2.3.5 and was tested in this work.

In the next section the experimental and computational approaches developed in this work are detailed.

# 3 EXPERIMENTAL

The first and second objectives of this work required development of experimental techniques. Details of this development are therefore shown in the Results and Discussion chapter. This section will describe the final apparatus designs arrived at and specify the experimental conditions examined, as well as experimental and computational details.

## 3.1 Producing Film Defects

### 3.1.1 Extrusion System and Downstream Equipment Design

Figure 3-1 shows a picture of the extrusion system and the film production equipment used in this study. A single screw extruder (Deltaplast Machinery Ltd.) was used to convert solid polymer pellets to polymer melt. The extruder melt channel is 3.8 cm in diameter with a length to diameter ratio of 25 to 1. A melt monitoring interface previously designed in this research group was attached to the extruder. Details on the original and modified melt monitoring interface design are available in Appendix 4-I.

The melt monitoring interface has two viewing ports located on opposite sides of the melt channel. During monitoring, a halogen light source equipped with a flexible light guide was used to illuminate the translucent polymer melt. This was achieved by horizontally pointing the light guide at one of the window ports. A plastic diffuser filter was placed in front of the light guide to increase illumination uniformity.

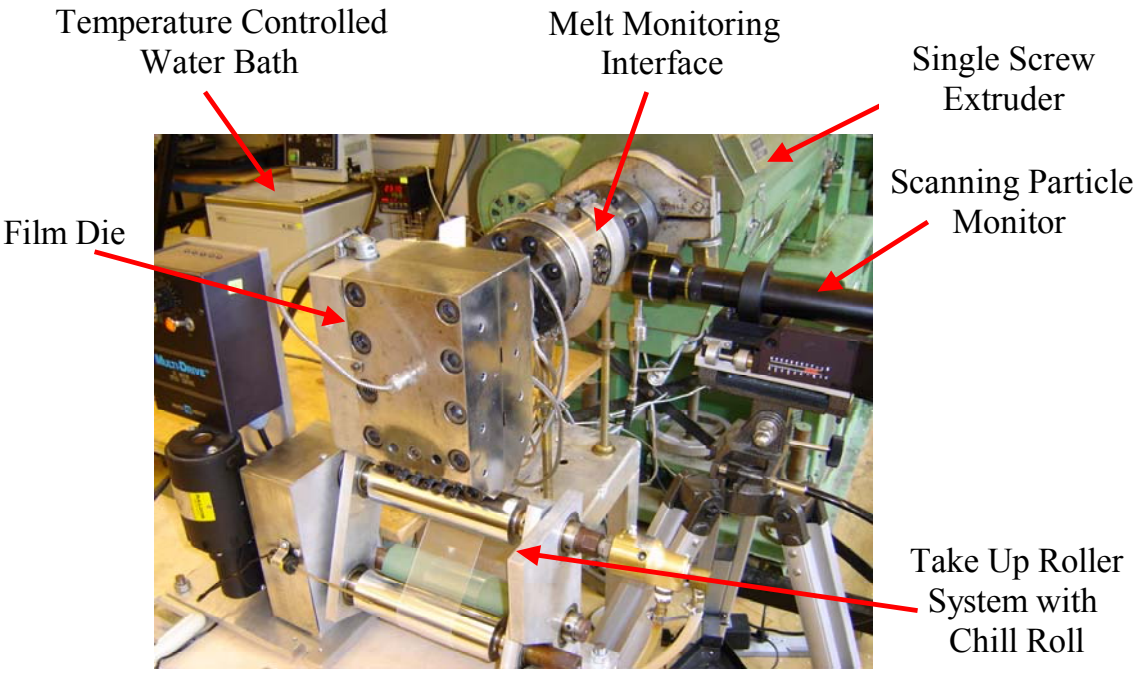


**Figure 3-1:**Extrusion and film production equipment.

To produce polymer film samples, a film die (Deltaplast Machinery Ltd.) was installed right after the monitoring interface. This die has a coat hanger design with a flex lip mechanism. (Figure 3-2) In the coat hanger design, polymer melt first enters a manifold region. The manifold acts as a reservoir to ensure constant and uniform pressure behind the die lips. (Kanai 1999) A group of cylindrical heaters embedded in the die body heat up the film die. In the flex lip mechanism, one of the die lips is rigid while the other one is flexible. This enables us to adjust the die thickness by a set of adjuster bolts in front of it. The discharge slot measures 7.6 cm in width and its thickness can be changed from 0.0025 cm to 0.051 cm. The die gap was set at the maximum thickness (0.051 cm) for all the experiments in this study.

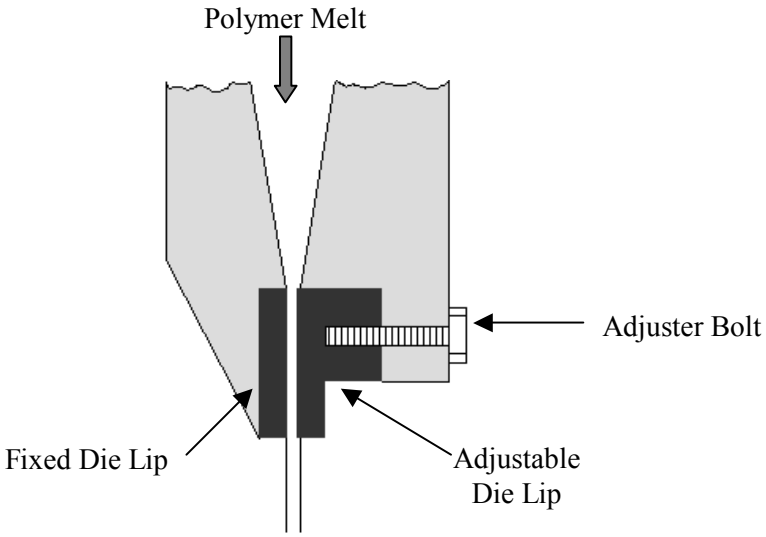


**Figure 3-2:** Schematic diagram of a flat film die with adjustable die thickness

The major part of the new downstream equipment is a bench mounted set of rollers consisting of a chill roll and a nip roll manufactured by Randcastle Extrusion Systems Inc. (Figure 3-3) All three rolls are 5.1 cm in diameter and 17.8 cm long. The chill roll is positioned right beneath the film die in Figure 3-3. The other two rolls under the chill roll provide the nip roll mechanism. The chill roll and one of the nip rolls are chrome-plated while the third roll is rubber coated.

A DC motor equipped with a variable speed drive provides the power for the roller set. A dial located in front of the variable speed drive adjusts the rotational speed of the rollers. There is a scale around this dial ranging from 0 to 100%. However, roller movement was negligible between 0 and 15%. A digital contact tachometer was used to measure the rotational velocity of each roller. Results are plotted against dial settings in Figure 3-4.

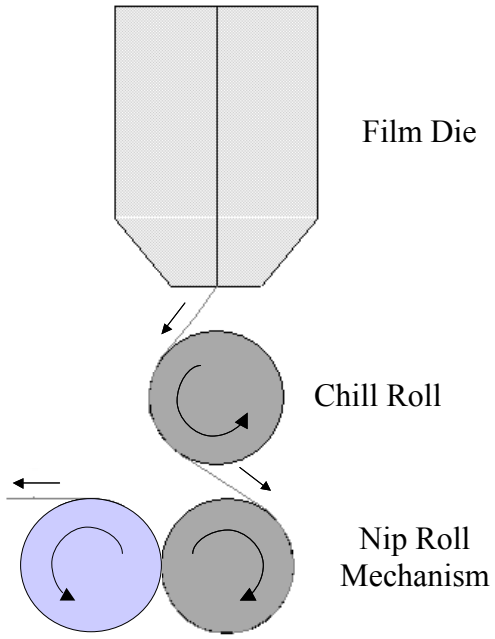


**Figure 3-3:** Side view of the take-up roller system showing the position of the rollers and the film path.

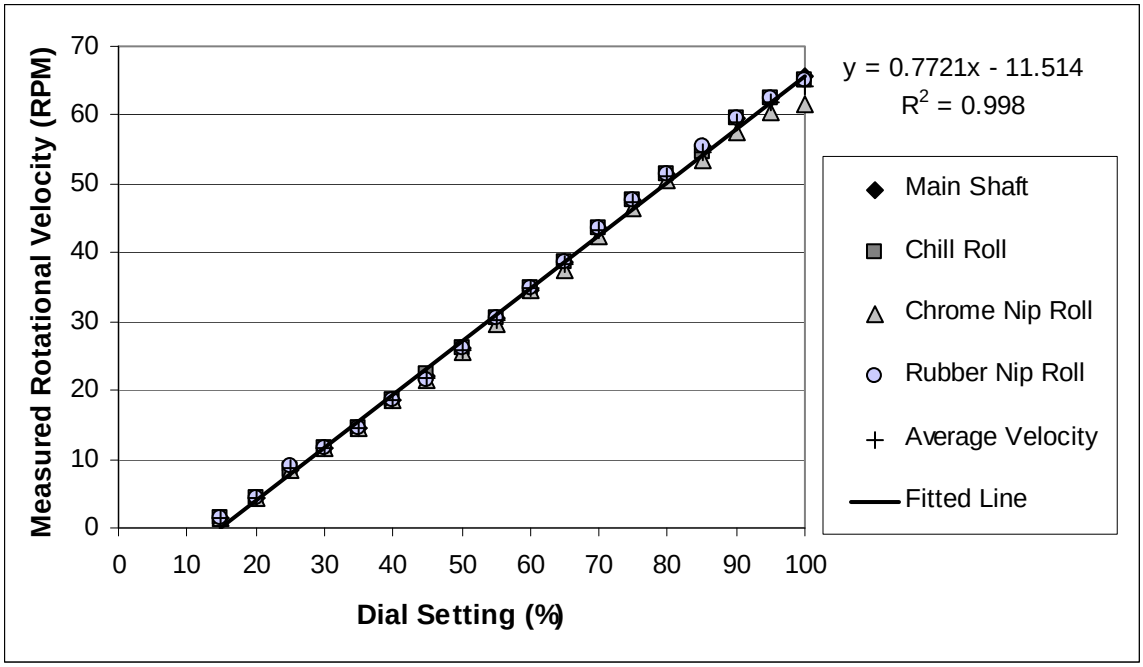


**Figure 3-4:** Measured roller rotational velocity versus dial setting.

The chill roll is bored and equipped with rotary union joints to allow cooling water to circulate inside it. A Lauda Compact Thermostat, Model K20KS, was used to control the temperature and flow rate of the water circulating inside the chill roll. Room temperature was measured with a thermometer right in between the chill roll and the nip roll.

The air gap between the die lip and the chill roll surface is an important factor in controlling the film quality and final dimensions of the product. (See Section 2.1.4) This distance was kept constant at 1 cm throughout the experiments.

### 3.1.2 Materials

Preliminary extruder runs were conducted using six different polymer batches. Table 3-1 provides a list of these polymers and their suppliers. Model and real particles were selected from the particles commonly used as fillers or in composite manufacturing. (Wypych 1999, Murphy 1996) A list of particles used in the experiments and some of their properties is available in Table 3-2. More details on the selected particles are available in Appendix 3-I. Cross-linked polyethylene samples used in this research were those generated by Ling (2003). Table 3-I-8 in Appendix 3-I provides details on the cross-linking procedure and the gel content of each sample used.

**Table 3-1:** Name and supplier of polymer batches used in extruder runs.

| Polymer Name | Supplier |
|---|---|
| LDPE530A | Canada Color Company |
| LDPE640I | Canada Color Company |
| LDPE68494A | Exxon Chemical Company |
| LDPE89823A | Exxon Chemical Company |
| LDPE88510A | Exxon Chemical Company |
| EVA1608V | AT Plastics Inc. |

**Table 3-2:** A list of particles added to polymer feed and their properties

| Particle | Density ($gcm^{-3}$) | Diameter (μm) | Shape | Color | Mohs Hardness |
|---|---|---|---|---|---|
| Solid Glass Microspheres | 2.4-2.55 | 10, 50, 100 | Spherical | Transparent | 6 |
| Blue Glass Microspheres | 2.4-2.55 | 100-250 | Spherical | Blue | 6 |
| Hollow Glass Microspheres | 0.6 | 30-55 | Spherical | White to transparent | 6 |
| Glass Fibers | 2.44 | 14<br>Max. Length: 4 mm | Fiber | White to transparent | 6 |
| Aluminum Powder | 2.7 | 10-30 | Spherical | Silvery white to gray | 2-2.9 |
| Ceramic Microspheres (Zeeospheres) | 2.1 | 100-200 | Spherical | Gray | 7 |
| Diatomite | 2-2.5 | 10 | Irregular | White to off-white | |
| Wood Dust | 0.4-1.35 | 10-300 | Irregular | Buff | |
| Cross-Linked Low Density Polyethylene | 0.93-0.94 | 20-500 | Irregular | Off-white | |

### 3.1.3 Extrusion Procedure

The single screw extruder used in this research has three heating zones; the film die is heated with a separate set of heaters. Based on preliminary exploratory work, a flat temperature profile of 185°C was selected for all the zones to increase the uniformity of film extrusion. Each extruder run started by heating up the extruder and the die zones to 185°C. After starting up the system, the extruder was purged for more than one hour at different screw speeds. For all the experiments, the temperature of the water circulating in the chill roll was set at 48 °C and the screw speed at 15 rpm.

Small quantities of particles (0.2-0.8 g) were added as a "pulse" to the feed port. In most cases, only one particle type was tested in each run. After particles started appearing in the melt monitor, the scanning particle monitor was used to capture images of particles flowing in the middle of the melt channel. In the next step, and when particles appeared in the film, a film sample (~2 m) was collected at eight roller speeds.

A list of all the extruder runs which provided in-line melt images and film samples is presented in Table 3-3. This table also shows the particle type and processing conditions for each run. With these experimental conditions, polymer mass flow rate was measured to be 32.0 g/min. In extruder runs 1 to 13, only one type of particle was injected into the extruder feed. The film samples collected in these extruder runs were used for defect selection and characterization.

**Table 3-3:** A list of extruder runs and processing conditions

| Run # | Polymer | Particle | Extruder and Die Zone Temp. (°C) | Water Bath Temp. (°C) | Screw Speed (RPM) |
|---|---|---|---|---|---|
| 1 | LDPE68494A | 10 μm Glass Microspheres | 185 | 48 | 15 |
| 2 | LDPE68494A | 50 μm Glass Microspheres | 185 | 48 | 15 |
| 3 | LDPE68494A | 100 μm Glass Microspheres | 185 | 48 | 15 |
| 4 | LDPE68494A | Blue Glass Microspheres | 185 | 48 | 15 |
| 5 | LDPE68494A | Glass Bubbles | 185 | 48 | 15 |
| 6 | LDPE68494A | Glass Fiber | 185 | 48 | 15 |
| 7 | LDPE68494A | Diatomite | 185 | 48 | 15 |
| 8 | LDPE68494A | Zeeospheres | 185 | 48 | 15 |
| 9 | LDPE68494A | Aluminum Powder | 185 | 48 | 15 |
| 10 | LDPE68494A | X-Linked LDPE #4 | 185 | 48 | 15 |
| 11 | LDPE68494A | X-Linked LDPE #5 | 185 | 48 | 15 |
| 12 | LDPE68494A | X-Linked LDPE #6 | 185 | 48 | 15 |
| 13 | LDPE68494A | Wood Dust | 185 | 48 | 15 |
| 14 | LDPE68494A | Mixture of Particles[1] | 185 | 48 | 15 |

**Mixture of Particles[1]**: 10, 50, and 100 μm Glass Microspheres, Glass Bubbles, Glass Fiber, Aluminum Powder, Zeeospheres, Diatomite, Blue Glass Microspheres, Wood Dust

### 3.1.4 Extrusion System Assessment

The extrusion system was evaluated by selecting film thickness as a reproducibility measure. Extruder runs with four particle types were conducted and film samples at eight roller speeds were collected. Each extruder run was repeated five times.

The polymer used was LDPE 68494A (Table 3-1). Particles injected as a pulse into the feed port during these runs to create film defects were: glass microspheres of different sizes, glass bubbles, glass fibers, and a mixture of all three particles. Film thickness was measured approximately in the middle of the film samples at ten random, particle free locations. Thickness measurements were performed using a Fowler Electronic Outside Micrometer. This device can measure increments as small as 0.25 μm. Measured values were used to model the relationship between the take-up roller speed and the film thickness as described in Section 4.1.

## 3.2 Characterization of Film Defects

### 3.2.1 Particle Characterization

For the second objective, the size, shape and other properties of film defects corresponding to properties of particles observed in the melt during in-line image monitoring need to be measured off-line. Furthermore, there is a need to match the defect image to the corresponding image of the particle in the melt causing the defect. As was mentioned in Section 2.4, it was recognized very early in the study that it was not feasible to track a particular particle from the melt into the film. Thus, it was not possible to attribute a specific

defect to a particular particle observed by the melt monitor. However, it proved unnecessary for two reasons. First, the capabilities of the melt monitor are now well known; it provides silhouettes of particles in the melt. The second reason is that the same information on the particle provided by the melt monitor could easily be obtained from the defect since the particle dimensions were generally clearly evident in the defect.

Thus, in this work, the particle size and shape information were actually obtained from the off-line measurement of the defect rather from the melt monitor images. Imaging will be conducted using polarized light and interferometry. Once the models relating particle and defect properties are developed using these off-line measurements, the model predictions can be obtained using particle properties obtained from in-line melt imaging.

### 3.2.2 Imaging of Defects

- **Polarized Light Imaging**

Figure 3-5 shows the apparatus developed to obtain polarized light images of the polymer film. This setup consisted of a CCD camera, lens assembly, two linear polarizing filters (termed “analyzer” and “polarizer”), and a sample holder. Details of the procedure used are described below.

Before scanning a defect, the light source was turned on and set to maximum intensity for one hour before imaging. The polarizer and the analyzer filters were kept at the same configuration for all the experiments. Selected film defects were marked and then placed in the sample holder under the camera lens. Depending on the magnification level of

the lens, one of the camera settings as shown in Table 3-4 was selected. After focusing the camera on the film surface, a color image of the film defect was acquired and saved.

**Table 3-4:** Camera Settings

| Lens | Gain (Maximum=255) | Blue Gain (Maximum=255) | Red Gain (Maximum=255) |
|---|---|---|---|
| 2x | 45 | 57 | 134 |
| 4x | 185 | 67 | 138 |

- **Optical Interferometry**

Interferometry was carried out using a manual, non-contact white light interferometer, the Wyko NT 2000, manufactured by Veeco Instruments. Figure 3-6 shows a schematic diagram of this instrument available at the Institute for Optical Sciences at the University of Toronto. (Veeco Instruments Corp. 1999) Details of the procedure used are described below.

The WYKO NT 2000 can employ one of two measurement techniques: Phase Shifting Interferometry (PSI) and Vertical Scanning Interferometry (VSI). VSI is a newer technique than PSI and was developed by Veeco Instruments Corp. (1999). It is capable of scanning rougher surfaces. The PSI mode of WYKO NT 2000 interferometer has a vertical resolution of 3 A° while the VSI mode has a vertical resolution of 3 nm for single measurements and < 1 nm for averaged multiple measurements. Since the film samples are not very smooth, the VSI technique was used to characterize surface profile of the defects in this research project.

The Wyko NT 2000 interferometer is coupled with Vision32$^{TM}$ software that provides fast surface profile visualization and analysis. The profiler is equipped with three objective

lenses: 2.5x, 10x, and 50x. Higher or lower magnification levels can be achieved by selecting different field of view (FOV) parameters. Most of the defects were scanned with the 10x lens and an FOV of 0.5 resulting in a final magnification level of 5.3x. (Veeco Instruments Corp. 1999)

Selected film defects were marked and placed in the sample holder on the microscope stage. Following the Wyko NT2000 user's guide manual, the stage tilt was adjusted. In Vision32$^{TM}$ software, the VSI technique was selected for all measurements. Depending on the size of defect, one of the available magnification settings was selected. The lens assembly was moved until it was focused slightly above the top of the defect. Then the defect was scanned. Raw and restored Optical Path Difference (".opd") files were saved for each selected film defect.

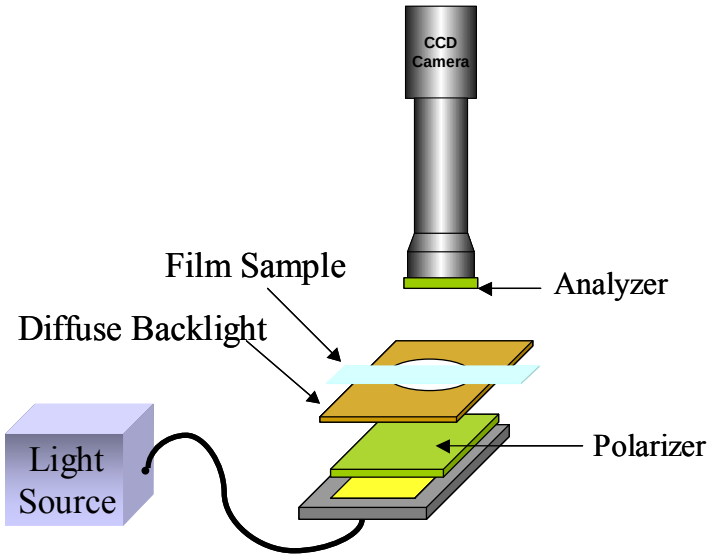


**Figure 3-5:** Diffuse polarized backlighting setup for off-line film monitoring.

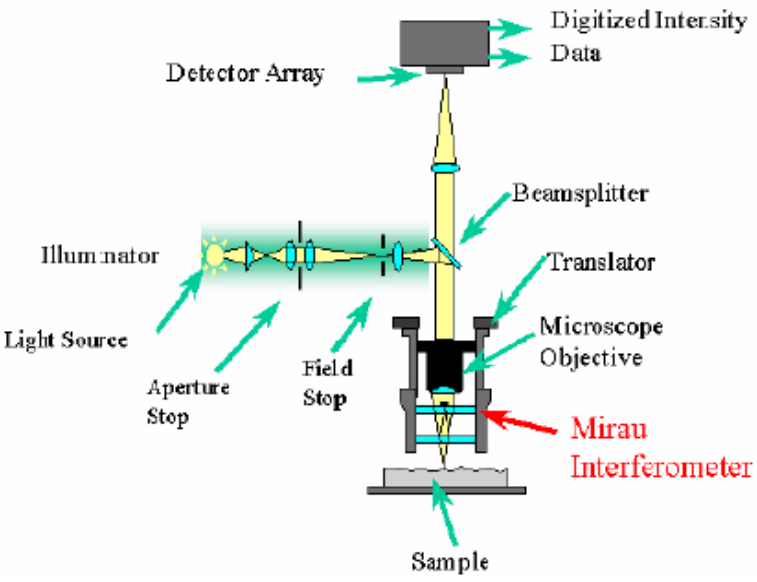


**Figure 3-6:** Schematic diagram of an interference microscope (Veeco Instruments Corp. 1999)

### 3.2.3 Image Analysis

Typical defect images obtained with polarized light and their corresponding surface profile images are shown in Appendix 3-II. Polarized light images were processed using Adobe Photoshop CS followed by Image Pro Plus 4.5. Details are available in the Results and Discussion chapter (Section 4.1.2.2.)

Interferometric images were processed using Wyko Vision32 software, Matlab 6.5 and Image Pro Plus 4.5. Additional details are provided in the Results and Discussion chapter (Section 4.1.2.4)

Clustering and Classification were done using commercial software:
Weka 3-4, SPSS Clementine 12.0, Matlab 6.5, and Scalable Learning Machine (SLM).

# 4 RESULTS AND DISCUSSION

## 4.1 Producing and Characterizing Film Defects

The first objective of this work was to produce plastic film containing defects using an extrusion system equipped with a melt monitor. A single screw extruder with a melt monitor (the "Scanning Particle Monitor") was equipped with a film die and take-up roller system (see Figure 3-1). Also, the extruder-melt monitor interface was modified as described in Appendix 4-I.

### 4.1.1 Extrusion Assessment

Figure 4-1 shows a plot of film thickness versus the speed of the take-up roller for five extrusion runs, each with eight roller speeds. For each condition, thickness was measured for ten random, particle-free locations along the centerline of the filmstrip. As shown by the random appearance of the plot of residuals (Figure 4-2) the 1,590 thickness measurements were well fit by the following equation with an overall standard error of 3.74 μm:

$$h_{roll} = 708.74(u_{roll})^{-0.966} \qquad (4\text{-}1)$$

Not only was Eqn. 4-1 an excellent fit to the data but it also was very close to that anticipated by Eqn. 2-2. Thus, Eqn. 4-1 was used to specify film thickness for all of the runs in the study. Table 4-1 shows a list of the measured take-up roller speeds and predicted film thickness values.

**Table 4-1:** Predicted film thickness by Eqn. 4-1 for each take-up roller speed.

| Take-Up Roller Speed ($u_{roll}$) [$cms^{-1}$] | Predicted Film Thickness ($h_{film}$) [μm] |
|---|---|
| 3.06 | 240.7 |
| 4.92 | 152.0 |
| 6.92 | 109.4 |
| 9.31 | 82.1 |
| 11.6 | 66.6 |
| 13.7 | 56.6 |
| 15.8 | 49.2 |
| 17.3 | 45.2 |

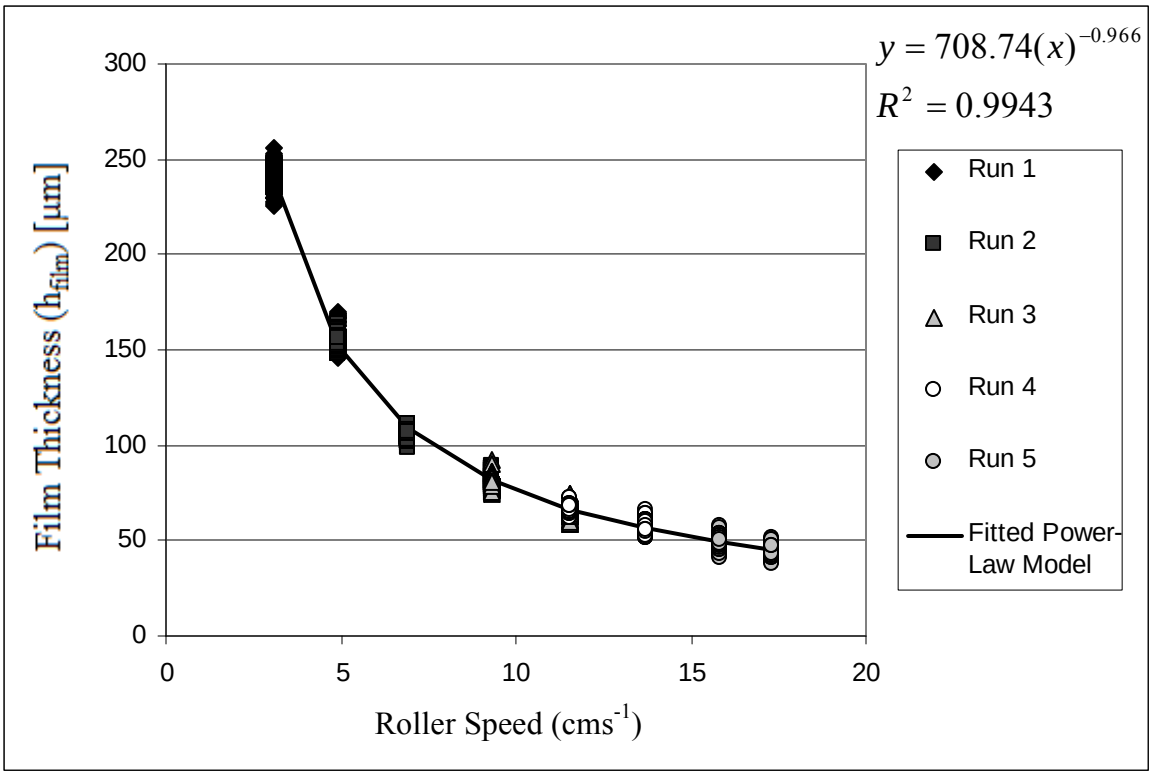


**Figure 4-1:** Measured film thickness versus roller speed.

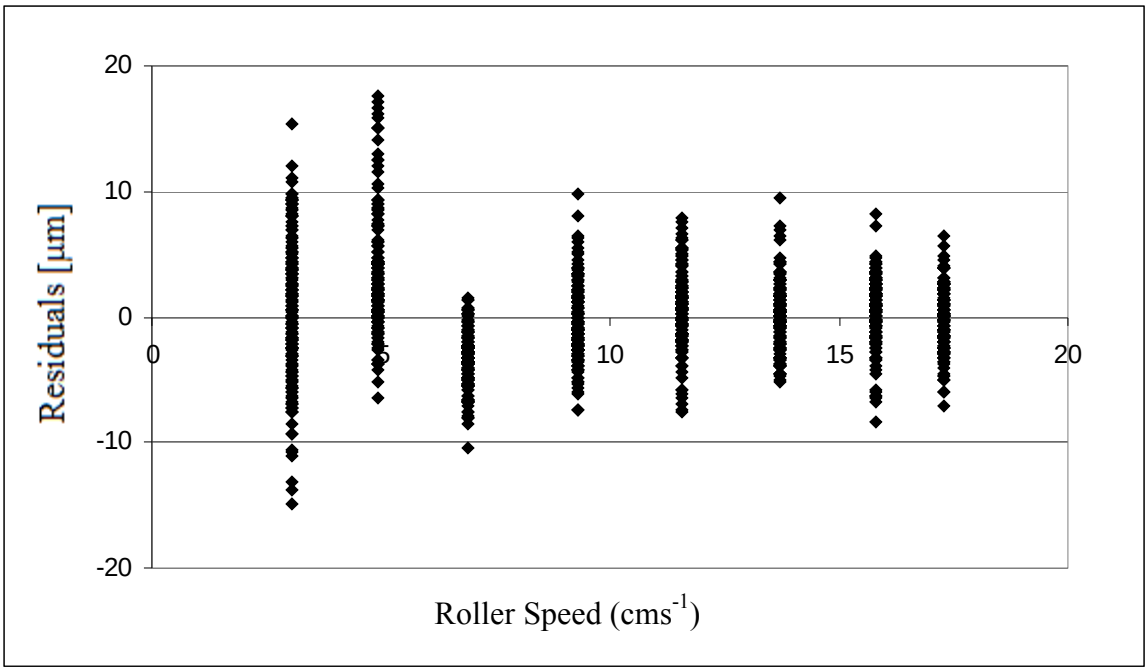


**Figure 4-2:** Film thickness residuals versus roller speed.

### 4.1.2 Off-Line Defect Characterization

The second objective of this work was to characterize the film defects using off-line analysis. Two methods were chosen: polarized light imaging and interferometric imaging. Table 4-2 compares these two approaches. The interferometer was a commercial instrument. However, the polarized light imaging required design of the appropriate experimental apparatus.

**Table 4-2:** A comparison between polarized light imaging and interferometry

| Polarized Light Imaging | Wyko NT2000 Interferometry |
|---|---|
| Relatively simple.<br>Rapid measurements. (~ < 1 s)<br>Suitable for on-line applications. | Very sensitive and has high resolution (3 nm).<br>Slow measurements (> 10s)<br>Likely unsuited to on-line application. |
| Can detect defects embedded inside the film. | Only detects defect that affect the surface profile. |
| Actual particle that caused the defect is visible in most cases. | Actual particle that caused the defect is not visible. |
| Provides a two dimensional view of the defect. | Provides a three dimensional view of the defect. |
| Film topography is not a problem. | Does not provide reliable data for areas with very steep changes in film profile. |

#### 4.1.2.1 Development of a Polarized Light Imaging Method

In the plastics film industry, backlighting is usually selected for monitoring clear plastic films. However, the type of the light source, the angle between lighting and imaging axes, the choice of optical lenses and filters vary. (Pratt and Warner 2000, Masi 2001, and Hackett Jr. 2004)

First, directional front illumination and diffuse backlighting methods were tested. The directional front illumination method (with one or two light guides illuminating the sample) resulted in a grainy image that only partly showed the particle and its corresponding deformed area. With diffuse backlighting, the particle was clearly visible but the deformed

area surrounding the particle was not visible. The third illumination setup, diffuse polarized backlighting with the film sample between two crossed polarized filters, clearly showed the particle and the surrounding defect. Figure 3-5 shows the apparatus finally used based upon diffuse polarized backlighting.

Qualitatively, the apparatus appeared to work: images of defects were obtained. However, it was known that the images were affected by many properties of the sample (e.g. thickness variation in the deformed area, surface profile variations, polymer molecule orientation). Also, results could be sensitive to the procedure used, notably the orientation of the polymer sample. Two methods were used to assess the value of the polarized light images:

i. To see if the results were qualitatively reasonable, the images were compared to images of the same defects obtained from the interferometer (more information is provided on the interferometric images in section 2.2.2).

ii. As will be seen in the following sections, the images were quantified using image processing and the resulting values used to assess reproducibility as well as in mathematical modeling for defect prediction.

#### 4.1.2.2 Quantifying Polarized Light Images

The main purpose of image segmentation is to separate objects of interest from the image background. This is accomplished by manually or automatically selecting a threshold value to separate the two areas. Usually, a binary image (a "mask image") is created based on the segmentation results. The main challenge is to find a pixel value threshold that can distinguish between object and background pixels.

Commonly used thresholding methods are gray level histogram thresholding, clustering based thresholding, and entropy based thresholding. (Otsu 1979, Kittler and Illingworth 1979, Lin 2003, Ng 2006, Chen and Lin 2006, Gonzales-Barron and Butler 2006) There is no thresholding method that is recommended for all images.

Figure 4-3 shows polarized light images of four typical defects caused by glass microspheres. Particles and defects similar to Figure 4-3(d) have good contrast with the background and are uniform in terms of intensity values. In corresponding grayscale images, these areas were easily separated from the background.

However, most defects and particles similar to the ones shown in Figure 4-3(a, c, d) made automatic thresholding of the grayscale images impractical for three reasons: the defect and/or particle had low contrast with the background; the defect and/or particle included a wide range of grayscale values (Some regions had the same intensity as the background.); and due to polarized light interaction with the sample, in some cases, there were extinction patterns (bright and dark areas) surrounding the particles.

It is possible to develop thresholding algorithms to overcome some of the above-mentioned obstacles and provide accurate results. However, the images obtained in this work showed such diversity that this was not practical. This situation and the fact that this was an off-line, not an in-line measurement, led to the use of manual segmentation for the polarized light images. The manual segmentation method is described in the following paragraphs.

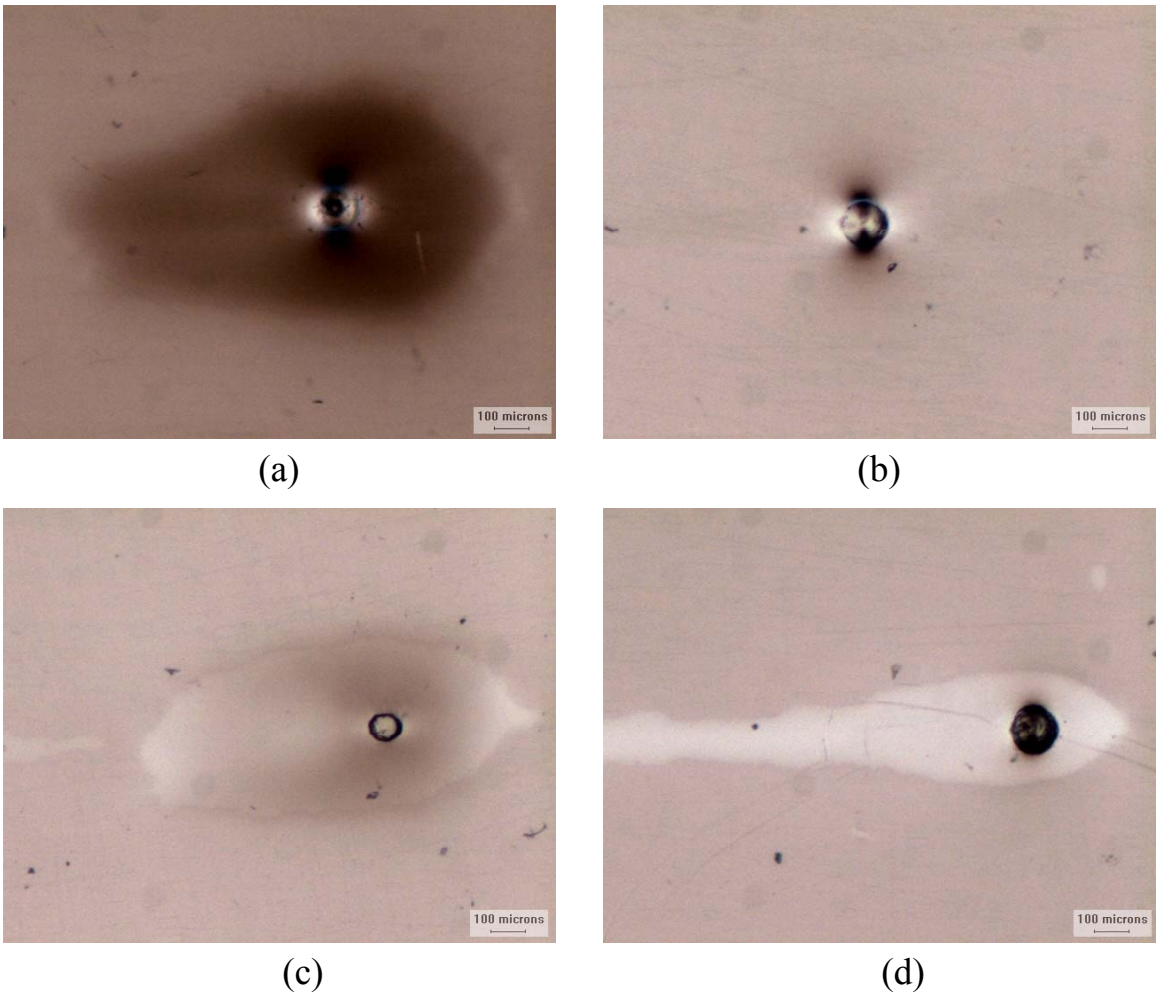


(a) (b)

(c) (d)

**Figure 4-3:** Sample film defects caused by glass microspheres at different take-up roller speeds: **(a)** 3.06 $cms^{-1}$ (Image name: R18R40-D3) **(b)** 6.92 $cms^{-1}$ (Image name: R18R50-D3) **(c)** 9.31 $cms^{-1}$ (Image name: R18R60-D1) **(d)** 15.8 $cms^{-1}$ (Image name: R18R90-D1)

The polarized light image of a typical film defect is shown in Figure 4-4 (a). The embedded particles and the deformed areas were manually segmented from the image background. Adobe Photoshop CS software was used to draw the particle and the defect outlines. (Figure 4-4 (b)) Then, based on the outlines, a mask image for the entire image was generated and saved. (4-4 (c))

In the next step, the mask image was applied to the original polarized light image using Image Pro Plus (IPP) software. This resulted in two individual images, one for the embedded particle and one for its corresponding deformed area, Figures 4-4 (d) and (e), respectively.

A description of each of the 54 attributes of an image object (defect or particle) provided by the image analysis software is shown in Appendix 4-II.

All the acquired defect images with the diffuse polarized backlighting setup were first manually processed to segment the particle and the deformed areas. Then, from the segmented mask images, particle and defect attributes were obtained and inserted in the dataset.

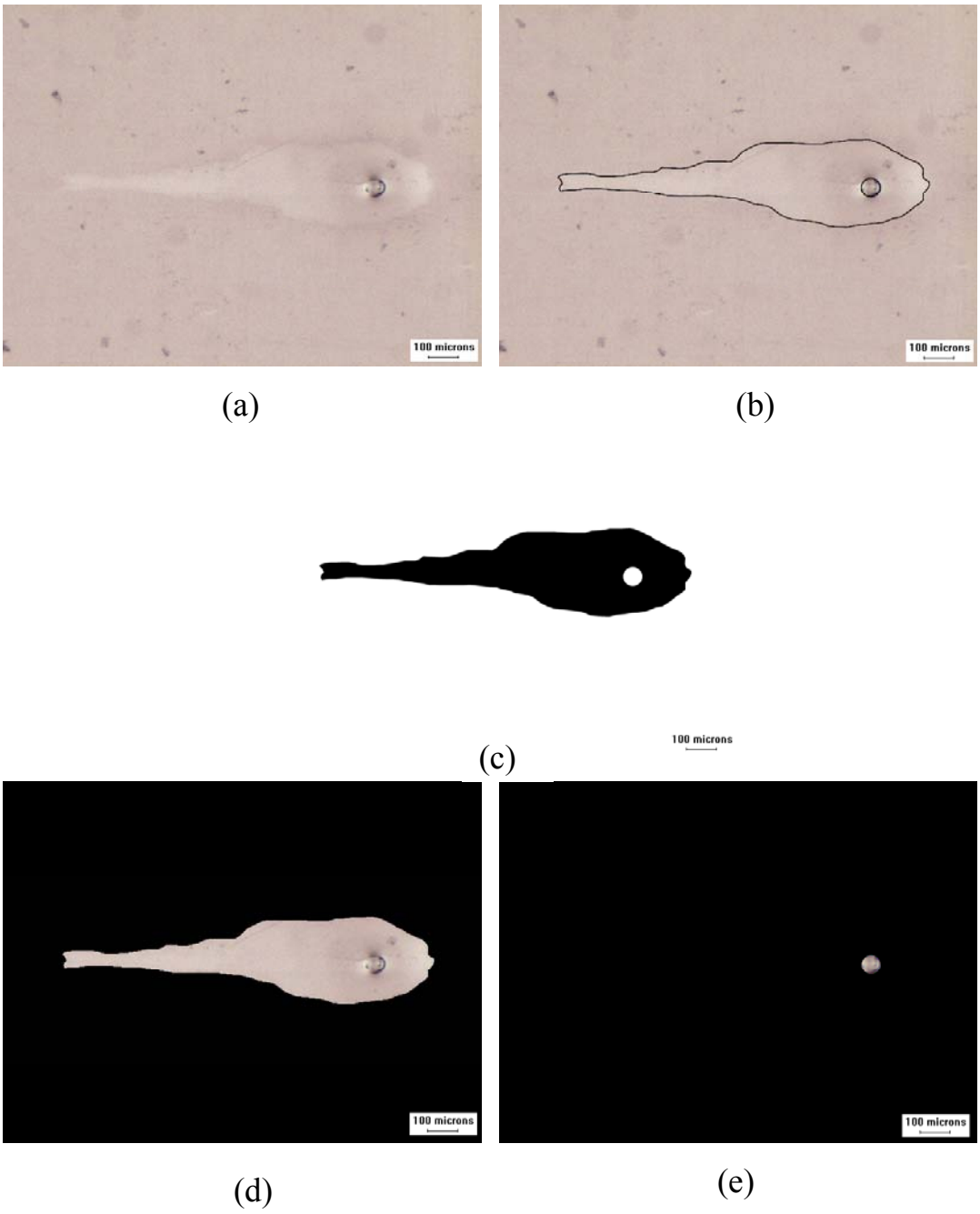


**Figure 4-4:** This figure shows how a typical defect and particle are separated from the image background. (Image name: R17R70-D5.tif) **(a)** Original image **(b)** The deformed area and the particle were outlined in Adobe Photoshop CS. **(c)** A mask image was created based on the defect and particle outlines. **(d)** Defect image obtained by processing the original image and the mask image in IPP. **(e)** Particle image obtained by processing the original image and the mask image in IPP.

Particle attributes can be readily obtained from the in-line images acquired by the scanning particle monitor. Figures 4-III-1 to 4-III-11 in Appendix 4-III show typical images of a variety of particles in polymer melt obtained by the scanning particle monitor. Figure 4-5 shows in-line particle images and off-line polarized light defect images of two particle types. As evident in Figure 4-5 and also in Figure 4-3, particles are visible in the polarized light images. Therefore, as mentioned earlier in Sections 2.4 and 3.2.1, to develop the models, particle attributes were obtained from the off-line polarized light images.

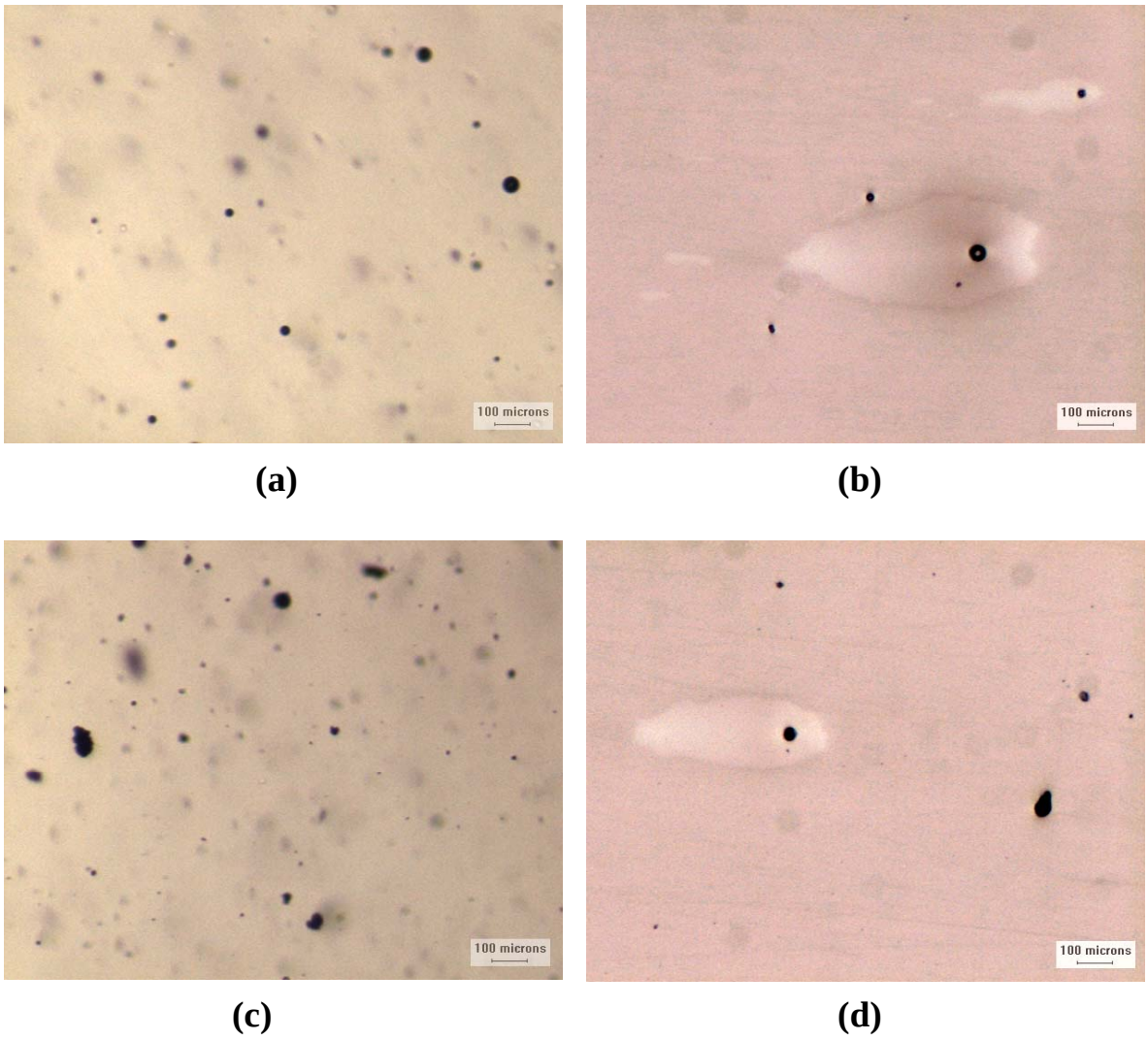


**(a)** **(b)**

**(c)** **(d)**

**Figure 4-5: (a)** In-line image of hollow glass microspheres in low-density polyethylene melt. **(b)** Polarized light image of sample defects caused by hollow glass microspheres. **(c)** In-line image of ceramic microspheres in low-density polyethylene melt. **(d)** Polarized light image of sample defects caused by ceramic microspheres.

#### 4.1.2.3 Evaluation of Polarized Light Imaging

To investigate the reproducibility of the polarized light imaging setup, a film defect was selected as the control defect and was imaged several times throughout the experiments. The shape and size of the segmented defects in the newly captured images of the control defect were compared with those of the previously captured images to ensure control was maintained.

Another factor that can affect the imaging reproducibility was sample alignment with respect to the polarizer/analyzer axes. While imaging defects with the polarized light setup, the sample holder was always aligned with a fixed point to keep the sample alignment the same for all images. However, due to the nature of the samples, slight changes in sample positioning could occur. Since the film samples were molecularly oriented during the film casting process, any change in sample alignment with respect to the transmission axes of the polarizing filters could result in a change in overall image intensity.

To assess the effect of small changes in sample alignment on the measured defect properties, a typical film defect was selected and imaged with the polarized light setup as it was intentionally and randomly tilted in both directions. Images were then processed for reproducibility analysis. Defect angle is defined as the angle between the image vertical axis and the major axis of the ellipse equivalent to the object (Appendix 4-II). Since the film sample was tilted about the horizontal axis (drawing direction), the tilt angle was calculated by subtracting 90° from the defect angle.

A rectangular area of interest (AOI) on the image background was selected to investigate the effect of sample alignment on background intensity. For the same AOI on each image, average intensity values for the red, green, and blue color channels were obtained. Figure 4-6 shows the background average RGB intensities versus tilt angle. As expected, the background intensity changed as the sample alignment and therefore the angle between the sample orientation and the polarizer/analyzer transmission axes changed. The RGB variations showed a direct relationship with the absolute tilt angle value.

However, visual inspection of the images and also superimposing them did not show a significant difference between the defect images. Defect properties were measured based on the procedure described in the previous section. The coefficient of variation percentage calculated for properties such as defect area, perimeter, length, and width was about 1%. This shows good reproducibility of the imaging and segmentation procedures even when the sample was considerably rotated. No trend was observed between changes in defect angle and other defect properties. It was concluded that small variations in sample orientation did not affect defect properties.

Obtaining images by interferometry was more straightforward since a commercial instrument was available. However, a procedure specific to these samples needed to be developed. This is described in the next section.

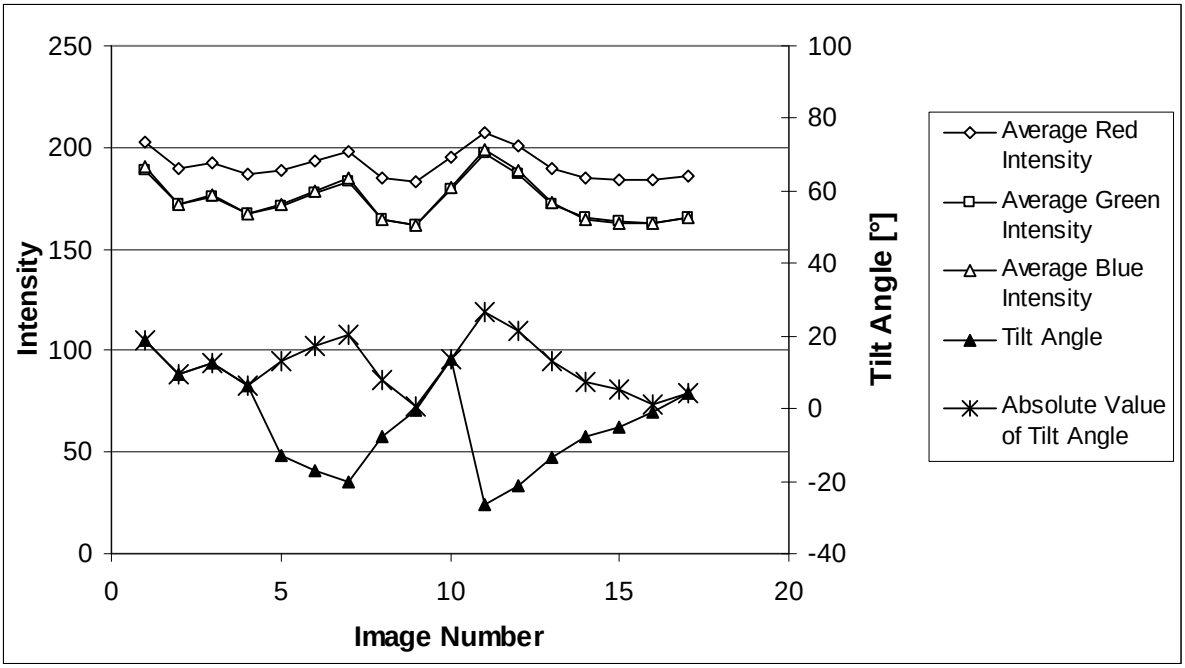


**Figure 4-6:** Effect of film sample orientation on average background RGB intensity values.

### 4.1.2.4 Defect Imaging by Interferometry

The raw data reported by the interferometer after scanning a sample was in Optical Path Difference (OPD) format. OPD measured the distance traveled by the incident light to reach the sample surface and a reference plate. OPD data files could be opened and viewed in Matlab using the "READOPD" Matlab function provided by the manufacturer. (Veeco Instruments Inc.) The result was a matrix of centered (zero mean) surface elevation values in microns for the scanned area.

The data matrix of centered surface elevation values sometimes contained missing values. Reasons for such missing values included: a surface too steep to be measured, non-reflective surface, and pixel brightness less than the threshold value. The Wyko Vision32 software used to process the images had a patented algorithm that could restore the missing

data. It identified missing data points in a two-dimensional array and interpolated between valid data points to fill in the missing values. The restoration results were reliable when at least 95% of the points were valid. (Veeco Instruments Corp. 1999) Therefore, for each raw surface profile, a restored surface profile was recorded and used in calculating attribute values.

In the next step, a procedure was developed to segment the deformed area from the film surface background. For each selected film defect, a restored surface profile image was obtained using WYKO NT2000 interferometer. The surface profile image of a typical defect is shown in Figure 4-7 (a).

The surface profile matrices were normalized between 0 and 1 using their maximum and minimum Optical Path Difference (OPD) values. Grayscale images were generated from the normalized matrices. (Figure 4-7 (b)) To obtain the cross sectional area of the deformation at the film surface, grayscale images were automatically thresholded with a modified Otsu thresholding algorithm. (Otsu 1979, Ng 2006) Then, a mask image was generated based on the thresholding results. (Figure 4-7 (c)) Combining the mask image with the normalized grayscale image provided an image of only the deformed area above the surface. (Figure 4-7 (d, e))

Segmented gray scale surface profiles were used to characterize the asperity caused on the film surface due to the presence of a particle. Important features were divided into two groups: those dealing with the three-dimensional characteristic of the defect, and those

representing the defect properties at the film surface cross section. The first group included attributes such as maximum defect height and defect volume above the surface. The second group consisted of features that defined shape and size of the cross section, such as area, perimeter, and roundness.

Using the corresponding recorded minimum and maximum OPD values for each grayscale image, surface height of each pixel in the segmented area was calculated. Individual pixel volume was calculated by multiplying surface height of each pixel by the pixel area. Finally, the volume of the asperity above the surface was obtained by adding the pixel volumes in the segmented deformed area.

Image Pro Plus software was used to obtain size and shape features of the defect cross sectional area on film surface. All the features shown in Appendix 4-II were measured for the segmented areas.

All the acquired interferometric defect images were processed as described above. Two-dimensional and three-dimensional defect attributes were obtained and inserted in the dataset.

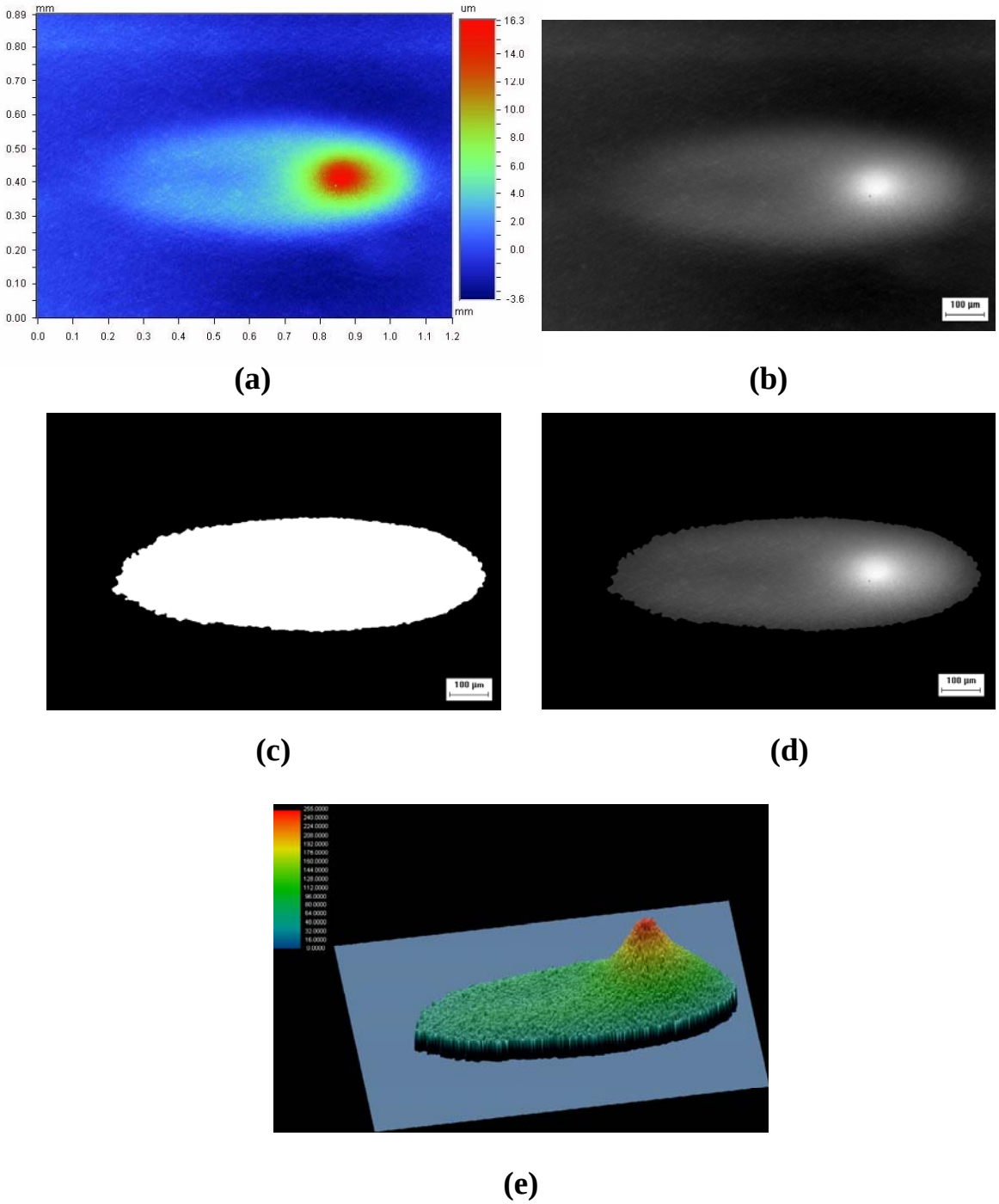


**Figure 4-7: (a)** Color coded surface profile image of defect "R24R70-D7". **(b)** Grayscale surface profile of the same defect. **(c)** Black and white mask image **(d)** Segmented deformed area **(e)** 3D surface plot of the segmented deformed area.

#### 4.1.2.5 Assessment of Defect Profiling by Interferometry

To assess the data reported by the interferometer, a film defect was selected as the control defect. Each time, the control defect was scanned before scanning other defects. The new surface profile of the control defect was compared with the profiles obtained previously. The surface profiles were visually inspected by means of overall height, shape, and area of the deformation.

Surface profiles of the control defect were converted into grayscale images and processed with Image Pro Plus software to obtain their various attribute values. Defect attributes such as area and perimeter showed a coefficient of variation of about 2 and 4 percent over time, respectively. Considering the many sources of error available in acquiring the surface profiles and processing them, this was considered an acceptable level of reproducibility.

#### 4.1.2.6 Constructing the Final Dataset

In the above sections, image processing and feature extraction steps were described. Measured particle and defect features from different methods were all combined to create the final dataset.

The particle and defect part of the dataset was composed of four sections:

1. Particle properties (physical and chemical properties) and processing conditions
2. Particle size, shape, and intensity features obtained from polarized light imaging

3. Defect size, shape, and intensity features obtained from polarized light imaging
4. Defect size, shape, and volume features obtained from interferometry

Appendix 4-IV shows a portion of this dataset. The whole dataset contained 100 measured values in a total of 525 data records. These data described one processing attribute (take-up roller speed), 33 particle attributes (measured from polarized light images), 33 defect attributes (also measured from polarized light images) and 34 defect attributes measured from interferometry images. The data records also contained a run number (indicating the type of particle added to polymer), image label and image number. Most of the data records (420) were for spherical particles: 217 for glass microspheres, 52 for glass bubbles, 78 for aluminum powder and 73 for ceramic microspheres. The 105 remaining data records included: 59 for cross-linked particles and 46 for wood particles. Glass fibers were also used to cause defects. 42 defects caused by glass fibers were characterized. However, results were so different from any of the other particles in the work that only a qualitative analysis of them was done. This analysis is provided in Appendix V.

At the two highest take-up roller speeds (15.8 and 17.3 $cms^{-1}$), presence of foreign particles tore the film apart and made it difficult to collect film samples. Due to lack of sufficient scanned defects at these roller speeds, we decided to focus on defects generated at the other six tested roller speeds for modeling. (Table 4-1)

Table 4-3 shows information on the dataset with regards to some of the particle, defect and film attributes. This table also shows information on two classes of defects: high

average height and low average height defects. That portion of the table will be explained in a later section. At this point, the attribute values listed for the whole database are of interest. These data show that defect diameter measured from polarized light imaging was as much as five times the diameter of the largest particle (986 versus 175 μm) and defect area as much as 32 times the maximum particle area (801,000 versus 24,600 $\mu m^2$). This implied that a small particle could cause a very visible defect!

Assuming the particles to be spheres and so calculating the area of the image as though it were a circle resulted in variable results: accuracy ranged from -0.504% to 6.29%. For defects, accuracy ranged from 2.44% to 4.67%. This indicated that particle and defect shape was not always spherical with defects sometimes being particularly non-spherical. These results agreed with observations of the images. Also, as already evident from Table 4-1, final film thickness ranged from 45.2 to 240.7μm. Interestingly this meant that sometimes particle diameter was almost four times the thickness of the film.

With completion of this large and diverse dataset a very significant challenge was now to accomplish the third and final objective of the work: mathematical modeling to relate processing and particle properties to the properties of the defects produced. The first step in accomplishing that was selection of a subset of attributes, which contained the needed information. Attribute selection is examined in the next section.

**Table 4-3:** Characteristics of database based upon spherical particles

| | **Whole Database** | | **Low Average Height Defects** | | **High Average Height Defects** | |
|---|---|---|---|---|---|---|
| | Minimum | Maximum | Minimum | Maximum | Minimum | Maximum |
| Particle Diameter (μm) | 13.3 | 175 | 26.7 | 175 | 13.3 | 161 |
| Defect Diameter (μm) | 15.4 | 986 | 294 | 986 | 15.4 | 235 |
| | | | | | | |
| Particle Area ($\mu m^2$) | 137.3 | 24600 | 656 | 24600 | 137.3 | 21000 |
| Defect Area ($\mu m^2$) | 175 | 801000 | 43300 | 801000 | 175 | 44500 |
| | | | | | | |
| Estimated Particle Area ($\mu m^2$) | 138 | 24000 | 560 | 24000 | 138 | 20400 |
| Estimated Defect Area ($\mu m^2$) | 186 | 763600 | 67900 | 763600 | 186 | 43400 |
| | | | | | | |
| % Error in Estimated Particle Area | -0.504 | 2.44 | 14.6 | 2.85 | -0.504 | 2.86 |
| % Error in Estimated Defect Area | -6.29 | 4.67 | -57.3 | 4.62 | -6.29 | 2.25 |
| | | | | | | |
| Film Thickness (μm) | 45.2 | 240.7 | 45.2 | 240.7 | 45.2 | 240.7 |
| | | | | | | |
| Particle Diameter/Thickness | 0.055 | 3.875 | 0.111 | 3.875 | 0.055 | 3.565 |

## 4.2 Attribute Selection and Classification

As mentioned earlier (Section 2.3.1), attribute selection for classification is a vitally important aspect of successful modeling. Image analysis software provided about 54 different attributes for each image object (defect or particle). Some of the reported attributes were obviously irrelevant and were deleted from the dataset. Each of the remaining 37 attributes had to be examined to see if it failed with respect to any one of the critical aspects mentioned in Section 2.3.1 (i.e. relevance, reproducibility, redundancy, sensitivity and accuracy). This analysis is shown in Appendix 4-VI. Results are in Table 4-4. This table shows a list of all the attributes reported by the image processing software when defect images were processed. It also shows the status of each attribute in each section of the dataset and, if eliminated, the reason for elimination.

**Table 4-4:** List of attribute status in the dataset and reasons for attribute elimination

| **Attribute** | **Description** | Embedded Particles in Polarized Light Images | Film Deformations in Polarized Light Images | Film Deformations in Interferometric Images | **Reason for Elimination** |
|---|---|---|---|---|---|
| Angle | Angle between the vertical axis and the major axis of the ellipse equivalent to the object | Eliminated | Eliminated | Eliminated | Low reproducibility, too sensitive, dependent on slight shape variations |
| Area | Area of each object (minus any holes) | Present | Present | Present | |
| Area/Box | Ratio between the area of each object, and the area of its imaginary bounding box | Eliminated | Eliminated | Eliminated | Irrelevant: Dependent on object orientation in image matrix |
| Area (Polygon) | Area of the polygon that defines the object's outline | Eliminated | Eliminated | Eliminated | Redundant due to very strong linear correlation with Area and Per-Area |
| Aspect | Ratio between the major axis and the minor axis of the ellipse equivalent to the object | Present | Present | Present | |
| Box Height | Height of the bounding box along the major axis | Eliminated | Eliminated | Eliminated | Irrelevant: Dependent on object orientation in image matrix |
| Box Width | Width of the bounding box along the major axis | Eliminated | Eliminated | Eliminated | Irrelevant: Dependent on object orientation in image matrix |

| | | | | | |
|---|---|---|---|---|---|
| Box X/Y | Ratio between the width (X) and height (Y) of each object's imaginary bounding box | Eliminated | Eliminated | Eliminated | Irrelevant: Dependent on object orientation in image matrix |
| Diameter (max) | Length of the longest line joining two outline points and passing through the centroid | Eliminated | Eliminated | Eliminated | Redundant due to strong correlation with Size-(length) |
| Diameter (mean) | Average length of the diameters measured at two degree intervals joining two outline points and passing through the centroid | Eliminated | Eliminated | Eliminated | Irrelevant: Uninformative for objects with complicated shapes |
| Diameter (min) | Length of the shortest line joining two outline points and passing through the centroid | Eliminated | Eliminated | Eliminated | Redundant due to strong correlation with Size-(width) |
| Feret (max) | Longest caliper (feret) length | Eliminated | Eliminated | Eliminated | Redundant due to strong correlation with Size- (length) |
| Feret (mean) | Average caliper (feret) length | Eliminated | Eliminated | Eliminated | Irrelevant: Uninformative for objects with complicated shapes |
| Feret (min) | Shortest caliper (feret) length | Eliminated | Eliminated | Eliminated | Redundant due to strong correlation with Size-(width) |
| Major Axis | Length of the main axis of the ellipse equivalent to the object | Eliminated | Eliminated | Eliminated | Redundant: Linear relationship with Size-(length) |

| | | | | | |
|---|---|---|---|---|---|
| Minor Axis | Length of the minor axis of the ellipse equivalent to the object | Eliminated | Eliminated | Eliminated | Redundant: Linear relationship with Size-(width) |
| Max Radius | Maximum distance between each object's centroid pixel position and its perimeter | Eliminated | Eliminated | Eliminated | Uninformative for complicated shapes. Redundant due to correlation with Size-(length) |
| Min Radius | Minimum distance between each object's centroid pixel position and its perimeter | Eliminated | Eliminated | Eliminated | Uninformative for complicated shapes. Redundant due to strong correlation with Size-(width) |
| Max Density | Maximum intensity or density inside the object | Eliminated | Eliminated | Eliminated | Irrelevant: Not representative of the overall object density |
| Min Density | Minimum intensity or density inside the object | Eliminated | Eliminated | Eliminated | Irrelevant: Not representative of the overall object density |
| Mean Density | Average intensity or density of each object | Present | Present | Present | |
| Perimeter | Length of the outline of each object | Eliminated | Eliminated | Eliminated | Redundant due to strong correlation with Perim.-(conv.) |
| Perimeter (Convex) | Perimeter of the convex outline of each object | Present | Present | Present | |
| Perimeter (Ellipse) | Perimeter of ellipse surrounding the object outline | Eliminated | Eliminated | Eliminated | Redundant due to strong correlation with Perim.- (conv.) |
| Perimeter (Ratio) | Ratio of the convex perimeter to the perimeter of each object | Eliminated | Eliminated | Eliminated | Irrelevant: Uninformative for objects with complicated shapes |

| | | | | | |
|---|---|---|---|---|---|
| Per-Area | Ratio between the area of the counted object to that of the entire area | Eliminated | Eliminated | Eliminated | Redundant: Linear transformation of Area (polygon) |
| Radius Ratio | Ratio between Max Radius and Min Radius for each object | Eliminated | Eliminated | Eliminated | Irrelevant: Easily influenced by shape variations |
| Roundness | Roundness of each object | Present | Present | Present | |
| Size (length) | Feret diameter (caliper length) along a major axis of the object | Present | Present | Present | |
| Size (width) | Feret diameter (caliper length) along a minor axis of the object | Present | Present | Present | |
| Std. Dev. Density | Standard deviation of density | Eliminated | Eliminated | Eliminated | Irrelevant: Uninformative |
| Density Sum | Sum of the intensity values of all the pixels of an object | Eliminated | Eliminated | Eliminated | Irrelevant: Uninformative |
| Volume | The volume of the segmented deformation above the film surface | | | Present | |

From Table 4-4 it can be seen that only eight attributes remained: area, aspect, mean density, perimeter (convex), roundness, size (length), size (width), and volume. Only the first seven were available for both particles visible in the film (embedded in the defect) and the defect itself. Volume was obtained from interferometry and available only for the defect.

The carefully selected subset of attributes and processing information were used in extensive data mining attempts to cluster and then classify the data. Various clusters of defects could be identified, some of which clearly agreed with the visual clustering results. However, disappointingly, the prediction rate in the defect classification step based on particle and processing information was unsatisfactory. In other words, particle and processing information was insufficient to predict the defect cluster. Efforts then turned towards mechanistic modeling along with an emphasis on physically meaningful measurements. As will be described in the next section, average defect height was the first characteristic to be examined.

## 4.3 Average Defect Height

### 4.3.1 Average Defect Height for Spherical Particles

As mentioned in Section 2.3.5, the Constant Defect Volume per Unit Particle Area model requires a measure of defect height. Interferometry provided a measure of defect volume and polarized light analysis provided defect area. It was expected that defect height could be obtained from defect volume divided by defect area. However, when individual values were calculated, large scatter resulted. Error propagation analysis of such ratios shows that ratios of experimental values often exhibit large errors. One way of circumventing the problem was to try to somehow average the data.

Figure 4-8 shows the first major advance in interpretation of the data obtained in this work. It shows a plot of defect volume obtained from interferometry versus defect area obtained from polarized light imaging for a film thickness of 109.4 μm when glass

microspheres were used to generate defects. Surprisingly only two straight lines through the origin fit all data at this film thickness. The slope of these lines defined an average height for the defects. Since only two average heights were needed to characterize this data it meant that the defects separated into only two classes: high average height and low average height defects. Furthermore, as evident in Figure 4-8, high average height defects (steep slope) occupied a much narrower and lower range of defect areas than did low average height defects (shallow slope).

Figures 4-9 through 4-20 show fits of defect volume from interferometry ($V_{DI}$) versus defect area from polarized light imaging ($A_{DP}$) using all spherical particles (glass microspheres, glass bubbles, aluminum powder and ceramic microspheres).

Because of the different range of defect areas encompassed by high average height and low average height defects, data for each film thickness is represented by two figures: one for the high average height defect data (Figures 4-9 through 4-14) and one for the low average height defect data (Figures 4-15 through 4-20). To enable comparisons, each set of figures has a single range of appropriate defect area and defect volume values.

Each set of data was well fit by a straight line passing through the origin, shown by a thick solid line. On each of the figures, the upper and lower 95% confidence limits about the mean defect volume (thin solid lines) and upper and lower 95% prediction limits for a single future observation of defect volume (thin dashed lines) are also shown. Tables 4-5 and 4-6

show the slope of each line, the 95% confidence interval for the slope and the correlation coefficient squared for each, in each defect group.

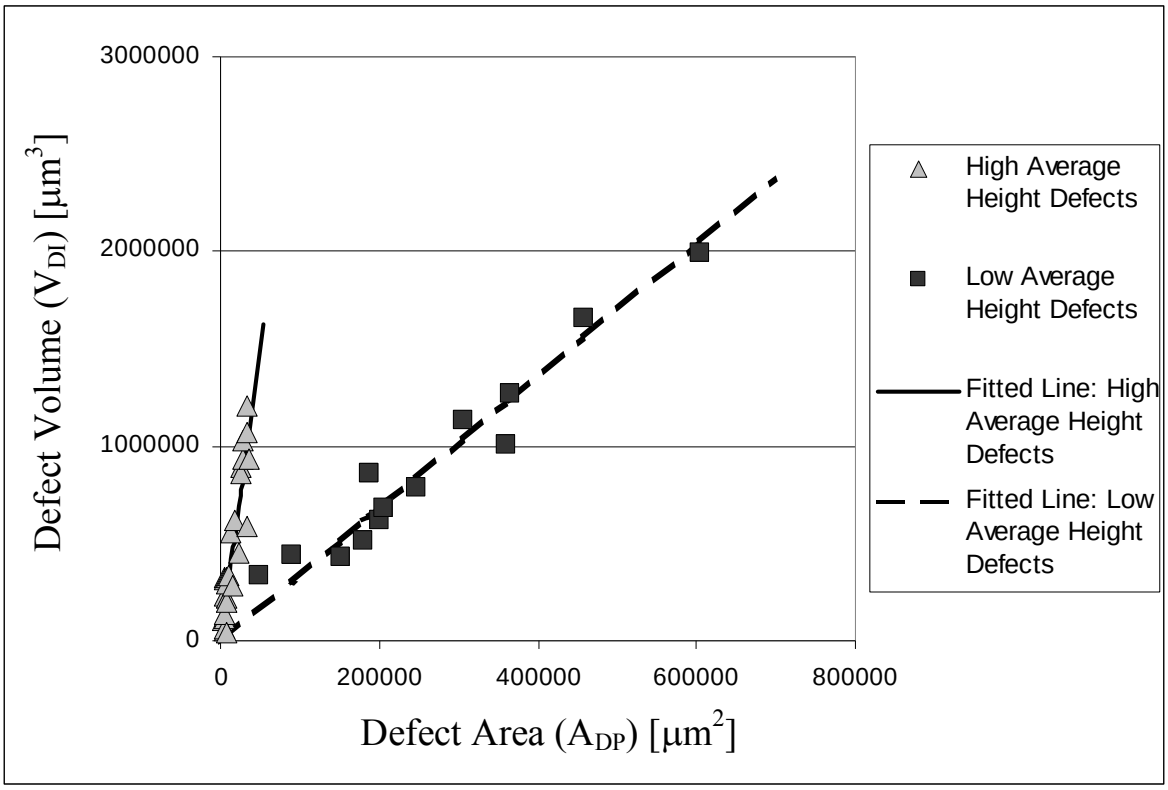


**Figure 4-8:** Defect volume from interferometry ($V_{DI}$) versus defect area from polarized light imaging ($A_{DP}$) for defects caused by all glass microspheres at a film thickness of 109.4 μm. Two straight lines passing through the origin show the best least squares fit for each defect group. Symbols: High average height defects (▲) Low average height defects (■).

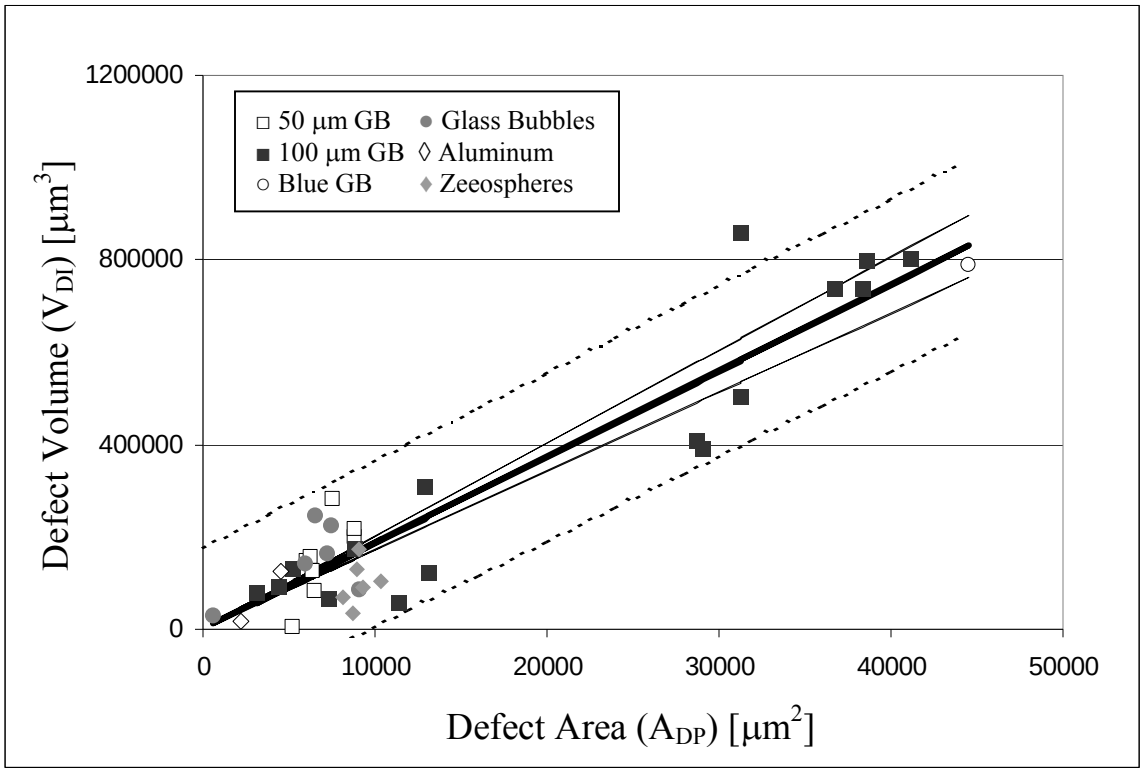


**Figure 4-9:** Defect volume from interferometry ($V_{DI}$) versus defect area from polarized light imaging ($A_{DP}$) for high average height defects caused by spherical particles at a film thickness of 240.7 μm.

Symbols: Fitted line with simple least squares regression (**—**), Upper and lower 95% confidence limits about the mean defect volume (—), Upper and lower 95% prediction limits for a single future observation of defect volume (---)

Note: GB stands for Glass Beads (also called glass microspheres).

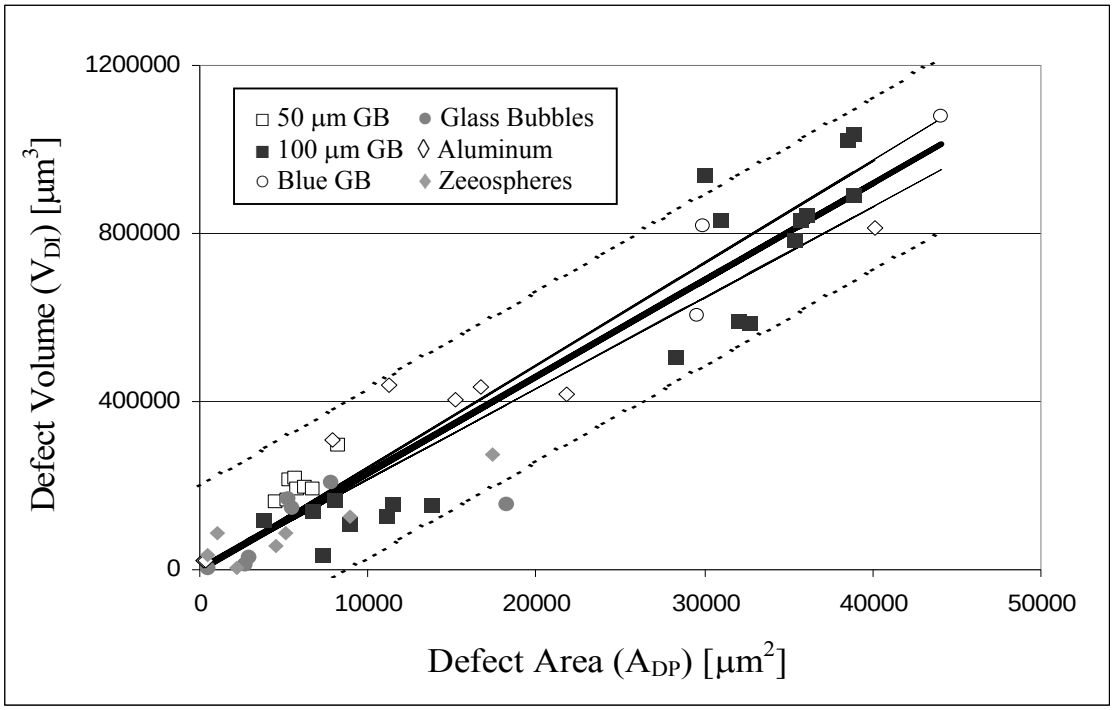


**Figure 4-10:** Defect volume from interferometry ($V_{DI}$) versus defect area from polarized light imaging ($A_{DP}$) for high average height defects caused by spherical particles at a film thickness of 152.0 µm.

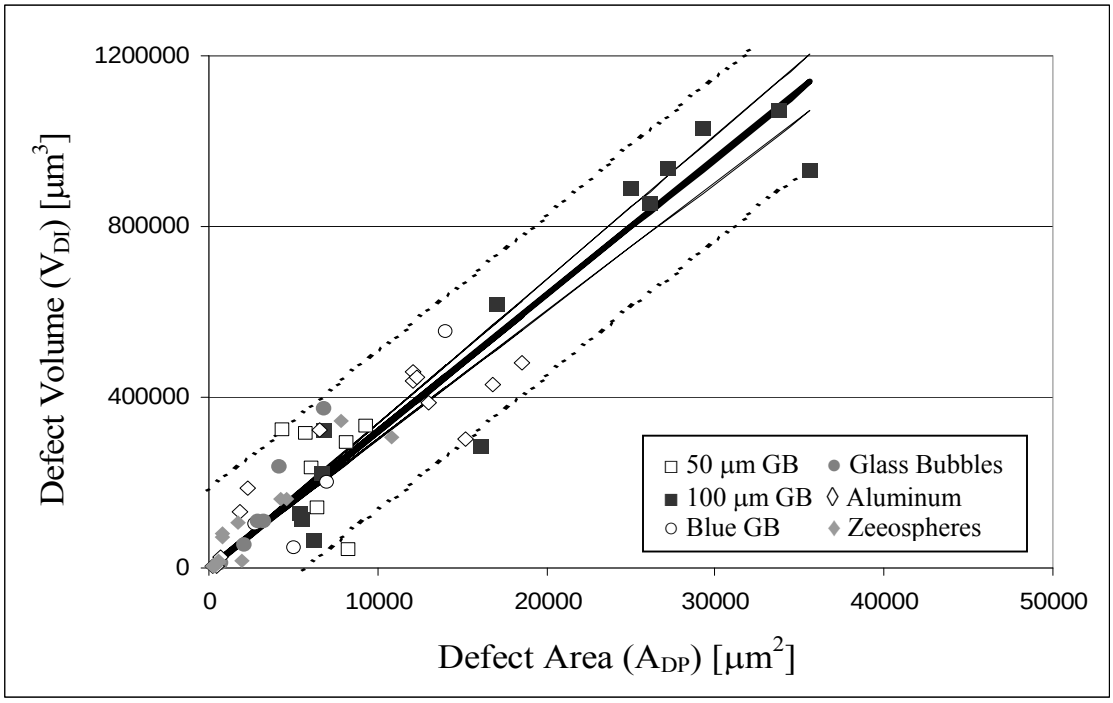


**Figure 4-11:** Defect volume from interferometry ($V_{DI}$) versus defect area from polarized light imaging ($A_{DP}$) for high average height defects caused by spherical particles at a film thickness of 109.4 µm.

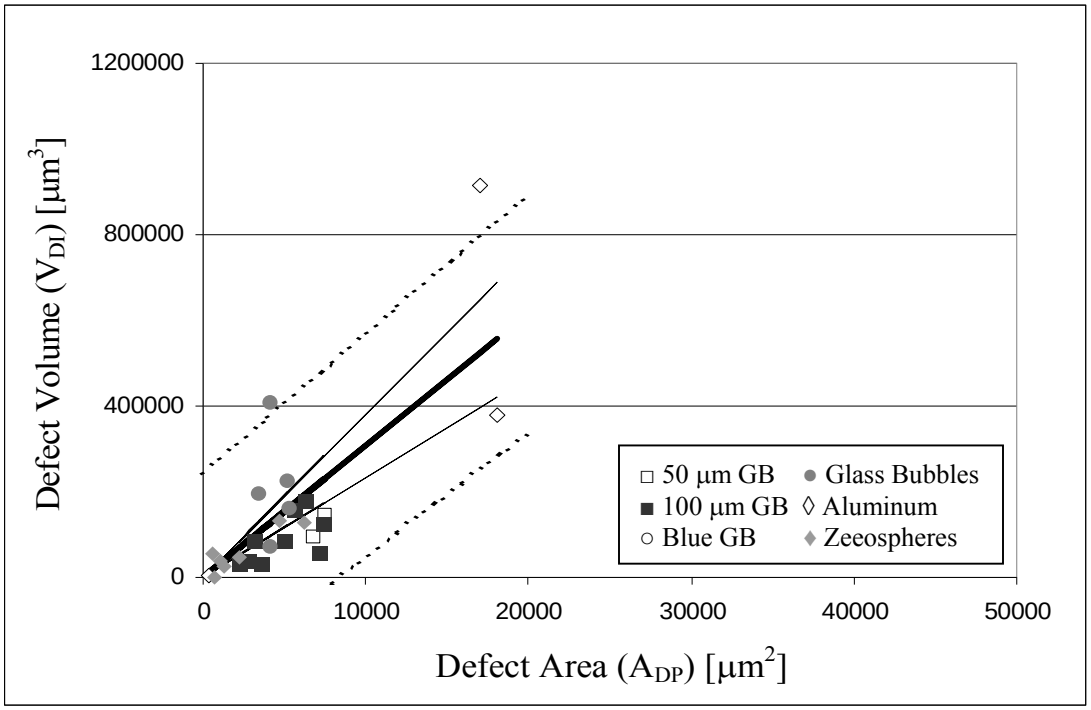


**Figure 4-12:** Defect volume from interferometry ($V_{DI}$) versus defect area from polarized light imaging ($A_{DP}$) for high average height defects caused by spherical particles at a film thickness of 82.1 µm.

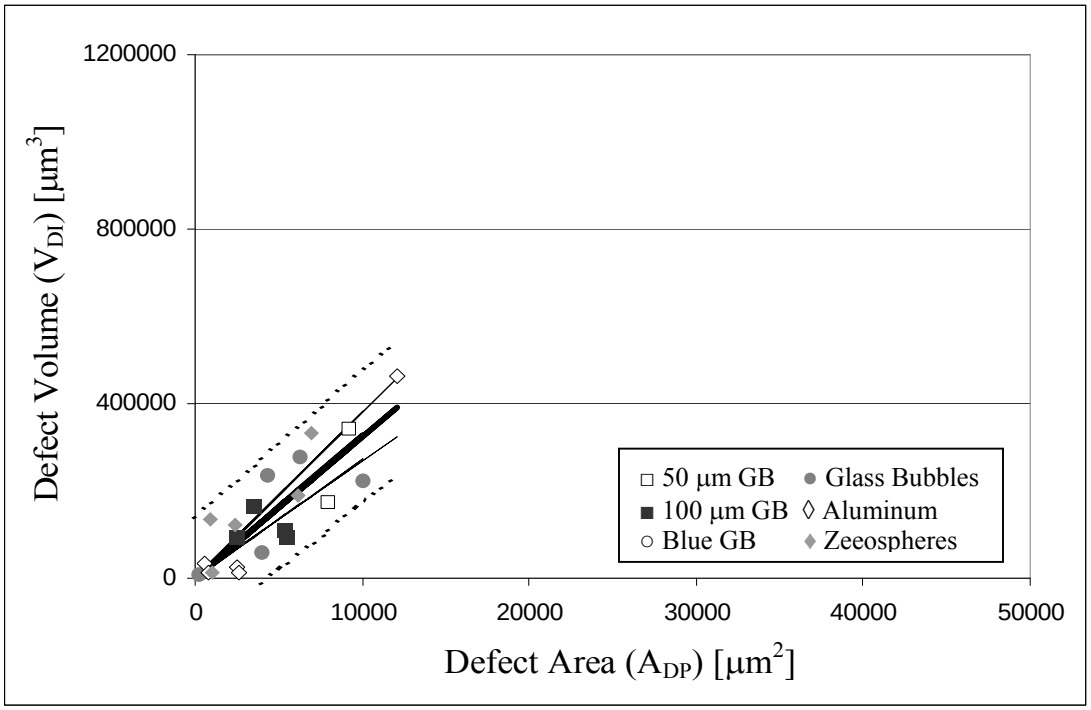


**Figure 4-13:** Defect volume from interferometry ($V_{DI}$) versus defect area from polarized light imaging ($A_{DP}$) for high average height defects caused by spherical particles at a film thickness of 66.6 µm.

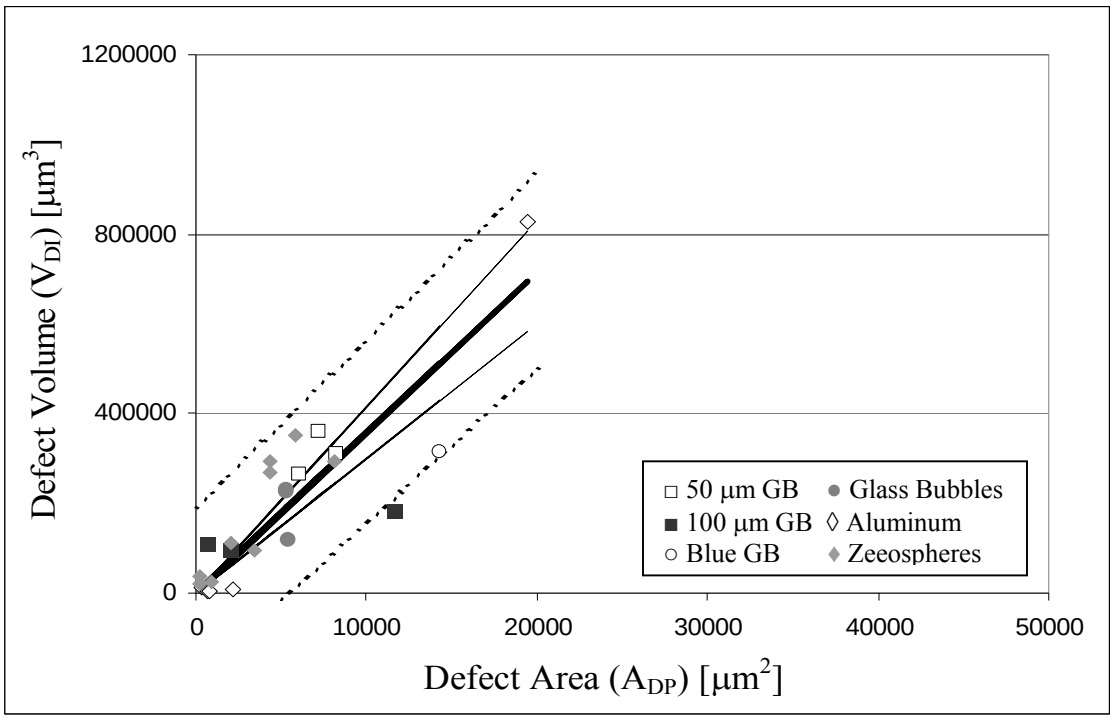


**Figure 4-14:** Defect volume from interferometry ($V_{DI}$) versus defect area from polarized light imaging ($A_{DP}$) for high average height defects caused by spherical particles at a film thickness of 56.6 µm.

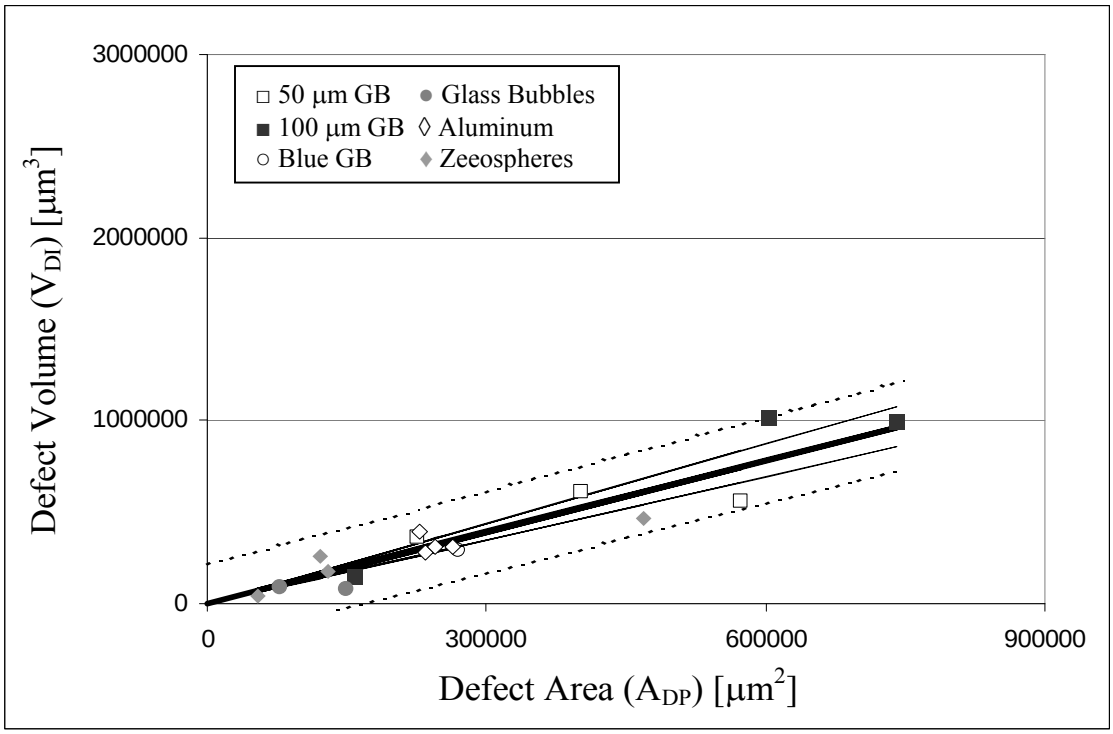


**Figure 4-15:** Defect volume from interferometry ($V_{DI}$) versus defect area from polarized light imaging ($A_{DP}$) for low average height defects caused by spherical particles at a film thickness of 240.7 µm.

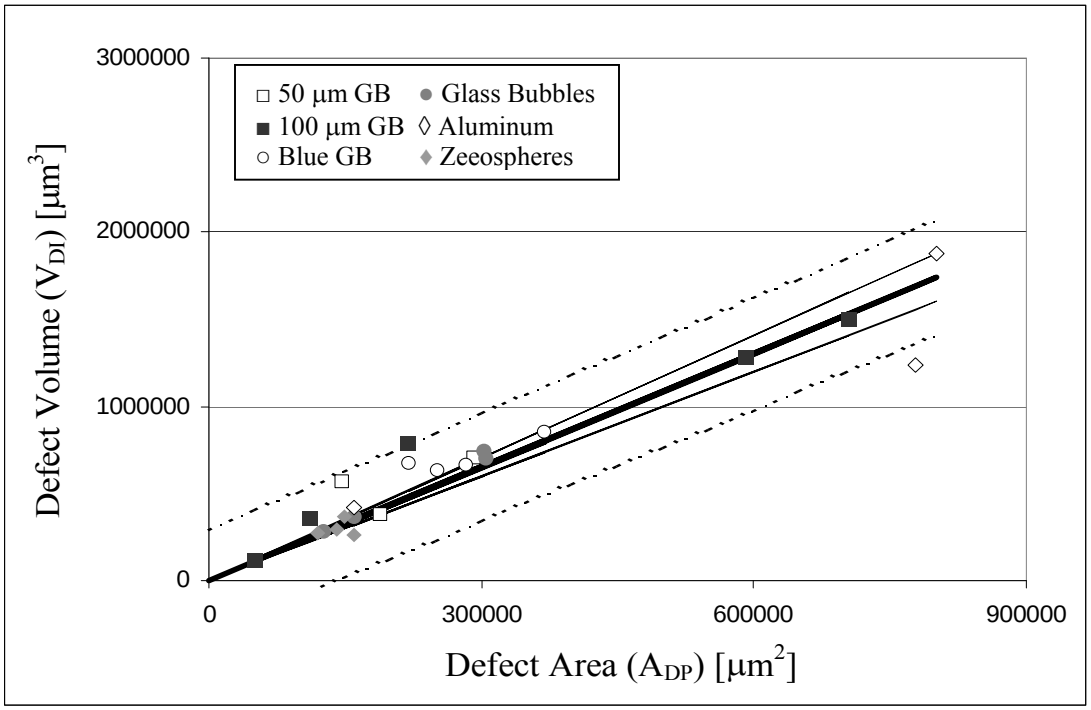


**Figure 4-16:** Defect volume from interferometry ($V_{DI}$) versus defect area from polarized light imaging ($A_{DP}$) for low average height defects caused by spherical particles at a film thickness of 152.0 μm.

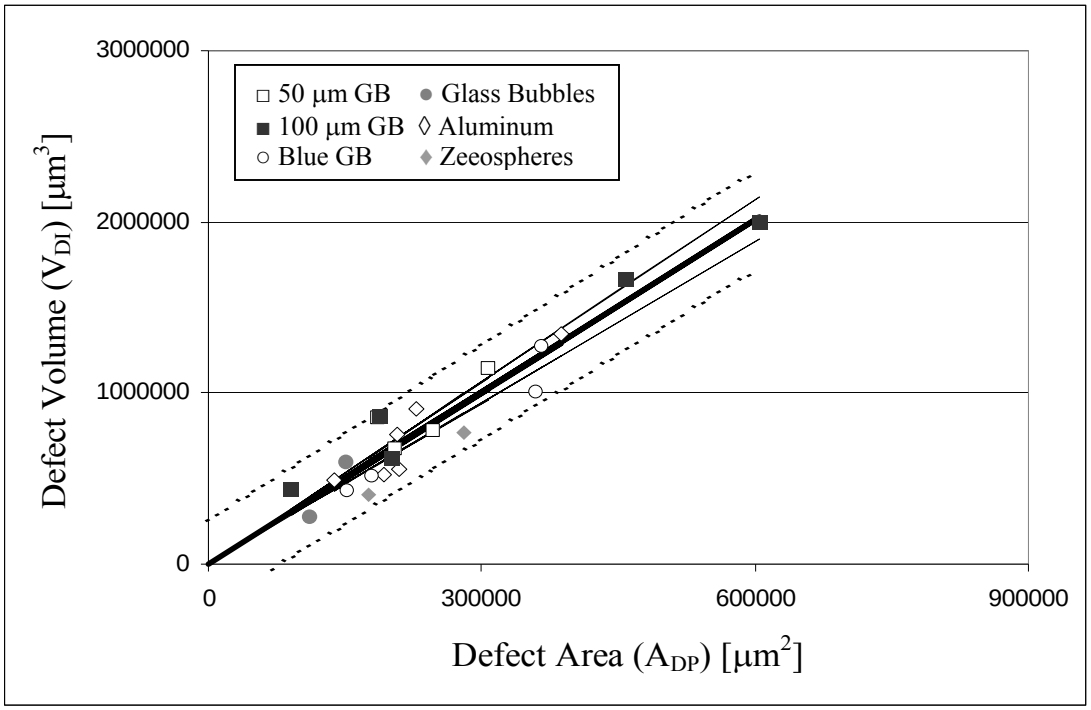


**Figure 4-17:** Defect volume from interferometry ($V_{DI}$) versus defect area from polarized light imaging ($A_{DP}$) for low average height defects caused by spherical particles at a film thickness of 109.4 μm.

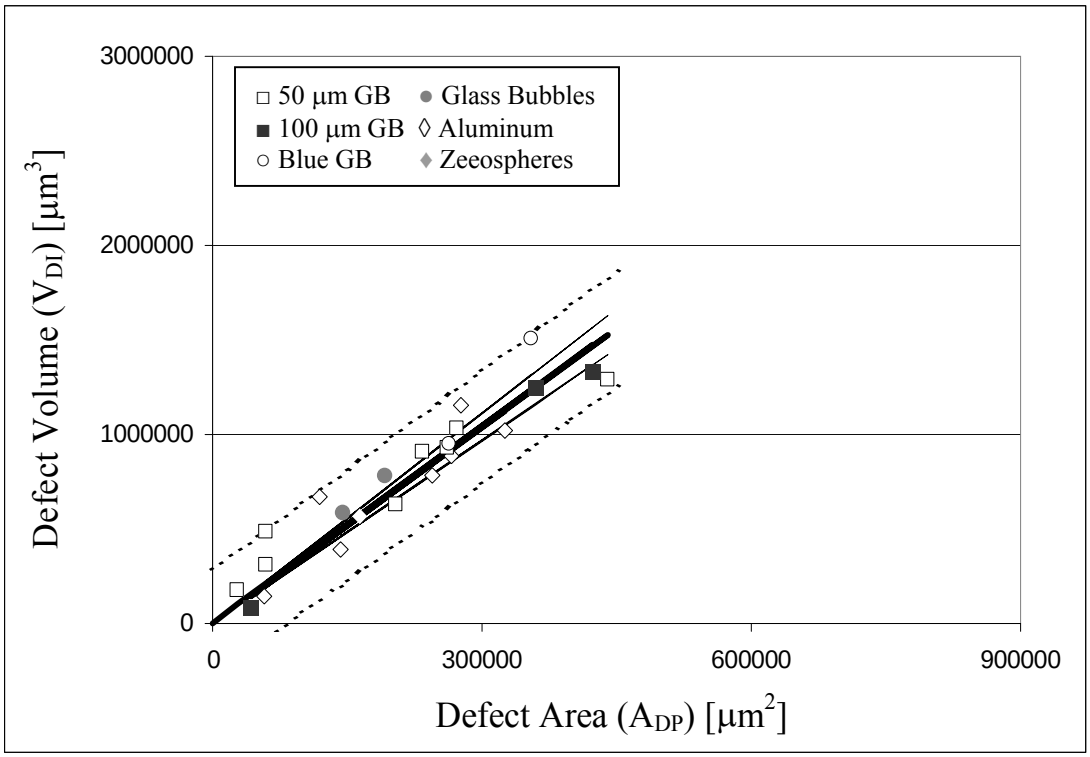


**Figure 4-18:** Defect volume from interferometry ($V_{DI}$) versus defect area from polarized light imaging ($A_{DP}$) for low average height defects caused by spherical particles at a film thickness of 82.1 μm.

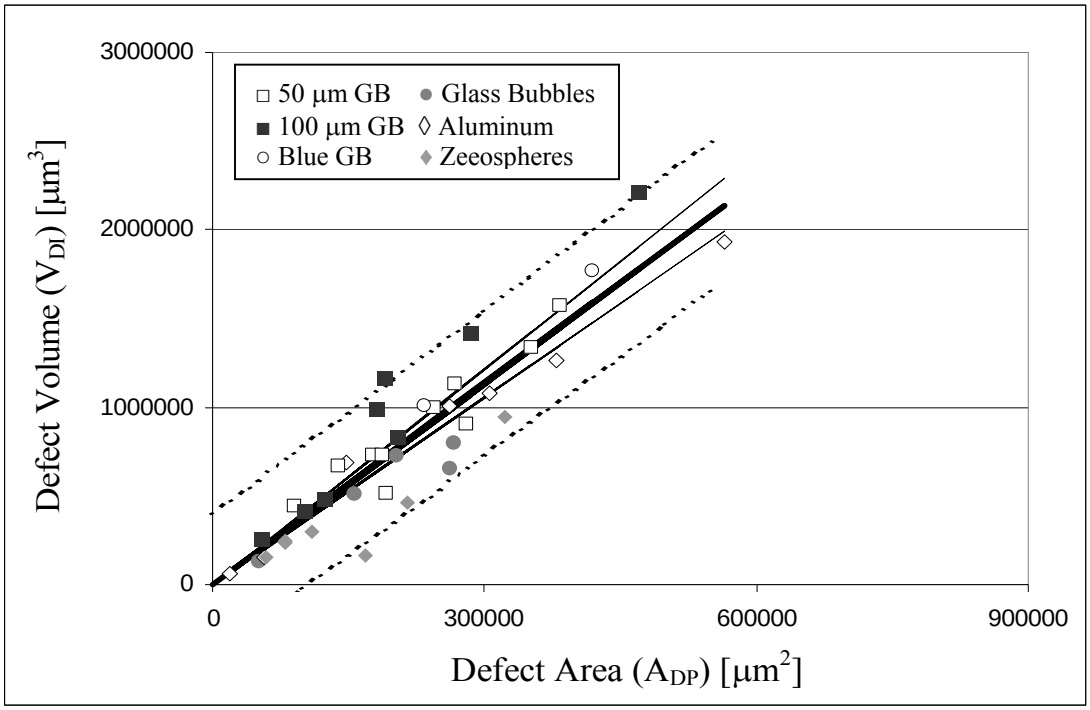


**Figure 4-19:** Defect volume from interferometry ($V_{DI}$) versus defect area from polarized light imaging ($A_{DP}$) for low average height defects caused by spherical particles at a film thickness of 66.6 μm.

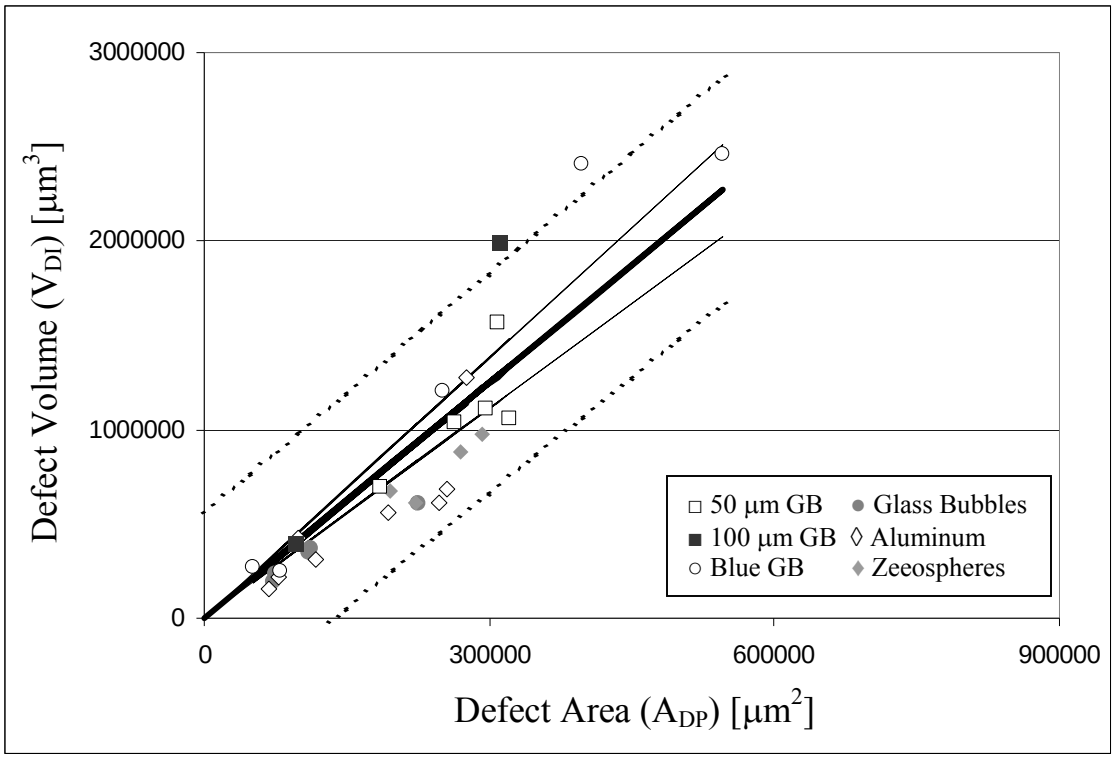


**Figure 4-20:** Defect volume from interferometry ($V_{DI}$) versus defect area from polarized light imaging ($A_{DP}$) for low average height defects caused by spherical particles at a film thickness of 56.6 µm.

**Table 4-5:** Summary of linear regression output for defect volume ($V_{DI}$) versus defect area ($A_{DP}$) for high average height defects caused by spherical particles.

| $h_{film}$ [µm] | H [µm] | $R^2$ | Standard Error of Estimated H [µm] | Lower 95% Confidence Limit about H [µm] | Upper 95% Confidence Limit about H [µm] |
|---|---|---|---|---|---|
| 240.7 | 18.6 | 0.941 | 0.760 | 17.1 | 20.2 |
| 152.0 | 22.9 | 0.957 | 0.678 | 21.6 | 24.3 |
| 109.4 | 31.9 | 0.955 | 0.931 | 30.1 | 33.8 |
| 82.1 | 30.7 | 0.747 | 3.57 | 23.4 | 38.1 |
| 66.6 | 32.5 | 0.882 | 2.65 | 26.9 | 38.0 |
| 56.6 | 35.9 | 0.878 | 2.79 | 30.1 | 41.7 |

**Table 4-6:** Summary of linear regression output for defect volume ($V_{DI}$) versus defect area ($A_{DP}$) for low average height defects caused by spherical particles.

| $h_{film}$ [μm] | H [μm] | $R^2$ | Standard Error of Estimated H [μm] | Lower 95% Confidence Limit about H [μm] | Upper 95% Confidence Limit about H [μm] |
|---|---|---|---|---|---|
| 240.7 | 1.31 | 0.954 | 0.0712 | 1.15 | 1.46 |
| 152.0 | 2.17 | 0.968 | 0.0847 | 1.99 | 2.35 |
| 109.4 | 3.36 | 0.981 | 0.0977 | 3.16 | 3.56 |
| 82.1 | 3.47 | 0.974 | 0.116 | 3.23 | 3.71 |
| 66.6 | 3.78 | 0.958 | 0.130 | 3.52 | 4.04 |
| 56.6 | 4.16 | 0.930 | 0.216 | 3.72 | 4.60 |

As detailed in Section 2.3.3, when more than a single observation of defect volume having the same defect area are averaged with other observations of the same volume then the prediction limits converge to the confidence limits as the number included in the average increases. In practice, to obtain this improved prediction precision, this would require locating identical defect areas in a film. This is possible but would require an automated approach.

If only a single observation of defect volume will be done then, in Figure 4-9 for example, the prediction interval is about constant over the entire range of defect areas at ±1800 $\mu m^3$. At the highest defect areas (those which would be most visible) this is a ±23% error. However, at the lowest end of the range the percentage error is hundreds of a percent. With an increasing number of replicates, the error approaches the minimum value and is defined by the confidence limits. This is a constant value of ± 8.25% across the entire range of defect areas. The prediction error and confidence boundaries shown in the other Figures define similar situations.

Tables 4-5 and 4-6 show the correlation coefficient squared and the confidence intervals for the slopes. All but three of the twelve fits show multiple correlation coefficient squared values exceeding 93% with the worst being 74.7% for a film thickness of 82.1 μm. The three thickest films for the high average height defects provided noticeably better correlations than the thinner. However, for low average height defects no such trend was evident. The average heights of high average height defects ranged from 18.6 to 35.9 μm while those for the low average height defects were from 1.3 to 4.2 μm.

It was considered particularly notable that no trend associated with particle type was observed. So long as the particles were spherical it did not matter whether they were glass microspheres, glass bubbles, aluminum powder or ceramic microspheres; they all followed the same lines at the same film thickness. This implied that particle properties (notably surface properties and particle density) were not influencing the results.

All of the above figures provided results particular to individual film thicknesses. That is, they each corresponded to a single roller speed. In this study, since roller speed was the only processing variable that was changed (aside from the particle type) it meant that each corresponded to one set of processing conditions. To generalize the results it was necessary to attempt to correlate them with film thickness. This is examined in the next section.

### 4.3.2 Variation of Average Defect Height of Spherical Particles with Film Thickness

Figures 4-21 and 4-23 show plots of average defect height versus film thickness for high average height and low average height defects, respectively. Also shown, as vertical error bars around each data point are the 95% confidence intervals for each defect average height. These intervals are those of the slope from each linear regression fit of the data in Figures 4-9 to 4-20. Error in the film thickness was considered negligible. (As mentioned in Sections 4.1.1, an overall standard error for the thickness values was determined to be 3.74 μm from the fit of thickness versus roller speed.).

With regards to the trend shown in these figures, at higher film thicknesses since there is more space in the film matrix for a particle to move then there are many particle location possibilities. Therefore, the probability of a particle being close to the surface decreases. In addition, the film was so thick that the presence of a typical particle tested in the experiments is unlikely to cause a hole or rip the film apart. Average defect height is defined as the volume of defect above the surface divided by the area of the deformed region as viewed with the polarized light. Thus, it would be expected that the average defect height value would decrease at higher thickness levels as shown in Figures 4-21 and 4-23.

In addition, for a very thin film, presence of a foreign particle in the film matrix under the experimented conditions is likely to create a hole in the film or to cause the filmstrip to tear. A particle has a high probability of being close to the surface, resulting in defects with higher volume and lower area with consequently higher average height. An interesting aspect is that particle size did not influence the average defect height (H). Also, no influence of

particle diameter to film thickness ratio on the average defect height was evident for either low or high average height defects.

The next consideration was how best to fit the data shown in these figures. It was concluded that, considering the error bars, the data could be fit almost equally well by several equations. However, the trend in the data and consideration of requirements of the mechanistic model (Section 2.3.5, Eq. 2-23) an exponential model appeared particularly suitable and was the equation selected. Thus a non-linear regression method (Solver in Microsoft Excel) was used to obtain the coefficient values $a_0$ and $a_1$ in the following equation for the data shown in Figures 4-21 and 4-23:

$$H = a_0 \exp(a_1 h_{film}) \qquad (2\text{-}23)$$

Eqn. (2-23) was fit using weighted least squares with the weighting factors being the reciprocal of the error variance of the average height values. Weighting in this way caused the more precise data to influence the choice of coefficients in the exponential function more than the less precise data. The fits are shown in Figures 4-21 and 4-23 with the coefficient values detailed in Table 4-7. It is possible to compute prediction limits, etc. for these fits. However, with only a few data points and considering the uncertainty in specifying weighting factors across the thickness range it was decided that showing the fit in Figures 4-21 and 4-23 is sufficient along with the plots of residuals in Figures 4-22 and 4-24.

**Table 4-7:** Fit of average defect height (H) versus film thickness ($h_{film}$) data. Coefficients for Equation 2-23:

| **Defect Type** | **$a_0$ [μm]** | **$a_1$ [$\mu m^{-1}$]** | **Standard Error of the Estimate of H [μm]** |
|---|---|---|---|
| High Average Height | 44.9 | -0.00397 | 2.20 |
| Low Average Height | 6.01 | -0.00644 | 0.213 |

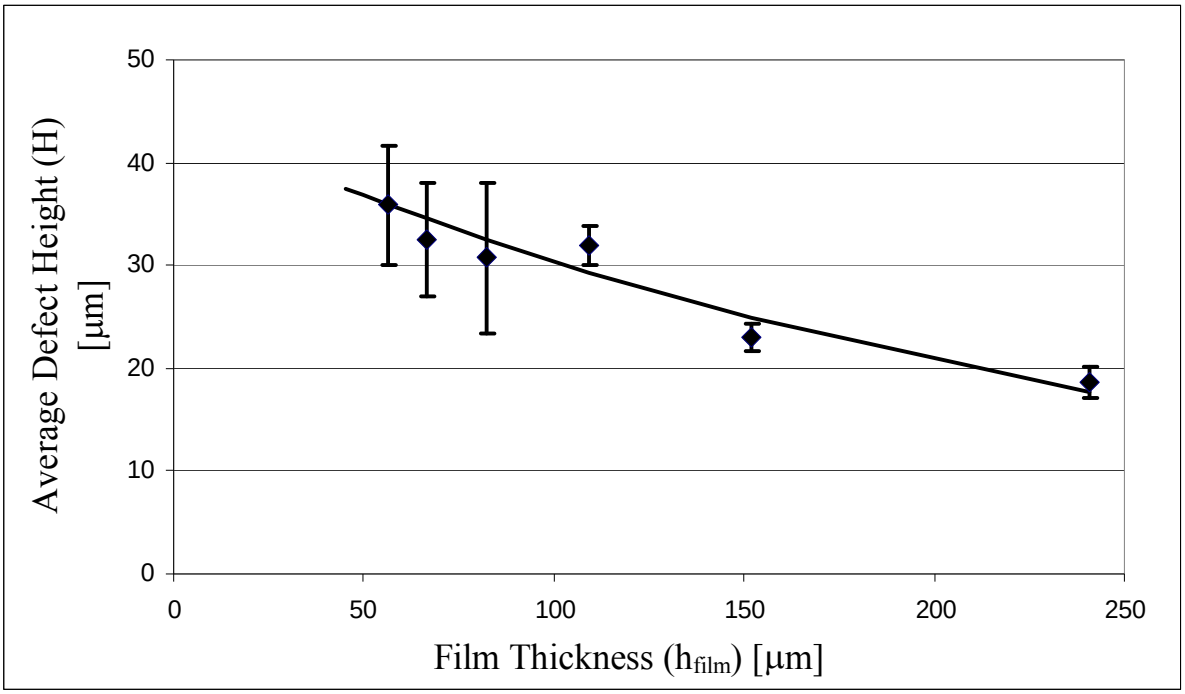


**Figure 4-21:** Average defect height (H) versus film thickness ($h_{film}$) for high average height defects generated by spherical particles. The error bands show the upper and lower 95% confidence limits about the mean average defect height.
Symbols: (♦) Experimental average defect height, (—) Exponential fit (Eqn. 2-23).

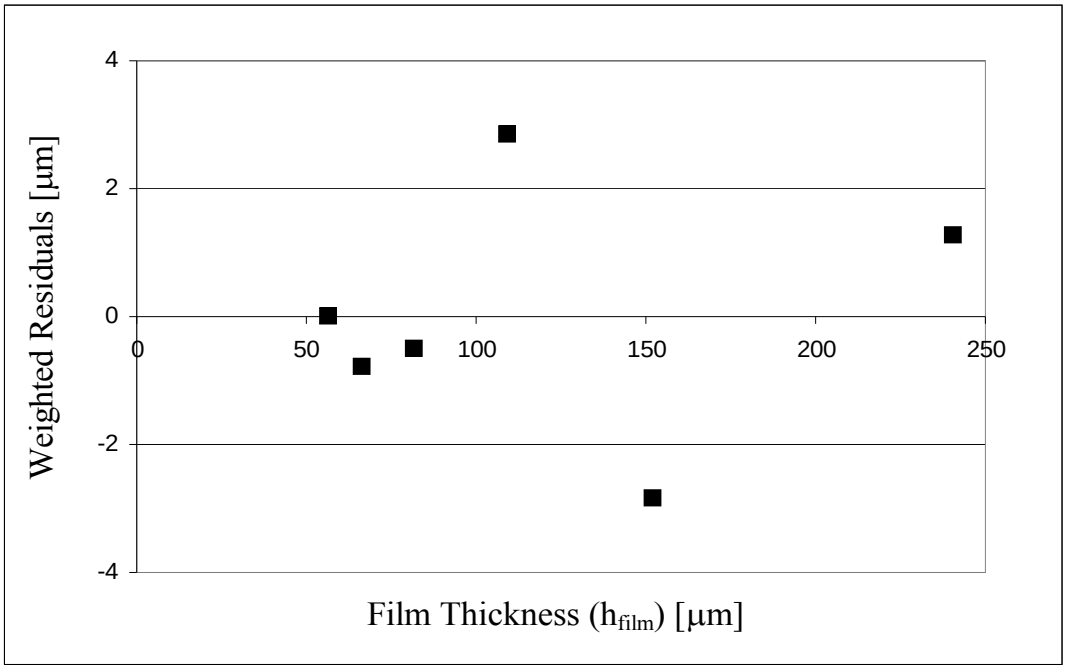


**Figure 4-22:** Weighted average defect height residuals versus film thickness for high average height defects and the fitted exponential model shown in Figure 4-21.

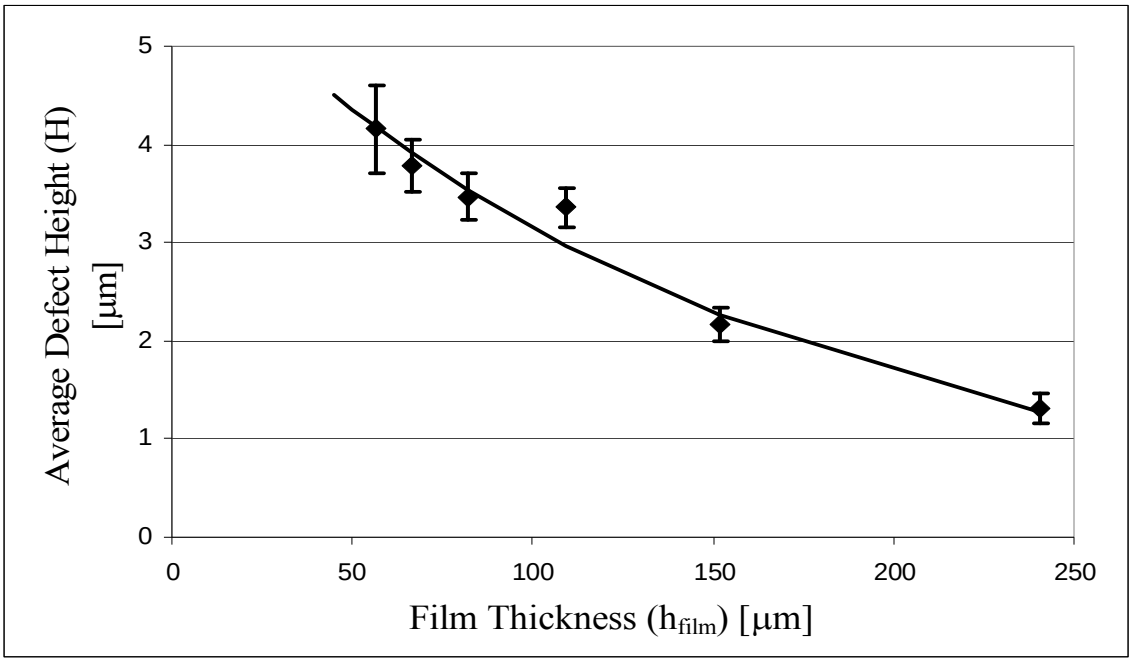


**Figure 4-23:** Average defect height (H) versus film thickness ($h_{film}$) for low average height defects generated by spherical particles. The error bands show the upper and lower 95% confidence limits about the mean average defect height.

Symbols: (♦) Experimental average defect height, (—) Exponential fit (Eqn. 2-23).

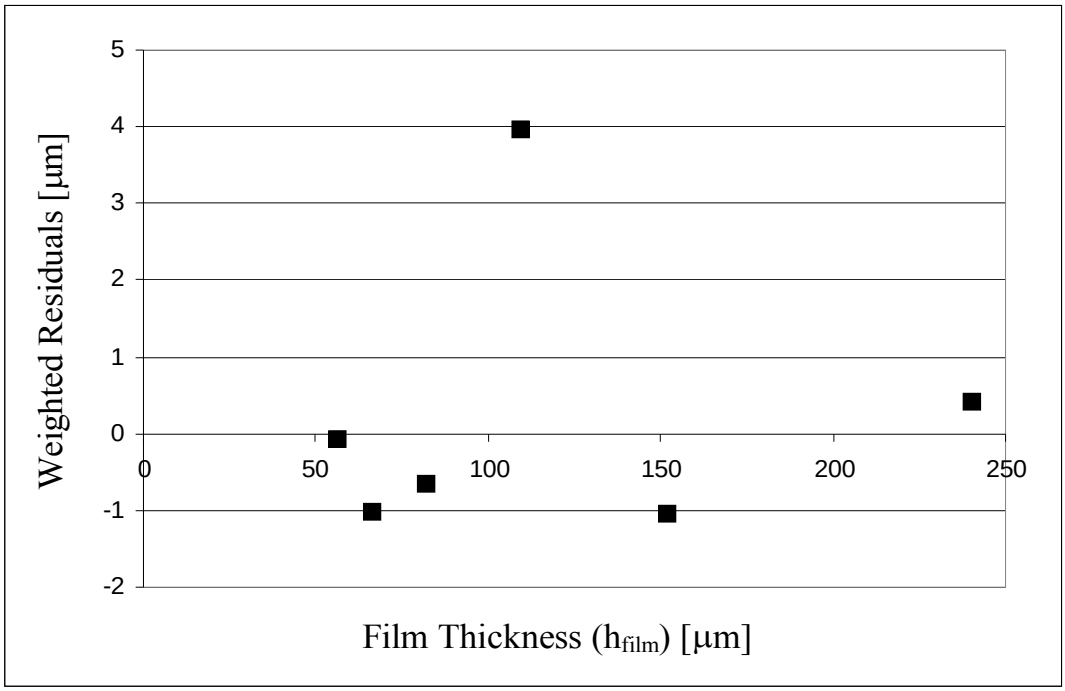


**Figure 4-24:** Weighted average defect height residuals versus film thickness for low average height defects and the fitted exponential model shown in Figure 4-23.

### 4.3.3 Average Defect Height for Non-Spherical Particles

As mentioned above, 105 data records of the total 525 records in the database were for non-spherical particles. These particles were sufficiently diverse that no attempt was made to develop a mathematical model for them. Instead, in the Appendices are shown polarized light images of typical defects resulting along with defect volume versus defect area plots at each film thickness. For each plot the data points for the non-spherical particle is shown superimposed on the fitted line and 95% prediction interval obtained for the spherical particles. There were two types of non-spherical particles: wood particles and cross-linked polymer particles. These are examined in turn in the following two sections.

#### 4.3.3.1 Average Defect Height: Wood Particles

Polarized light images of two typical film defects caused by wood particles are shown in Figure 4-25. Images of other high and low average height defects caused by these particles are available in Figure 4-VII-1 in Appendix 4-VII and also in Figure 3-II-9 in Appendix 3-II. The polarized light images of most wood particles show them to be approximately rectangular in shape. Their three-dimensional shape is uncertain. Variations in thickness were likely.

Figures 4-VII-2 to 4-VII-10 in Appendix 4-VII show defect volume ($V_{DI}$) versus defect area ($A_{DP}$) plots of high and low average height defects caused by wood particles superimposed on the spherical data results. Both the images and many of the figures show that the wood particles often generated similar defects to those of spherical particles. Defect variety appeared about the same and often the data points in the figures lay within prediction

limits obtained for spherical particles. However, some startling exceptions, especially those evident in Figure 4-VII-6, possibly due to particle thickness, caused exclusion of these types of particles from the spherical analysis.

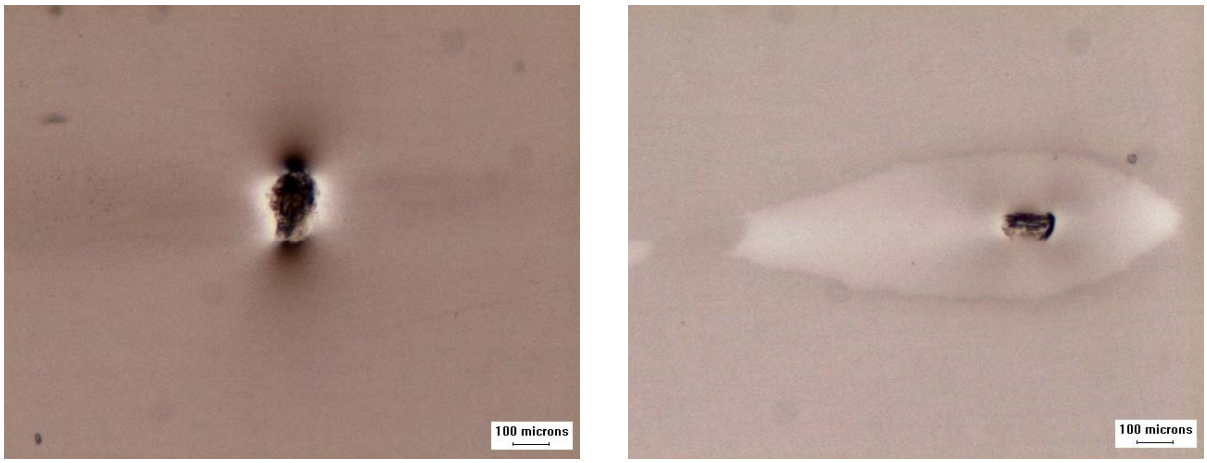


**Figure 4-25:** Polarized light images of typical defects caused by wood particles. **(Left)** High average height defect, (Image name: R28R40-D9) **(Right)** Low average height defect, (Image name: R28R70-D7)

#### 4.3.3.2 Average Defect Height: Cross-Linked Particles

The cross-linked low-density polyethylene particles were different from all other tested particles in this project since they softened at the extruder operating temperatures. That is, in addition to deforming the film, these particles themselves could deform. Polarized light images of two defects caused by cross-linked polymer particles are presented in Figure 4-26. Additional images of defects generated by these particles are available in Figure 4-VIII-1 in Appendix 4-VIII and in Figure 3-II-8 in Appendix 3-II. The defects often appear very different from those of other particles. Figures 4-VIII-2 to 4-VIII-11 in Appendix 4-VIII show defect volume ($V_{DI}$) versus defect area ($A_{DP}$) plots.

Not unexpectedly for these very different particles, practically all of the data points are remote from the lines obtained from spherical particles. An added source of the observed difference was increased uncertainty in the measured defect area: in some polarized light images of these defects it was difficult to distinguish the embedded particle from the deformed area and from the background. Despite this situation, it was interesting to note that the defect volume data often did show a linear correlation with defect area in much the same way as did the spherical particles. However, the slope (i.e. the average defect height) was consistently much different.

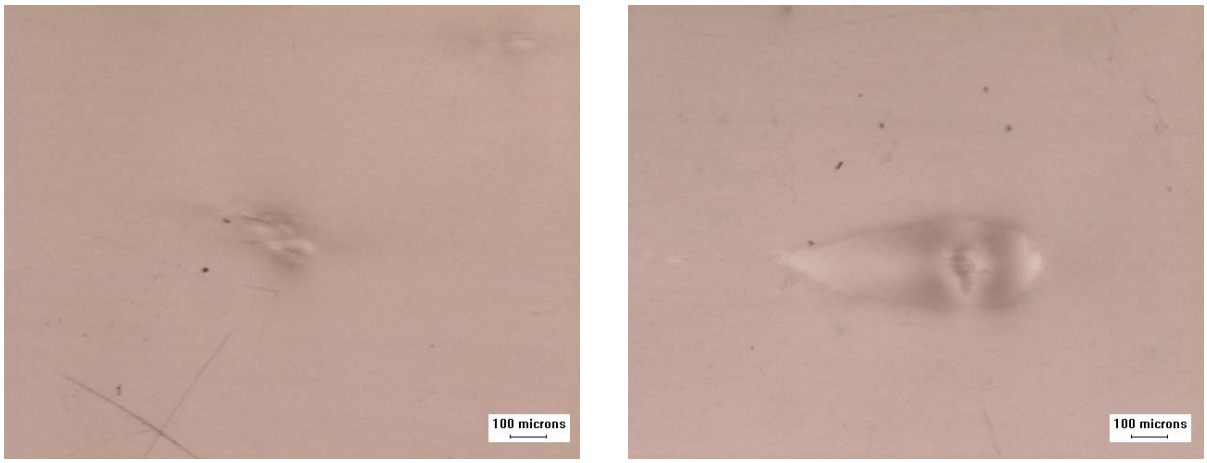


**Figure 4-26:** Polarized light images of typical defects caused by cross-linked polyethylene particles. **(Left)** High average height defect, (Image name: R26R50-D5) **(Right)** Low average height defect. (Image name: R27R60-D5)

## 4.4 Defect Classes

### 4.4.1 Identification of Defect Classes

The previous sections showed that the spherical particle data resulted in two main defect classes: defects with a low average height and defects with a high average height. It is important to realize that because the heights are averages it is quite possible for a high average height defect to have a lower maximum height than a low average height defect. This is shown in Appendix IX.

These classes could be readily distinguished by plotting defect volume (from interferometric images) versus defect area (from polarized light images). Table 4-3 summarizes some of the main particle, defect and film attributes for each of these classes. This table was already discussed with reference to the whole dataset. Now it can be examined to see how these attributes compare for the two classes.

From the data in Table 4-3, first, it was evident that both low and high average height defects had very strongly overlapping particle diameters and particle areas. That is, specifying a particle diameter or particle area alone could not reveal the defect class. However, in contrast to the particle diameter, the defect diameter for each class appeared in two distinct ranges. The diameter of the low average height defects range from 294 to 986 μm while the diameter of the high average height defects range from 15.4 to 235 μm. The situation is essentially the same for defect area: low average height defects having an area from 43,300 to 801,000 $\mu m^2$ while high average height defects showing areas from 175 to

44,500 $\mu m^2$ [A defect area of about 44,000 appears to be the boundary between the two classes and there may be some overlap around that value.]

Table 4-3 also shows that when a circular shape was assumed in calculating area from the mean diameter of a particle the accuracy of the resulting area was less than about 3% for high average height defects but ranged as high as 14.6% for low average height defects. This likely means that the low average height defects were more often caused by the less spherical particles. When a circular shape was assumed in the calculation of defect area the error was about ±6% for high average height defects. However, for low average height defects the calculated defect area could be as much as 57% higher than the experimentally measured value of defect area. This agreed with the observation that low average height defects were often non spherical. The range of particle diameter to film thickness does not appear to be very different for the two classes despite the intuitive belief that this ratio should make a difference.

Elucidating the mechanistic reason for there being two distinct groups of defects is a new research topic deserving of an experimental and theoretical development with this specific objective and is beyond the scope of this thesis. That said, it is possible to hypothesize reasons and test the hypotheses with the limited data obtained in this work. In Appendix 4-IX, four different hypotheses are proposed. Of the four, only particle debonding is tentatively supported by the available data.

No influence of particle diameter to film thickness ratio ($D_P/h_{film}$) or particle area ($A_P$) on the average defect height (H) was evident for either low or high average height defects. However, Figures 4-IX-4 to 4-IX-9 in Appendix IX show that at each film thickness, defect maximum height ($H_{max}$) (as opposed to average defect height, H) increased as particle area increased. The scatter in the data is more significant for thicker films. Figure 4-IX-2 in Appendix IX also shows that defect maximum height of low average height defects is directly correlated with the $D_P/h_{film}$ ratio.

### 4.4.2 Predicting Defect Class

The two classes identified by determining average defect height by combining interferometric and polarized light data show major differences in average defect height (from Tables 4-5 and 4-6) and in defect area. If we wish to predict these two properties it is necessary to determine which class of defects we are dealing with in a film extrusion line. Extensive effort with spherical particles revealed that the particle properties were not useful for classification. That is, no particle property or combination of particle properties could be found that could predict into which class the resulting defect would fall. Another way of stating this is that a given spherical particle could result in either a high or a low average height defect.

However, another solution to the problem was evident. From the previous section we could see that information on the defect mean diameter (and, less effective, defect area) could immediately be used to classify the defect as high or low average height. Further investigation of the database revealed many more attributes that could serve as discriminating

attributes. In addition to DDiameter(mean), measurements of DAxis-(major), DDiameter-(max), DRadius-(max), DPerimeter, DSize-(length), DPerim.-(convex), DPerim.-(ellipse), and DFeret-(max) provided excellent discrimination.

In practice, the most conveniently measured attribute could be selected to determine whether high or low average height defects were the dominant type present. Then the appropriate exponential equation for average defect height could be used to predict the average defect height from the film thickness. This solution is not as satisfactory as using particle properties available from an in-line melt monitor. However, the polarized light imaging method is easily done off-line and even adapted for in-line use. It is anticipated that in an industrial situation, once initial measurements were done using polarized light the operator would soon know which class of defect to expect during normal operation. If desired, the attribute could be measured for many defects in the film and the relative amounts of low and high average height defects in the product estimated. Then the relative frequency of their corresponding predicted average height values could be estimated.

Thus, at this point, two defect classes have been identified, equations for average defect height as a function of film thickness have been developed, and a method for predicting the defect class from defect mean diameter (or area) has been revealed. The remaining task is the prediction of defect area.

## 4.5 Defect Area

The area of a defect is an important defect property because the human eye is particularly sensitive to area. Thus, the aesthetic appeal of a polymer film is very dependent upon the area of the defects that are present. This section examines the problem of predicting defect area from particle properties and focuses upon a particular quantity: magnification. Magnification is defined as the ratio of defect area (determined from polarized light imaging) to particle area (here also obtained from the polarized light image but in practice would be obtained from images from the in-line melt monitor). As mentioned earlier, in this work average defect height and magnification are termed "primary defect properties" because of their fundamental importance in characterizing the defects.

### 4.5.1 Particle Area Magnification for Spherical Particles

As in the case of average defect height calculations, calculating magnification as a ratio of two experimental quantities was too error prone to be useful. However, as in the average defect height case, the problem was overcome by obtaining magnification from the slope of a fitted line. Figure 4-27 shows a plot of defect area ($A_{DP}$) versus particle area ($A_P$) for a film thickness of 109.4 μm for high and low average height defects when glass microspheres were used to generate the defects. As in the defect volume ($V_{DI}$) versus defect area ($A_{DP}$), although the scatter is worse in this case and the ordinate scale for the lower set of data obviously needs to be expanded and the data plotted separately, two linear correlations were evident. Using the same approach as with the average defect height analysis, the slope of lines fitted through each of these correlations could be used to define two classes: high and low magnification factors. To see if this was feasible, the same

procedure was carried out with these data as was done with the defect volume versus defect area data.

What was almost immediately realized was that each of the two classes of magnification (high and low) corresponded to one of the classes of average defect height: the high magnification defects were also the low average height defects and the low magnification defects were also the high average height defects. Thus, there were only two classes (or, synonymously, "types") of defects in the data from spherical particles and these classes would continue to be termed here "high average height" and "low average height" based on their average defect height values.

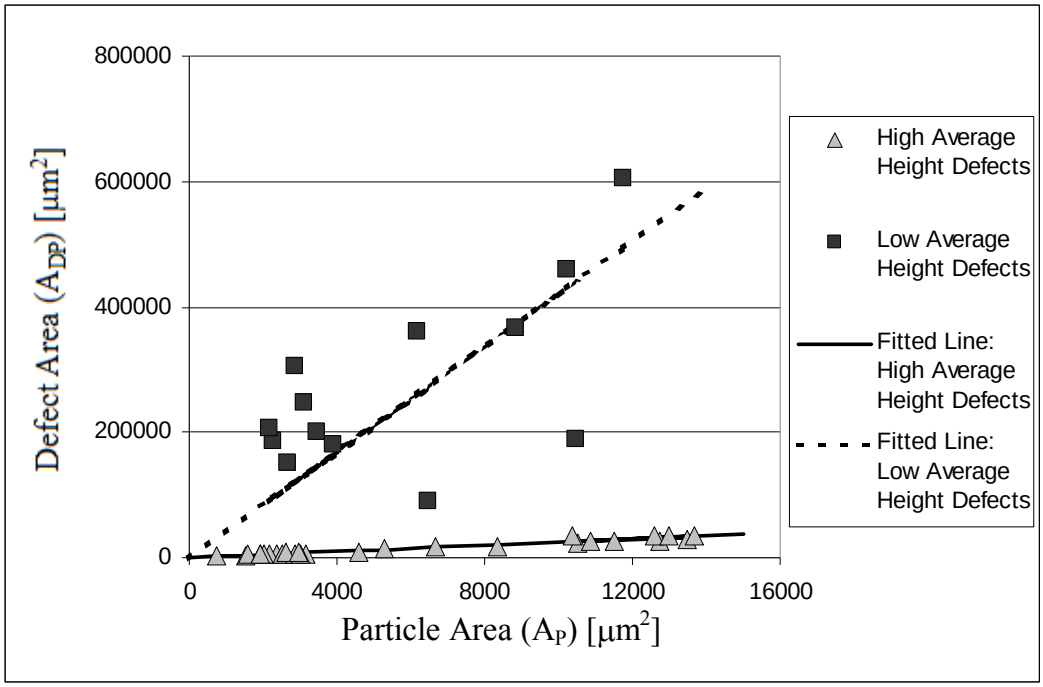


**Figure 4-27:** Defect area obtained from polarized light imaging ($A_{DP}$) versus particle area obtained with the same method ($A_P$) for high and low average height defects caused by glass microspheres at a film thickness of 109.4 μm. Two straight lines passing through the origin show the best least squares fit for each defect group.
Symbols: High average height defects (▲) Low average height defects (■).

Figures 4-28 to 4-33 show fits of defect area versus particle area for high average height defects using all spherical particles (glass microspheres, glass bubbles, aluminum powder and ceramic microspheres). The same scatter plots for low average height defects are shown in Figures 4-34 through 4-39. For some of the latter, scatter was quite large. Similar to the previous average defect height analysis, data for each film thickness is represented by two figures: one for the high average height data and one for the low, so that an appropriate $A_{DP}$ scale could be used for each. Each set of data was fit by a straight line passing through the origin (the thick solid line). On each of the Figures the lines above and below the fitted line show the upper and lower 95% confidence interval for the slope (thin solid lines). Upper and lower 95% prediction limits for the defect area are also shown (thin dashed lines).

Tables 4-8 and 4-9 show the slope of each line (i.e. the magnification), the 95% confidence limits for the slope and the correlation coefficient squared for each line for high and low average height defects. These tables show that the correlation coefficient squared was 90% or better for the high average height defects but ranged from 70% to 89% for the low average height defects. For the former, the defect area was double or even triple the area of the particle causing the defect. However, for the latter, magnifications were 39 to 83 times the particle area! Earlier the average defect height was shown to decrease with an increase in final film thickness. However, the values in these tables show that, as anticipated by the Constant Defect Volume per Unit Particle Area Model of Section 2.3.5, magnification increased as final film thickness increased. This variation with film thickness is examined in the next section.

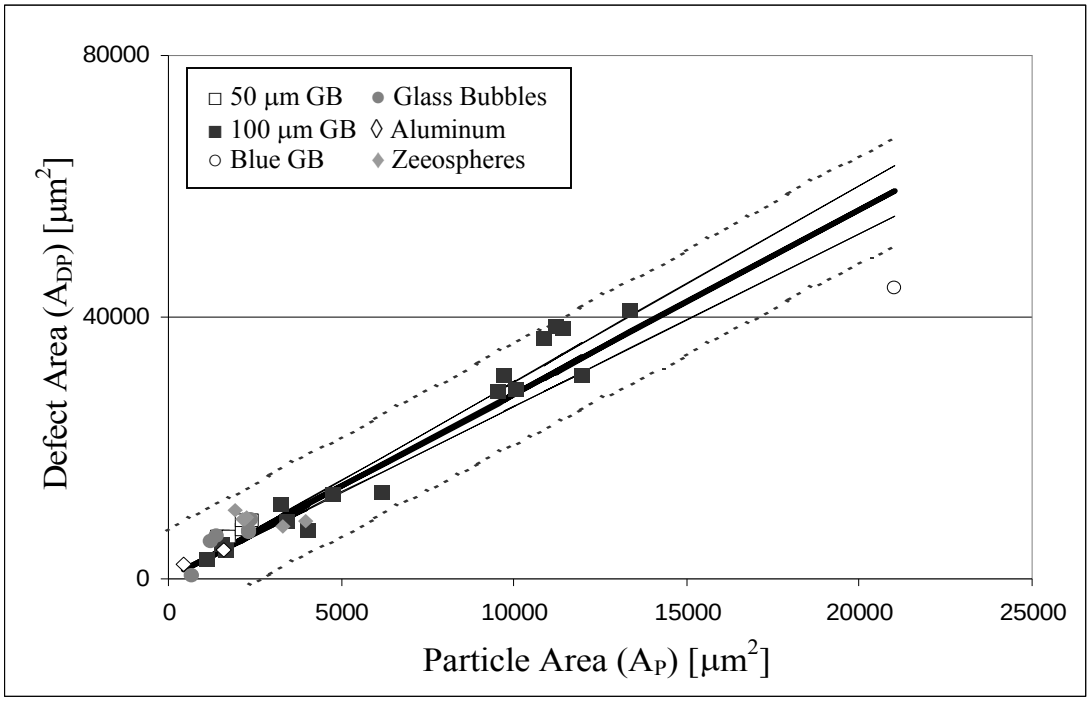


**Figure 4-28:** Defect area from polarized light imaging ($A_{DP}$) versus particle area from polarized light imaging ($A_P$) for high average height defects caused by spherical particles at a film thickness of 240.7 μm.

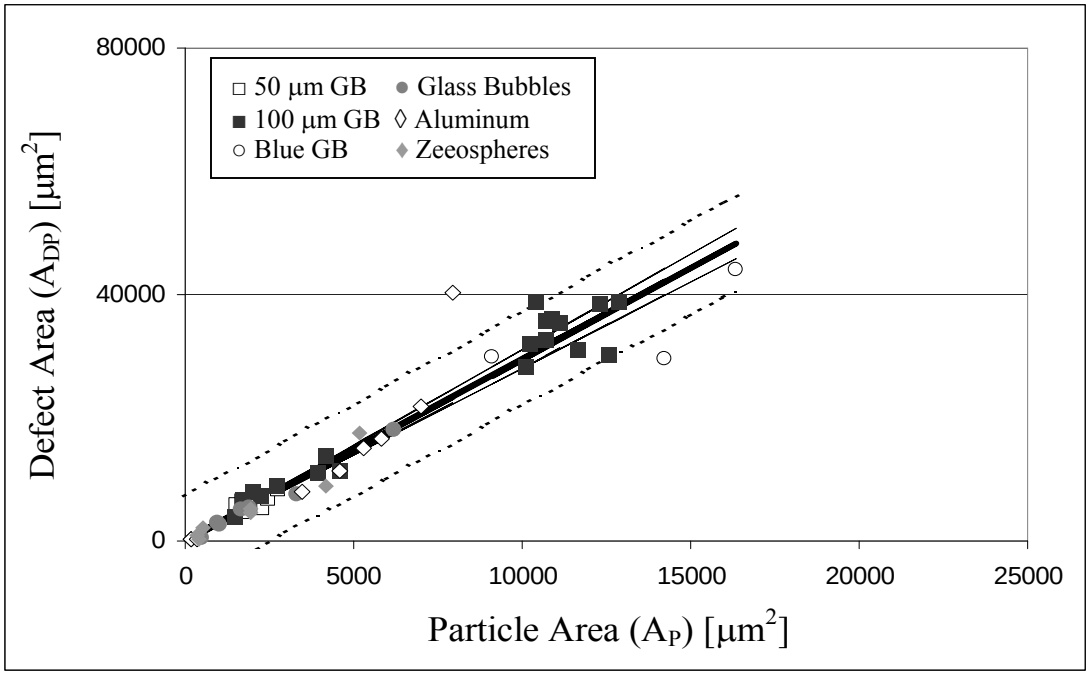


**Figure 4-29:** Defect area from polarized light imaging ($A_{DP}$) versus particle area from polarized light imaging ($A_P$) for high average height defects caused by spherical particles at a film thickness of 152.0 μm.

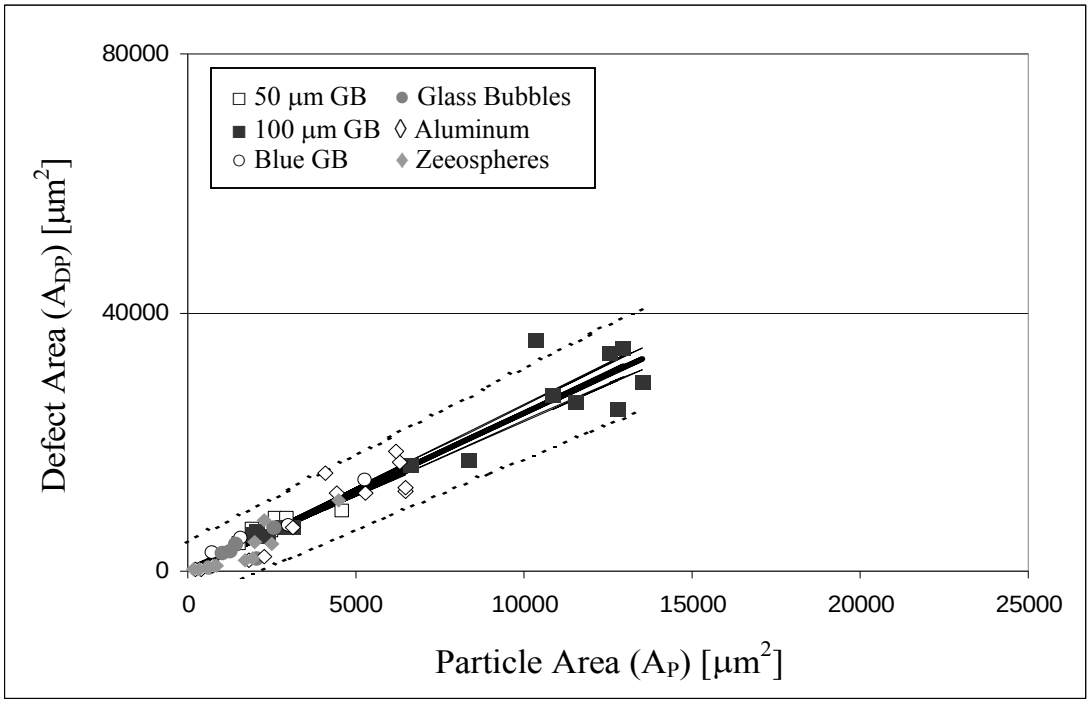


**Figure 4-30:** Defect area from polarized light imaging ($A_{DP}$) versus particle area from polarized light imaging ($A_P$) for high average height defects caused by spherical particles at a film thickness of 109.4 μm.

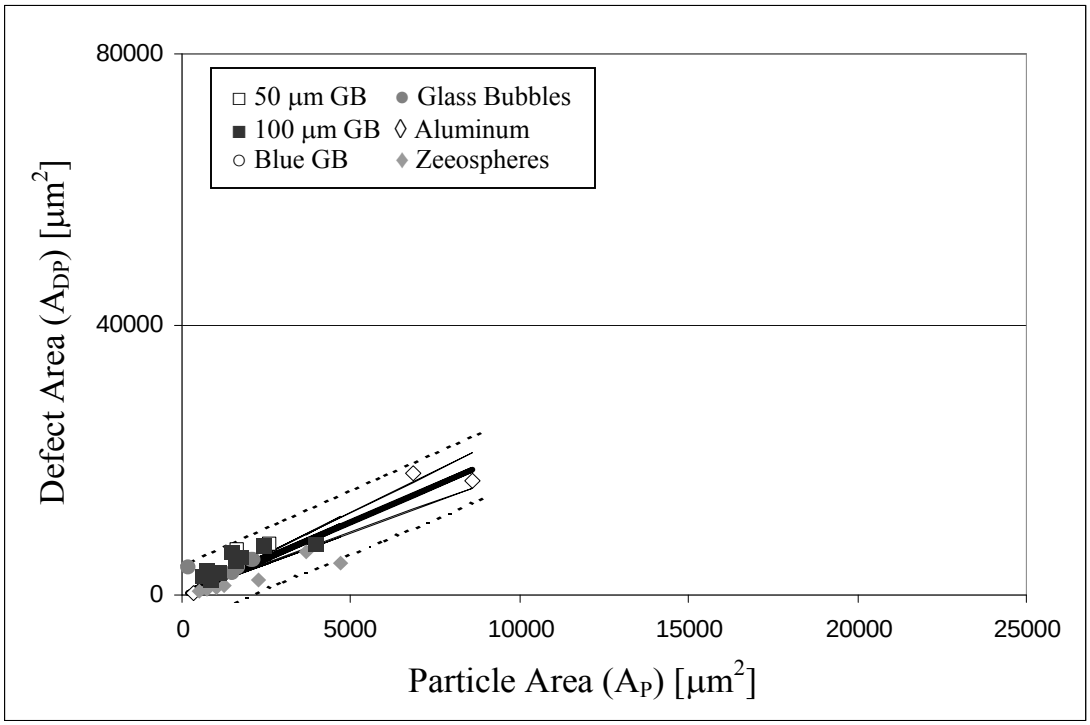


**Figure 4-31:** Defect area from polarized light imaging ($A_{DP}$) versus particle area from polarized light imaging ($A_P$) for high average height defects caused by spherical particles at a film thickness of 82.1 μm.

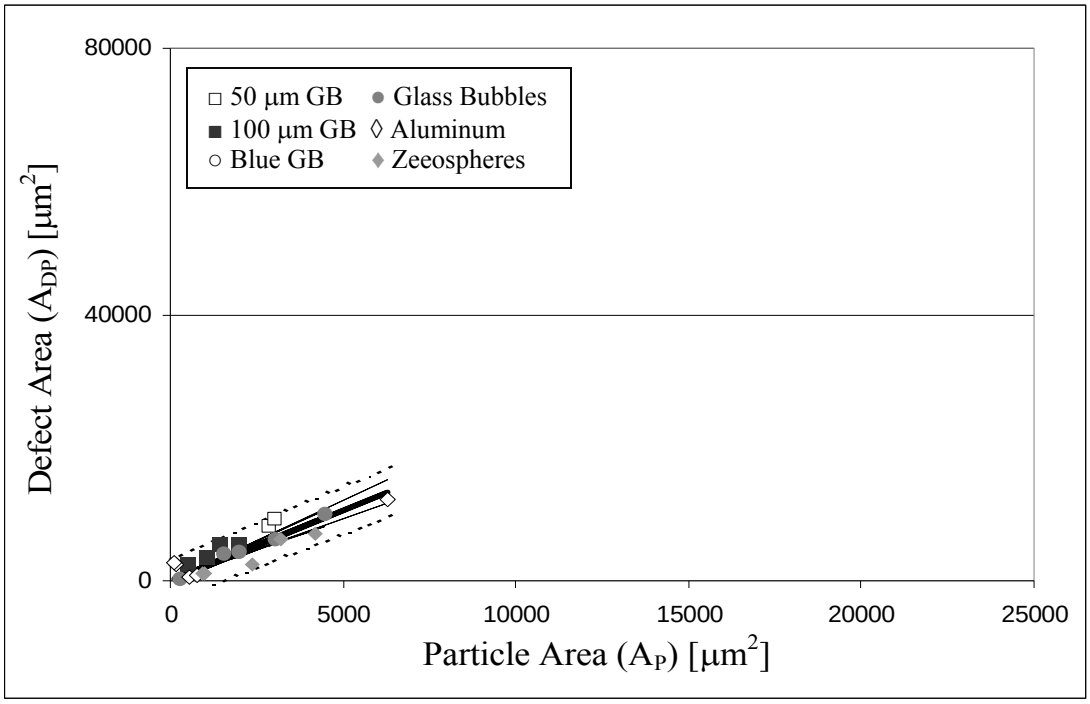


**Figure 4-32:** Defect area from polarized light imaging ($A_{DP}$) versus particle area from polarized light imaging ($A_P$) for high average height defects caused by spherical particles at a film thickness of 66.6 μm.

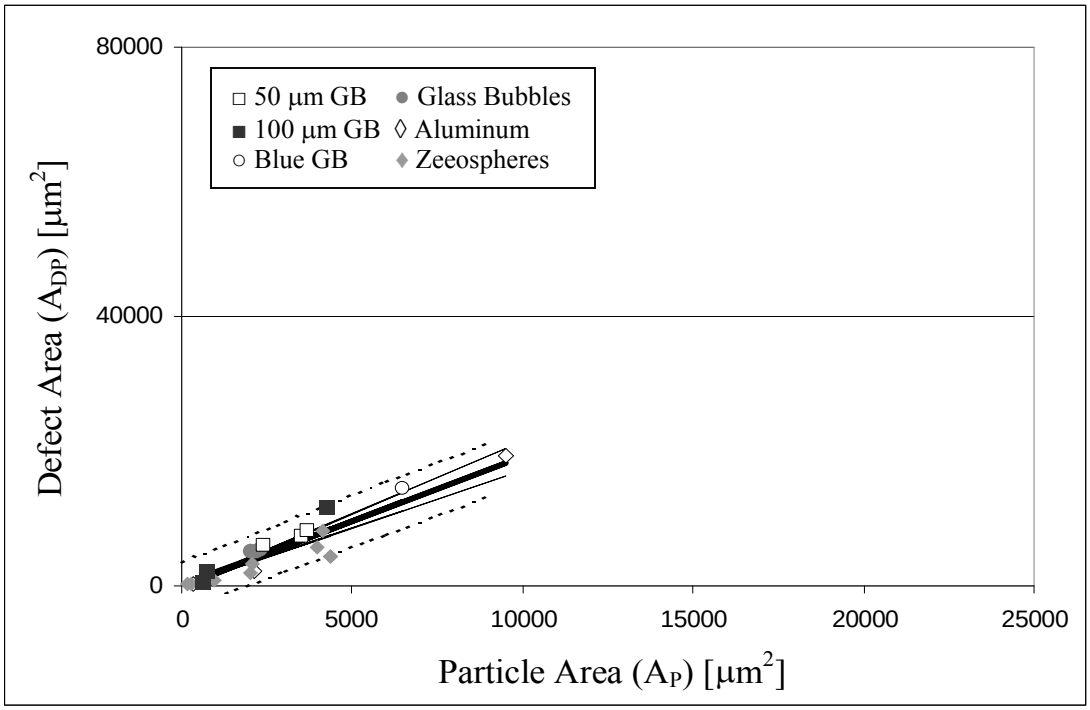


**Figure 4-33:** Defect area from polarized light imaging ($A_{DP}$) versus particle area from polarized light imaging ($A_P$) for high average height defects caused by spherical particles at a film thickness of 56.6 μm.

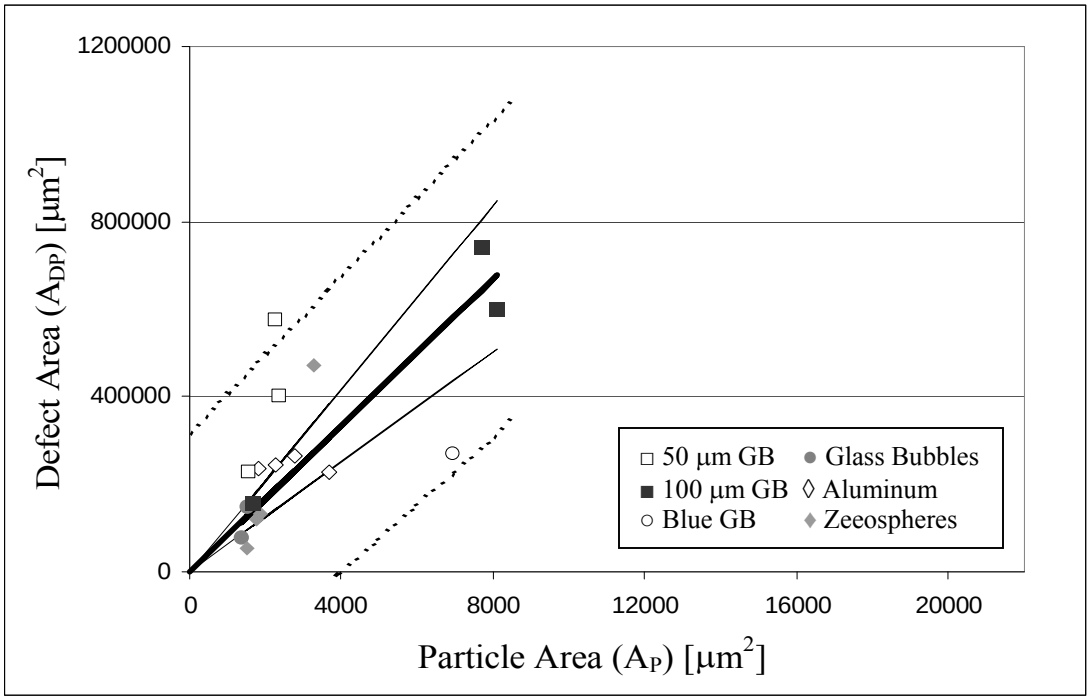


**Figure 4-34:** Defect area from polarized light imaging ($A_{DP}$) versus particle area from polarized light imaging ($A_P$) for low average height defects caused by spherical particles at a film thickness of 240.7 µm.

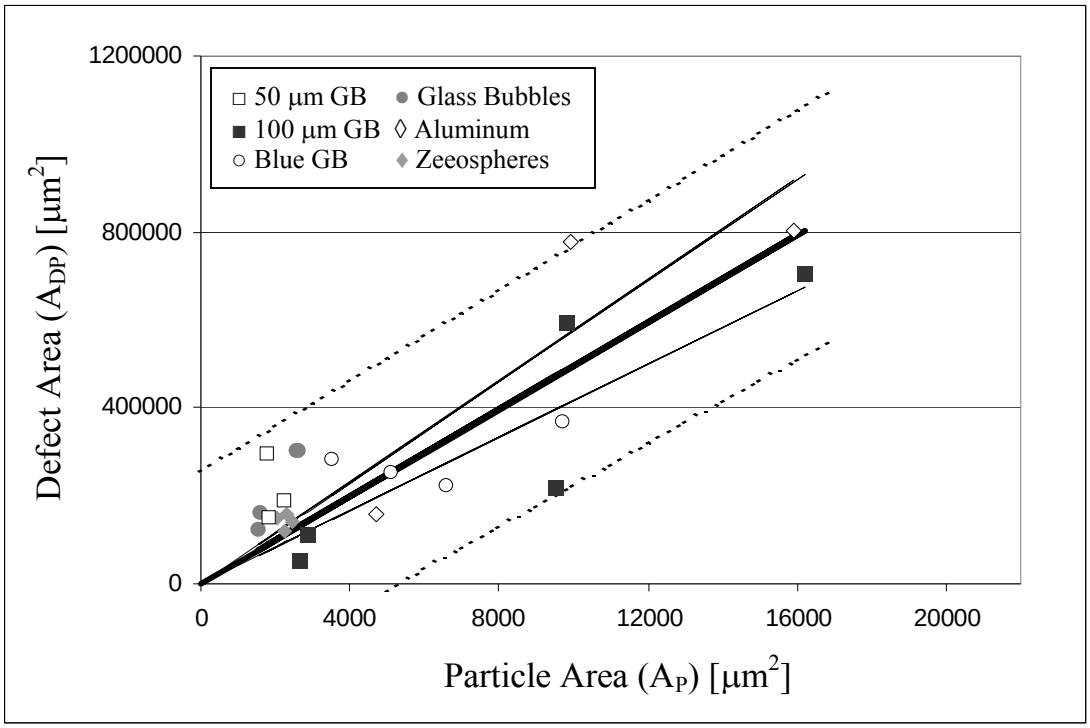


**Figure 4-35:** Defect area from polarized light imaging ($A_{DP}$) versus particle area from polarized light imaging ($A_P$) for low average height defects caused by spherical particles at a film thickness of 152.0 µm.

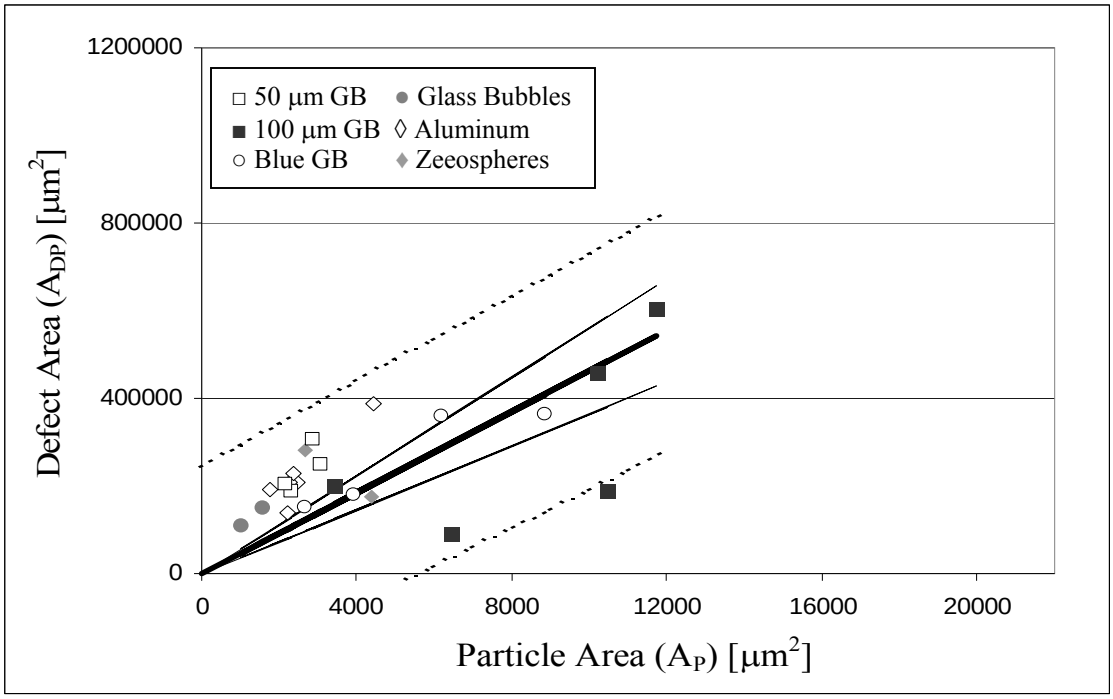


**Figure 4-36:** Defect area from polarized light imaging ($A_{DP}$) versus particle area from polarized light imaging ($A_P$) for low average height defects caused by spherical particles at a film thickness of 109.4 μm.

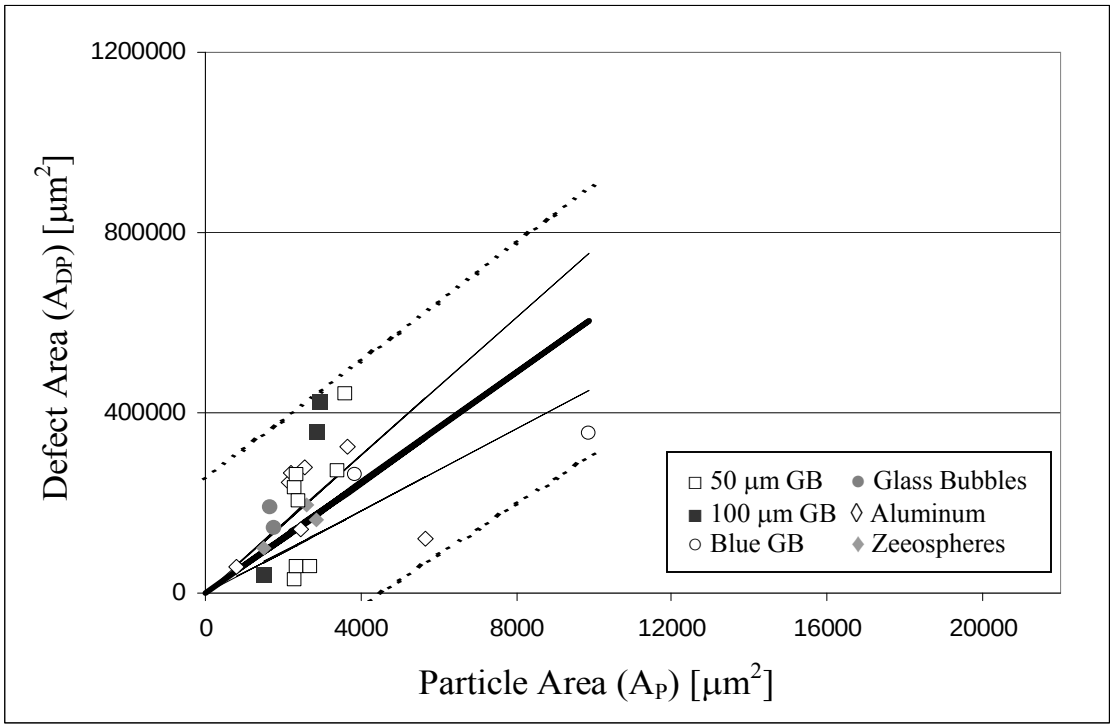


**Figure 4-37:** Defect area from polarized light imaging ($A_{DP}$) versus particle area from polarized light imaging ($A_P$) for low average height defects caused by spherical particles at a film thickness of 82.1 μm.

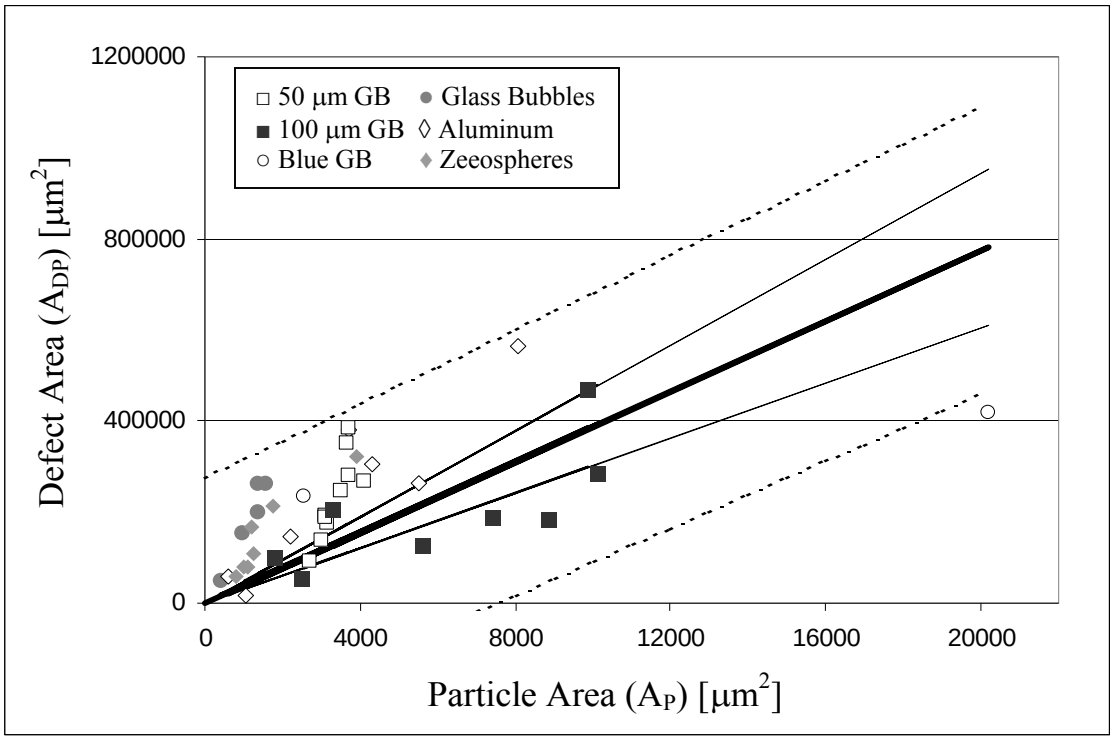


**Figure 4-38:** Defect area from polarized light imaging ($A_{DP}$) versus particle area from polarized light imaging ($A_P$) for low average height defects caused by spherical particles at a film thickness of 66.6 μm.

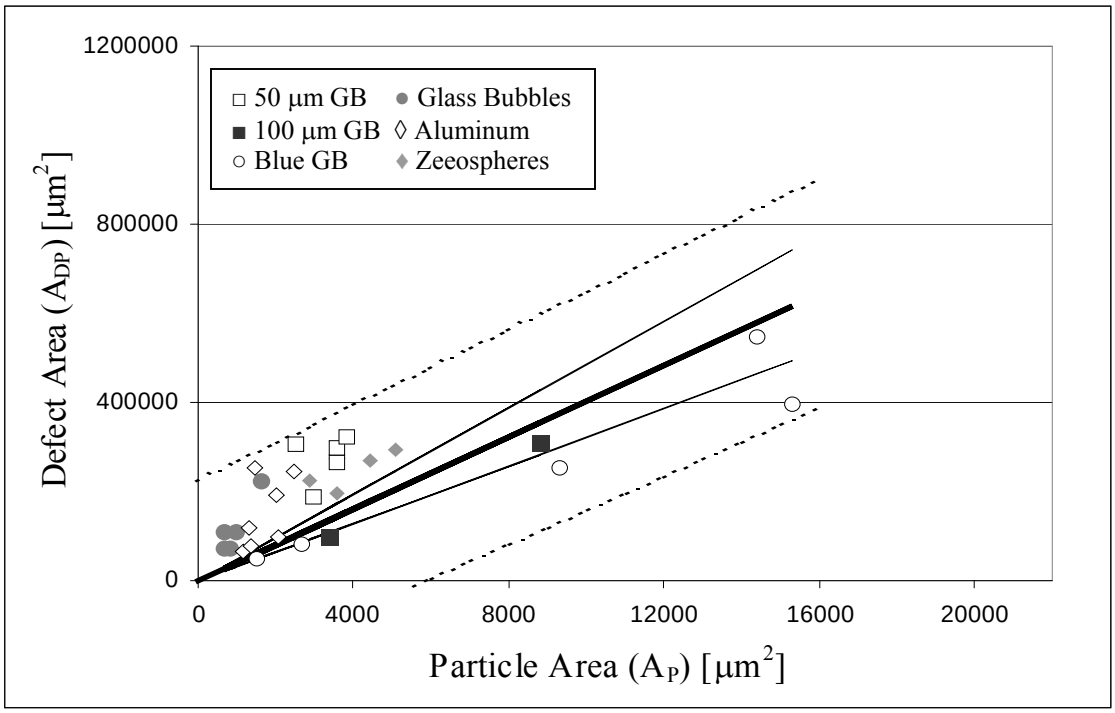


**Figure 4-39:** Defect area from polarized light imaging ($A_{DP}$) versus particle area from polarized light imaging ($A_P$) for low average height defects caused by spherical particles at a film thickness of 56.6 μm.

**Table 4-8:** Summary of $A_{DP}$ versus $A_P$ linear regression modeling output for high average height defects caused by spherical particles.

| $h_{film}$ [μm] | M | $R^2$ | Standard Error of Estimated M | Lower 95% Confidence Limit about M | Upper 95% Confidence Limit about M |
|---|---|---|---|---|---|
| 240.7 | 2.82 | 0.961 | 0.0922 | 2.64 | 3.01 |
| 152.0 | 2.96 | 0.968 | 0.0750 | 2.81 | 3.11 |
| 109.4 | 2.44 | 0.966 | 0.0617 | 2.32 | 2.56 |
| 82.1 | 2.15 | 0.897 | 0.145 | 1.85 | 2.45 |
| 66.6 | 2.11 | 0.925 | 0.135 | 1.83 | 2.39 |
| 56.6 | 1.92 | 0.937 | 0.104 | 1.71 | 2.14 |

**Table 4-9:** Summary of $A_{DP}$ versus $A_P$ linear regression modeling output for low average height defects caused by spherical particles.

| $h_{film}$ [μm] | M | $R^2$ | Standard Error of Estimated M | Lower 95% Confidence Limit about M | Upper 95% Confidence Limit about M |
|---|---|---|---|---|---|
| 240.7 | 83.7 | 0.819 | 9.83 | 62.9 | 104 |
| 152.0 | 49.6 | 0.885 | 3.82 | 41.7 | 57.5 |
| 109.4 | 46.1 | 0.811 | 4.75 | 36.3 | 55.9 |
| 82.1 | 61.0 | 0.732 | 7.54 | 45.5 | 76.6 |
| 66.6 | 38.7 | 0.692 | 4.20 | 30.2 | 47.2 |
| 56.6 | 40.3 | 0.786 | 3.98 | 32.2 | 48.5 |

### 4.5.2 Variation of Area Magnification of Spherical Particles with Film Thickness

Figures 4-40(a) and 4-41(a) show particle area magnification versus film thickness for high average height defects and low average height defects, respectively. For the high average height defect data a definite increase in magnification with film thickness was observed. For the low average height defect data the presence of a correlation was more uncertain. As before with the average defect height versus thickness data, this data was fit by

an exponential model. (Section 2.3.5, Eqn. 2-22) but this time with a positive coefficient in the exponential. Fits are shown in Figures 4-40(a) and 4-41(a) and coefficient values in the first two rows of Table 4-10. Figures 4-40(b) and 4-41(b) show the corresponding plots of residuals.

$$M = b_o \exp(b_1 h_{film}) \qquad (2\text{-}22)$$

The high scatter and almost flat variation of magnification for the low average height defects showed that when the defect area is so much larger than the area of the particle that created it then that defect area is not strongly affected by film thickness at the lower film thicknesses. Also, for all thicknesses, high average height defects generally appear very circular in the images. In contrast, comet-shaped defects were often observed in the low average height defect data.

At higher roller speeds, the low average height defects are narrower and longer. Since the filmstrip is thinner at these roller speeds, the particle and its surrounding area are more likely to cool down faster. This prevents the stressed region around the particle from becoming as large as it does in thicker films. In addition, the higher pulling force means that the film elongates more. This causes the stressed region around the particle to become more elongated as well, resulting in elongated deformations.

**Table 4-10:** Fit of magnification (M) versus film thickness ($h_{film}$) data. Coefficients for Equation 2-22:

| Defect Type | $b_0$ | $b_1$ [$\mu m^{-1}$] | Standard Error |
|---|---|---|---|
| High Average Height | 1.99 | 0.00178 | 0.272 |
| Low Average Height | 32.6 | 0.00336 | 10.8 |
| High Average Height (for $h_{film}$<240.7 μm) | 1.52 | 0.00438 | 0.0517 |

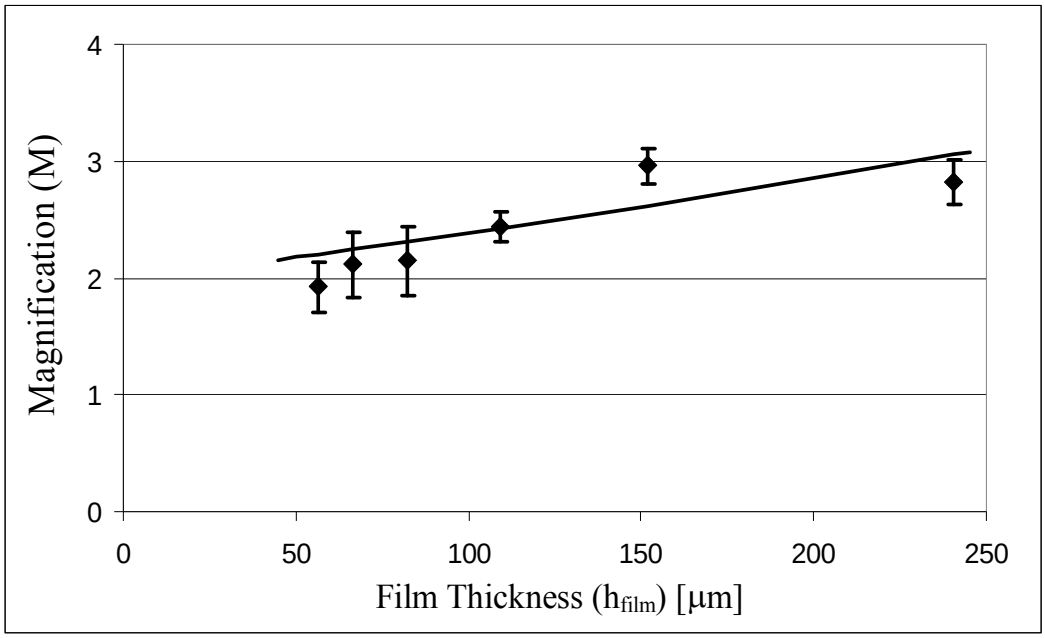


**(a)**

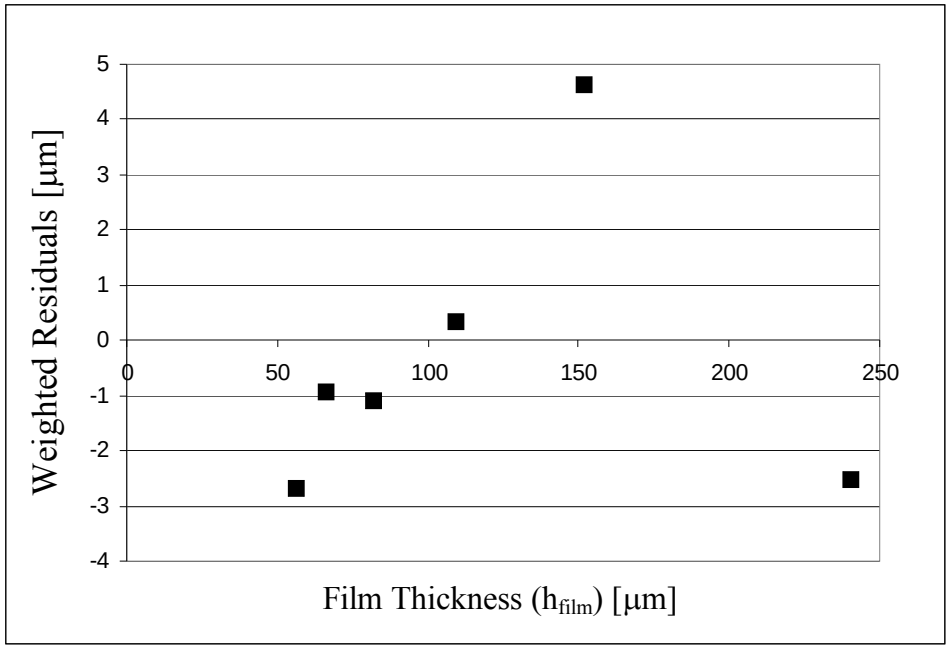


**(b)**

**Figure 4-40: (a)** Particle area magnification (M) versus film thickness ($h_{film}$) for high average height defects caused by all spherical particles. The error bars show the upper and lower 95% confidence limits. Symbols: (♦) Experimental magnification, (▬) Eqn. 2-22.
**(b)** Weighted magnification residuals versus film thickness for high average height defects and the fitted exponential model shown in part (a).

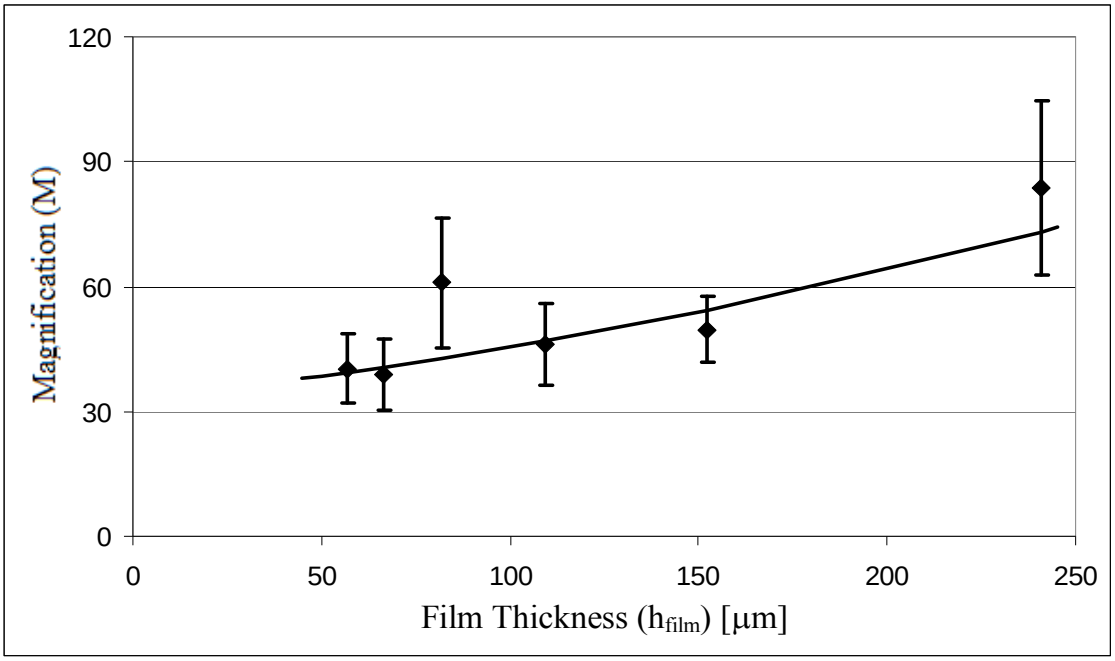


**(a)**

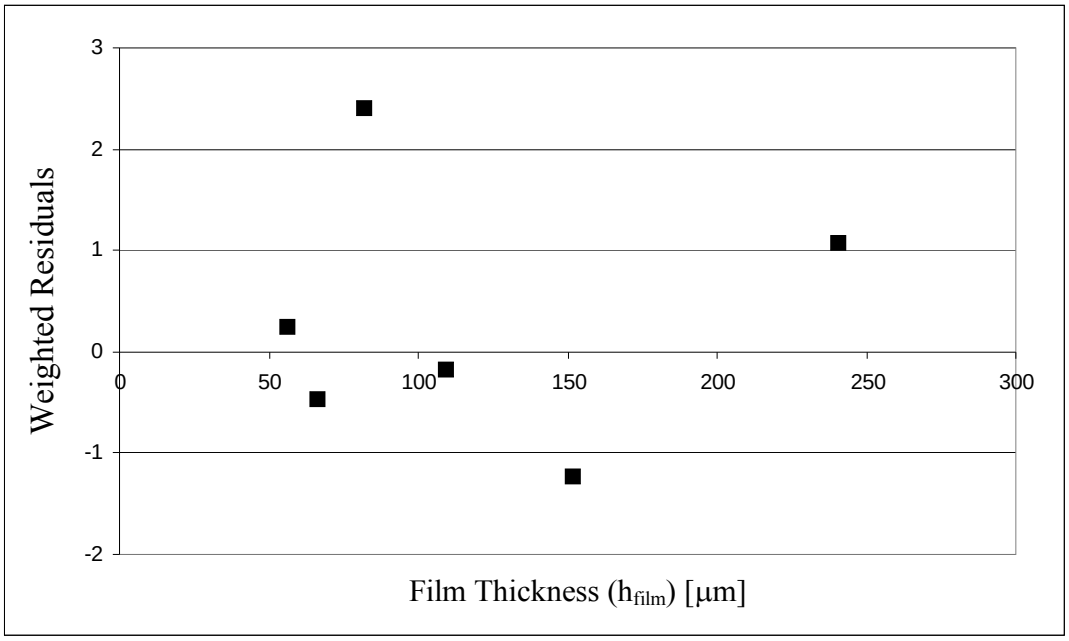


**(b)**

**Figure 4-41: (a)** Particle area magnification (M) versus film thickness ($h_{film}$) for low average height defects caused by all spherical particles. The error bands show the upper and lower 95% confidence limits about the mean magnification. Symbols: (♦) Experimental magnification, (—) Eqn. 2-22. **(b)** Weighted magnification residuals versus film thickness for low average height defects and the fitted exponential model shown in part (a).

### 4.5.3 Particle Area Magnification for Non-Spherical Particles

As for the average defect height analysis, results for the wood and cross-linked polyethylene particles were placed in appendices and compared with the fitted lines and prediction intervals for the spherical particles. The two types of non-spherical particles (wood particles and cross-linked particles) are examined in turn in the following sections.

#### 4.5.3.1 Particle Area Magnification: Wood Particles

Figures 4-VII-11 to 4-VII-19 in Appendix 4-VII show defect area ($A_{DP}$) versus particle area ($A_P$) plots for high and low average height defects caused by wood particles. In these figures the same fitted lines and prediction limits as shown in Figures 4-28 to 4-39 for the spherical particles are plotted along with only data points for the wood particles. Results were very analogous to those obtained for average defect height data (defect volume versus defect area). Generally good correlations coinciding with spherical particle results were obtained with some exceptions (e.g. Figure 4-VII-15).

#### 4.5.3.2 Particle Area Magnification: Cross-Linked Polymer Particles

Figures 4-VIII-12 to 4-VIII-21 in Appendix 4-VIII show defect area ($A_{DP}$) versus particle area ($A_P$) plots for the cross-linked polyethylene particles. In these figures the same fitted lines as shown in Figures 4-28 to 4-39 for the spherical particles are plotted along with only data points for the cross-linked particles. Some good correlations were obtained (Figures 4-VIII-13, 4-VIII-15, 4-VIII-16, 4-VIII-17 for high average height defects) although they did not superimpose on the spherical particle fits. Data on low

average height defects was consistently scattered with no strong evidence of a correlation. The same factors were influencing results here as were mentioned earlier with respect to average defect height plots for these particles (notably deformation of particles and uncertainty in measured particle and defect area).

## 4.6 Testing the Constant Defect Volume Per Unit Particle Area Model

According to the Constant Defect Volume Per Unit Particle Area Model the product of magnification (M) and average defect height (H) is a constant. That can only be the case if there is no variation of this product with thickness. In the previous sections, M versus thickness and H versus thickness were both fit with exponential equations. For the high average height defect data the value of magnification for the highest film thickness (240.7 μm), although quite high in precision, could obviously not be well fit by the exponential equation. It is possible that magnification levels off at a value of three, which corresponds to an average defect height of about 20 μm for the thickest film. It may be relevant that only this thickness of film exceeded the maximum mean spherical particle diameter used (175 μm). Figure 4-42 shows this fit without the high thickness data point. The coefficients for this new fit are shown in the third row of Table 4-10. If the equations for average defect height versus thickness (Eqn. 2-23) and magnification versus thickness (Eqn. 2-22) are multiplied together then the expression obtained for the product is similar to Eqn. 2-24 (Section 2.3.5):

$$HM = a_0 b_0 \exp(h_{film}(a_1 + b_1)) \qquad (2\text{-}24)$$

Using the coefficient values from Tables (4-7) and (4-10 (third row)) the pre-exponential term ($a_0b_0$) is 68.12 while the coefficient in the exponential ($a_1+b_1$) is only 0.00041, one order of magnitude smaller than the absolute value of either $a_1$ or $b_1$.

To test the model for the high average height defect data we will assume the coefficient in the exponential to be zero and calculate the value of magnification at each thickness for the high average height defect data using a constant product value of 68.12 along with the exponential equation for average defect height versus film thickness ($a_0$=44.902; $a_1$=-0.00397). The result is shown in Figure 4-42. The line is lower than the best fit to the data but within the scatter of the data and provides some encouragement that there is some validity and utility for the proposed model.

When the same approach was tried with the low average height defect data the prediction was much too high using the computed value of $a_0b_0$ of 195.8. An $a_0b_0$ of 129.6 was found using optimization to provide a reasonable fit to the data. However, in general, the imprecision of the low average height defect magnification data really precludes using it in this test.

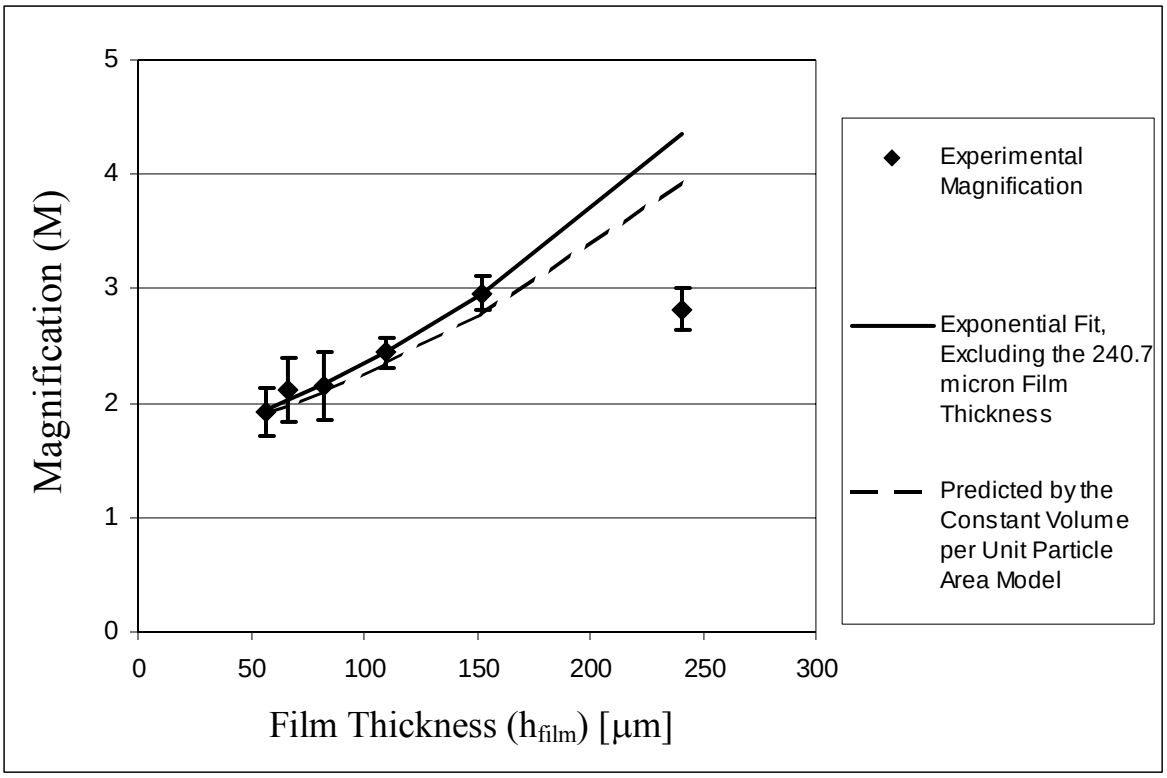


**Figure 4-42:** Magnification (M) versus film thickness ($h_{film}$) for high average height defects caused by spherical particles. The error bands show the 95% confidence limits about the average magnification. The solid line shows the predicted magnification by the exponential model fit to the data points excluding the data at the thickest film (240.7 μm). The dashed line shows the predicted magnification by the Constant Defect Volume Per Unit Particle Area model.

## 4.7 Monitoring Film Quality

A common way of specifying film quality is the number of visible film defects per square meter of film. In this work visible defects were randomly selected for off-line analysis. Examination of the database showed that the smallest defects detected were invariably high average height defects from about 175 to 400 $\mu m^2$ (15 to 22 μm in diameter) except for the thickest film where the smallest defect was 638 $\mu m^2$ (28 μm in diameter). This was expected since high average height defects were invariably smaller than low average

height defects. Assuming a maximum magnification of 3 then particles of area 60 to 212 $\mu m^2$ (9 to 16 μm) caused the smallest defects. These numbers are obviously quite uncertain because detection depended on the eyesight of a human observer. For example, sometimes the smallest defect happened to be noticed because it was located near a large, very visible, defect.

A more objective measure would be to define a defect as one which had a minimum specified area and to know the magnification factor for particle area based upon the film thickness being produced from an extruder equipped with a scanning melt monitor such as the one used in this study.

For the particular system used in this work a systematic approach to monitoring film quality may be summarized as a series of steps as shown in Figure 4-43. Figure 4-44 shows application of these calculation steps for a glass microsphere 40 μm in diameter observed in the polymer melt. The steps shown in Figure 4-43 may be summarized as follows:

1. From the take-up roller speed obtain the final film thickness.

2. Use Eqns. 2-23 and 2-22 to predict the primary defect properties: magnification and average defect height, for both low and high average height defect groups.

3. From in-line image monitoring of the polymer melt obtain the area of contaminant particles. If desired, particle shape can also be obtained and either used to identify non-spherical particles or to associate a particular shape with its own specific correlation.

4. Obtain two estimates of predicted defect area by multiplying the particle area by the magnification factor assuming first high average height defects and then low average height defects. At this point the predicted defect area can be compared to the product requirement and product quality predicted.

5. To refine this prediction, obtain samples of defects and measure one of the discriminating attributes for each defect (e.g. maximum diameter, etc. as listed in Section 4.4.2).

6. From the discriminating attribute decide which class of defects is being generated. Use this information to decide which of the average defect height and magnification estimates are most applicable.

In the example shown in Figure 4-44 for a 40 μm glass sphere, a roller speed of 11.6 $cms^{-1}$ and an extruder screw speed of 15 rpm are specified. Average defect height predicted by the model is shown to be 34.5 μm for high average height defects and 3.9 μm for low average height defects; defect area is predicted to be 2550 $\mu m^2$ for high average height defect and 51,200 $\mu m^2$ for low average height defect. The estimated range of defect area can be compared with the product quality requirements to evaluate the impact of the defect created by this particle on film quality. It may well be that both low and high average height defects are being produced in the product. However, if only one type is suspected then samples of film need to be examined and the length of defects measured. In this case, for a 66.6 μm film, if a typical defect length is larger than 200 μm then the operator would know that low average height defects are the case.

The above approach provides film thickness, particle shape, particle area, magnification, average defect height, and defect area for this system. If no measurements on the defects are available then it provides two estimates of average defect height and two of magnification. The respective magnification values each provide a measure of defect area once the particle area is specified: a maximum and a minimum value. As discussed in Sections 4.3.3 and 4.5.3, for non-spherical particles, particularly deformable particles, deviations can be expected. Data in Appendices 4-VII and 4-VIII should provide a preview of what to expect.

Another way of using the results of this work is to infer the particle area causing a measured defect. For example, an in-line camera scanning the film web could find all defects and their area. Then the magnification correlation with thickness could be used to calculate the area of the particle that created the defect and serve to help diagnose the source of the defect.

By providing two primary defect properties, average defect height and magnification, as well as two types of defects (high average height and low average height defects) this work goes well beyond a simple size measurement for describing film defects and relating them to film performance. A limitation is that for systems different from the one used here, the necessary correlations need to be established experimentally before the approach can be used. However, even for systems quite different from the one employed, the correlations obtained in this work provide new directions for data interpretation. Precision of measurements will sometimes be an issue, particularly in anticipating magnification for low average height defects. Automated replication and averaging is needed in those cases.

The above specific example shows how this work can be used in practical applications. More generally, the contributions of this work may be summarized as follows:

The main contribution of this thesis is the development of a methodology to predict defect properties from in-line melt monitoring of particle properties and processing variables. The results are limited to the extruder system that was used. However, others can use this work as a guideline to accomplish prediction on their own systems. Previous to this work there were no such published guidelines.

The main contribution is supported by two secondary contributions: the formation of the database of defect properties, particle properties and processing variables, and the development of methods to interpret the acquired images.

The formation of the database is further supported by another lower level contribution: development of two off-line defect and particle characterization methods.

In addition, three lower level contributions support the development of data interpretation methods. They are: the definition of average defect height (H) and magnification (M) for defect classification, the development of empirical models for predicting H, M, and defect area, and the development of a mechanistic model for the same purpose. Various hypotheses were also tested to help explain the results (Appendix 4-IX).

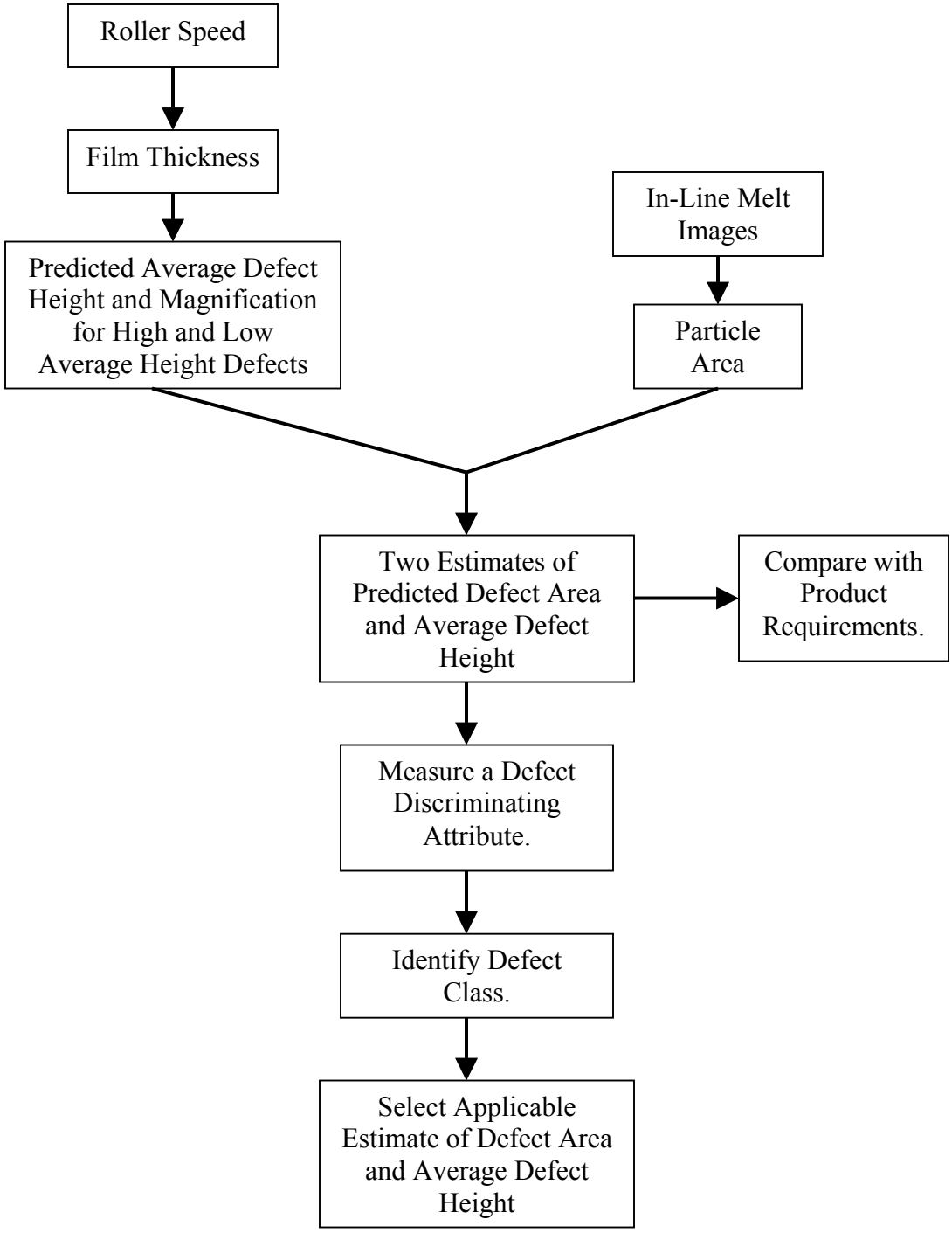


**Figure 4-43:** A diagram showing the film monitoring steps.

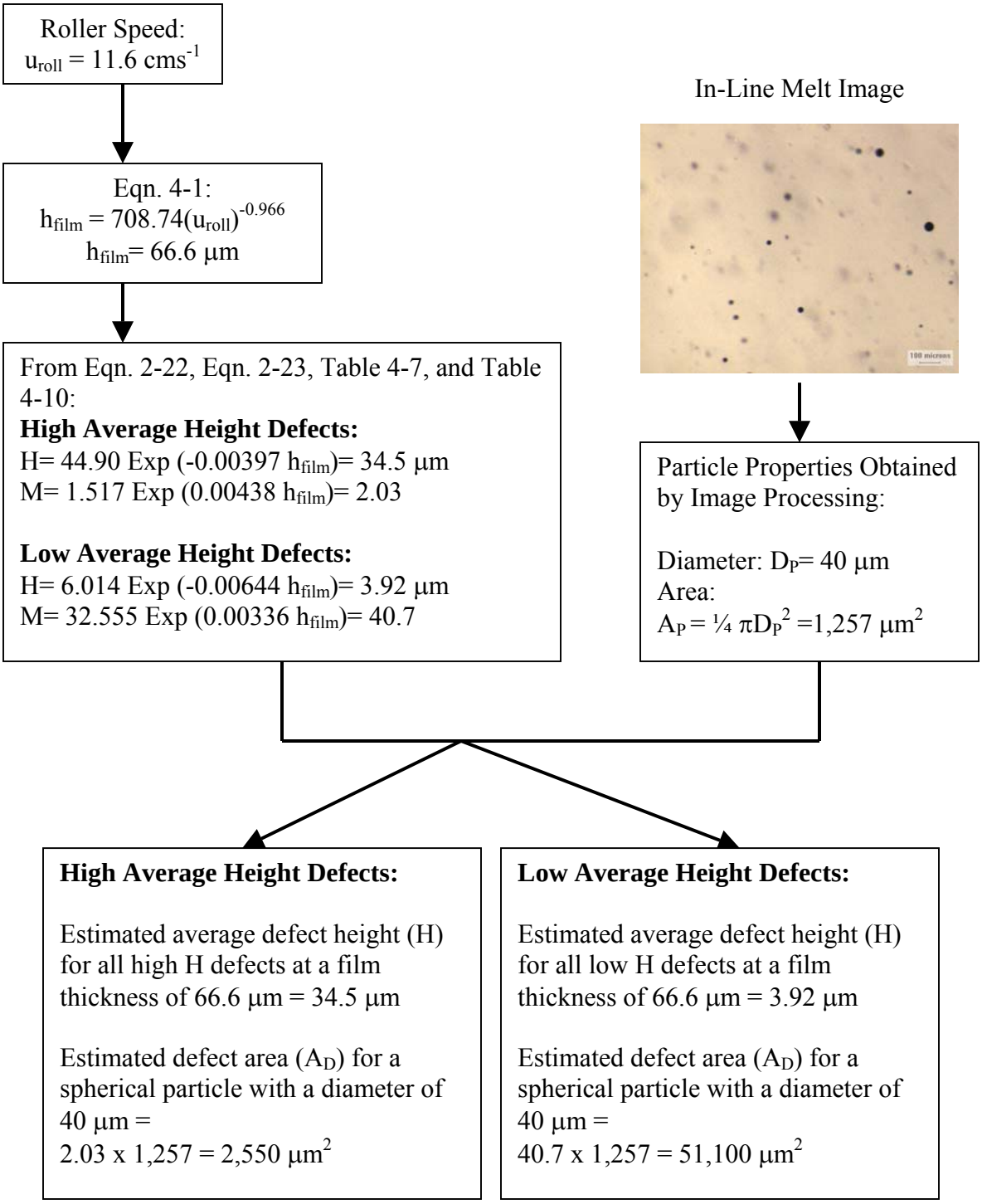


**Figure 4-44:** This diagram shows how defect area and average defect height can be estimated for a new particle at a specified roller speed.

# 5 CONCLUSIONS

Results of this work support the hypothesis that in-line image monitoring of the polymer melt during plastics extrusion can be used to associate the properties of observed particles, along with processing variables, to the presence and properties of film defects. The work provides a practical methodology, based on both experimental and theoretical work, to serve as a starting point for establishing the necessary correlations. However, it was found that apparently identical particles could produce either of two types of defects. Thus, a limitation is that if it is necessary to know which pair of primary defect property values are most likely in a given system, then a simple defect length measurement in the product film is necessary to determine what type of defect is being produced.

Conclusions from each of the three objectives defining this work are as follows:

**i Visible defects in polymer films were created by pulse addition of a variety of particles at the extruder feedport.** The particles included solid and hollow glass microspheres, glass fibers, aluminum powder, ceramic microspheres, diatomite, wood dust and cross-linked polyethylene. Films were produced by addition of a film die and take-up roller system to the extruder. Images of the particles in the melt were obtained in-line using a specialized digital camera and samples for off-line analysis were obtained by sampling the film for thicknesses from 45.2 to 240.7 μm.

ii. **Off-line quantitative characterization of the defects formed was accomplished by further developing and applying two off-line imaging methods to the film: a polarized light imaging method and an interferometric method.** A database consisting of a total of 525 data records were created. Each record represented one polarized light image and one interferometer image. These data described one processing attribute (take-up roller speed), 33 particle attributes (measured from polarized light images), 33 defect attributes (also measured from polarized light images) and 34 defect attributes measured from interferometry images. Most of the data records (420) were for spherical particles: 217 for glass microspheres, 52 for glass bubbles, 71 for aluminum powder and 73 for ceramic microspheres. The 105 remaining data records included 59 for cross-linked particles and 46 for wood particles. 42 defects caused by glass fibers were characterized. However, results were so different than any of the other particles used that only a qualitative analysis of glass fiber images was done.

**iii. Mathematical modeling identified two groups of defects and provided equations that could be used for defect property prediction for the extrusion system employed here. For other extrusion systems the modeling work provides a quantitative approach that serves as a starting point for defect property prediction. The primary conclusions of mathematical modeling were as follows:**

- Two new "primary defect properties" were found to be useful for characterizing film quality: average defect height and magnification. For a specific film thickness,

average defect height is the slope of a line fitted to defect volume versus defect area and magnification is the slope of a line fitted to defect area versus particle area.

- Surprisingly, it was found that for all spherical particles (independent of the composition of the particle) all of the defects divided into only two groups: those with a high average height and those with low average height. At each film thickness these defects showed only one of two average height values. Furthermore, at each thickness they also showed only two magnification values with the lower magnification values corresponding to the defects with the higher average height values and vice versa. Average defect height showed an exponential decrease as film thickness increased while magnification showed an exponential increase. Average defect heights ranged from 1.305 to 4.159 μm for low average height defects and from 18.636 to 35.891 μm for high average height defects. The low average height defects had magnification values ranging from 40.328 to 83.701 while the magnification of high average height defects ranged from 1.924 to 2.821. Some of the data did show considerable scatter, particularly the plots for magnification factors of the thinnest films and lowest average defect heights.

- Flow diagrams for using the work to monitor film quality were provided along with a specific numerical example. Each prediction yields two pairs of primary defect property values (average defect height and magnification) corresponding to low average height defects and high average height defects, respectively. As alluded to above, if it is necessary to distinguish which pair is correct for a given system then

any one of several dimensions of the defect in the product film needs to be measured (e.g. the longest diameter of the defect). Also, empirical correlations are probably specific to the extrusion system employed. Thus, in general the work shows the measurements and correlations that need to be obtained from other systems as well as how these correlations can be used.

- Images of defects from non-spherical particles were also obtained and analyzed. Results for wood particles and for cross-linked polyethylene particles were superimposed upon the fitted lines obtained for spherical particles. Often the wood particle data obeyed the same correlations. Deviations from the correlations for spherical particles were attributed to either shape effects or, in the case of cross-linked polyethylene particles, to particle deformation. Glass fibers were also used to create defects. The images were not quantitatively analyzed. However, qualitatively they did show two, rather than one, distinct defect region, each located at one end of the defect.

- At the beginning of the modeling part of the work, an extensive study of particle and defect attributes resulted in a small subset being identified as being useful to mathematical modeling. However, empirical modeling (clustering, classification and multiple-linear regression) modeling was unsuccessful. Later it was discovered that two classes of defects could be identified via simple property correlations (high and low average height defects) and that particle information was not relevant to the class

obtained. That is, apparently identical particles could provide a high or a low average height defect.

# 6 RECOMMENDATIONS

- The work reported here needs to be repeated using other extrusion film casting systems. It is expected that the identity of the various measures and correlations will be useful for other systems since a "standard" film casting extrusion system was used here. However, there are many variables associated with the process and the particles causing film defects in industry. Modifications to adapt the work to new situations will be required.

- Methods of improving precision, especially for the area of low average height defects, through averaging with the use of an in-line defect monitor should be explored.

- An investigation directed at elucidating the reasons for the presence of only two defect classes should be conducted. Information relevant to particle debonding would likely be particularly relevant. Scanning electron microscopy and cross sectioning of defects followed by microscopy hold promise.

- Further work using cross-linked particles needs to be done. These particles are industrially important, have complex properties and are amongst the most difficult to characterize.

- Rheological behavior of the polymer and polymer-particle interactions have the potential to greatly affect defect properties. Future studies should investigate their specific roles.

# 7 REFERENCES


Aniunoh, K. K., Harrison, G. M. (2006) Experimental Investigation of Film Formation: Film Casting, Journal of Plastic Film and Sheeting, 22, 177-192

Bai, S. L., Chen, J. K., Huang, Z. P., Yu, Z. Z. (2000) The Role of Interfacial Strength in Glass Bead Filled HDPE, Journal of Materials Science Letters, 19, 1587-1589

Bai, S. L., Chen, J. K., Huang, Z. P., Liu, Z. D. (2001) Interface Effect on the Mechanical Behaviour Rigid Particle Filled Polymer, Society of Chemical Industry, Polymer International, 50, 222-228

Bai, S. L., Wang, M., Zhao, X. F. (2003) Interfacial Debonding Behavior of a Rigid Particle Filled Polymer Composite, Composite Interfaces, 10, 2-3, 243-253

Baignan, V. B., Bourbakis, N. G., Moghaddamzadeh, A., Yfantis, E. (1995) Visual Detection of Defects in Solder Joints **In** Wu, F. Y., Wilson, S. S. (Eds.) (1995) Machine Vision Applications in Industrial Inspection III, Proceedings from the SPIE, The International Society for Optical Engineering, 2423, 22-33

Bobberts, F. and Van Allen, K. R. (1995) Monitoring Film Quality On-Line Using CCD Technology, Proceedings from ANTEC 1995, Society of Plastics Engineers, Boston, MA

Brassell G. W., Wischmann K.B. (1974) Mechanical and Thermal Expansion Properties of a Particulate Filled Polymer, Journal of Materials Science, 9, 307-314

Campbell, G. A., and Kanai, T. (1999) Film Processing: Overview and Introductory Rheology **In** Kanai, T., and Campbell, G.A., (Eds.) Film Processing, (pp. 1-13) Munich, Hanser/Gardner Publications

Canning, K., Bian, B., Co, A. (2001) Film Casting of a Low Density Polyethylene Melt, Journal of Reinforced Plastics and Composites, 20(5), 366-376

Canning, K., Co, A. (2000) Edge Effects in Film Casting of Molten Polymers, Journal of Plastic Film and Sheeting, 16, July Issue, 188-203

Chen, J. K., Huang, Z. P., Mai, Y.-W. (2003) Constitutive Relation of Particulate-Reinforced Viscoelastic Composite Materials with Debonded Microvoids, Acta Materialia, 51, 3375-3384

Chen, S., Li, D. (2006) Image Binarization Focusing on Objects, Neurocomputing, 69, 2411-2415

Cho, J., Joshi, M. S., Sun, C. T. (2006) Effect of Inclusion Size on Mechanical Properties of Polymeric Composites with Micro and Nano Particles, Composites Science and Technology, 66, 1941-1952

Chou, P. B., Rao, A. R., Sturzenbecker, M. C., Wu, F. Y., Brecher, V. H. (1997) Automatic Defect Classification for Semiconductor Manufacturing, Machine Vision Applications, 9, 201-214

Cognex Corp. (2009) SmartView® Plastics Brochure, On-Line Detection, Identification, and Visualization of Plastics Defects, Retrieved on March 14, 2009 from http://www.cognex.com/ProductsServices/SurfaceInspection/SmartViewPlastic.aspx?id

Desa, S. (1995) Quality monitoring of recycled plastic waste during extrusion: in-line particle detection, M.A.Sc. Thesis, Department of Chemical Engineering and Applied Chemistry, University of Toronto

Desa, S., Cluett, W.R., Balke, S.T., and Horn, J.T. (1995) Quality Monitoring of Recycled Plastic Waste During Extrusion: II. In-Line Particle Detection, Proceedings from ANTEC 1995, Society of Plastics Engineers, Boston, MA

d'Halewyu, S., Agassant, J. F., Demay, Y. (1990) Numerical Simulation of the Cast Film Process, Polymer Engineering and Science, 30(6), 335-340

Dobroth, T., Erwin, L. (1986) Causes of Edge Beads in Cast Film, Polymer Engineering and Science, 26(7), 462-467

Dominey, S. and Goeckel, W.F. (2003) Particle Defect Detection and Classification Utilizing Camera Optics, Real Time Computation, and Small Scale Resin Sample Processing, Proceedings from ANTEC 2003, Society of Plastics Engineers, Nashville, TN

Feingold, J. M. (2005) Stress Analysis, Plastics Technology, December Issue, 50-53

Gerlach, C. G. F., Dunne, F. P. E. (1994) An Elastic-Viscoplastic Large Deformation Model and Its Application to Particle Filled Polymer Film, Computational Materials Science, 3,146-158

Gerlach, C. G. F., Dunne, F. P. E., Jones, D. P., Mills, P. D. A., Zahlan, N. (1996) Modeling the Influence of Filler Particles on Surface Geometry in Drawn PET Film, Journal of Strain Analysis, 31(1), 65-73

Gibson, R. F. (1994) Principles of Composite Material Mechanics, New York, NY, McGraw Hill, Inc.

Gonzales-Barron, U., Butler, F. (2006) A Comparison of Seven Thresholding Techniques with the K-means Clustering Algorithm for Measurement of Bread-crumb Features by Digital Image Analysis, Journal of Food Engineering, 74, 268-278

Hackett Jr., E. (2004) Film Inspection Using Cross-Polarized Light, Pharmaceutical and Medical Packaging News, July Issue

Halliday, D., Resnick, R., Walker, J. (1993) Fundamentals of Physics, (4th ed.), New York, NY, John Wiley and Sons, Inc.

Hardin, R.W. (Ed.) (2004) Vision System Tracks Defects in DVD Plastic Wrap, Vision Systems Design, 33-35

Harris, B. (1978) Shrinkage Stresses in Glass Resin Composites, Journal of Materials Science, 13, 173-177

Hecht, E. (1984) Optics, (2nd ed.), New York, NY, Addison-Wesley Publishing

Iivarinen, J. (2001) In Unsupervised segmentation of defect images **In** Casasent, D. P., Hall, E. L. (Eds.) Intelligent Robots and Computer Vision XX: Algorithms, Techniques, and Active Vision, Proceedings from the SPIE - The International Society for Optical Engineering, 4572, 488 495, Boston, MA

Iivarinen, J., Heikkinen, K., Rauhamaa, J., Vuorimaa, P., Visa, A. (2000) International Journal of Pattern Recognition and Artificial Intelligence, 14, 735-755

Iivarinen, J., Rauhamaa, J. (1998) Surface Inspection of Web Materials Using the Self Organizing Map **In** Casasent, D. P. (Ed.) (1998) Intelligent Robots and Computer Vision XVII: Algorithms, Techniques, and Active Vision, Proceedings from the SPIE, The International Society for Optical Engineering, 3522, 96-103, Boston, MA

Iivarinen, J.,Visa, A., Jain, A. K. (1998) An Adaptive Texture and Shape Based Defect Classification, Proceedings from 14th International Conference on Pattern Recognition (ICPR'98), 1, 117-122, Brisbane, Qld., Australia

Ing, L.D., Balke, S.T., Brewster, N.V. (2002) In-Line Measurement of Dispersed Phase Properties Using the Scanning Particle Monitor, Proceedings from ANTEC 2002, Society of Plastics Engineers, San Francisco, CA

Ing, L.D., Balke, S.T., Stoev, N., Tamber, H., Planta, M. (2001) In-Line Monitoring of Particles in a Polymer Melt During Extrusion Using a Scanning Particle Monitor, Proceedings from ANTEC 2001, Society of Plastics Engineers, Dallas, TX

Ito, H., Doi, M., Isaki, T., Takeo, M., Yagi, K. (2003) 2D Flow Analysis of Film Casting Process", Journal of the Society of Rheology, Japan, 31(3), 149-155

Kanai, T. (1999) Flat Die Analysis **In** Kanai, T., and Campbell, G.A., (Eds.) Film Processing, (pp. 14-38) Munich, Hanser/Gardner Publications

Kantardzic, M. (2003) Data Mining: Concepts, Models, Methods, and Algorithms, Piscatawny, NJ, IEEE Press

Kittler, J., Illingworth, J. (1979) On Threshold Selection Using Clustering Criteria, IEEE Transactions on System Man Cybernet SMC, 15, 5, 652-656

Kody, R. S., Martin, D. C. (1996) Quantitative Characterization of Surface Deformation in Polymer Composites Using Digital Image Analysis, Polymer Engineering and Science, 36(2), 298-304

Konig, J. G. (2009) WebFeat: An Essential Component for the Quality Assurance and Process Control of Plastic Films, Online Publications, dr. Schenk GmbH, Retrieved on March 14, 2009 from: http://www.drschenk.com/fileadmin/downloads/04_Web_inspection/WebFeat%20Article_Plastic%20Film_e.pdf

Kumpinsky, E. (1993) Heat Transfer Model Assessment of Chill Rolls for Polymer Film Extrusion, Industrial and Engineering Chemistry Research, 32 (11), 2866-2872

Kunttu, I., Lepisto, L., Rauhamaa, J., Visa, A. (2003) Classification Method for Defect Images Based on Association and Clustering **In** Dasarathy, B. V. (Ed.) (2003) Data Mining and Knowledge Discovery: Theory, Tools, and Technology V, Proceedings from SPIE, The International Society for Optical Engineering, 5098, 19-27, Orlando, FL

Laitinen, L., Silven, O., Pietikainen, M. (1990) Morphological Image Processing for Automated Metal Strip Inspection **In** Gader, P.D. (Ed.) Image Algebra and Morphological Image Processing, Proceedings from the SPIE, The International Society for Optical Engineering, 1350,241- 250, San Diego, CA

Lamberti, G., Titomanlio, G. (2005) Analysis of Film Casting Process: The Heat Transfer Phenomena, Chemical Engineering and Processing, 44, 1117-1122

Lamberti, G., Titomanlio, G., Brucato, V. (2001) Measurement and Modeling of the Film Casting Process 1. Width Distribution along Draw Direction, Chemical Engineering Science, 56, 5749-5761

Lamberti, G., Titomanlio, G., Brucato, V. (2002) Measurement and Modeling of the Film Casting Process 2. Temperature Distribution along Draw Direction, Chemical Engineering Science, 57, 1993-1996

Lavagnini, I., Magno, F. (2007) A Statistical Overview on Univariate Calibration, Inverse Regression, and Detection Limits: Application to Gas Chromatography/Mass Spectrometry Technique, Mass Spectrometry Reviews, 26, 1-18

Lin, K. C. (2003) Fast Image Thresholding by Finding the Zero(s) of the First Derivative of Between Class Variance, Machine Vision and Applications, 13, 254-262

Ling, J. Y. K. (2003) Offline ultraviolet induced cross-linking of polyethylene, M. Eng. Thesis, Department of Chemical Engineering and Applied Chemistry, University of Toronto

Masi, C. G. (2001) Web Inspection System Finds Film Defects, Vision Systems Design, June Issue,

Mehra, M. (1995) In-line monitoring of contaminants during polymer extrusion, M.Eng. Thesis, Department of Chemical Engineering and Applied Chemistry, University of Toronto

Murphy, J. (1996) Additives for Plastics Handbook, Oxford, UK, Elsevier Advanced Technology

National Instruments Corp., (2006) Inspecting Transparent Materials for Material Defects, NI Developer Zone, On-Line Tutorial, from http://zone.ni.com/devzone/cda/tut/p/id/3505

Ng, H. (2006) Automatic Thresholding for Defect Detection, Pattern Recognition Letters, 27, 1644-1649

Oldenbourg, R. (1996) A New View on Polarization Microscopy, Nature, 381, 811-812

Olszak, A.G., Schmit, J., Heaton, M.G. (2001) Interferometry: Technology and Applications, Veeco Metrology Group, Application Note 47

Otsu, N. (1979) A Threshold Selection Method from Gray-Level Histograms, IEEE Transactions on System Man Cybernet SMC, 9, 1, 62-66

Peacock, A.J. (2000) Handbook of Polyethylene: Structures, Properties, and Applications, New York, NY, Marcel Dekker, Inc.

Pratt, V. and Warner, J. (2000) Defect Inspection in Transparent Material, Sensor Review, 20(4), 294-298

Rauwendaal, C. (2002) What's Causing Your Gels?, Plastics Technology, March, 1-4

Redner, A. S., Hoffman, B. (1997) Measuring Residual Stress in Transparent Plastics, Medical Plastics and Biomaterials Magazine, January Issue

Redner, A. S., Hoffman, B. (1999) Residual Stress Testing for Transparent Polymers, Medical Device and Diagnostic Industry Magazine, March Issue

Russ, J. C. (1999) The Image Processing Handbook, (3rd ed.), Boca Raton, FL, CRC Press

Ryu, D. S., Inoue, T., Osaki, K. (1998) A Birefringence of Polymer Crystallization in the Process of Elongation of Films", Polymer, 39(12), 2515-2520

Seyfzadeh, B., Harrison, G. M., Carlson, C. D. (2005) Experimental Studies on the Development of a Cast Film, Polymer Engineering and Science, 443-450

Silagy, D., Demay, Y., Agassant, J.F. (1999) Numerical Simulation of the Film Casting Process, International Journal for Numerical Methods in Fluids, 30, 1-18

Simonds, H.R., Weith, A. J., and Schack, W. (1952) Extrusion of Plastics, Rubber, and Metals, New York, NY, Reinhold Publishing Corp.

Smith, W. S. (1997) Nonisothermal film casting of a viscous fluid, B. Eng. C. S. Thesis, Department of Civil Engineering, McMaster University

Swain, M., Ballard, D. (1991) Color Indexing, International Journal of Computer Vision, 7, 11-32

Sweeting, O.J. (1968) The Science and Technology of Polymer Films (Vol. 1), New York, NY, Wiley InterScience, Inc.

Tcharkhtchi, A., Anderson, E. (2002) Examining Elliptical Surface Defects on Angioplasty Balloons, Medical Device and Diagnostic Industry, May Issue

Torabi, K. (2004) Data mining methods for qualitative in-line image monitoring in polymer extrusion, Ph.D. Thesis, Department of Chemical Engineering and Applied Chemistry, University of Toronto

Torabi, K., Sayad, S., Balke, S.T. (2005) On-Line Adaptive Bayesian Classification for In-Line Particle Image Monitoring in Polymer Film Manufacturing, Computers and Chemical Engineering, 30(1), 18-27

Utracki, L.A. and Fisa, B. (1982) Rheology of Fiber- or Flake-Filled Plastics, Polymer Composites, 3(4), 193-211

van Helvoirt, J., Leenknegt, G. A. L., Steinbuch, M., Goosens, H. J. (2005) Disk Defect Classification for Optical Disk Drives, IEEE Transactions on Consumer Electronics, 51, 856-863

Veeco Instruments Corp. (1999) WYKO Surface Profilers Technical Reference Manual, Version 2.2.1,Veeco Metrology Group, Veeco Instruments Corp.

Voros, G., Pukanszky, B. (1995) Stress Distribution in Particulate Filled Composites and Its Effect on Micromechanical Deformation, Journal of Materials Science, 30, 4171-4178

Vujnovic, E. (1996) In-line monitoring of particulate contaminants in polyethylene during extrusion", B.A.Sc. Thesis, Department of Chemical Engineering and Applied Chemistry, University of Toronto

Witten, I. H., Frank, E. (2000) Data Mining: Practical Machine Learning Tools and Techniques with JAVA Implementations, San Francisco, CA, Morgan Kaufmann Publishers

Wypych, G. (1999) Handbook of Fillers, (2nd ed.), Toronto, Ontario, ChemTec Publishing

Yamada, T. (1999) Theoretical Analysis of Film Deformation Behavior in Casting **In** Kanai, T., and Campbell, G.A., (Eds.) Film Processing, (pp. 180-209) Munich, Hanser/Gardner Publications

Yan, S. (2007) Adaptive image quality improvement with Bayesian classification for in line monitoring, Ph.D. Thesis, Department of Chemical Engineering and Applied Chemistry, University of Toronto

Yan, S., Sayad, S., Balke, S. T. (2009) Image Quality in Image Classification: Design and Construction of an Image Quality Database, Computers and Chemical Engineering, 33, 421-428

Yan, S., Sayad, S., Balke, S. T. (2009a) Image Quality in Image Classification: Adaptive Image Quality Modification with Adaptive Classification, Computers and Chemical Engineering, 33, 429-435

Zhang, X., Krewet, C., Kuhlenkotter, B. (2006) Automatic Classification of Defects on the Product Surface in Grinding and Polishing, International Journal of Machine Tools and Manufacture, 46, 59-69

# 8 APPENDICES

**APPENDIX 3-I:** Properties of Selected Particles for Extruder Runs (Wypych 1999, Murphy 1996)

**Table 3-I-1:** Aluminum Powder[1]

| Product Name and Manufacturer: Valimet H-30, Valimet Inc., Stockton, CA | | | |
|---|---|---|---|
| Chemical Formula | Al (99.5 wt%) | Color | Silvery white to gray |
| Density ($gcm^{-3}$) | 2.7 | Appearance | Fine powder |
| Mohs Hardness | 2-2.9 | Particle Shape | Spherical |
| Melting Point (°C) | 660 | Particle Size (μm) | 10-55 |
| Specific Heat ($kJkg^{-1}K^{-1}$) | 0.90 | Aspect Ratio | N/A |
| Thermal Conductivity ($WK^{-1}m^{-1}$) | 204 | Specific Surface Area ($m^2g^{-1}$) | 5-35 |
| Thermal Expansion Coefficient ($K^{-1}$) | $25x10^{-6}$ | Porosity | N/A |

[1] http://www.valimet.com/documents/aluminum.htm

**Table 3-I-2:** Diatomite[2]

| Product Name and Manufacturer: Super Floss Celite, World Minerals Inc., Lompoc, CA | | | |
|---|---|---|---|
| Chemical Formula | $SiO_2$ (~90 wt%) | Color | White to off white |
| Density ($gcm^{-3}$) | 2-2.5 | Appearance | Fine powder |
| Mohs Hardness | NA | Particle Shape | Irregular |
| Melting Point (°C) | ~1700 | Particle Size (μm) | 9 (median) |
| Specific Heat ($kJkg^{-1}K^{-1}$) | N/A | Aspect Ratio | N/A |
| Thermal Conductivity ($WK^{-1}m^{-1}$) | N/A | Specific Surface Area ($m^2g^{-1}$) | 0.7-3.5 |
| Thermal Expansion Coefficient ($K^{-1}$) | N/A | Porosity | 85%(void space) |

[2] http://www.matweb.com/search/datasheet.aspx?matguid=83f9d2bdd4c7490ab5fa67d275395f34

**Table 3-I-3:** Borosilicate Glass Microspheres[3]

| Manufacturer: Duke Scientific Inc., Palo Alto, CA | | | |
|---|---|---|---|
| Chemical Formula | $SiO_2$ | Color | Transparent |
| Density ($gcm^{-3}$) | 2.5-2.55 | Appearance | Solid beads |
| Mohs Hardness | 6 | Particle Shape | Spherical |
| Softening Point (°C) | 720 | Particle Size (μm) | 10 |
| Specific Heat ($kJkg^{-1}K^{-1}$) | 1.17 | Aspect Ratio | 1 |
| Thermal Conductivity ($WK^{-1}m^{-1}$) | N/A | Specific Surface Area ($m^2g^{-1}$) | 0.4-0.8 |
| Thermal Expansion Coefficient ($K^{-1}$) | $85x10^{-7}$ | Porosity | N/A |

[3] http://www.thermo.com/com/cda/product/detail/0,1055,10142049,00.html

**Table 3-I-4:** Soda Lime Glass Microspheres[4]

| Manufacturer: Duke Scientific Inc., Palo Alto, CA | | | |
|---|---|---|---|
| Chemical Formula | $SiO_2$ | Color | Transparent |
| Density ($gcm^{-3}$) | 2.4-2.5 | Appearance | Solid beads |
| Mohs Hardness | 6 | Particle Shape | Spherical |
| Softening Point (°C) | 720 | Particle Size (μm) | 50, 100 |
| Specific Heat ($kJkg^{-1}K^{-1}$) | 1.17 | Aspect Ratio | 1 |
| Thermal Conductivity ($WK^{-1}m^{-1}$) | N/A | Specific Surface Area ($m^2g^{-1}$) | 0.4-0.8 |
| Thermal Expansion Coefficient ($K^{-1}$) | $85x10^{-7}$ | Porosity | N/A |

[4] http://www.thermo.com/com/cda/product/detail/0,1055,10142049,00.html

**Table 3-I-5:** Soda Lime Borosilicate Hollow Glass Microspheres[5]

| Product Name and Manufacturer: 3M Scotchlite Glass Bubble-S60, 3M Performance Materials Division, St. Paul, MN | | | |
|---|---|---|---|
| Chemical Formula | $SiO_2$ | Color | White to transparent |
| Density ($gcm^{-3}$) | 0.60 | Appearance | Dry powder |
| Mohs Hardness | 6 | Particle Shape | Spherical |
| Softening Point (°C) | 704 | Particle Size (μm) | 30-55 |
| Specific Heat ($kJkg^{-1}K^{-1}$) | 1.17 | Aspect Ratio | 1 |
| Thermal Conductivity ($WK^{-1}m^{-1}$) | 0.2 | Specific Surface Area ($m^2g^{-1}$) | 0.4-0.8 |
| Thermal Expansion Coefficient ($K^{-1}$) | $85x10^{-7}$ | Porosity | N/A |

[5] http://multimedia.3m.com/mws/mediawebserver?66666UuZjcFSLXTtNXMEl8&_EVuQEcuZgVs6EVs6E666666--

**Table 3-I-6:** Glass Fiber[6]

| Product Name and Manufacturer: 415A CRATEC Chopped Strands, Owens Corning, Toledo, OH | | | |
|---|---|---|---|
| Chemical Formula | $SiO_2$ | Color | White to off-white |
| Density ($gcm^{-3}$) | 2.44 | Appearance | Solid fibers |
| Mohs Hardness | 6 | Particle Shape | Fiber |
| Softening Point (°C) | 830-920 | Particle Size (μm) | Diameter: 14μ, Length: 4mm |
| Specific Heat ($kJkg^{-1}K^{-1}$) | N/A | Aspect Ratio | ~285 |
| Thermal Conductivity ($WK^{-1}m^{-1}$) | N/A | Specific Surface Area ($m^2g^{-1}$) | N/A |
| Thermal Expansion Coefficient ($K^{-1}$) | $73x\ 10^{-7}$ | Porosity | N/A |

[6] http://www.owenscorningchina.com/upload/File/761852443.pdf

**Table 3-I-7:** Ceramic Microspheres[7]

| Product Name and Manufacturer: G-850, 3M Zeeospheres, Gray Microspheres, 3M Specialty Materials Division, St. Paul, MN | | | |
|---|---|---|---|
| Chemical Formula | Silica-Alumina Ceramic | Color | Gray (L value: 50+) |
| Density ($gcm^{-3}$) | 2.1 | Appearance | Fine gray powder |
| Mohs Hardness | 7 | Particle Shape | Hollow spheres |
| Softening Point (°C) | 1020 | Particle Size (μm) | 100-200 |
| Specific Heat ($kJkg^{-1}K^{-1}$) | N/A | Aspect Ratio | N/A |
| Thermal Conductivity ($WK^{-1}m^{-1}$) | 2 | Specific Surface Area ($m^2g^{-1}$) | 0.95 |
| Thermal Expansion Coefficient ($K^{-1}$) | N/A | Porosity | N/A |

[7] http://www.thecarycompany.com/adobe/3m/Zeeospheres_Gray-data.pdf

**Table 3-I-8:** Cross-Linked Low-Density Polyethylene Samples (Ling 2003)

| **Sample** | **Polymer** | **Benzophenone wt%** | **Triallyl cyanurate wt %** | **Irradiation Time (s)** | **Temp. (°C)** | **Gel Content wt%** |
|---|---|---|---|---|---|---|
| #4 | LDPE530A | 0.5 | 0.5 | 120 | 140 | ~12 |
| #5 | LDPE530A | 1.0 | 0.5 | 20 | 140 | ~19 |
| #6 | LDPE530A | 1.0 | 0.5 | 60 | 140 | ~24 |

**Table 3-I-9:** Polymer Batches With High Gel Content

| **Polymer** | **Polymer Batch** | **Melt Index (g/10 min)** | **Density ($gcm^{-3}$)** | **Additives** |
|---|---|---|---|---|
| Low Density Polyethylene | LDPE640I | 2.0 | 0.9215 | None |
| Ethylene Vinyl Acetate Copolymer | EVA1608V (16 wt% VA) | 8.0 | 0.938 | None |

## Wood dust:

Density: 0.4-1.35 $gcm^{-3}$
Maximum temperature of use: 200°C
Color: buff, tan
Particle size: 10-500 μm

**Appendix 3-II:** Polarized Light and Interferometric Images of Defects

Defect: R17R30-D6

$h_{film}$ = 240.7 μm

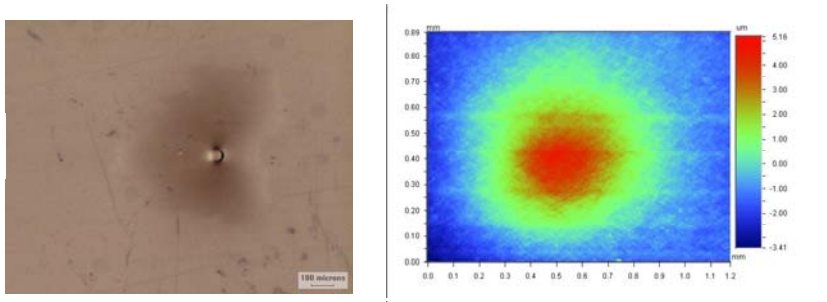

Defect: R17R50-D6

$h_{film}$ = 109.4 μm

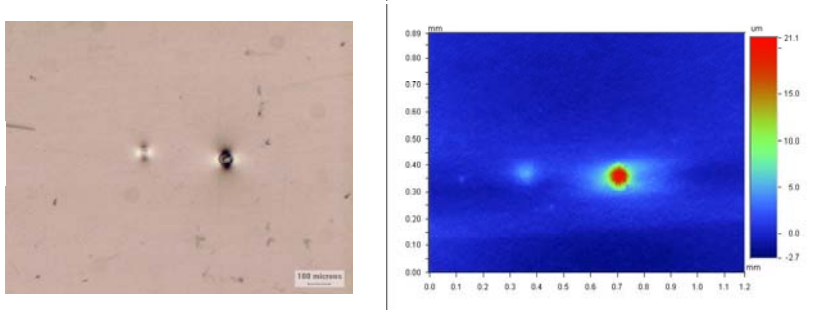

Defect: R17R60-D8

$h_{film}$ = 82.1 μm

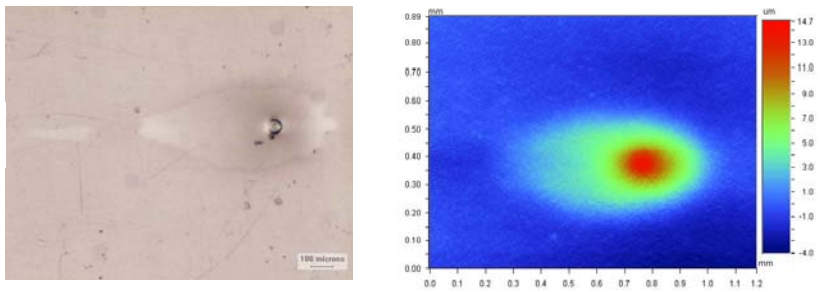

Defect: R17R70-D8

$h_{film}$ = 66.6 μm

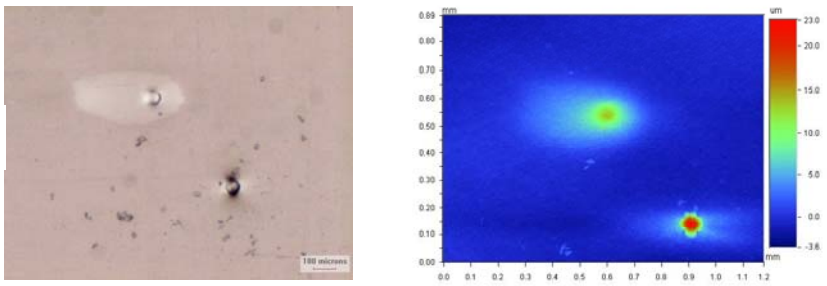

Defect: R17R80-D1

$h_{film}$ = 56.6 μm

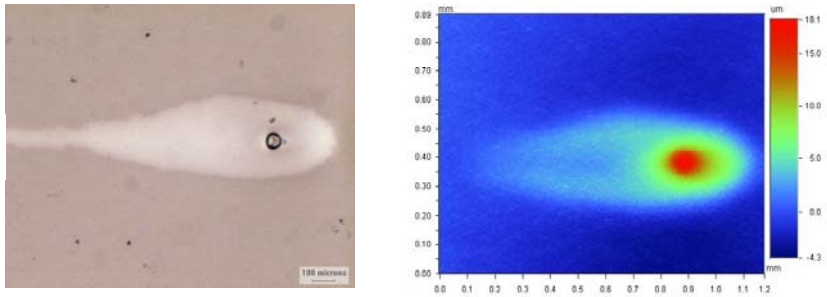

**Figure 3-II-1:** Polarized light and interferometric images of five defects caused by glass microspheres (~ 50 μm in diameter) in Extruder Run 2 (Table 3-3).

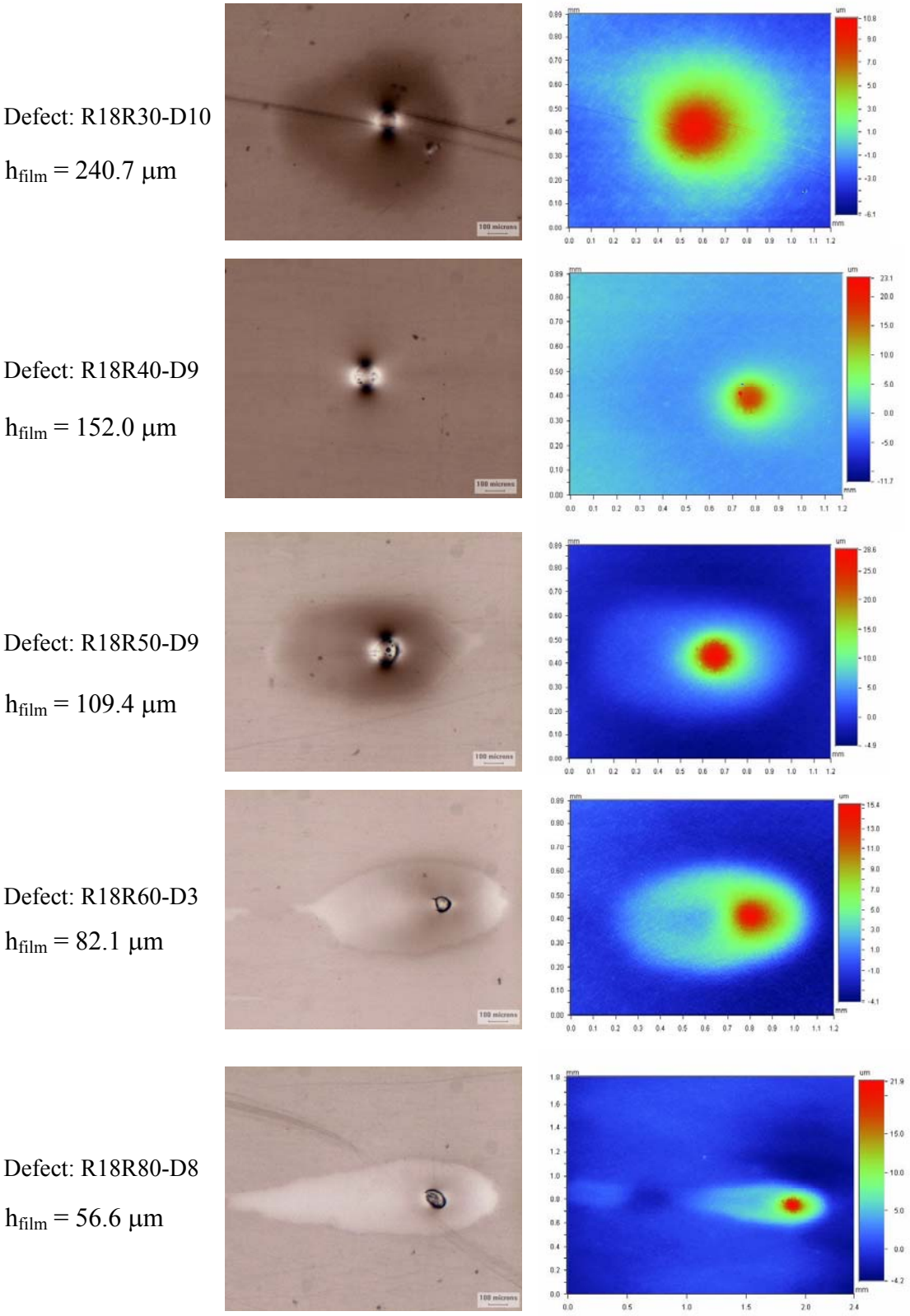


**Figure 3-II-2:** Polarized light and interferometric images of five defects caused by glass microspheres (~100 μm in diameter) in Extruder Run 3 (Table 3-3).

Defect: R19R30-D4

$h_{film}$ = 240.7 μm

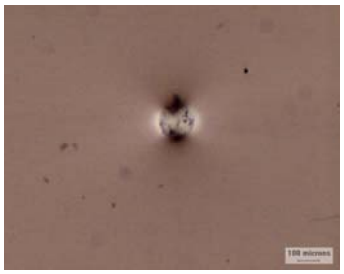

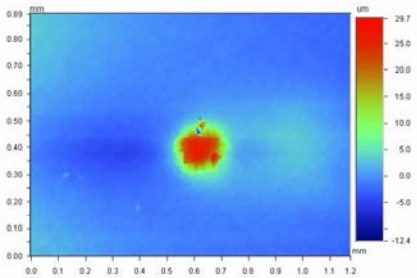

Defect: R19R40-D8

$h_{film}$ = 152.0 μm

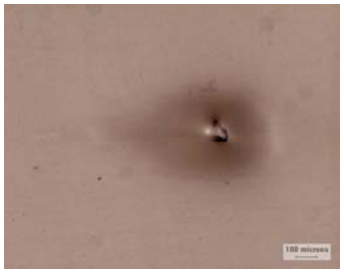

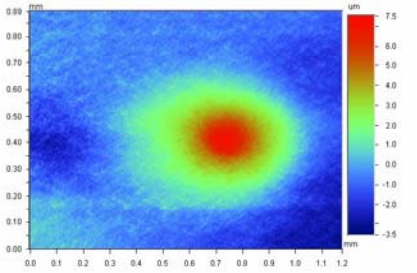

Defect: R19R50-D9

$h_{film}$ = 109.4 μm

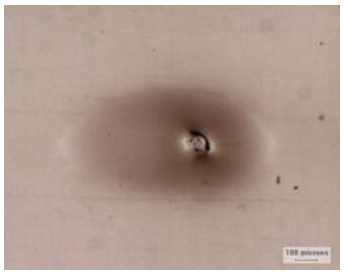

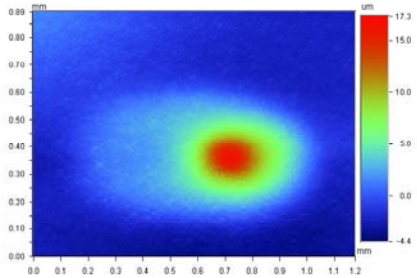

Defect: R19R60-D6

$h_{film}$ = 82.1 μm

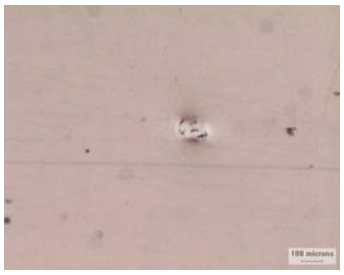

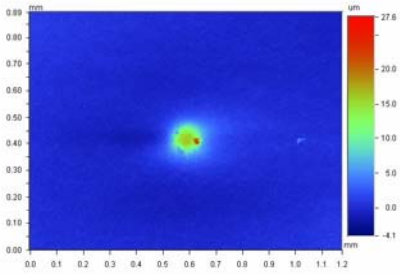

Defect: R19R80-D1

$h_{film}$ = 56.6 μm

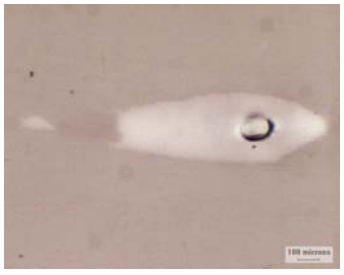

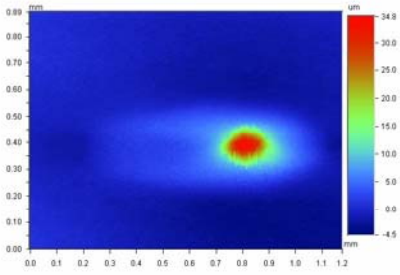

**Figure 3-II-3:** Polarized light and interferometric images of five defects caused by blue glass microspheres (~250 μm in diameter) in Extruder Run 4 (Table 3-3).

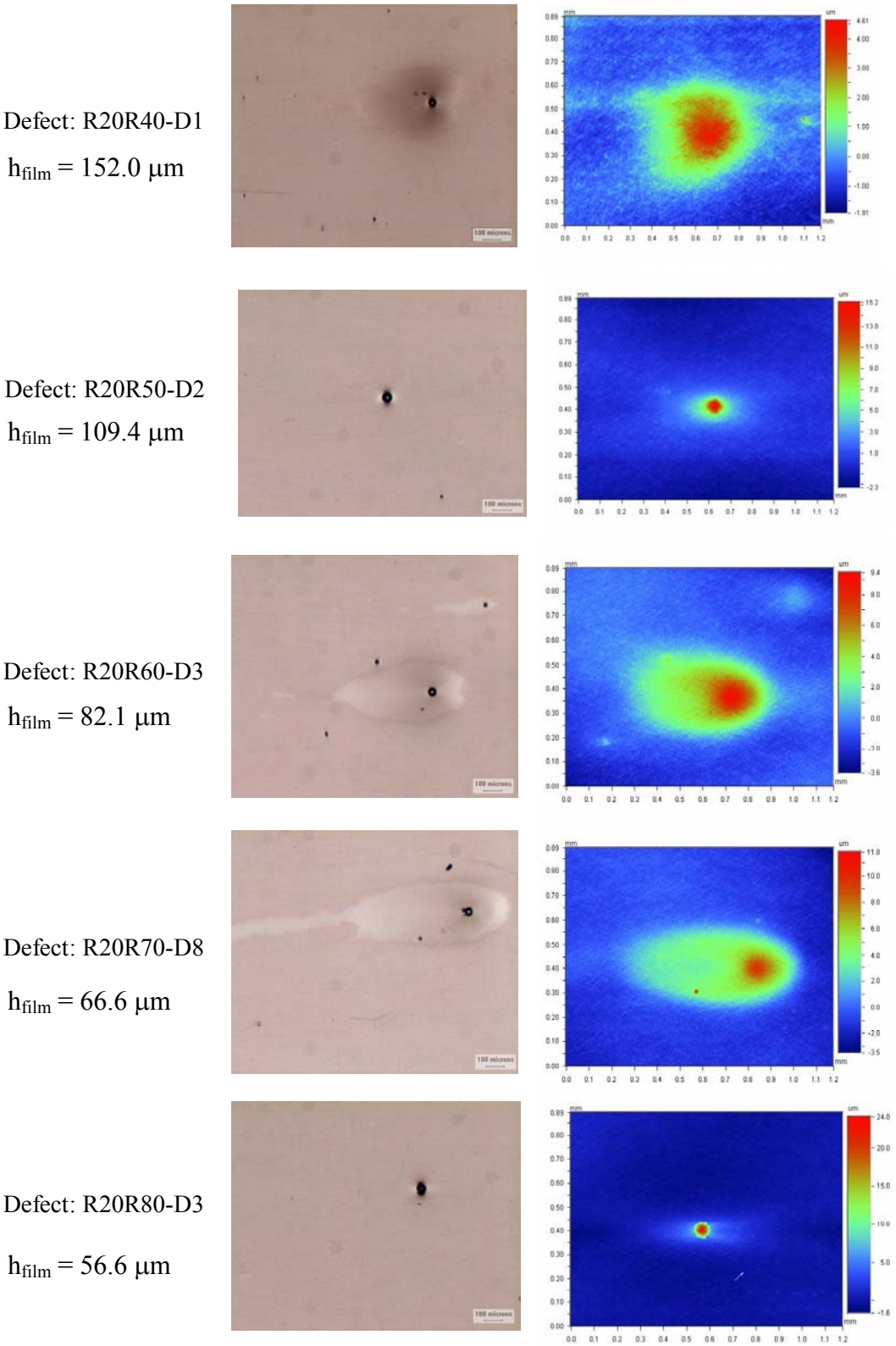


**Figure 3-II-4:** Polarized light and interferometric images of five defects caused by glass bubbles in Extruder Run 5 (Table 3-3).

Defect: R21R30-D4

$h_{film}$ = 240.7 μm

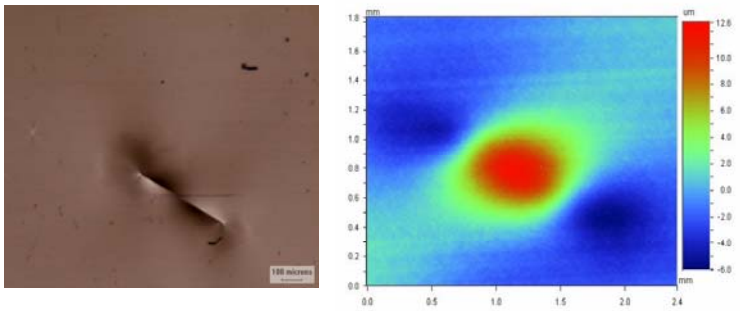

Defect: R21R40-D2

$h_{film}$ = 152.0 μm

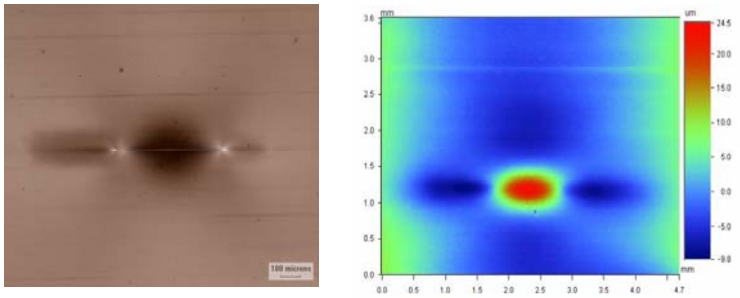

Defect: R21R50-D3

$h_{film}$ = 109.4 μm

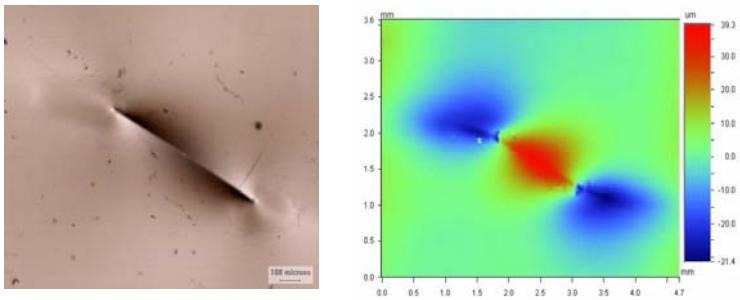

Defect: R21R60-D7

$h_{film}$ = 82.1 μm

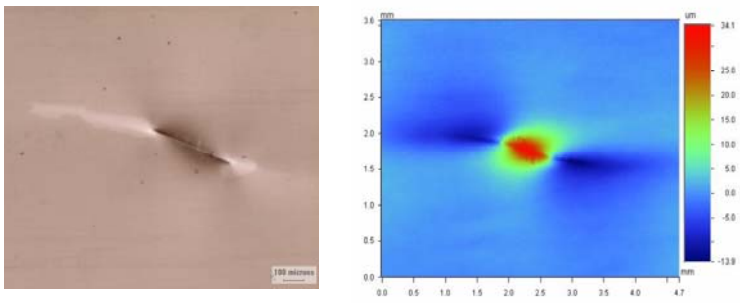

Defect: R21R80-D4

$h_{film}$ = 56.6 μm

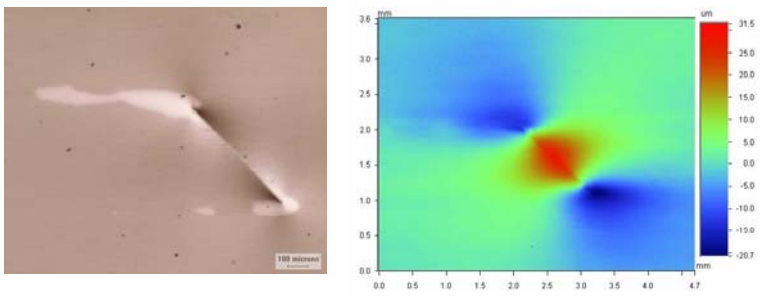

**Figure 3-II-5:** Polarized light and interferometric images of five defects caused by glass fibers in Extruder Run 6 (Table 3-3).

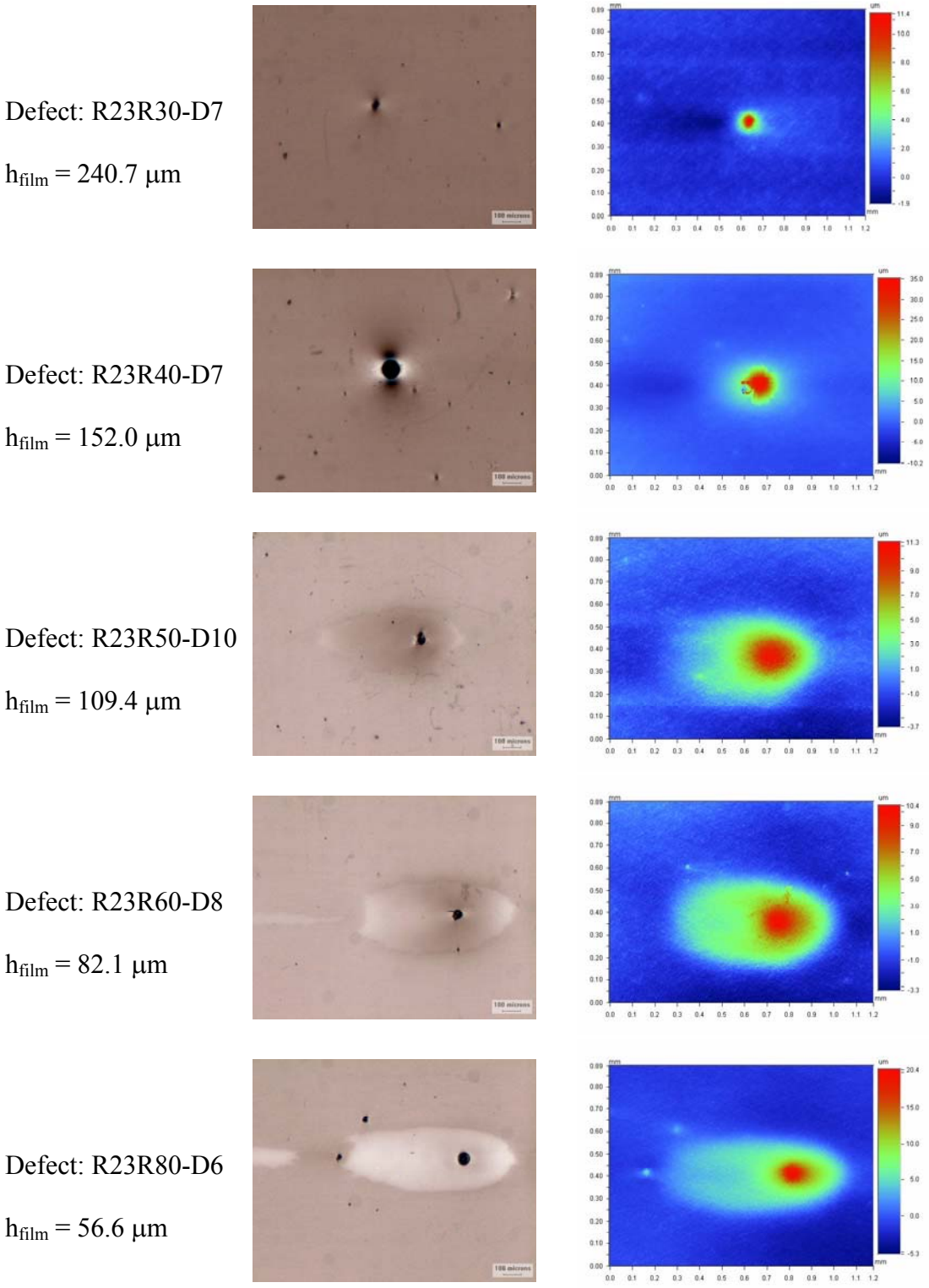


**Figure 3-II-6:** Polarized light and interferometric images of five defects caused by Aluminum powder in Extruder Run 9 (Table 3-3).

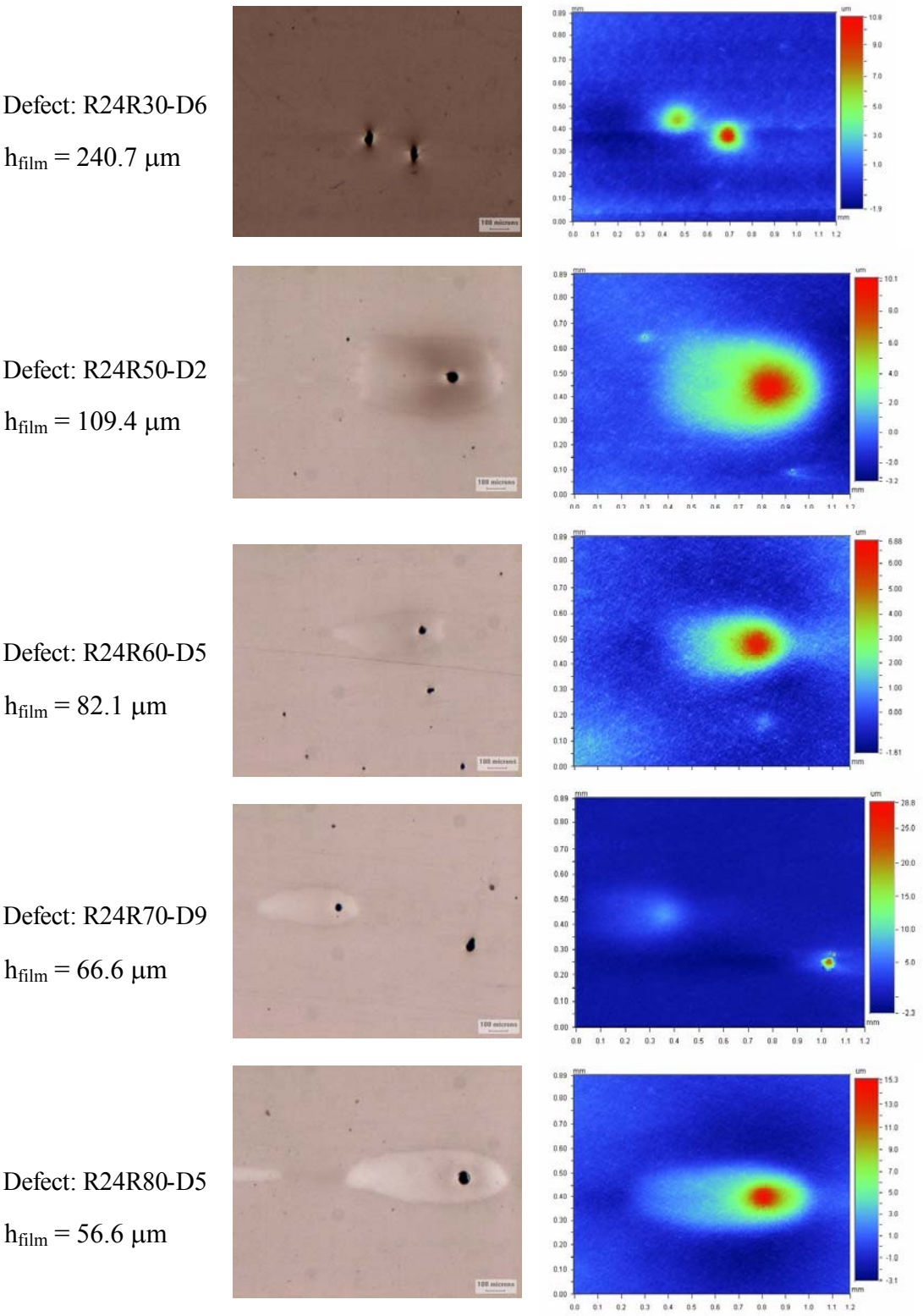


**Figure 3-II-7:** Polarized light and interferometric images of five defects caused by ceramic microspheres (Zeeospheres) in Extruder Run 8 (Table 3-3).

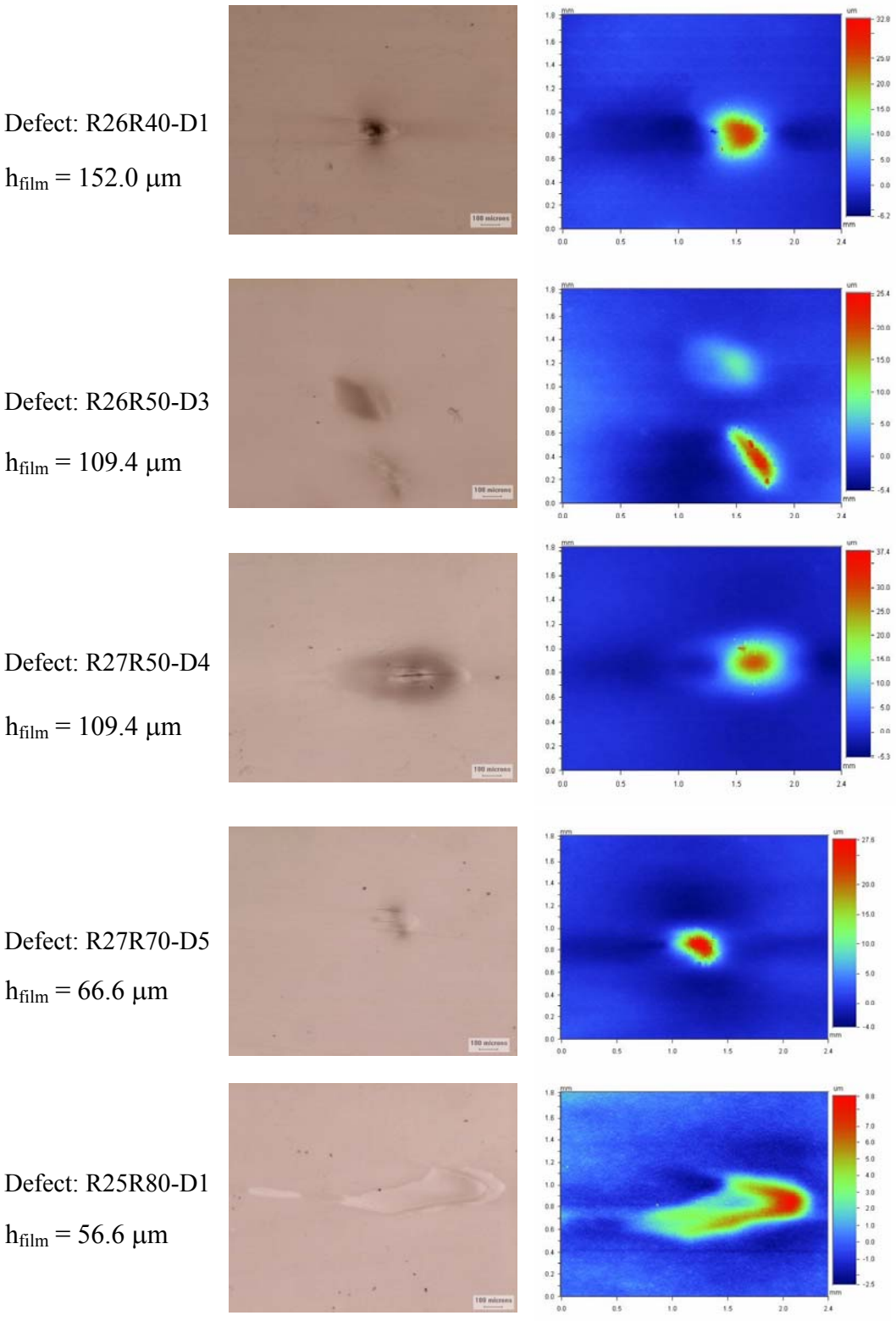


**Figure 3-II-8:** Polarized light and interferometric images of five defects caused by cross-linked polymer pieces in Extruder Runs 10, 11, and 12 (Table 3-3).

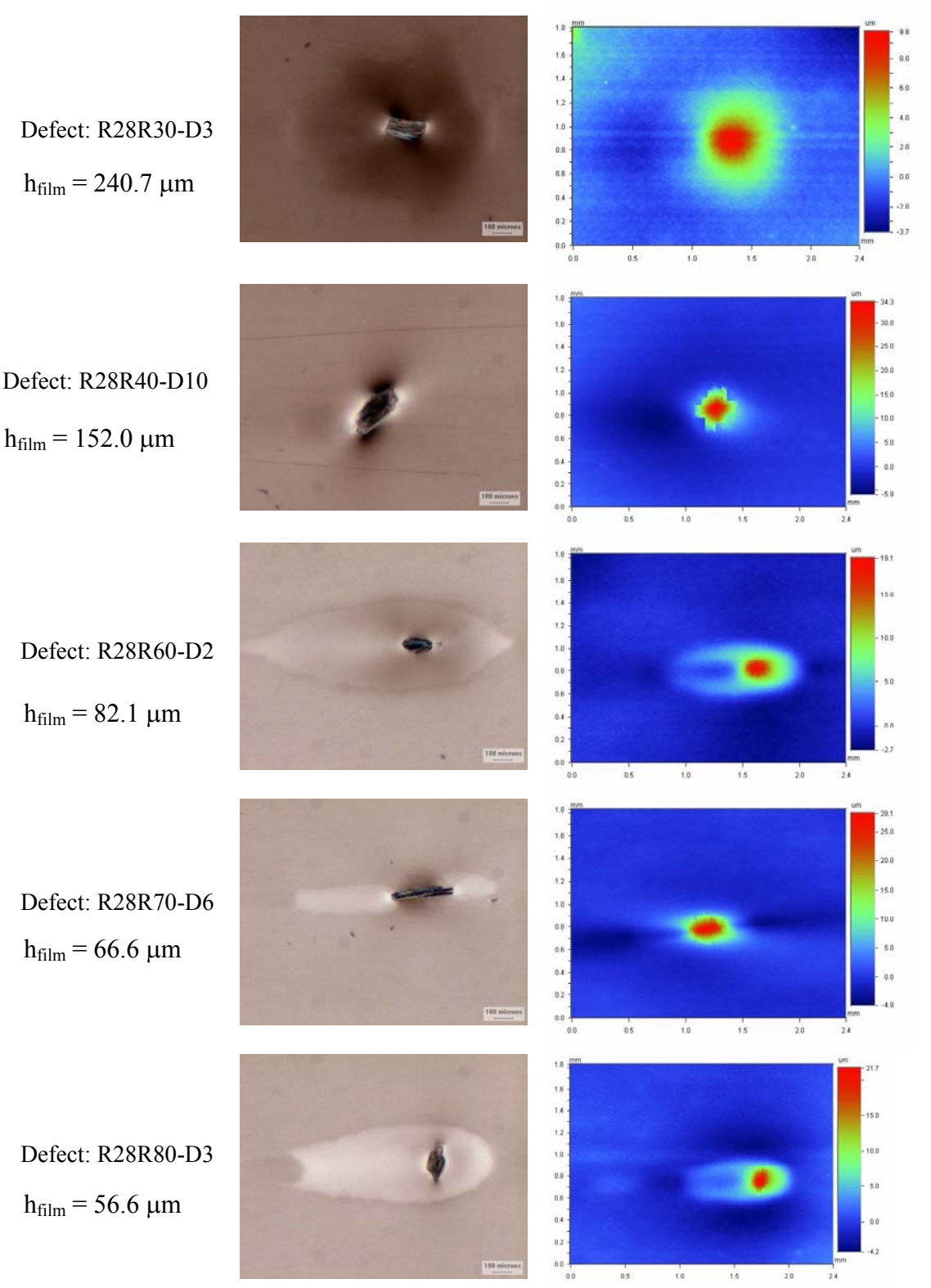


**Figure 3-II-9:** Polarized light and interferometric images of five defects caused by wood particles in Extruder Run 13 (Table 3-3).

## **APPENDIX 4-I:** Modifying the Extruder Melt Monitor

Figure 4-I-1 shows a schematic diagram of the original melt monitoring interface. The main reason for redesigning the window housing of the interface was to avoid the risk of introducing foreign particles into the melt stream while replacing a broken window. These particles could get stuck in the die, disturb the melt flow and affect the film quality.

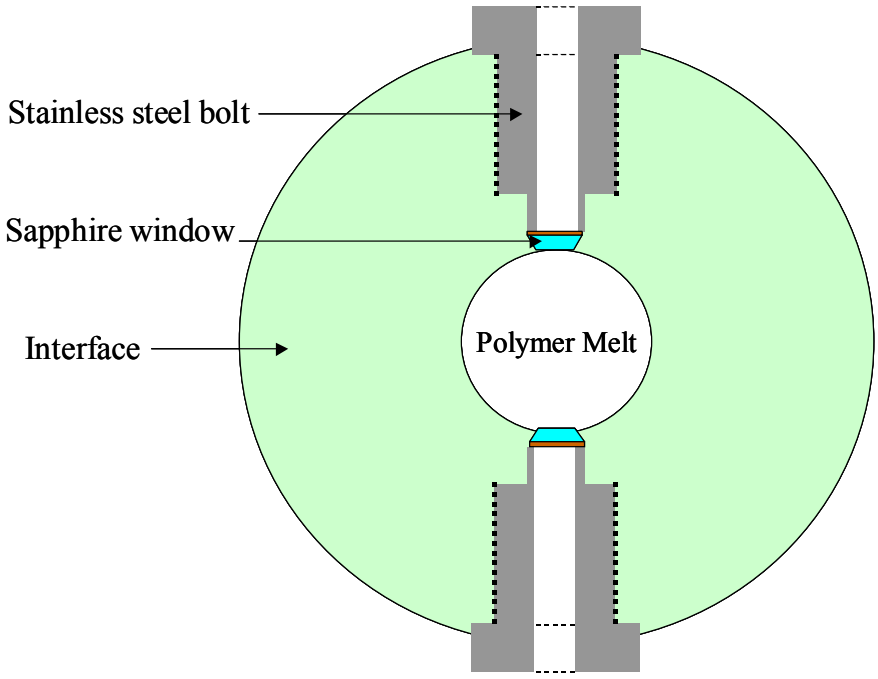


**Figure 4-I-1:** The original design of the melt monitoring interface.

The window replacement procedure with the original design was very difficult and time consuming. These points were taken into account in redesigning the window housing to make the window replacement an easier task. Below is a list of problems encountered in replacing a broken sapphire window with the original design.

- Window Removal: In some cases, the only practical method of removal was to break the window and remove the pieces one by one. This could damage the window seat and some of the broken pieces could get into the melt.
- Polymer melt fouling of the monitoring port
- Positioning of the window and the copper gasket was critical: any misalignment resulted in window breakage during installation

Figure 4-I-2 illustrates a diagram of the new design for the melt monitoring interface. The new window housing design consists of two parts, a copper part (Part 1) and a stainless steel part (Part 2). Part 1 is designed to hold the sapphire window and the copper gasket in place. It was made out of copper to take advantage of the self-sealing property of copper and increase the seal between this piece and the main interface body. The window and the gasket are placed in Part 1 off-line and without any difficulty. Part 1 is then threaded on to Part 2 and inserted into the interface port where it is held in place by a set of six small bolts.

Most of the extruder runs for film sample generation was conducted after the melt-monitoring interface was modified. This modification proved to be very effective and considerably cut down the number of broken sapphire windows. In addition, replacing a broken window was much easier and faster than before.

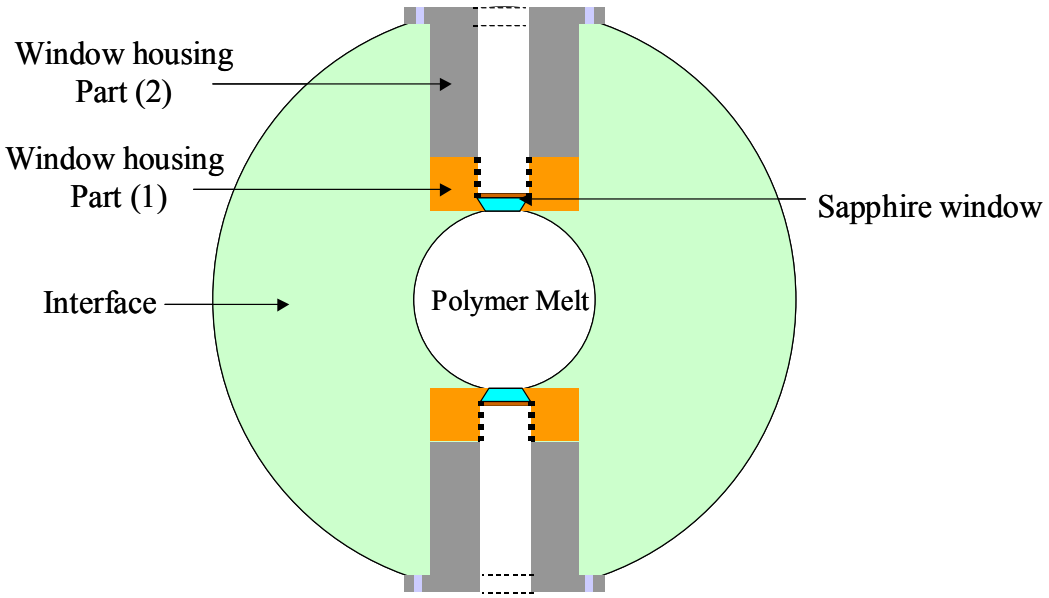


**Figure 4-I-2:** The new design of the melt monitoring interface.

## **APPENDIX 4-II:** Object Attribute Description

In the following, attribute description and illustration as provided by the Image Pro Plus software are shown:

**Angle:** Angle between the vertical axis and the major axis of the ellipse equivalent to the object

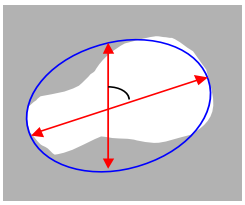

**Area:** Area of object. Does not include holes' area if "Fill Holes" option is turned off

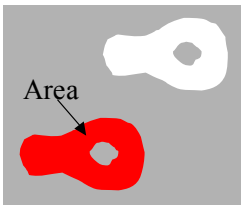


**Area (Polygon):** Area included in the polygon defining the object's outline. Same polygon as that used for Perimeter

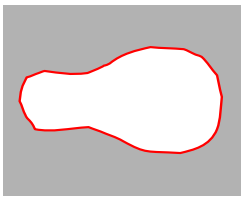

**Area/Box:** Ratio between the area of each object, and the area of its imaginary bounding box

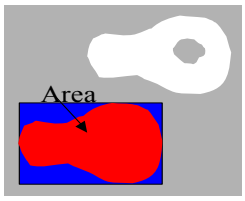


**Aspect:** Ratio between the major axis and the minor axis of the ellipse equivalent to the object

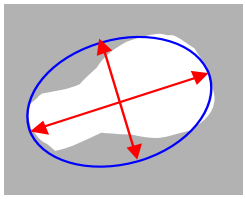

**Axis (major):** Length of the major axis of the ellipse equivalent to the object

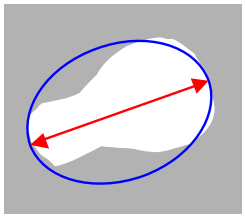

**Axis (minor):** Length of the minor axis of the ellipse equivalent to the object

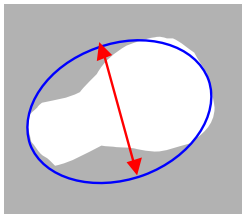

**Box Height:** Height of the bounding box along the major axis

**Box Width:** Width of the bounding box along the major axis

**Box X/Y:** Ratio between the width (X) and height (Y) of each object's imaginary bounding box

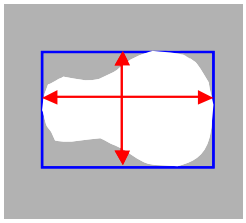

**Center-X:** X-coordinate position of the centroid of the object from the left side of the image

**Center-X (mass):** X-coordinate position of the centroid of the object based on intensity measurements

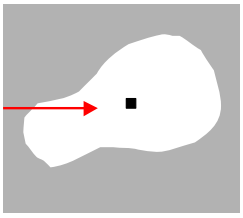

**Center-Y:** Y-coordinate position of the centroid pixel of the object from the top of the image

**Center-Y (mass):** Y-coordinate position of the centroid pixel based on intensity measurements

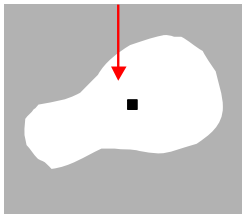

**Class:** Class number to which the object belongs

**Clumpiness:** Fractions of heterogeneous pixels remaining in an object after an erosion process, reflecting texture variations. (Fraction of pixels deviating from the average remaining after applying a dilation filter)

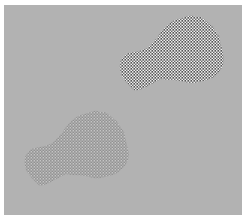

**Cluster:** Group of objects defined by an AOI (Area Of Interest)

**Count (adjusted):** Size-weighted object count

**Dendrites:** Number of dendrites (one-pixel-thick open branches)

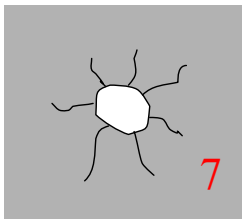


**Dendrite Length:** Total length of all the dendrites

**Density (Red):** Mean Red value for the measured object in a true color image

**Density (Green):** Mean Green value for the measured object in a true color image

**Density (Blue):** Mean Blue value for the measured object in a true color image

**Density (max):** Maximum intensity or density inside the object

**Density (min):** Minimum intensity or density inside the object

**Density (mean):** Average optical density (or intensity) of the object

**Density (std):** Standard deviation of intensity or density inside the object

**Density (sum):** Sum of the intensity values of all the pixels of a counted object

**Diameter (max):** Length of the longest line that can be drawn to pass through the centroid position and join two points on each object's perimeter

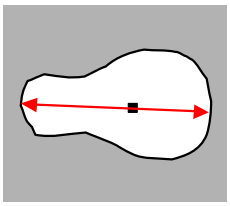

**Diameter (min):** Length of the shortest line that can be drawn to pass through the centroid position and join two points on each object's perimeter

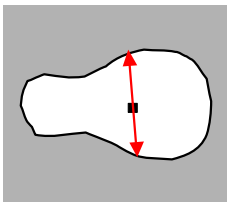

**Diameter (mean):** Average length of the diameters measured at two-degree intervals joining two outline points and passing through the centroid

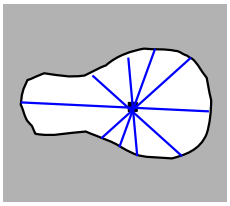

**Radius (max):** Maximum distance between each object's centroid pixel position and its perimeter

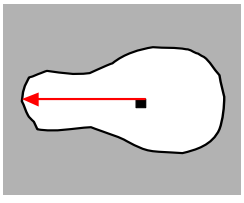

**Radius (min):** Minimum distance between each object's centroid pixel position and its perimeter

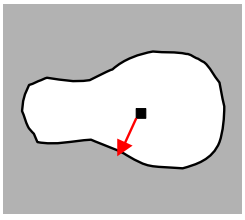

**Radius (ratio):** Ratio between Max Radius and Min Radius for each object

**End Points:** Number of end points (points at the end of one-pixel-thick open branches)

**Feret (max):** Longest caliper (feret) length

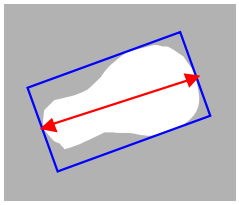

**Feret (min):** Shortest caliper (feret) length

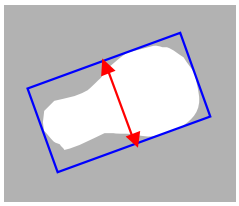

**Feret (mean):** Average caliper (feret) length

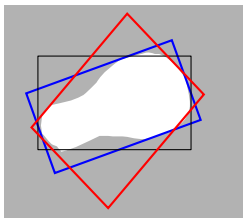

**Fractal Dimension:** Fractal dimension of the object's outline

**Heterogeneity:** Fraction of pixels that vary more than 10% from the average intensity of the object

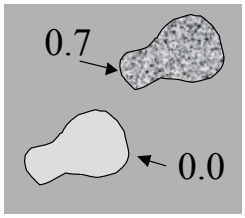


**Hole Area:** Area of holes within an object

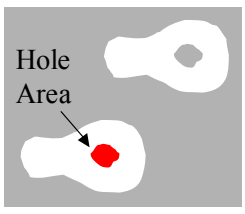


**Hole Ratio:** Ratio of the object area excluding holes, to the total area of the object

**Holes:** Number of holes inside an object

**IOD:** Integrated Optical Density (or integrated intensity) of the object. It is equal to object area multiplied by its average density (or intensity).

**Margination:** Relative distribution of intensity between the center of an object and the edge of the object, with larger values from brighter centers. A value of 0.33 indicates a homogeneous object.

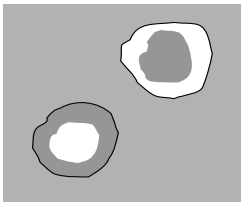

**Per-Area:** Ratio between the area of the counted object to that of the entire image.

**Perimeter:** Length of the outline of each object

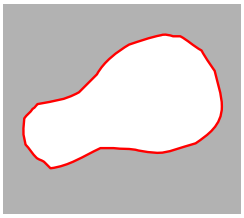

**Perimeter (Convex):** Perimeter of the convex outline of each object

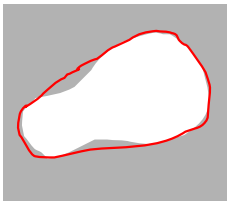

**Perimeter (Ellipse):** Perimeter of the ellipse surrounding the outline of each object

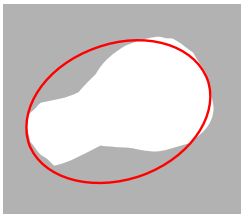

**Perimeter (Ratio):** Ratio of the convex perimeter to the perimeter of the outline of each object

**Roundness:** $\frac{Perimeter^2}{4\pi \times Area}$

**Size (length):** Feret diameter (caliper length) along a major axis of the object

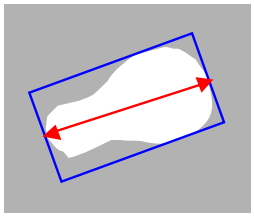

**Size (width):** Feret diameter (caliper length) along a minor axis of the object

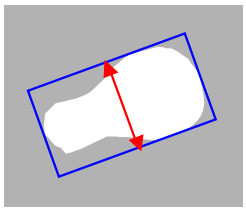

## **APPENDIX 4-III:** In-Line Images of Particles in Polymer Melt

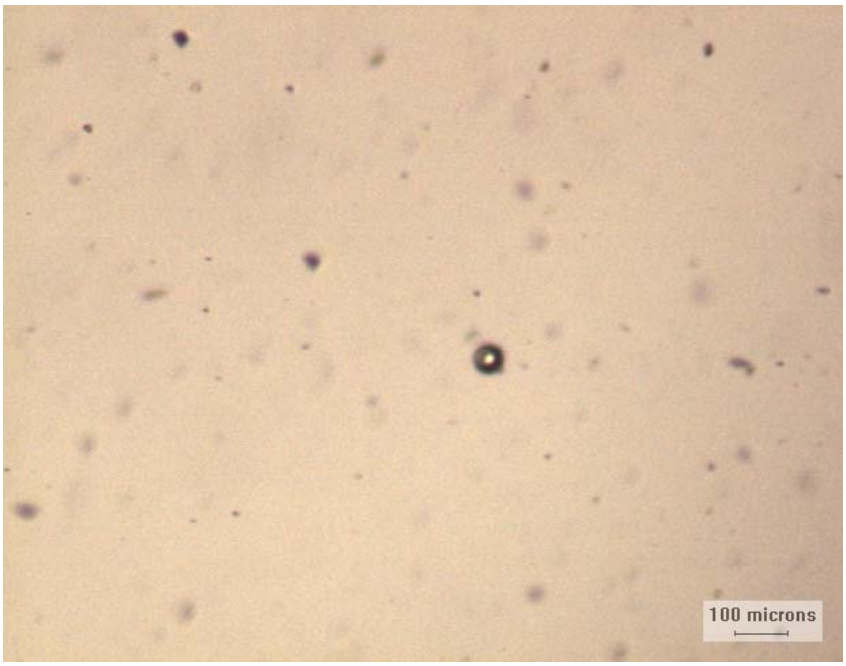


**Figure 4-III-1:** In-line image of a glass microsphere (~50 μm in diameter) in low-density polyethylene melt obtained by the scanning particle monitor.

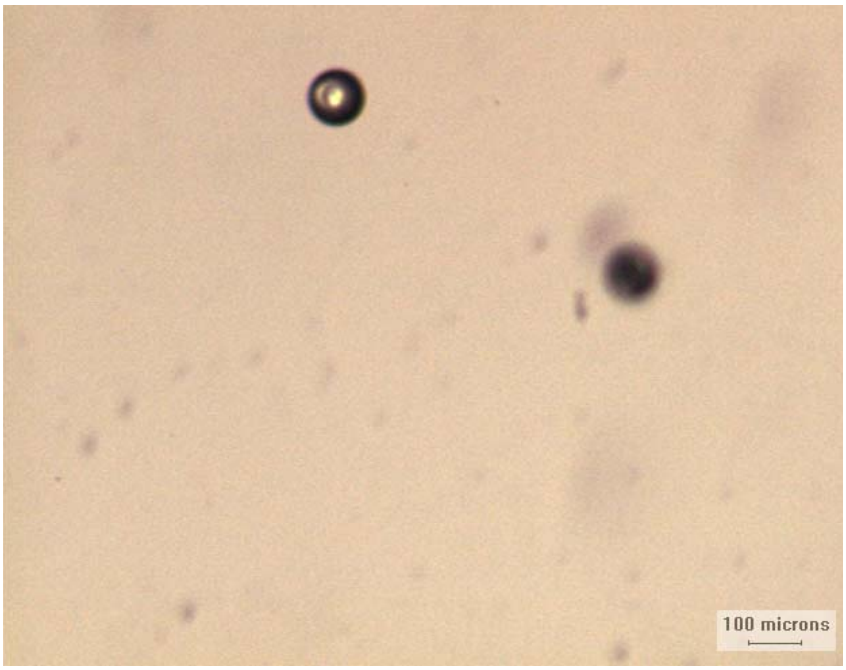


**Figure 4-III-2:** In-line image of glass microspheres (~100 μm in diameter) in low-density polyethylene melt obtained by the scanning particle monitor.

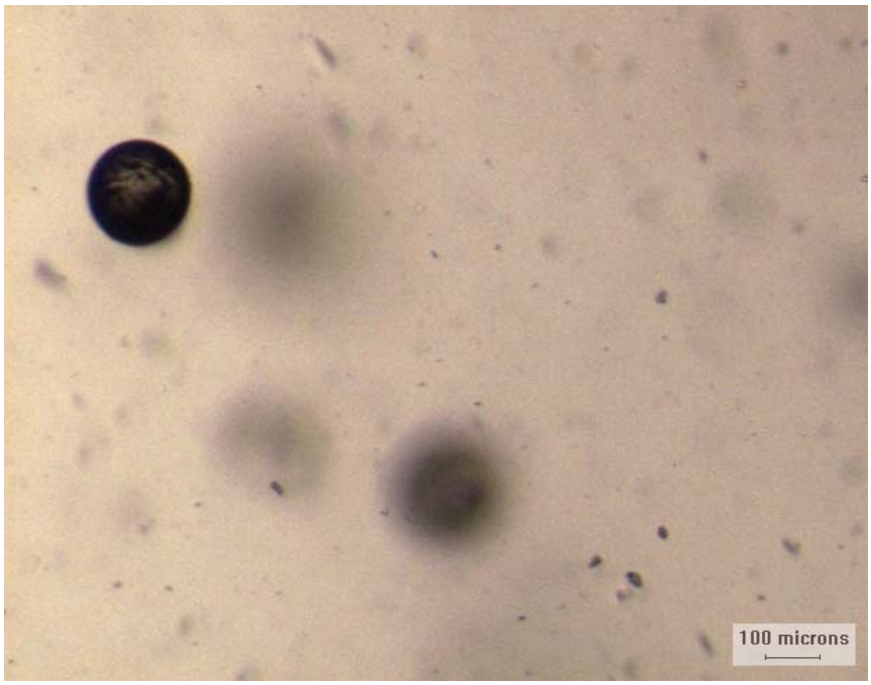


**Figure 4-III-3:** In-line image of blue glass microspheres (~200 μm in diameter) in low-density polyethylene melt obtained by the scanning particle monitor.

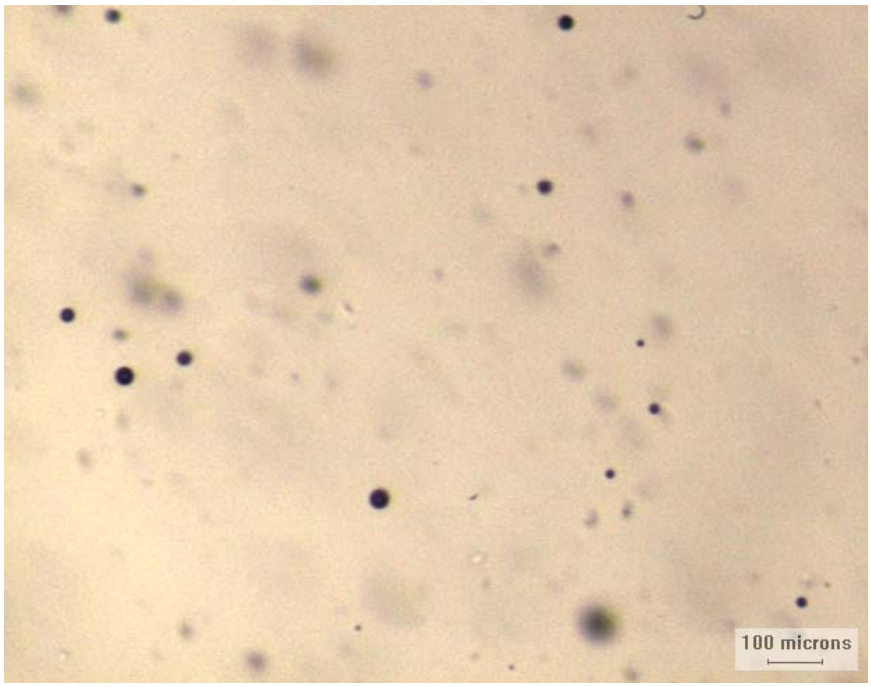


**Figure 4-III-4:** In-line image of hollow glass microspheres in low-density polyethylene melt obtained by the scanning particle monitor.


**Figure 4-III-5:** In-line image of glass fibers in low-density polyethylene melt obtained by the scanning particle monitor.

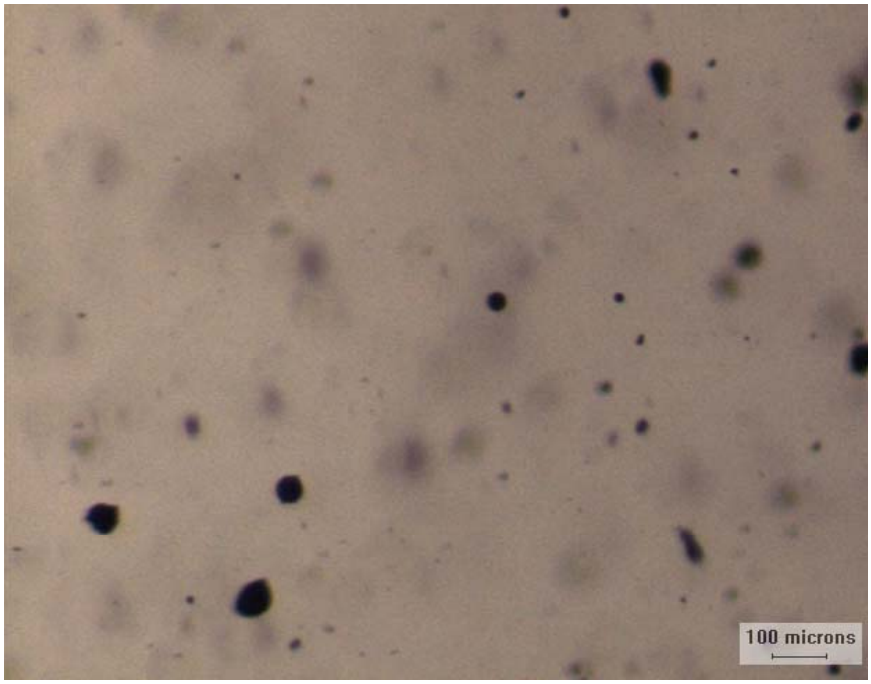


**Figure 4-III-6:** In-line image of Aluminum particles in low-density polyethylene melt obtained by the scanning particle monitor.

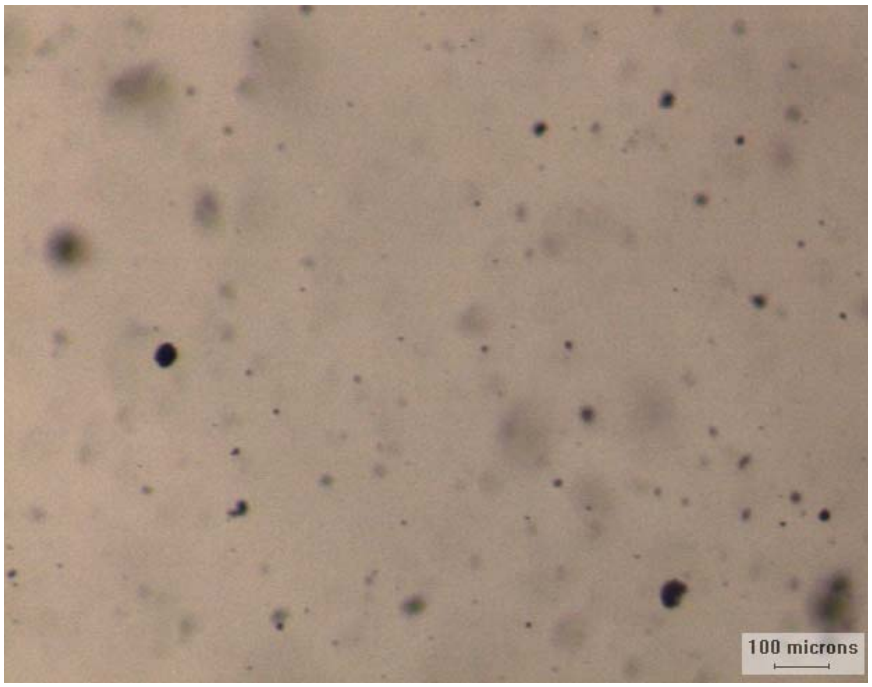


**Figure 4-III-7:** In-line image of ceramic microspheres in low-density polyethylene melt obtained by the scanning particle monitor.

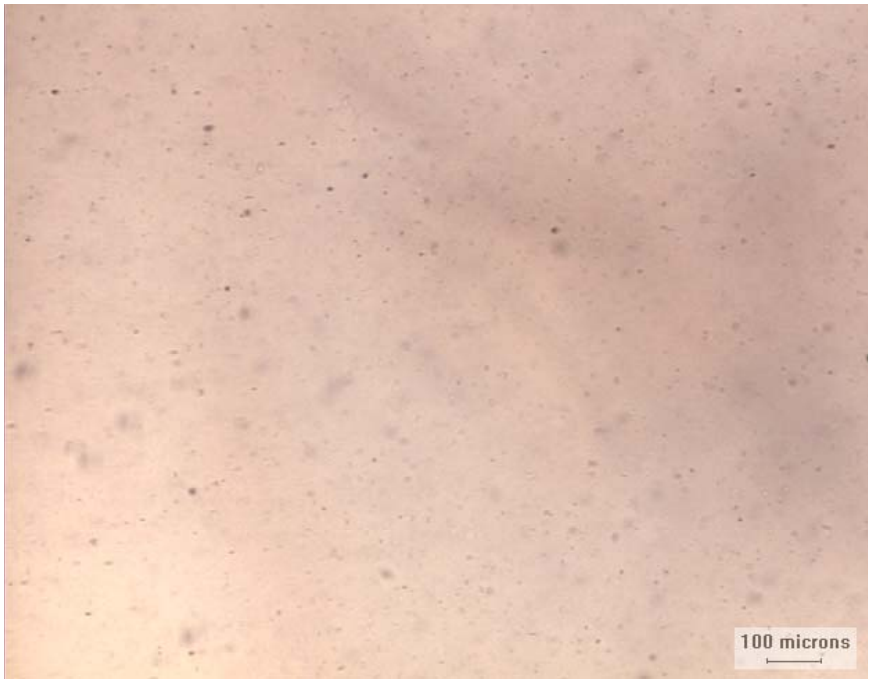


**Figure 4-III-8:** In-line image of Diatomite particles in low-density polyethylene melt obtained by the scanning particle monitor.


**Figure 4-III-9:** In-line image of wood pieces in low-density polyethylene melt obtained by the scanning particle monitor.

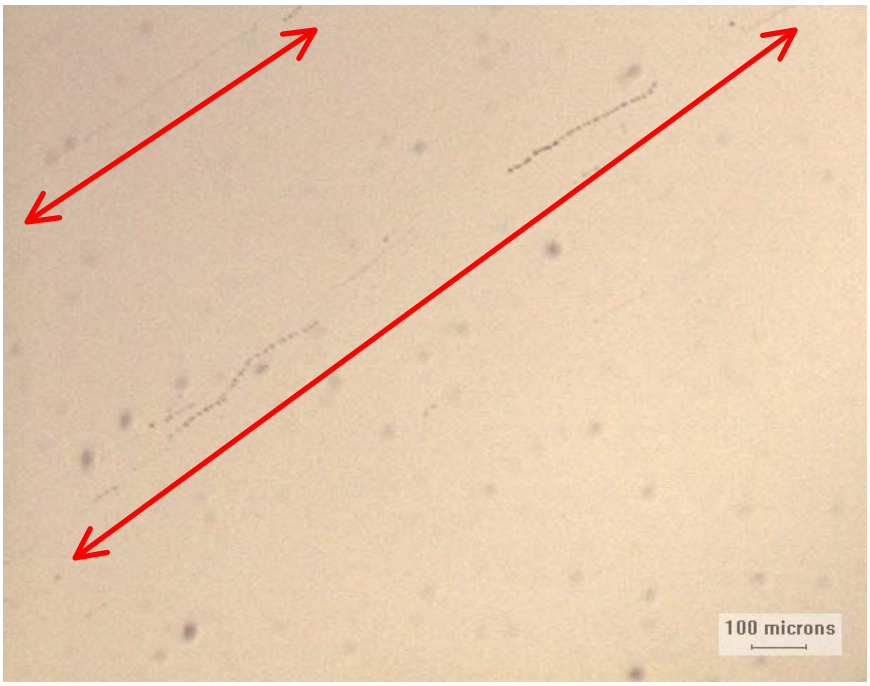


**Figure 4-III-10:** In-line image of partially melted cross-linked polymer pieces in low-density polyethylene melt obtained by the scanning particle monitor.

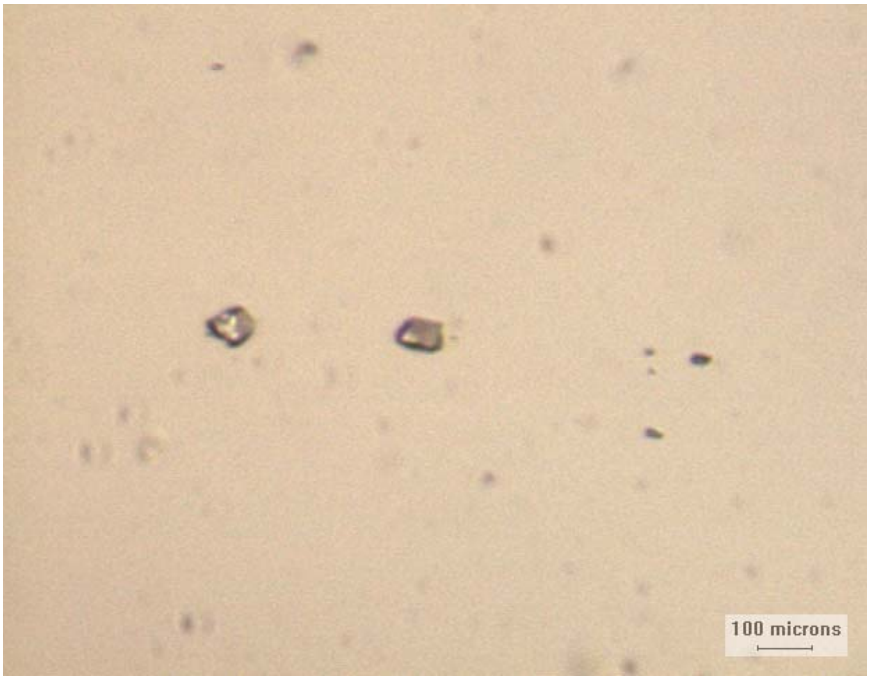


**Figure 4-III-11:** In-line image of cross-linked or degraded polymer pieces in low-density polyethylene melt obtained by the scanning particle monitor.

## **APPENDIX 4-IV:** A Portion of the Dataset

The dataset can be divided into four sections:

1. Particle type and processing conditions attributes
2. Particle features obtained by polarized imaging
3. Defect features obtained by polarized imaging
4. Defect features obtained by Interferometry

Each section of the data collected for five defects is shown in Table 4-IV-1. The first column shows the attribute name followed by the data for five defects. The attributes highlighted in orange are the image name and processing variables. The attributes highlighted in green and blue are the respective attributes of the embedded particles and of the defects, both obtained from polarized light images. The attributes highlighted in pink are the defect attributes measured from the interferometric images.

**Table 4-IV-1:** The data collected for five film defects.

| Image Name | R17R30-D01 | R17R30-D02 | R17R30-D03 | R17R30-D04 | R17R30-D05 |
|---|---|---|---|---|---|
| Image ID | 9 | 10 | 11 | 12 | 13 |
| Run | 17 | 17 | 17 | 17 | 17 |
| Roller Speed | 30 | 30 | 30 | 30 | 30 |
| PArea | 1562.8801 | 1456.604 | 1600.389 | 2131.769 | 1412.844 |
| PAspect | 1.01317 | 1.036805 | 1.044379 | 1.032113 | 1.063244 |
| PArea/Box | 0.81699345 | 0.8062283 | 0.748538 | 0.7732426 | 0.8308823 |
| PBox-X/Y | 0.94866071 | 1.004464 | 1.060268 | 1.004464 | 0.9453782 |
| PDensity-(mean) | 78.58518 | 130.3219 | 120.2398 | 95.56497 | 122.3945 |
| PAngle | 0.00016468 | 0.0003217 | 90 | 179.9997 | 180 |
| PAxis-(major) | 44.903332 | 43.8476 | 46.13903 | 52.92604 | 43.71888 |
| PAxis-(minor) | 44.319641 | 42.29107 | 44.17845 | 51.2793 | 41.11837 |
| PDiameter-(max) | 44.540321 | 43.6001 | 45.38094 | 52.11098 | 41.83614 |
| PDiameter-(min) | 40.1716 | 38.89025 | 41.65202 | 47.52462 | 37.58818 |
| PDiameter-(mean) | 42.268448 | 40.878 | 42.89006 | 49.93325 | 39.92843 |
| PRadius-(max) | 22.270161 | 21.97891 | 22.98842 | 26.15355 | 21.63846 |
| PRadius-(min) | 20.0858 | 19.02444 | 20.05817 | 23.12058 | 18.79492 |
| PPerimeter | 133.79346 | 129.7177 | 135.9688 | 157.5607 | 127.3569 |

| | | | | | |
|---|---|---|---|---|---|
| PRadius-Ratio | 1.1087515 | 1.155299 | 1.146088 | 1.131181 | 1.151293 |
| PRoundness | 1.0770844 | 1.048248 | 1.066061 | 1.057774 | 1.086666 |
| PPer-Area | 0.00081763 | 0.000762 | 0.0008372 | 0.0011152 | 0.0007391 |
| PSize-(length) | 42.410675 | 40.09412 | 45.10583 | 50.11765 | 39.91589 |
| PSize-(width) | 40.094116 | 39.91592 | 42.41064 | 49.8949 | 37.58815 |
| PPerimeter-(convex) | 131.37962 | 129.7177 | 133.6532 | 155.3449 | 125.1411 |
| PPerimeter-(ellipse) | 140.15262 | 135.3174 | 141.8871 | 163.6956 | 133.2933 |
| PPerimeter-(ratio) | 0.98195851 | 1 | 0.9829692 | 0.9859364 | 0.9826012 |
| PArea-(polygon) | 1322.5442 | 1277.394 | 1380.024 | 1867.641 | 1187.789 |
| PBox-Width | 42.599942 | 42.59994 | 47.6117 | 52.62346 | 40.09406 |
| PBox-Height | 44.90535 | 42.41061 | 44.90535 | 52.38958 | 42.41061 |
| PFeret-(min) | 40.094055 | 39.91583 | 42.41064 | 49.52722 | 37.58813 |
| PFeret-(max) | 44.528076 | 43.59015 | 45.69928 | 52.1109 | 42.63126 |
| PFeret-(mean) | 43.352322 | 41.83281 | 43.90662 | 50.80688 | 41.00775 |
| PDensity-(min) | 8 | 64 | 61 | 0 | 56 |
| PDensity-(max) | 130 | 182 | 168 | 192 | 173 |
| PDensity-(stdev) | 25.43805 | 23.80454 | 20.90288 | 50.31733 | 24.31635 |
| PMargination | 0.3097381 | 0.350138 | 0.3482385 | 0.2964367 | 0.3547357 |
| PDensity-(sum) | 21218 | 30365 | 29579 | 33830 | 26682 |
| DArea | 226311.3 | 6401.557 | 6239.018 | 8889.662 | 6026.466 |
| DAspect | 1.1350752 | 1.289164 | 1.319112 | 1.38756 | 1.426862 |
| DArea/Box | 0.76214236 | 0.7804878 | 0.7665131 | 0.79 | 0.7914614 |
| DBox-X/Y | 0.95942104 | 0.7839721 | 0.7413903 | 0.7232143 | 0.6935587 |
| DDensity-(mean) | 90.39913 | 102.9284 | 96.13714 | 86.16968 | 94.47692 |
| DAngle | 156.71901 | 180 | 0.0000212 | 179.3882 | 0.2103227 |
| DAxis-(major) | 578.36786 | 102.5052 | 102.3682 | 125.3193 | 104.6324 |
| DAxis-(minor) | 509.54144 | 79.51295 | 77.60384 | 90.31626 | 73.33038 |
| DDiameter-(max) | 599.55035 | 100.2918 | 102.3151 | 122.8828 | 103.049 |
| DDiameter-(min) | 436.05148 | 78.04195 | 74.7393 | 87.70576 | 70.16461 |
| DDiameter-(mean) | 530.16138 | 89.50647 | 86.52916 | 104.8062 | 88.11557 |
| DRadius-(max) | 329.11331 | 50.57979 | 51.16776 | 61.97858 | 51.83776 |
| DRadius-(min) | 166.48753 | 37.56313 | 36.72053 | 43.22839 | 34.8087 |
| DPerimeter | 1807.4099 | 281.8433 | 278.781 | 335.5338 | 276.4279 |
| DRadius-Ratio | 1.9768045 | 1.346528 | 1.393438 | 1.433747 | 1.489219 |
| DRoundness | 1.1636707 | 1.057515 | 1.06568 | 1.072179 | 1.088445 |
| DPer-Area | 0.11839678 | 0.003349 | 0.0032639 | 0.0046507 | 0.0031528 |
| DSize-(length) | 575.42554 | 99.78967 | 102.2844 | 122.4227 | 102.3297 |
| DSize-(width) | 534.96674 | 77.68225 | 75.17639 | 87.96713 | 70.26483 |
| DPerimeter-(convex) | 1759.8148 | 279.5285 | 276.3518 | 332.9236 | 273.8678 |
| DPerimeter-(ellipse) | 1710.5943 | 287.0552 | 284.0391 | 340.9544 | 281.7095 |
| DPerimeter-(ratio) | 0.97366669 | 0.9917869 | 0.9912865 | 0.9922208 | 0.9907385 |
| DArea-(polygon) | 223394.97 | 5977.495 | 5803.497 | 8355.939 | 5586.6 |
| DBox-Width | 533.75221 | 80.18813 | 77.68225 | 90.21164 | 72.67049 |
| DBox-Height | 556.3274 | 102.2844 | 104.7792 | 124.7371 | 104.7792 |
| DFeret-(min) | 516.46558 | 77.68225 | 75.17639 | 87.70575 | 70.16461 |
| DFeret-(max) | 606.50378 | 100.8055 | 102.2844 | 123.3731 | 103.02 |
| DFeret-(mean) | 560.15576 | 90.26778 | 89.47742 | 107.4833 | 88.60471 |
| Density (min) | 20 | 0 | 0 | 0 | 0 |

| | | | | | |
|---|---|---|---|---|---|
| Density (max) | 139 | 206 | 202 | 204 | 197 |
| Density (stdev) | 13.61307 | 58.86046 | 55.37116 | 58.05849 | 52.96557 |
| Margination | 0.3568375 | 0.4173855 | 0.4133964 | 0.3775172 | 0.4378539 |
| DDensity-(sum) | 3263951 | 86254 | 79217 | 100043 | 73692 |
| WArea | 255580.16 | 57110.2 | 85580.24 | 121034.9 | 82943.17 |
| WAspect | 1.1337537 | 1.275892 | 1.318512 | 1.746658 | 1.255897 |
| WArea/Box | 0.67447844 | 0.6850583 | 0.7186703 | 0.6874127 | 0.7037429 |
| WBox-X/Y | 1.150901 | 1.178211 | 1.226447 | 1.629647 | 1.228809 |
| WDensity-(mean) | 189.17802 | 86.41547 | 93.00494 | 56.54856 | 91.51207 |
| WAngle | 111.72267 | 96.1981 | 85.55173 | 85.74729 | 88.64992 |
| WAxis-(major) | 611.18768 | 306.0788 | 381.199 | 522.1343 | 367.3209 |
| WAxis-(minor) | 539.08331 | 239.8941 | 289.1131 | 298.9333 | 292.477 |
| WDiameter-(max) | 640.51868 | 316.8727 | 402.515 | 533.9432 | 388.5344 |
| WDiameter-(min) | 516.2041 | 224.5646 | 256.6356 | 258.0734 | 274.0029 |
| WDiameter-(mean) | 564.7561 | 266.8743 | 333.7281 | 405.1714 | 332.7706 |
| WRadius-(max) | 349.20737 | 169.4172 | 211.2456 | 273.3409 | 201.1046 |
| WRadius-(min) | 244.99773 | 104.3513 | 126.8354 | 108.964 | 127.1023 |
| WPerimeter | 2402.2769 | 1078.572 | 1266.567 | 1675.697 | 1309.179 |
| WRadius-Ratio | 1.4253494 | 1.623528 | 1.66551 | 2.508544 | 1.582226 |
| WRoundness | 1.8231926 | 1.64419 | 1.518928 | 1.861656 | 1.66851 |
| WPer-Area | 0.23812556 | 0.0532099 | 0.0797356 | 0.1127689 | 0.0772786 |
| WSize-(length) | 668.79968 | 311.6234 | 379.3085 | 520.646 | 370.7567 |
| WSize-(width) | 602.57422 | 262.5562 | 305.1926 | 329.1041 | 304.33 |
| WPerimeter-(convex) | 1921.191 | 907.3857 | 1127.602 | 1382.075 | 1120.169 |
| WPerimeter-(ellipse) | 1808.6169 | 860.7657 | 1057.897 | 1313.668 | 1039.745 |
| WPerimeter-(ratio) | 0.79973756 | 0.8412847 | 0.8902821 | 0.8247762 | 0.855627 |
| WArea-(polygon) | 251885.83 | 56303.59 | 84044.48 | 120027.7 | 81744.64 |
| WBox-Width | 660.387 | 313.404 | 382.161 | 535.665 | 380.562 |
| WBox-Height | 573.8 | 266 | 311.6 | 328.7 | 309.7 |
| WFeret-(min) | 552.64429 | 252.8049 | 303.4619 | 324.9 | 298.8729 |
| WFeret-(max) | 670.94946 | 320.3607 | 415.434 | 526.3981 | 394.9885 |
| WFeret-(mean) | 612.57715 | 288.8481 | 358.9835 | 439.9626 | 356.6947 |
| WDensity-(min) | 148 | 44 | 46 | 33 | 45 |
| WDensity-(max) | 255 | 214 | 255 | 255 | 255 |
| WDensity-(std.) | 23.288084 | 37.49353 | 43.02937 | 32.5551 | 42.18034 |
| WMargination | 0.29914469 | 0.2232609 | 0.22342 | 0.2926971 | 0.2174285 |
| WDensity-(sum) | 15914601 | 1624438 | 2619856 | 2252838 | 2498371 |
| WVolume | 363434.626 | 123917.6571 | 157445.2895 | 216124.9035 | 145182.054 |

## **APPENDIX 4-V:** Film Defects Caused by Glass Fibers

Figure 4-V-1 shows polarized light images of defects obtained from the introduction of glass fibers into the polymer feed. These images show that film defects caused by fibers exhibited two distinct regions of deformation, each located at one end of the particle. This observation is also illustrated by the defect images shown in Figure 3-II-5. This behavior was quite different from that of the other spherical or irregular shapes of particles used in this study. The deformations observed at the fiber ends resembled the "low average height" defects of spherical particles.

The literature on glass fiber composites provides some information that appears relevant to these observations. In studies of isolated fibers in glass fiber composites the fibers rotate during processing and buckle due to the forces applied as well as because of the thermal expansion coefficient mismatch between the matrix and the fiber. Stress is concentrated at both ends of the fibers. (Harris 1978, Gibson 1994)

Therefore, fibers usually have the potential to create larger defects since each end of the fiber acts like a separate particle. In addition, buckling of the fibers can increase the impact of the particle on the surface.


**Figure 4-V-1:** Polarized light images of film defects caused by glass fibers.

# **APPENDIX 4-VI:** Attribute Examination and Selection

The presence of too many attributes in a dataset makes it hard to understand or model the data. Some of the irrelevant attributes may introduce error and influence the modeling outcome. In the attribute selection (or elimination) step, the main goal is to eliminate unimportant or unneeded attributes and reduce the size of the dataset as much as possible.

The dataset used for this analysis consisted of only the defects caused by spherical particles with known chemical properties; it has 420 instances. Some of the clearly irrelevant or redundant attributes were already eliminated. At this stage, the dataset had a total of 94 measured defect and particle attributes. The aim of this document is to provide details of analysis and reasoning used in attribute selection.

## 1.0 Angle Attributes

**Angle:** Angle between the image vertical axis and the major axis of the ellipse equivalent to the object.

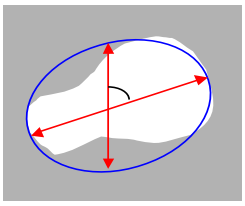

### 1.1 Defect Angle in Interferometric Images (WAngle)

WAngle reports the angle between the major axis of the surface deformation and the image vertical axis. For elongated defects, in most cases, the length of the major axis is much greater than the variation caused by the uneven defect contour. Therefore, this variation does not affect the choice of the major axis. In addition, during experiments, film samples were aligned such that the image x axis was approximately parallel with the machine direction. As

a result, for most elongated defects, WAngle is close to 90 degrees. An example is shown below:

Defect: R18R70D25-1
WAngle = 90.80 °

**Figure 4-VI-1:** Mask image of an elongated surface deformation and its measured WAngle.

However, in the case of approximately round objects with uneven and wavy contours, the value of WAngle could be misleading. Three objects with different WAngle values are shown in Figure 4-VI-2. As you can see, WAngle is easily influenced by unimportant object boundary variations. Some statistics of WAngle for defects caused by spherical particles are shown in Table 4-VI-1. Figure 4-VI-3 shows the histogram of this attribute.

**Table 4-VI-1:** Descriptive statistics for WAngle, DAngle, and PAngle attributes

| Attribute | Minimum | Maximum | Mean | Std. Deviation |
|---|---|---|---|---|
| WAngle | 0.165 | 179 | 90.8 | 15.1 |
| DAngle | 0 | 180 | 89.2 | 53.5 |
| PAngle | 0 | 180 | 95.7 | 63.5 |

Defect: R18R30D17
WAngle = 0.68 °

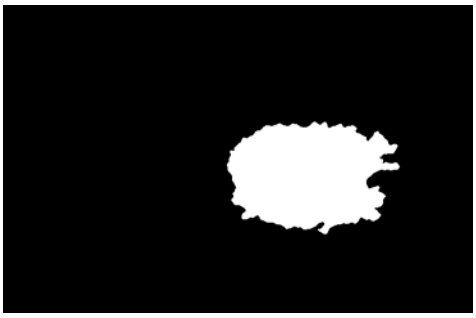

Defect: R18R30D18
WAngle = 88.12 °

Defect: R18R30D19
WAngle = 127.82 °

**Figure 4-VI-2:** Three mask images of surface deformations belonging to three different film defects and their corresponding WAngle values.

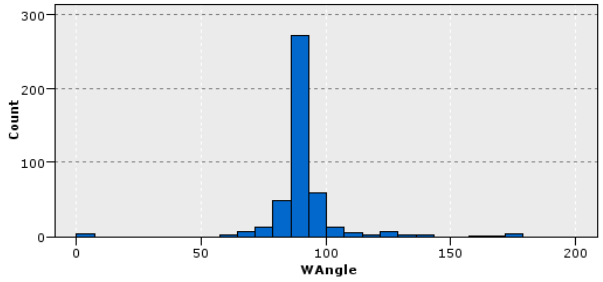


**Figure 4-VI-3:** Histogram of WAngle attribute measured for defects caused by spherical particles

In the scatter plot matrix of all the attributes, WAngle does not show any noticeable relationship with the rest of the attributes in the dataset. The Pearson's correlation coefficient

between this attribute and the rest of the attributes is close to zero. WAngle does not help us in recognizing or clustering the film defects. Therefore, it was eliminated from the dataset.

### 1.2 Defect Angle in Polarized Light Images (DAngle)

DAngle reports the angle between the major axis of the film defect captured with polarized light setup and the image vertical axis. In other words, it shows the elongation direction of the defect as shown by the polarized light. The situation here is very similar to the WAngle case explained above. The value of DAngle depends on the direction of the major axis of the object, which is influenced by small variations in object's shape. Examples are shown in Figure 4-VI-4.


**Figure 4-VI-4: (Left)** Polarized light image of R24R30D06-1 and R24R30D06-2 defects caused by ceramic microspheres, **(Right)** Mask image of these defects. As you can see, these particles and defects are very similar. (The major axes of these defects are approximately parallel with the image vertical axis. The major axis of the top defect is slightly tilted to the right hand side of the vertical and the other is slightly tilted to its left hand side. This resulted in the huge difference in the DAngle values.)

As you can see, DAngle is easily influenced by the small shape variations. Besides, knowing DAngle is simply not enough recognize or cluster the defects. Basic descriptive statistics of DAngle are available in Table 4-VI-1. Its histogram is shown in Figure 4-VI-5.

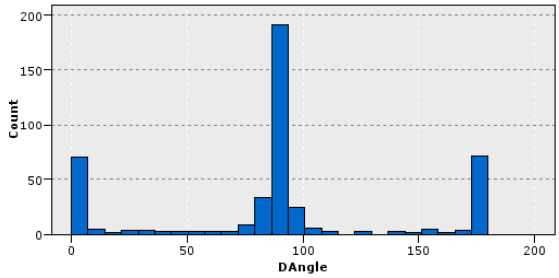


**Figure 4-VI-5:** Histogram of DAngle attribute for defects caused by spherical particles.

Figure 4-VI-5 shows that majority of DAngle values are 0, 90, or 180 degrees. The scatter plot matrix shows that DAngle is not related to any of the attributes in this dataset. Similar results are shown by the correlation coefficient analysis between this attribute and other attributes in the dataset. The presence of DAngle is not informative towards clustering the defects and so it was eliminated.

### 1.3 Particle Angle in Polarized Light Images (PAngle)

PAngle measures the angle between the major axis of particle in a polarized light image with the vertical axis of the image. This attribute provides valuable information in recognizing the orientation of significantly elongated particles. However, like WAngle and DAngle, its value greatly depends on object shape and is easily changed by particle contour fluctuations. (Table 4-VI-1 and Figure 4-VI-6)

As expected, majority of particles have PAngle values of 0, 180, or 90. In addition, the scatter plot matrix does not show any significant relationship between PAngle and other attributes in the Round dataset.

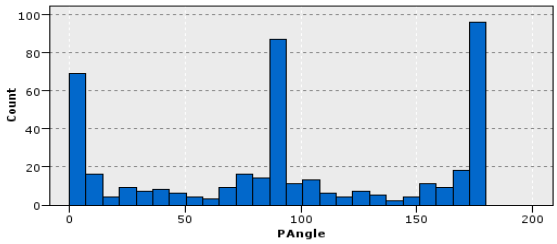


**Figure 4-VI-6:** Histogram of PAngle for defects caused by spherical particles.

PAngle, similar to DAngle and WAngle, is influenced by a number of factors such as boundary fluctuations and sample alignment during imaging. Therefore, for a dataset that does not include elongated particles such as glass fibers, PAngle was eliminated from the dataset.

---

## 2.0 Density Standard Deviation Attributes

### 2.1 **Particle and Defect Density Standard Deviation in Polarized Light Images (PDensity-(stdev) and DDensity-(stdev))**

PDensity-(stdev) and DDensity-(stdev) report the standard deviation of the grayscale pixel values (pixel density) in the segmented particle and defect objects in the polarized light images, respectively. The appearance of a particle or defect in a polarized light image depends on the type of particle (or defect), its interaction with polarized light, film thickness, film orientation, noise, etc. Therefore, it is hard to pinpoint the cause of intensity variation of a particle (or defect) in these images.

In addition, scatter plot matrix and correlation coefficient analysis of the dataset showed no significant relationship between PDensity-(stdev) and DDensity-(stdev) and other attributes in the dataset. The variation in these attributes cannot be clearly linked to defect appearance. Therefore, PDensity-(stdev) and DDensity-(stdev) were eliminated for the dataset.

### 2.2 Defect Density Standard Deviation in Interferometric Images WDensity-(stdev)

The grayscale Wyko images represent the surface profile of the film in the deformed area. In other words, each pixel value represents the film surface height at that point. WDensity-(stdev) represents the standard deviation of the height values in the segmented deformed areas. Its value is highly affected by noise (caused by interferometer, camera, etc.) and the details of the surface profile.

The scatter plot matrix and the correlation analysis do not show a significant relationship between this attribute and others in the dataset. The information provided by this attribute is not useful in distinguishing between defects. WDensity-(stdev) was removed form the dataset.

## 3.0 Minimum and Maximum Density Attributes for Particles and Defects in Polarized Light and Interferometric Images

**(PDensity-(min), PDensity-(max), DDensity-(min), DDensity-(max), WDensity-(min), and WDensity-(max))**

**Density-(min):** Minimum grayscale pixel value (intensity) of the object of interest.

**Density-(max):** Maximum grayscale pixel value (intensity) of the object of interest.

Object of interest could be segmented particle in a polarized light image, segmented defect in a polarized light image, or segmented surface deformation in an interferometric image.

Minimum and maximum intensity values represent the value of only one pixel of the segmented object. Therefore, they may not be representative of the overall intensity of the object. They are strongly influenced by noise or abnormally high or low pixel values. The scatter plot matrix of the entire dataset and the correlation coefficient analysis did not show a significant relationship between these attributes and any other attribute in the dataset. As a result, all six attributes were eliminated from the dataset.

## 4.0 Margination Attributes

**(PMargination, DMargination, and WMargination)**

**Margination:** Relative distribution of object intensity between the center and margin, with larger values from brighter centers. A value of 0.33 indicates a homogeneous object.

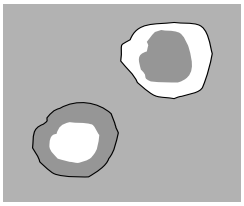

Because of the way Margination is calculated for an object and the complexity and diversity of the particle and defects appearances in this dataset, interpreting and comparing Margination values is very difficult. It is not a clear and reliable object property. For example, in Figure 4-VIII-7, relating the reported Margination values for segmented particles

and defects in polarized light images (PMargination and DMargination) (Table 4-VI-3) to the visual appearance of particles and defects is not straightforward.

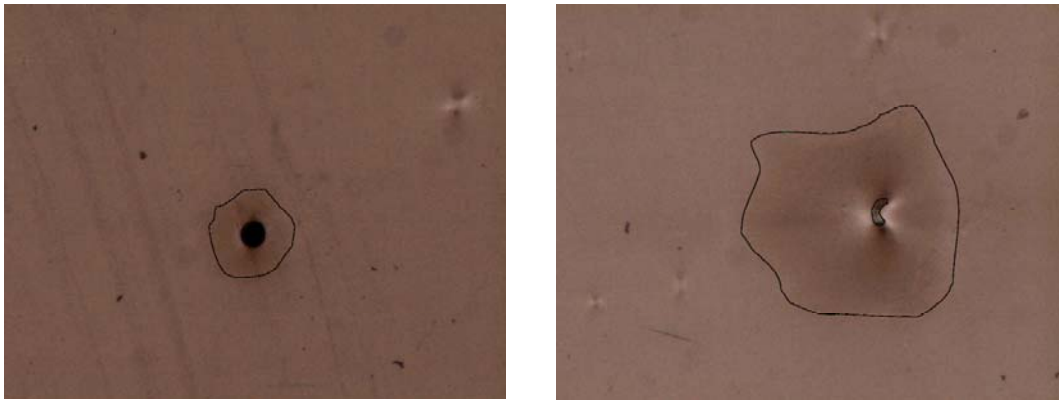

**Figure 4-VI-7: (Left)** Polarized light image of R19R30D09 with particle and defect outlines, **(Right)** Polarized light image of R19R30D03 with particle and defect outlines.

**Table 4-VI-3:** Margination data of the particles and defects shown in Figure 4-VI-7.

| Defect | PMargination | DMargination | WMargination |
|---|---|---|---|
| R19R30D03 | 0.378 | 0.350 | 0.265 |
| R19R30D09 | 0.924 | 0.344 | 0.300 |

As you can see slight intensity variations can change the Margination value. In addition, its value greatly depends on the distribution of intensity values in the center and margin of an object. The objects in this dataset do not show a pattern that can be easily characterized or clustered based on Margination.

The scatter plot matrix and correlation coefficient analysis did not show a significant relationship between these three attributes and the rest of the attributes in the dataset. In conclusion, based on the complexity of the overall intensity distribution of the objects in this dataset and the results of the bivariate analysis, PMargination, DMargination, and WMargination were eliminated.

## 5.0 Density Summation Attributes

**(PDensity-(sum), DDensity-(sum), and WDensity-(sum)**

PDensity-(sum) DDensity-(sum) are equal to the summation of the pixel values for segmented particles and defects in grayscale polarized light images. WDensity-(sum) shows the summation of the intensity values for the segmented deformed region of a grayscale surface profile image. Here, intensity values are in fact normalized surface height values.

The size of the segmented objects and their intensity distribution considerably affect the final value of these attributes. Therefore, this piece of information by itself is not enough to help us recognize the particles or defects. A more reliable and meaningful attribute is the average density of an object (PDensity-(mean), DDensity-(mean), and WDensity-(mean)) which is already included in the dataset. In addition, the scatter plot matrix of the dataset did not show a noticeable relationship between these and the other attributes present in the dataset. As a result, the three of them were eliminated from the dataset.

## 6.0 Area/Box Attributes

**(PArea/Box, DArea/Box, and WArea/Box)**

Area/Box measures the ratio between area of an object and area of its bounding box. It is a shape attribute and is can help detect certain shape changes. PArea/Box represents the value of this attribute for a segmented particle in a polarized light image; DArea/Box shows the same property for the segmented defect in the same type of image. WArea/Box shows the same property measured for the segmented deformed area in an interferometric image.

Figure 4-VI-8 provides an illustration and two examples from our own dataset. The value of Area/Box ratio increases as the object covers more and more of the bounding box. This attribute may be helpful in comparing specific known shapes but it may not be useful when dealing with many different and complicated shapes. Area/Box ratio of an object is influenced by many factors that may or may not be important in clustering. It is possible to have objects of completely different shapes and areas have the same Area/Box ratio.

The correlation coefficient analysis showed that these attributes are somewhat correlated with a few other attributes in the dataset. However, their corresponding scatter plots did not reveal a clear relationship. Based on this analysis and knowing the complexity of the objects in our dataset, all three attributes were eliminated from the dataset.

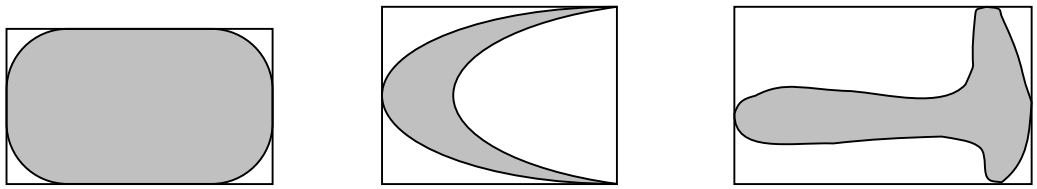

High Area/Box Value  Low Area/Box Value  Low Area/Box Value

**(a)**

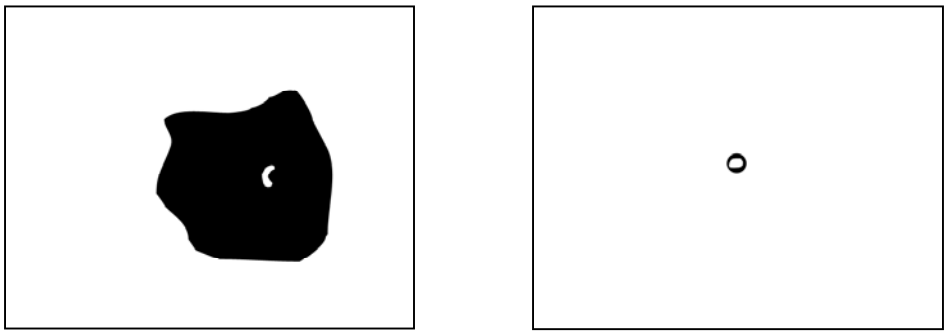

**R19R30D3:**
Particle: PArea/Box = 0.584
Defect: DArea/Box = 0.773

**R18R30D15:**
Particle: PArea/Box = 0.888
Defect: DArea/Box: 0.767

**(b)**

**Figure 4-VI-8: (a)** A schematic diagram of objects with different shapes and their bounding boxes. The center and right objects have low Area/Box values because of their shapes. However, we cannot learn more about these shape differences knowing the Area/Box value. **(b)** Two masks of polarized light images and their PArea/Box and DArea/Box values. Note how PArea/Box values are different but DArea/Box values are close.

## 7.0 Perimeter Attributes

**Perimeter, Perim-(convex), Perim-(ellipse), and Perim-(ratio)**

The definition of the properties measured by these attributes is available in Appendix 4-II.

### 7.1 PPerimeter, PPerim-(ellipse), PPerim-(convex), and PPerim-(ratio)

These attributes show the value of different perimeter related attributes for the segmented particles in the polarized light images.

Different ways of measuring object perimeter is a way to help us distinguish between objects having different shapes. For example, for an approximately round object, all three measures of perimeter will be very close and perimeter ratio will be close to 1. However, for more complex shapes, different values for these perimeter measures are expected.

Figure 4-VI-9 shows a scatter plot of only perimeter related attributes for the particle section. PPerimeter, PPerim-(convex) and PPerim-(ellipse) demonstrate a clear linear relationship. The correlation coefficient values are shown in Table 4-VI-4. Therefore, two of these three attributes are clearly redundant.

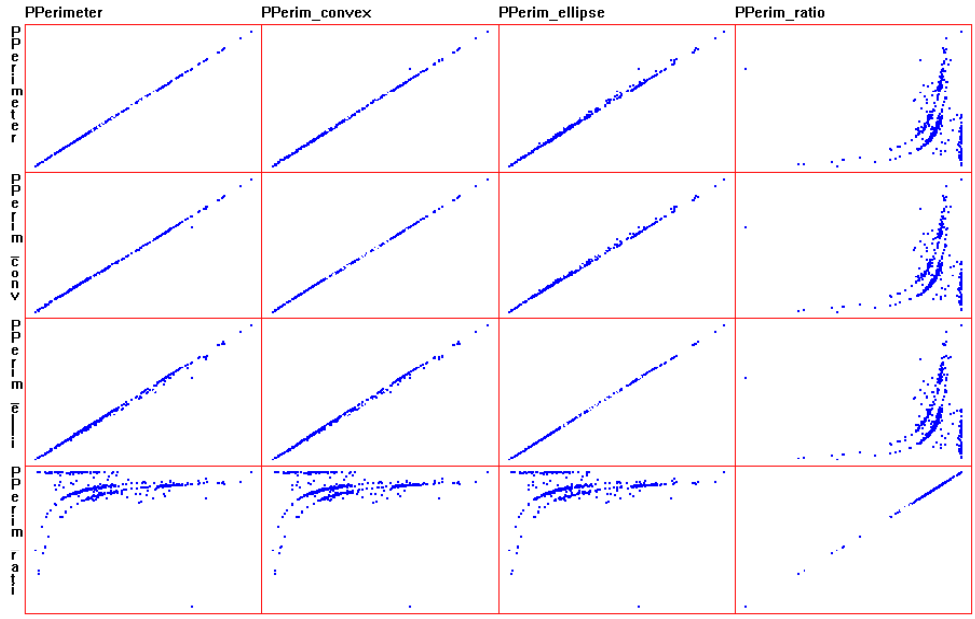


**Figure 4-VI-9:** Scatter plot matrix of the perimeter related attributes of segmented particles for the defects caused by spherical particles.

**Table 4-VI-4:** Correlation coefficients of the perimeter attributes in the Particle section.

| Variable 1 | Variable 2 | Correlation |
|---|---|---|
| PPerim-(convex) | PPerimeter | 0.984 |
| PPerim-(ellipse) | PPerimeter | 0.944 |
| PPerim-(ellipse) | PPerim-(convex) | 0.983 |

Perimeter is the actual length of the object outline, including the length of all the small bumps and valleys on the outline, which will increase the measured value. Convex perimeter, on the other hand, is based on a convex outline drawn around the object. The shape of the convex outline depends on the details of the object's shape and may not be easy to visualize. As a result, PPerim-(convex) and PPerim-(ellipse) were removed.

In Figure 4-VI-9, PPerim-(ratio) shows a more complicated relationship with perimeter measures. This attribute is a shape descriptor. However, considering the complexity of the objects shapes in this dataset, it is not possible to recognize the shape based on its value. As a result, PPerim-(ratio) was also removed from the dataset.

The correlation coefficient analysis shows a high level of correlation between PPerimeter and several other attributes in the dataset. Table 4-VI-5 shows a list of attribute pairs with a correlation coefficient greater than 90%. The strong correlation between these attributes was also confirmed by the strong linear trends visible in their scatter plot matrix.

**Table 4-VI-5:** A list of attributes with high correlation coefficient with PPerimeter.

| Variable 1 | Variable 2 | Correlation |
|---|---|---|
| PFeret-(mean) | PPerimeter | 0.984 |
| PFeret-(max) | PPerimeter | 0.967 |
| PRadius-(max) | PPerimeter | 0.967 |
| PSize-(length) | PPerimeter | 0.965 |
| PDiameter-(max) | PPerimeter | 0.964 |
| PBox-width | PPerimeter | 0.953 |
| PDiameter-(mean) | PPerimeter | 0.934 |
| PAxis-(major) | PPerimeter | 0.925 |

## 7.2 DPerimeter, DPerim-(convex), DPerim-(ellipse), and DPerim-(ratio)

Perimeter attributes for the segmented defects in polarized light images show a pattern similar to the one explained for the segmented particles. Figure 4-VI-10 shows the scatter plot matrix of the perimeter attributes for the segmented defects caused by the spherical particles. Table 4-VI-6 has the related correlation coefficients.

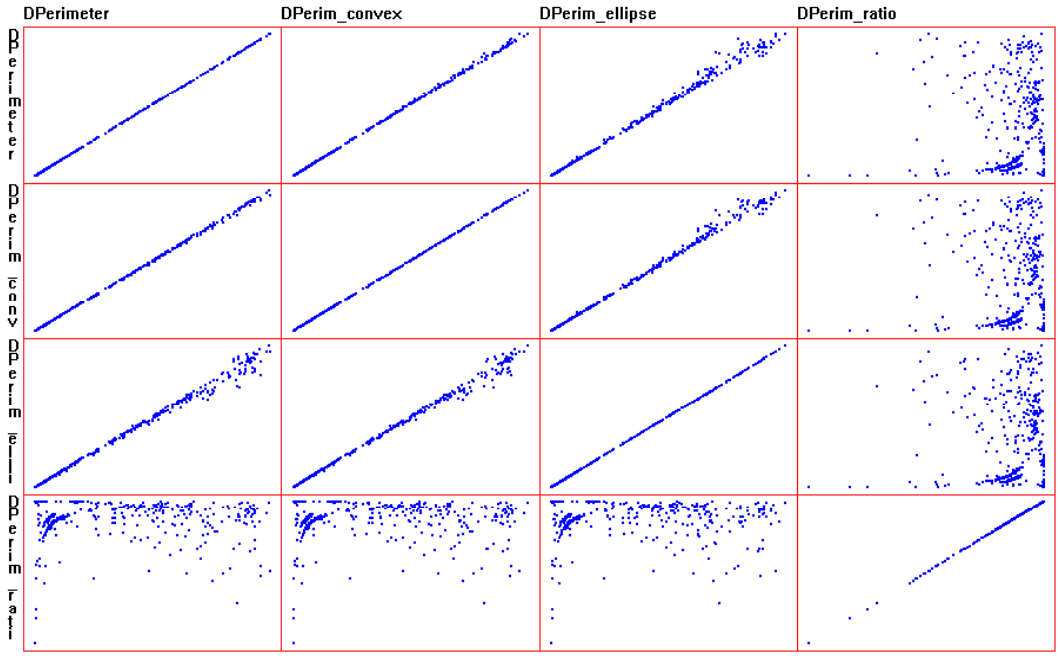


**Figure 4-VI-10:** Scatter plot matrix of the perimeter related attributes for the segmented defects caused by spherical particles.

**Table 4-VI-6:** Correlation coefficients of the perimeter attributes for the segmented defects caused by spherical particles.

| Variable 1 | Variable 2 | Correlation |
|---|---|---|
| DPerim-(convex) | DPerimeter | 0.999 |
| DPerim-(ellipse) | DPerimeter | 0.994 |
| DPerim-(ellipse) | DPerim-(convex) | 0.997 |

As you can see from the scatter plot matrix and the correlation coefficients, the defect perimeter attributes (except DPerimeter-(ratio)) are linearly correlated. Therefore, at least

two of these attributes are redundant. Based on this observation and attribute definition, DPerim-(convex) and DPerim-(ellipse) were removed from the dataset.

DPerim-(ratio) is not significantly correlated with any attributes in the dataset. In addition, it may be influenced by unimportant contour fluctuations and is not very helpful in clustering the objects. As a result, it was eliminated from the dataset.

7.3 WPerimeter, WPerim-(convex), WPerim-(ellipse), and WPerim-(ratio)

For segmented defects in the interferometric images, the scatter plots of the perimeter related attributes have more scatter. This is mainly due to higher complexity of the objects outlines in these images. A scatter plot matrix of these attributes is shown in Figure 4-VI-11. Related correlation coefficients are shown in Table 4-VI-7.

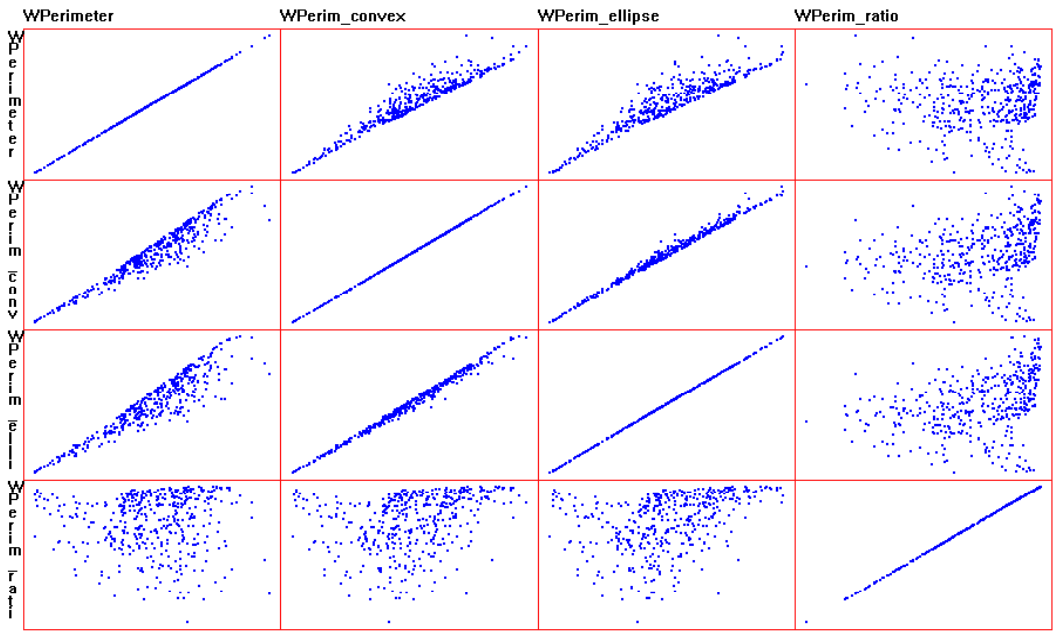


**Figure 4-VI-11:** Scatter plot matrix of the perimeter related attributes for the segmented defects in interferometric images and caused by spherical particles.

**Table 4-VI-7:** Correlation coefficients of the perimeter attributes in the Wyko section.

| Variable 1 | Variable 2 | Correlation |
|---|---|---|
| WPerim-(convex) | WPerimeter | 0.970 |
| WPerim-(ellipse) | WPerimeter | 0.949 |
| WPerim-(ellipse) | WPerim-(convex) | 0.995 |

A relatively good linear relationship exists between WPerim-(ellipse) and WPerim-(convex). However, the scatter in the WPerimeter scatter plots is considerably higher. Segmented deformed areas in interferometric images have very rough edges and this is the main factor causing the difference between reported values for WPerimeter, WPerim-(convex) and WPerim-(ellipse). Segmented Particles and Defects in the polarized light images have much smoother outlines.

Knowing the attribute definition, trends shown by the scatter plots, and the reason for the observed differences, WPerim-(convex), WPerim-(ellipse), and WPerim-(ratio) were eliminated from the dataset.

## 8.0 Average Caliper Length Attributes

Feret-(mean) reports the average caliper (feret) length of an object.

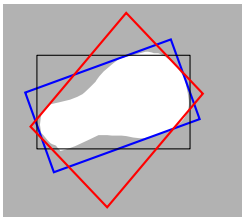

Its value depends on the overall shape of the object and also on fluctuations of the object contour. For a round object, the value of Feret-(mean) would be close to the actual feret measure of the object.

In our dataset, considering the complexity and variety of object shapes, knowing the average feret value is not useful. Relating the average value to the appearance of the objects is not straightforward. Another drawback is that objects of different shapes may have similar average feret values. In other words, Feret-(mean) is not a reliable representative of objects with complex shapes.

In addition, Feret-(mean) is highly correlated with a number of other attributes in all three sections of the dataset. Among the scatter plots, PFeret-(mean) and DFeret-(mean) show a strong linear relationship with PPerimeter and DPerimeter, respectively.

Based on the property measured by these attributes, ease of understanding, and the fact that Perimeter is kept in the dataset for all the objects, it was concluded that PFeret-(mean), DFeret-(mean), and WFeret-(mean) were redundant and they were eliminated from the dataset.

## 9.0 Average Diameter Attributes

Diameter-(mean) reports the average length of the diameters measured at two-degree intervals joining two outline points and passing through the centroid.

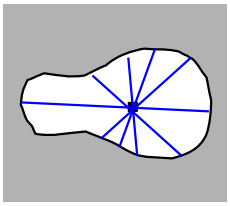

This attribute may be helpful in special cases, for example when trying to cluster mostly round objects of different sizes. However, interpreting its value in the case of objects with complicated shapes seems difficult. For example, the Diameter-(mean) value reported for a thin elongated object is not representative of the object shape. Objects of different sizes

and shapes may have approximately same average diameter values. (Figure 4-VI-12) The use of this attribute in object clustering or classification depends on the shape of the objects available in a dataset.

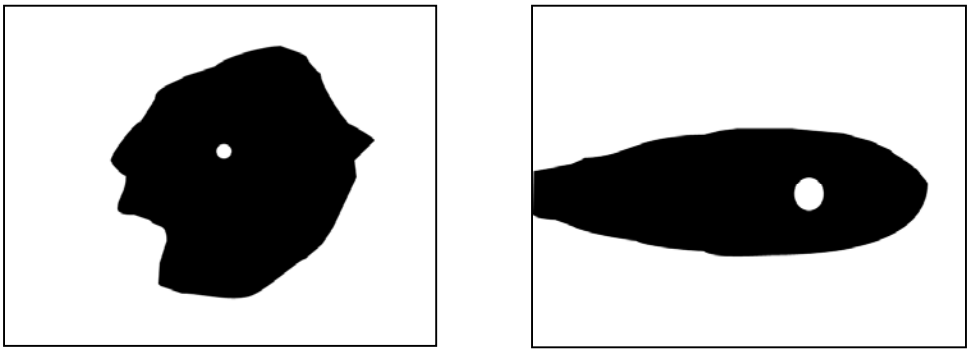

DDiameter-(mean) = 856.96 DDiameter-(mean) = 855.15

**Figure 4-VI-12: (Left)** Mask image obtained from the polarized light image of R17R30D7 defect, **(Right)** Mask image obtained from the polarized light image of R23R90D7 defect. These defects have completely different shapes, however their DDiameter-(mean) values are quite close.

## 10.0 Attribute Related to the Bounding Box of an Object

**(Box-(width), Box-(height), Box-X/Y)**

These attributes report the properties of each object's imaginary bounding box. (Appendix 4-II) Box-(width) and Box-(height) attributes measure the dimensions of the object's bounding box. The important point is that the sides of the bounding box are parallel with the image axes. Therefore, the reported Box-(width) and Box-(height) values depend on the orientation of the object with respect to the image axes. Figure 4-VI-13 illustrates that rotating the object resulted in a significant change in its Box-(width) and Box-(height) values.

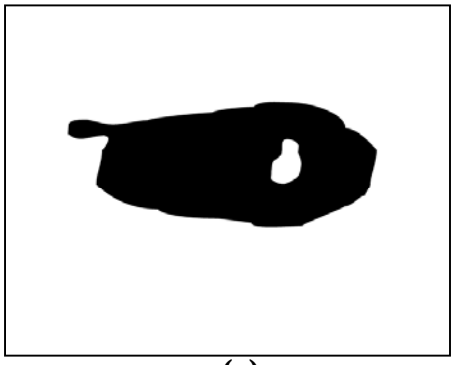

**(a)**

**(b)**

| **Particle** | **Box-(width)** | **Box-(height)** |
|---|---|---|
| Original | 105.25 | 157.17 |
| After Rotation | 152.86 | 122.24 |
| **Defect** | | |
| Original | 1087.55 | 439.08 |
| After Rotation | 784.34 | 910.58 |

**(c)**

**Figure 4-VI-13: (a)** Mask image of the polarized light image of "D19D60-D9" defect. **(b)** The same mask image after 45 ° rotation. **(c)** Box-(width) and Box-(height) values measured for the segmented particles and defects in parts (a) and (b) are listed in this table. The values of these attributes changed significantly after the object was rotated.

Slight variations in the film sample alignment in defect characterization step are possible. Therefore, due to the significant effect of object orientation in image matrix on the dimensions of object's bounding box, the dimensions of the bounding box are not reliable. Box-(width), Box-(height), and Box-X/Y measured for particles and defects in polarized light images and in interferometric images were removed from the dataset.

## 11.0 Axis-(major), Diameter-(max), Size-(length), and Feret-(max)

The definition of the properties measured by these attributes is available in Appendix 4-III. They measure similar object properties. Therefore, depending on the object shape, their

values could be quite close or very different. Each pair of attributes shows high correlation and a strong linear trend. This is observed for all the spherical particles and their corresponding defects both in polarized light and in interferometric images. (Figures 4-VI-14 to 16)

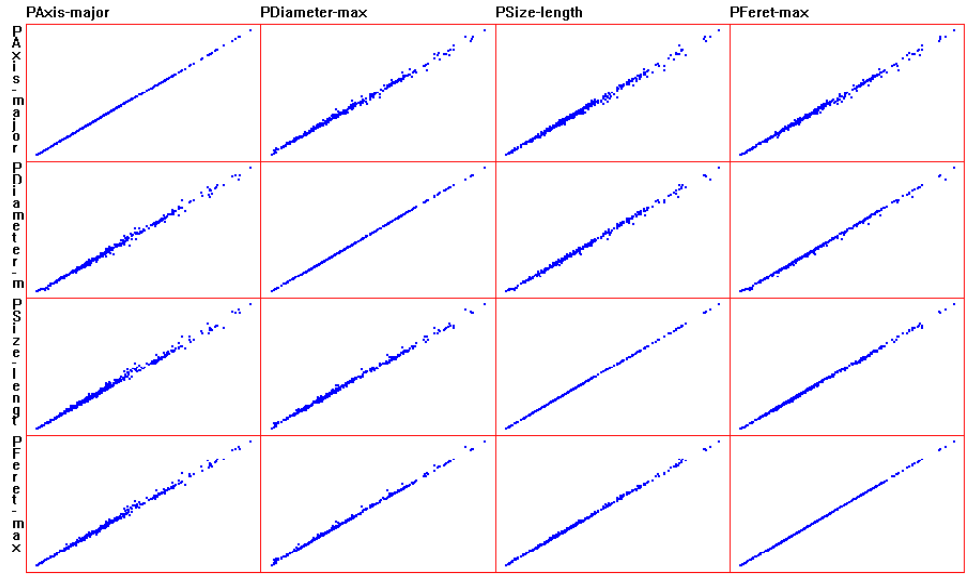


**Figure 4-VI-14:** Scatter plot matrix of four dimensional attributes of the segmented spherical particles in polarized light images.

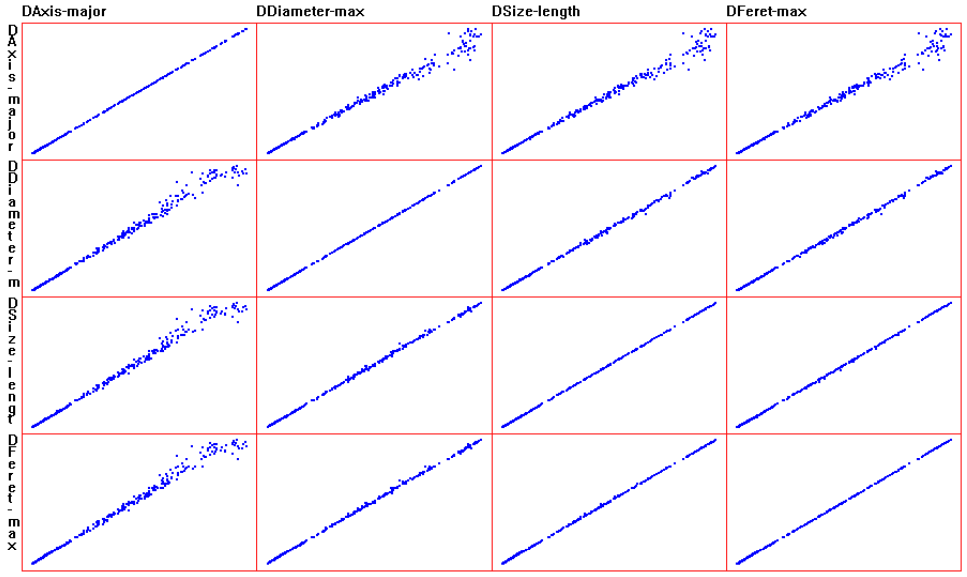


**Figure 4-VI-15:** Scatter plot matrix of four dimensional attributes of the segmented defects caused by spherical particles in polarized light images.

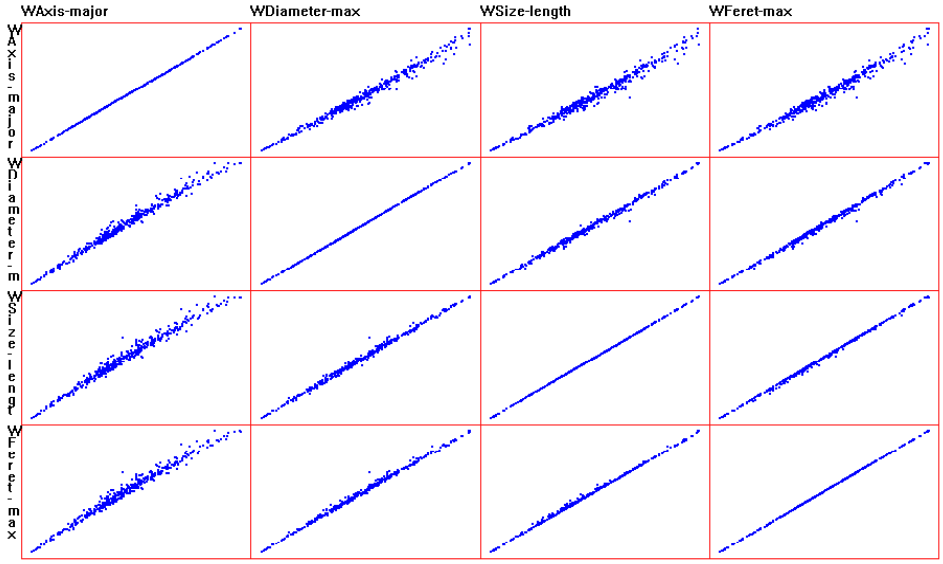


**Figure 4-VI-16:** Scatter plot matrix of four dimensional attributes of the segmented defects caused by spherical particles in interferometric images.

Most of the scatter plots show a strong and clear linear relationship between attribute pairs, this is not unexpected knowing the attributes definitions. Therefore, three of the four attributes are redundant in each section.

Axis-(major) is the major axis of the ellipse equivalent to the object with the same moments of 0, 1, and 2 as object. It may be difficult to visualize where the ellipse is drawn around an object. The measured Diameter-(max) value depends on the location of the object's centroid. Feret-(max) and Size-(length) are very similar attributes and are strongly correlated in each section of the data. Therefore, a simple and easy-to-understand attribute to quantify the length of an object is Size-(length). The other three attributes were eliminated for all the objects.

## 12.0 Axis-(minor), Diameter-(min), Size-(width), and Feret-(min)

The definition of the properties measured by these attributes is available in Appendix 4-II. The relationship between each pair of this group of attributes was investigated for all objects, segmented particles and defects in polarized light images and segmented defects in interferometric images. Correlation coefficient of each pair of attributes was above 0.96 for all the defects and particles. The scatter plot matrices of these attributes for particles and defects are shown in Figures 4-VI-17 to 4-VI-19.

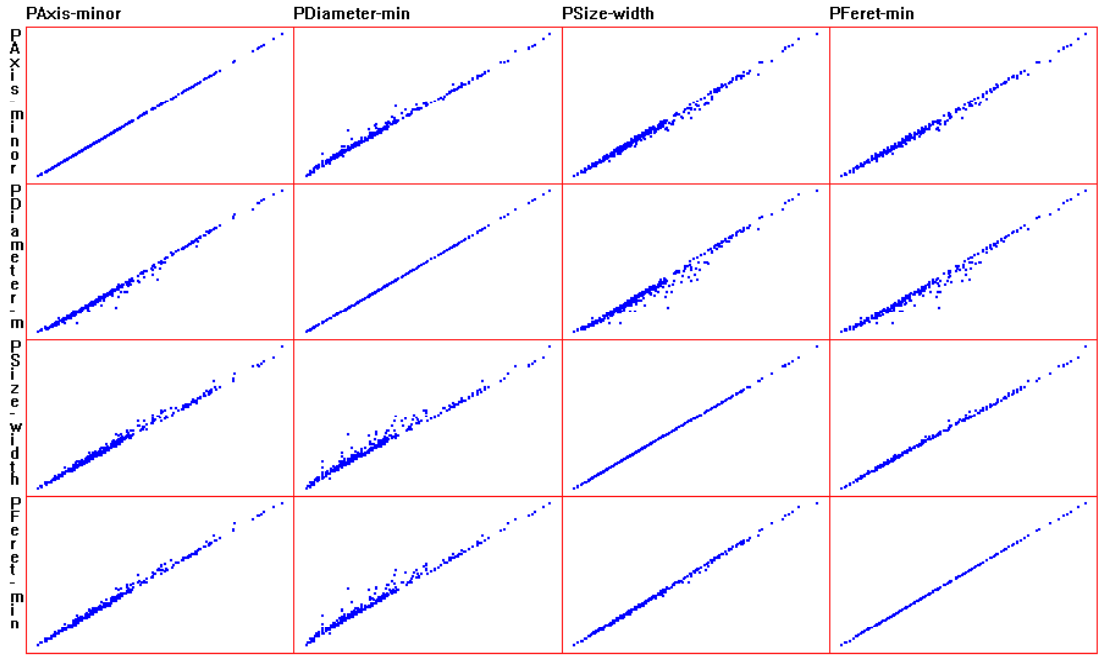


**Figure 4-VI-17:** Scatter plot matrix of four attributes of the segmented particles caused by spherical particles in polarized light images.

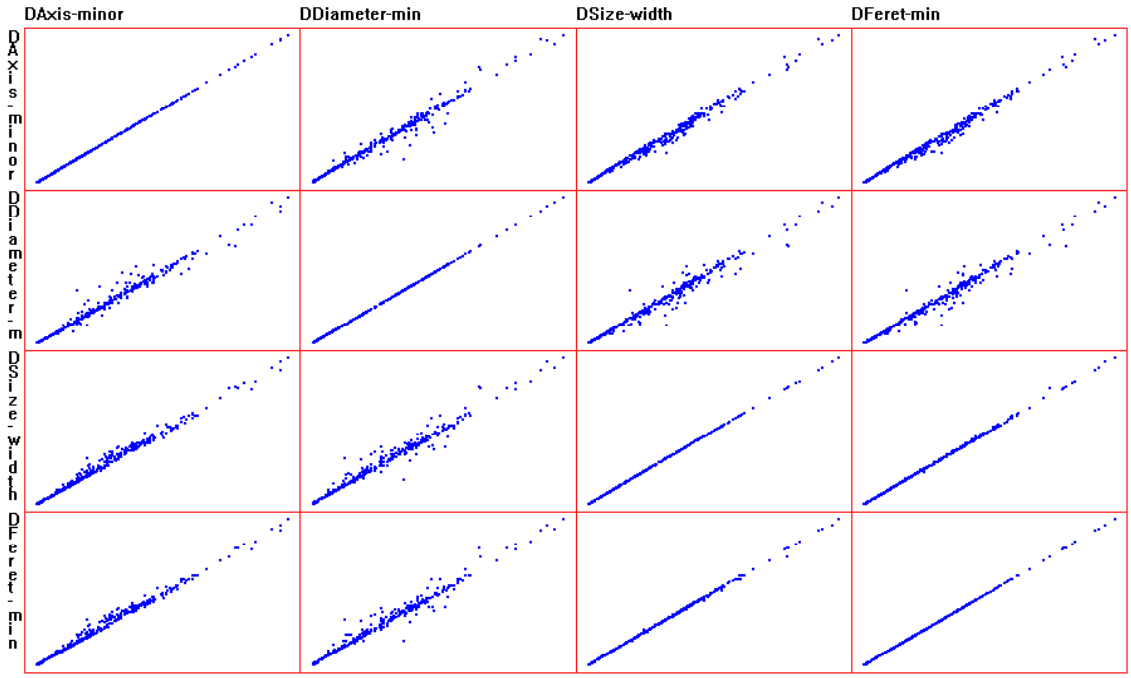


**Figure 4-VI-18:** Scatter plot matrix of four attributes of the segmented defects caused by spherical particles in polarized light images.

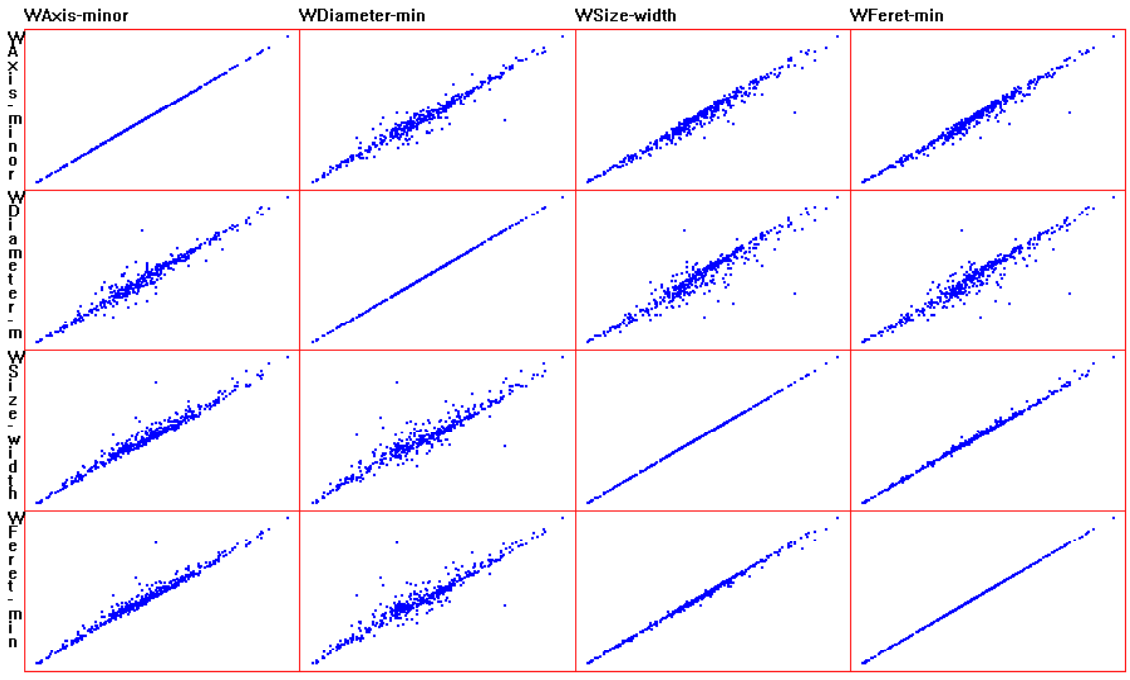


**Figure 4-VI-19:** Scatter plot matrix of four attributes of the segmented defects caused by spherical particles in interferometric images.

A linear relationship between each pair of attributes is visible for segmented particles and defects in polarized light images. (Figures 4-VI-17 and 4-VI-18) However, higher scatter in data points is visible on the same scatter plots for the interferometric images. (Figure 4-VI-19) This is because the segmented particles and defects in polarized light images have much smoother outlines.

Because of the similarity in the measured properties by these attributes, the high correlation among them, and the observed linear trend, it was concluded that for the objects in dataset, three of these attributes could be removed. As a result, Diameter-(min), Axis-(minor), and Feret-(min) attributes for all objects were removed.

## 13.0 Radius-(max), Radius-(min), and Radius-(ratio):

Radius-(max) and Radius-(min) report the maximum and minimum distance between each object's centroid pixel position and its perimeter. The scatter plot matrix for the entire dataset revealed a significant linear relationship between Radius-(max) and Size-(length) for all three object types. (Figure 4-VI-20 (a), (b), and (c)) In addition, a linear trend with more scatter was observed between Radius-(min) and Size-(width) attributes. (Figure 4-VI-20 (d), (e), and (f))

The values of radius attributes are dependent on the object's centroid location. Considering the complex shape of objects in this dataset, it seems that having Size-(width) and Size-(length) to represent the overall dimensions of an object is enough. Therefore, based on these points, Radius-(min) and Radius-(max) for all objects were eliminated from the three dataset.

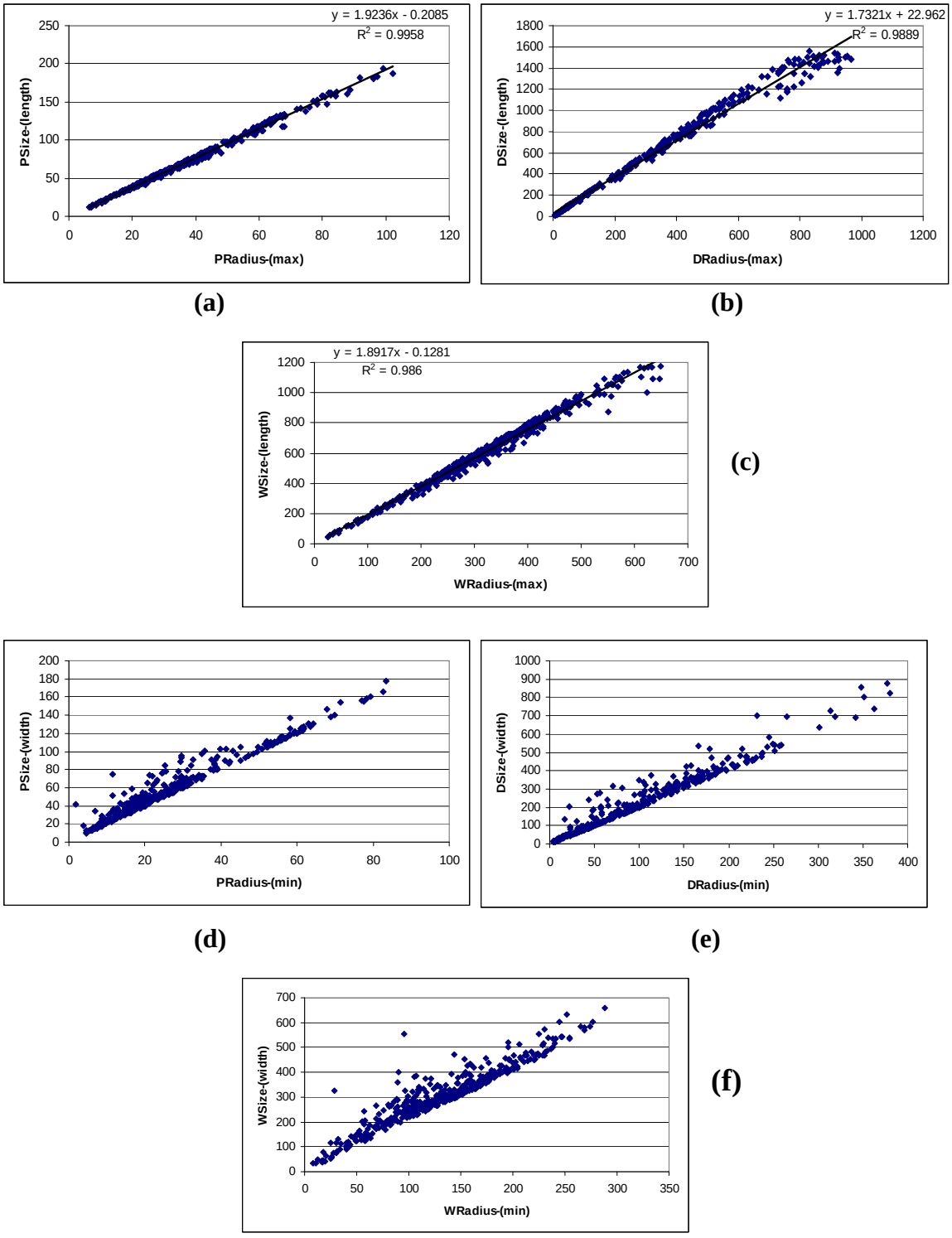


**Figure 4-VI-20: (a)** PSize-(length) vs. PRadius-(max), **(b)** DSize-(length) vs. DRadius-(max), **(c)** WSize-(length) vs. WRadius-(max), **(d)** PSize-(width) vs. PRadius-(min), **(e)** DSize-(width) vs. DRadius-(min), **(f)** WSize-(width) vs. (WRadius-(min

Radius-(ratio) is a measure of how elongated or round an object is. It does not show a significant correlation with any of the attributes in the dataset. Since, we already have Aspect ratio and Roundness attributes in the dataset which are also representative of the object elongation, Radius-(ratio) was eliminated from the dataset for all object types.

## Conclusions

The original dataset had 94 attributes plus 4 processing attributes (Image ID, Extruder Run No., and Roller Speed). A total of 72 attributes were deleted. This reduced the number of attributes to 22 plus 4 processing attributes. Table 4-VI-8 presents a list of the remaining attributes.

**Table 4-VI-8:** A list of the remaining attributes for each object.

| Processing Attributes | Particle Attributes from Polarized Light Imaging | Defect Attributes from Polarized Light Imaging | Defect Attributes from Interferometry |
|---|---|---|---|
| Particle Type | PArea | DArea | WArea |
| Roller Speed | PAspect | DAspect | WAspect |
| | PDensity- (mean) | DDensity- (mean) | WDensity- (mean) |
| | PPerimeter | DPerimeter | WPerimeter |
| | PRoundness | DRoundness | WRoundness |
| | PSize- (length) | DSize- (length) | WSize- (length) |
| | PSize- (width) | DSize- (width) | WSize- (width) |
| | | | WVolume |

**APPENDIX 4-VII:** Average Defect Height and Magnification for Wood Particles

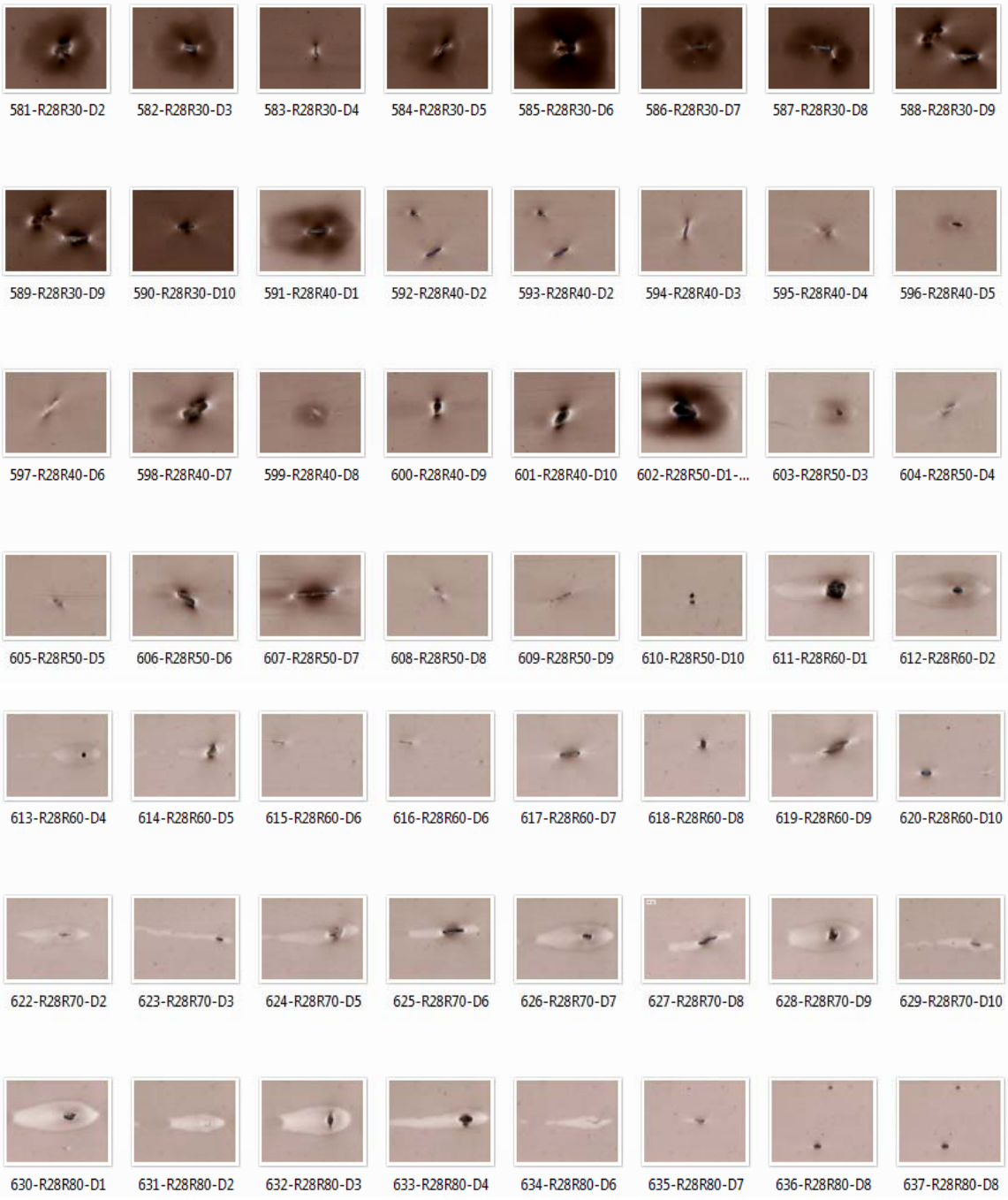


**Figure 4-VII-1:** Polarized light images of high average height and low average height defects caused by wood particles.

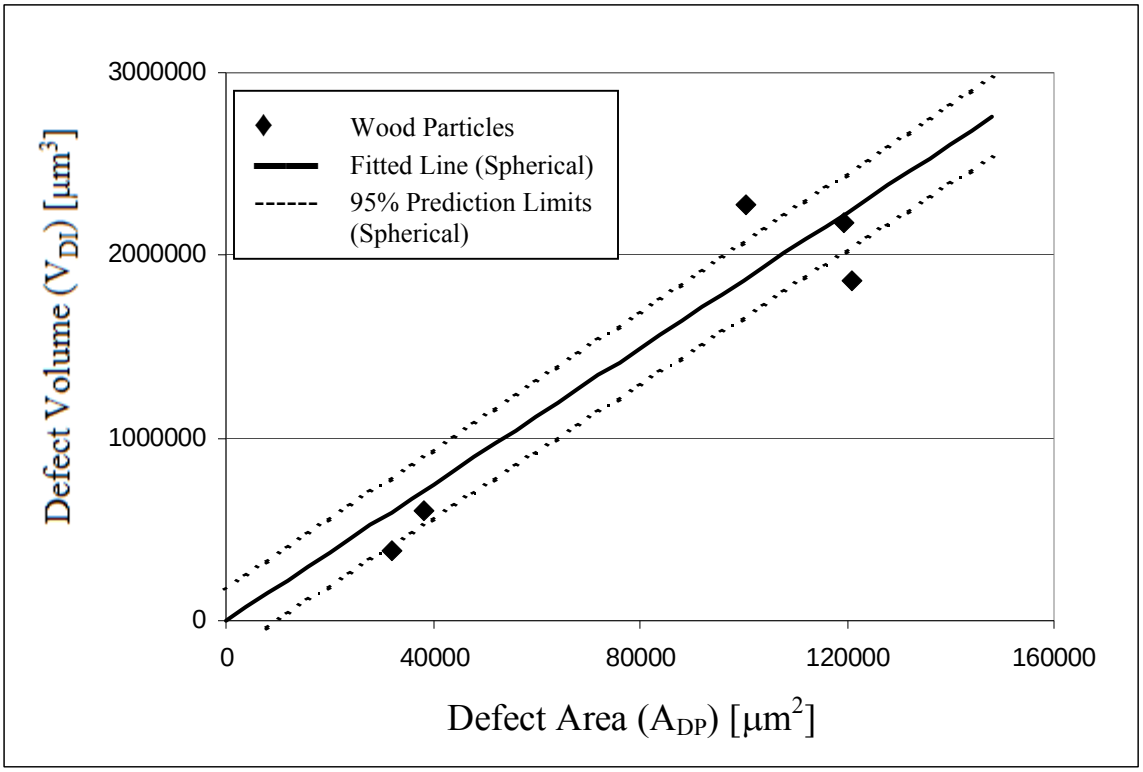


**Figure 4-VII-2:** Defect volume ($V_{DI}$) versus defect area ($A_{DP}$) for high average height defects caused by wood particles at a film thickness of 240.7 µm. This graph shows that the scanned high average height defects caused by wood particles at this film thickness level follow the trend shown by the defects caused by spherical particles.

Symbols: (♦) Wood particles, (—) The simple least squares line fitted to the spherical particle dataset at each film thickness. (---) 95% prediction limits for the dependent variable for a single future observation calculated from the spherical particle dataset at each film thickness.

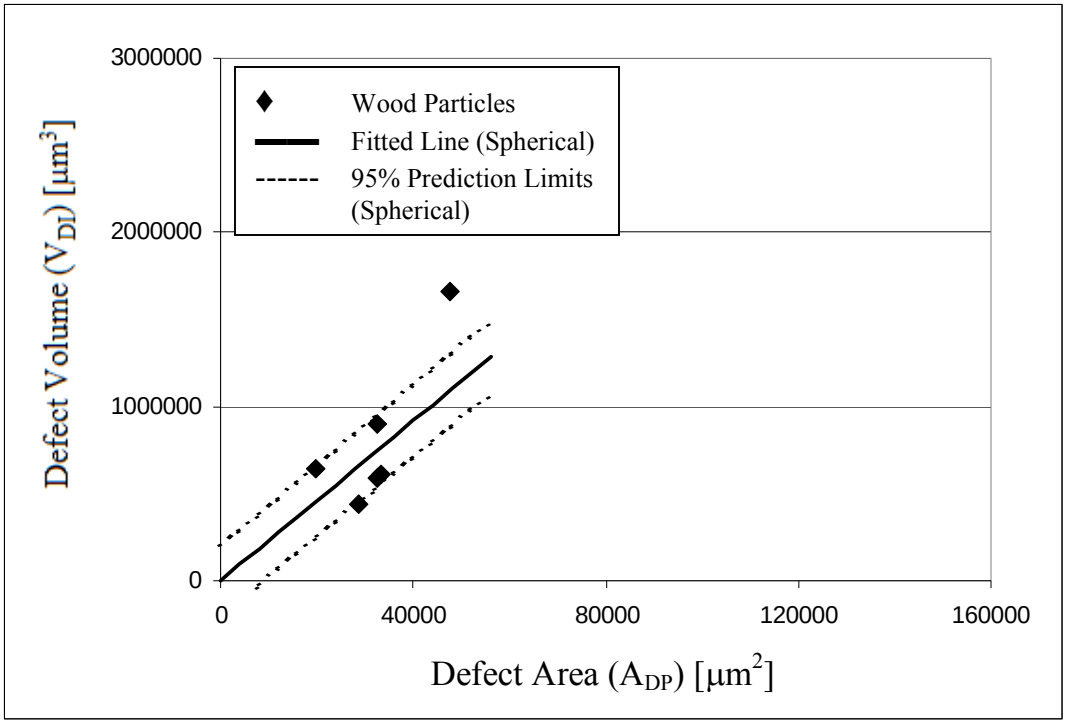


**Figure 4-VII-3:** Defect volume ($V_{DI}$) versus defect area ($A_{DP}$) for high average height defects caused by wood particles at a film thickness of 152.0 µm.

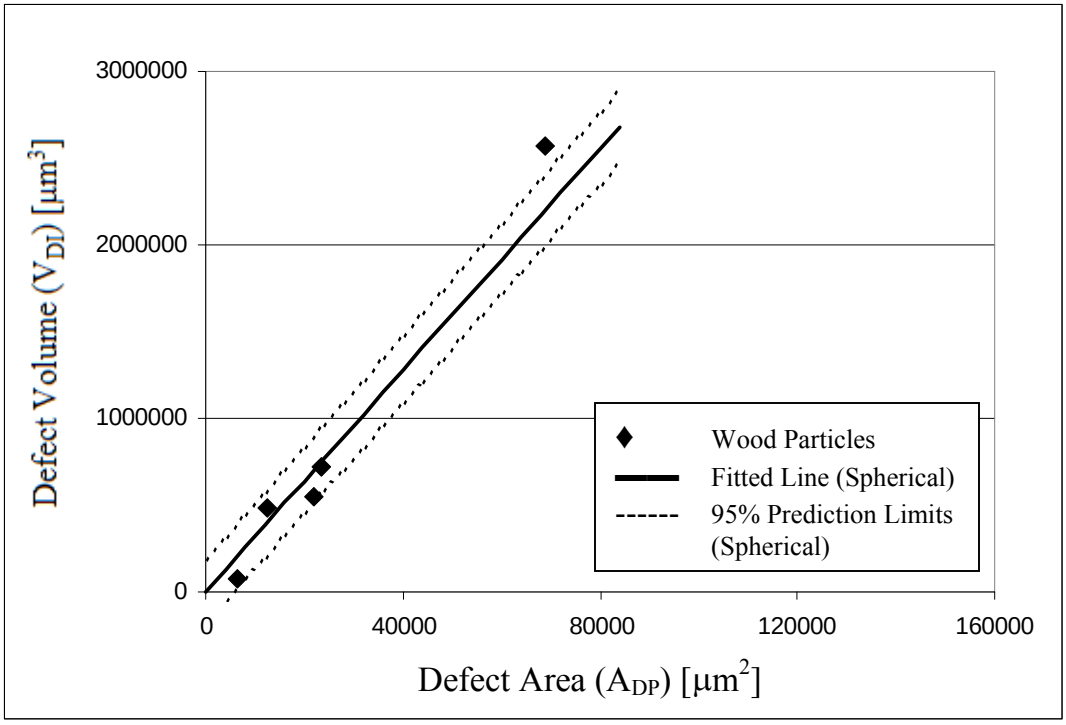


**Figure 4-VII-4:** Defect volume ($V_{DI}$) versus defect area ($A_{DP}$) for high average height defects caused by wood particles at a film thickness of 109.4 µm.

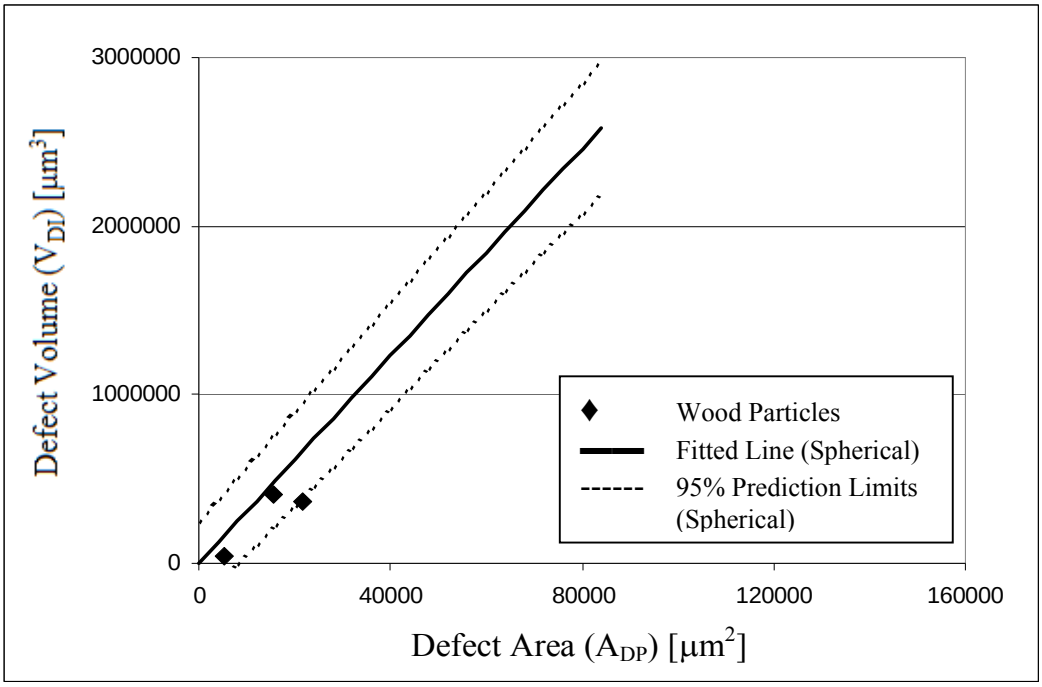


**Figure 4-VII-5:** Defect volume ($V_{DI}$) versus defect area ($A_{DP}$) for high average height defects caused by wood particles at a film thickness of 82.1 µm.

**Note:** The data does not contain any high average height defects caused by wood particles at 66.6 and 56.6 µm film thickness levels.

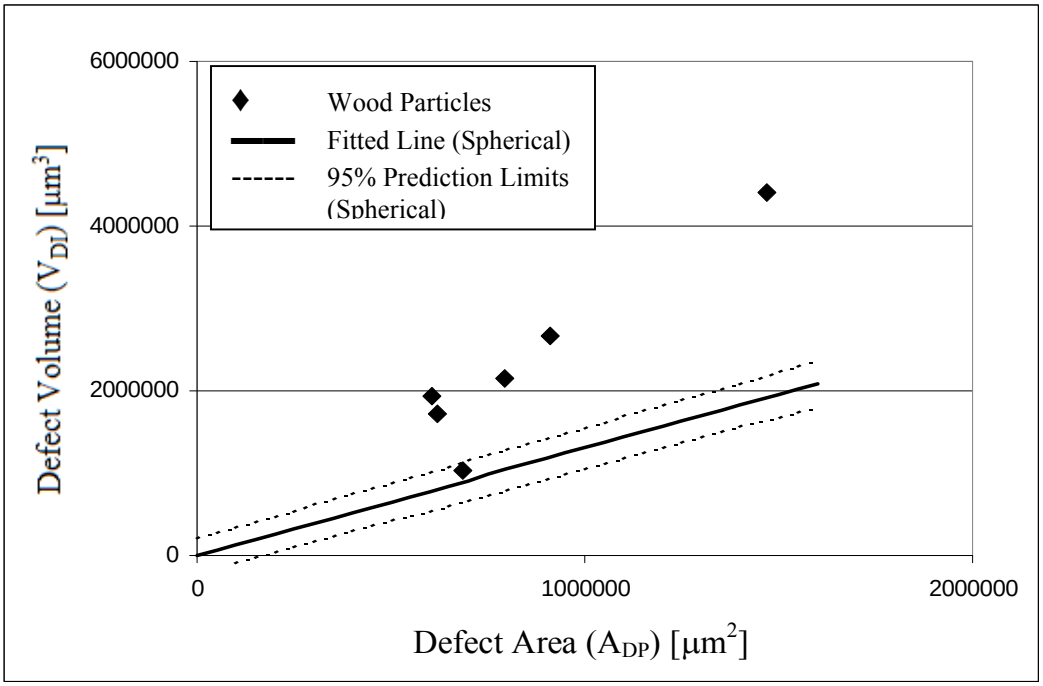


**Figure 4-VII-6:** Defect volume ($V_{DI}$) versus defect area ($A_{DP}$) for low average height defects caused by wood particles at a film thickness of 240.7 µm.

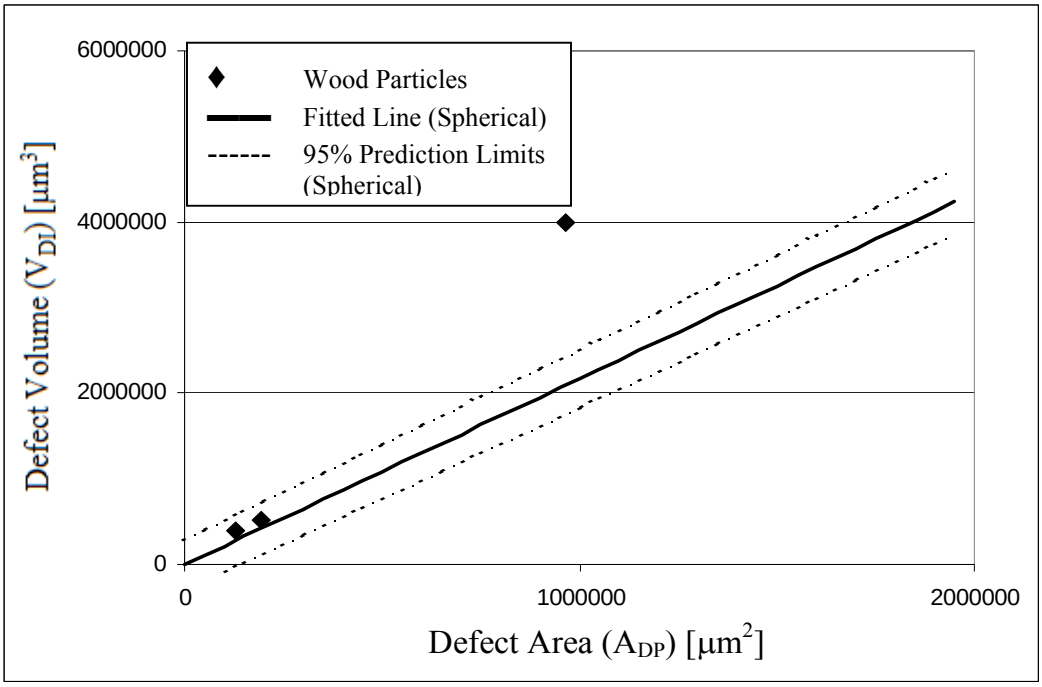


**Figure 4-VII-7:** Defect volume ($V_{DI}$) versus defect area ($A_{DP}$) for low average height defects caused by wood particles at a film thickness of 152.0 μm.

**Note:** The data does not contain any low average height defects caused by wood particles at 109.4 μm film thickness.

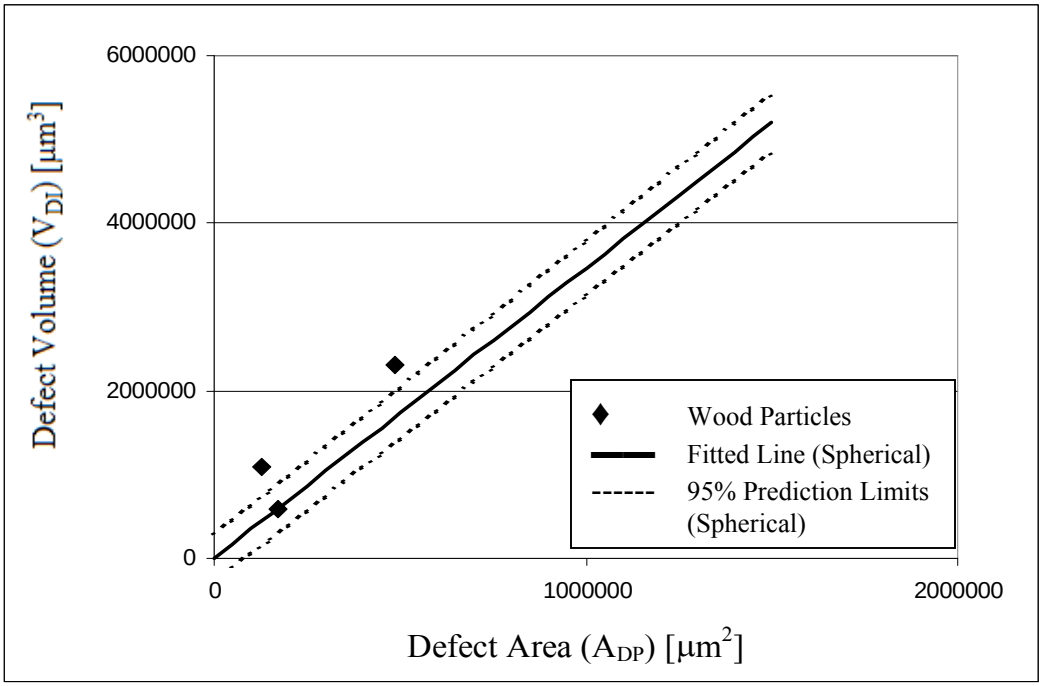


**Figure 4-VII-8:** Defect volume ($V_{DI}$) versus defect area ($A_{DP}$) for low average height defects caused by wood particles at a film thickness of 82.1 μm.

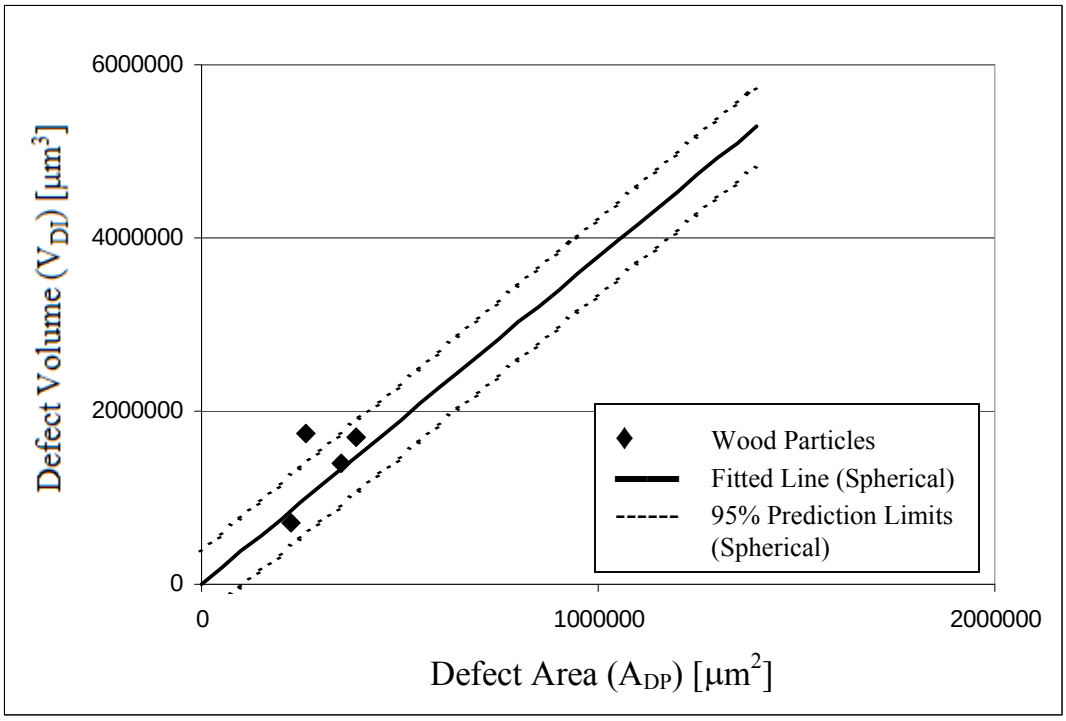


**Figure 4-VII-9:** Defect volume ($V_{DI}$) versus defect area ($A_{DP}$) for low average height defects caused by wood particles at a film thickness of 66.6 µm.

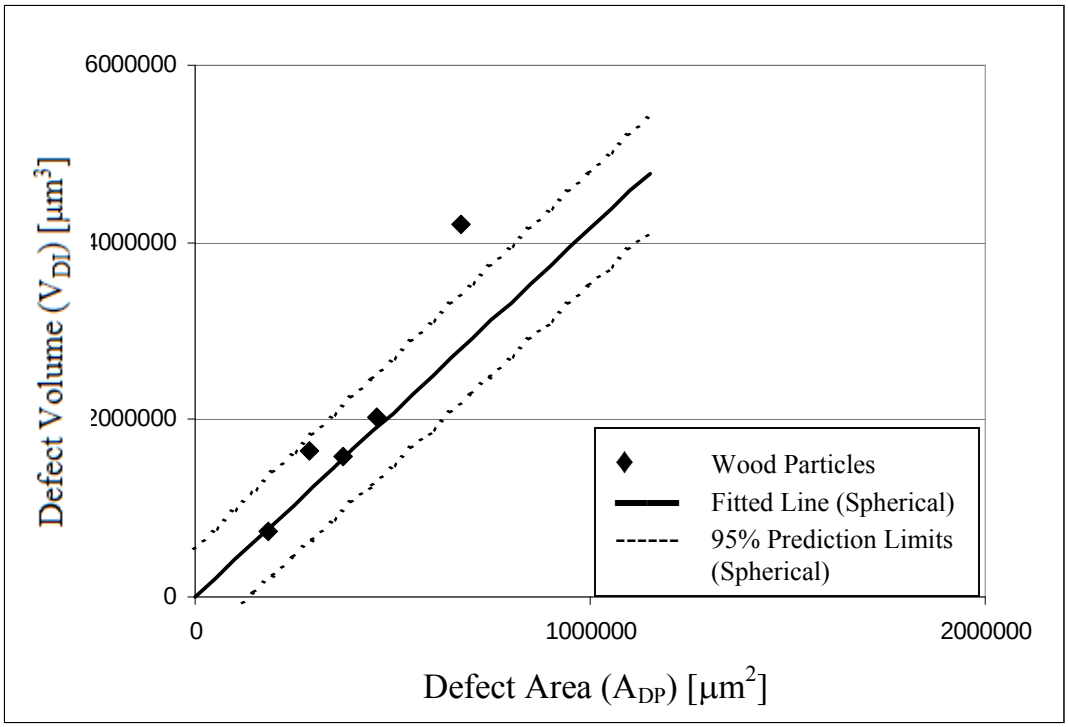


**Figure 4-VII-10:** Defect volume ($V_{DI}$) versus defect area ($A_{DP}$) for low average height defects caused by wood particles at a film thickness of 56.6 µm.

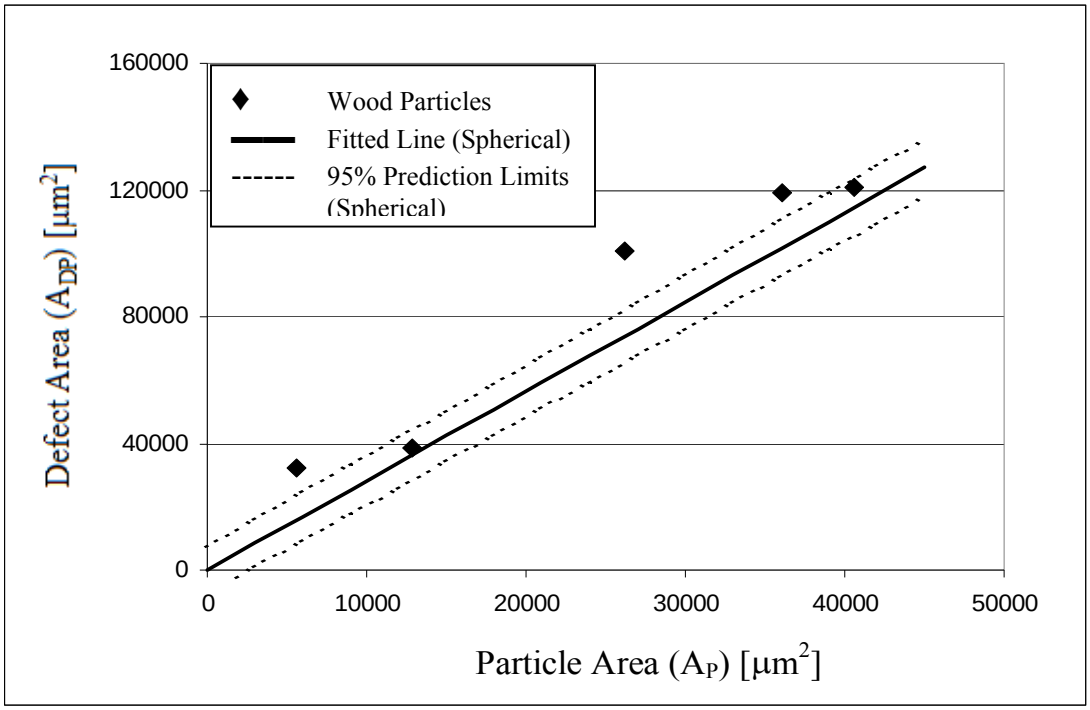


**Figure 4-VII-11:** Defect area ($A_{DP}$) versus particle area ($A_P$) for high average height defects caused by wood particles at 240.7 μm film thickness.

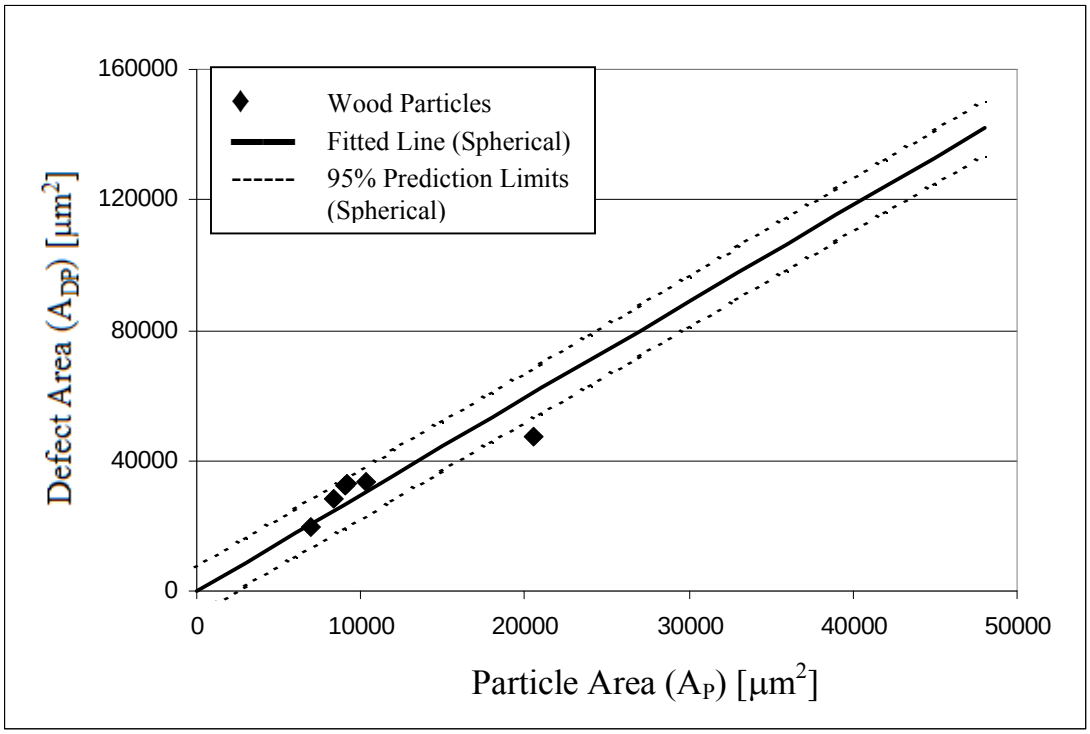


**Figure 4-VII-12:** Defect area ($A_{DP}$) versus particle area ($A_P$) for high average height defects caused by wood particles at 152.0 μm film thickness.

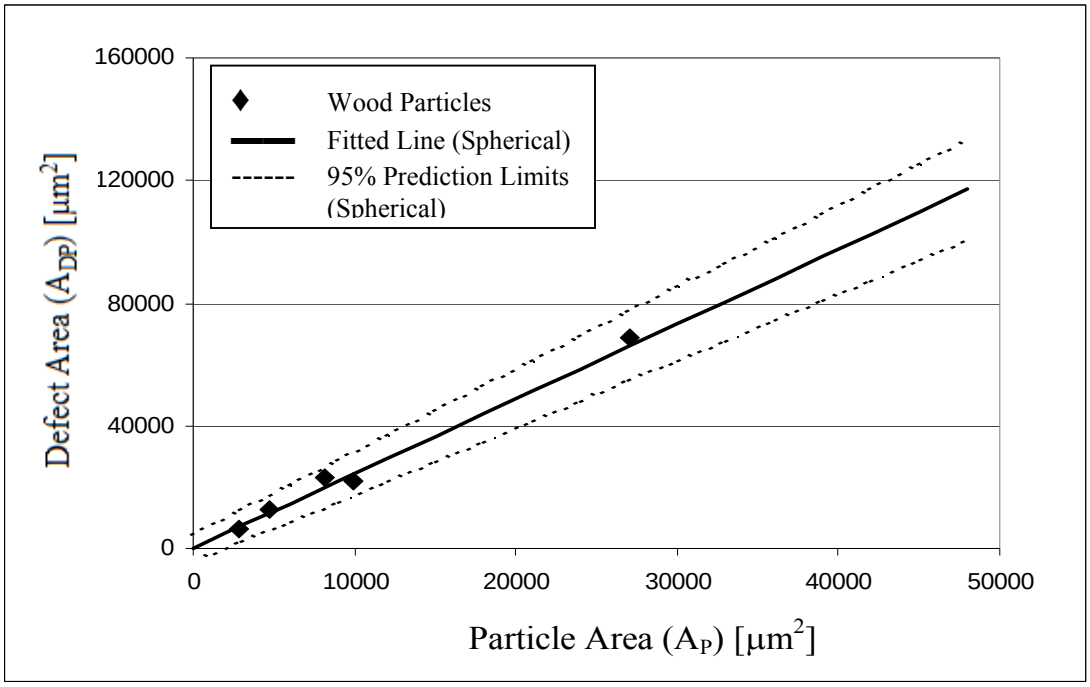


**Figure 4-VII-13:** Defect area ($A_{DP}$) versus particle area ($A_P$) for high average height defects caused by wood particles at 109.4 μm film thickness.

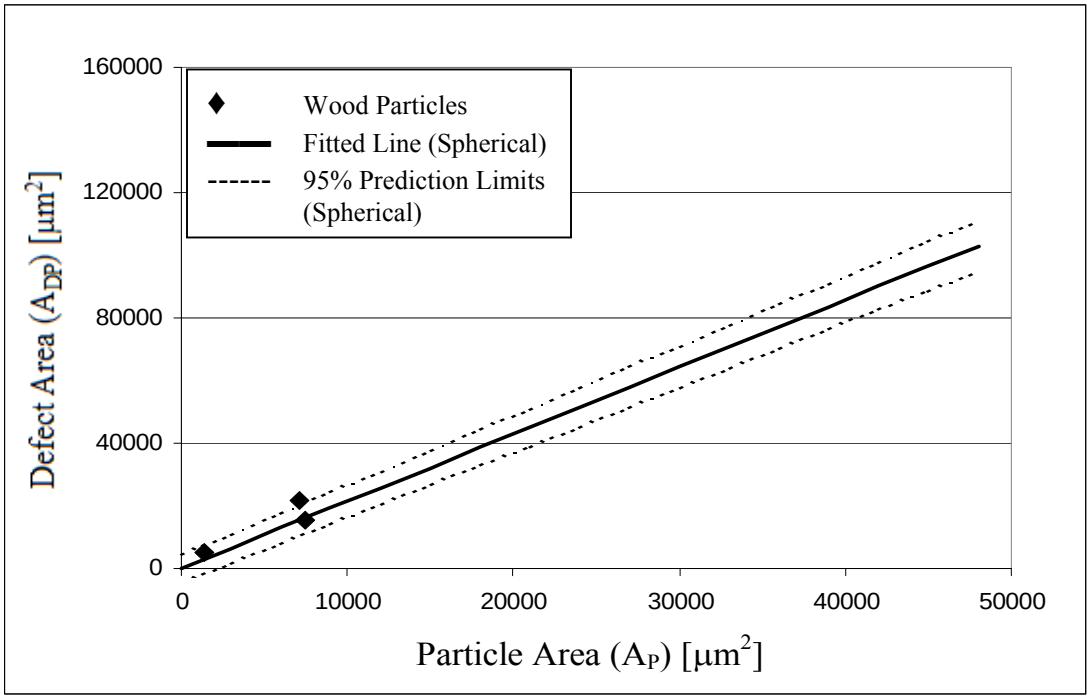


**Figure 4-VII-14:** Defect area ($A_{DP}$) versus particle area ($A_P$) for high average height defects caused by wood particles at 82.1 μm film thickness.

**Note:** The data does not contain any high average height defects caused by wood particles at 66.6 and 56.6 µm film thickness levels.

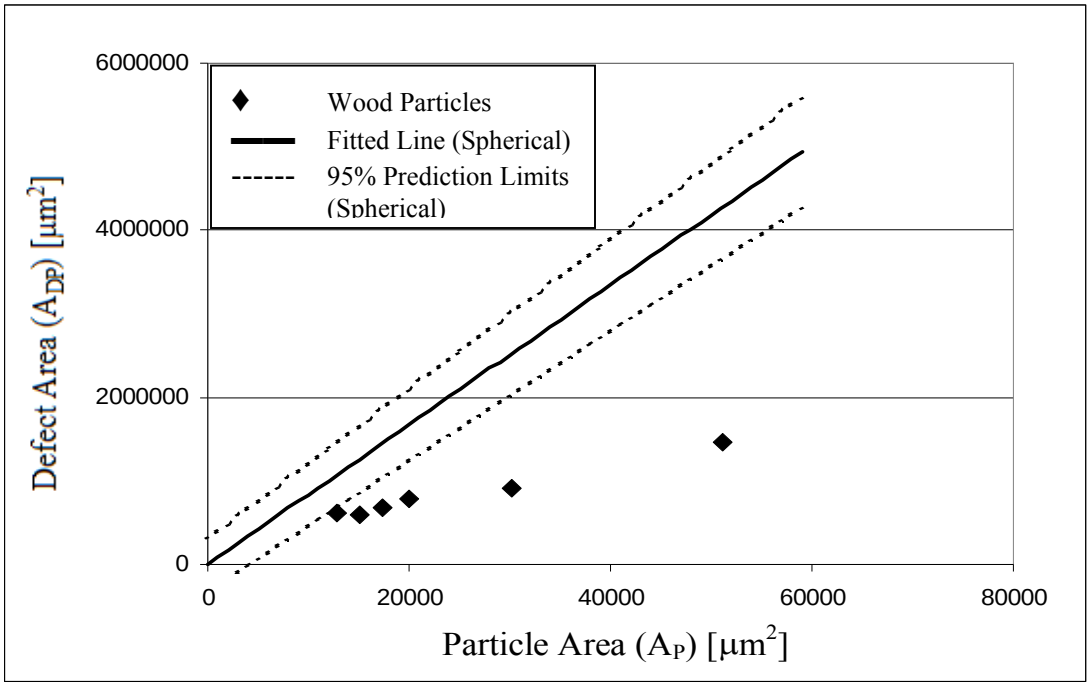


**Figure 4-VII-15:** Defect area ($A_{DP}$) versus particle area ($A_P$) for low average height defects caused by wood particles at 240.7 µm film thickness.

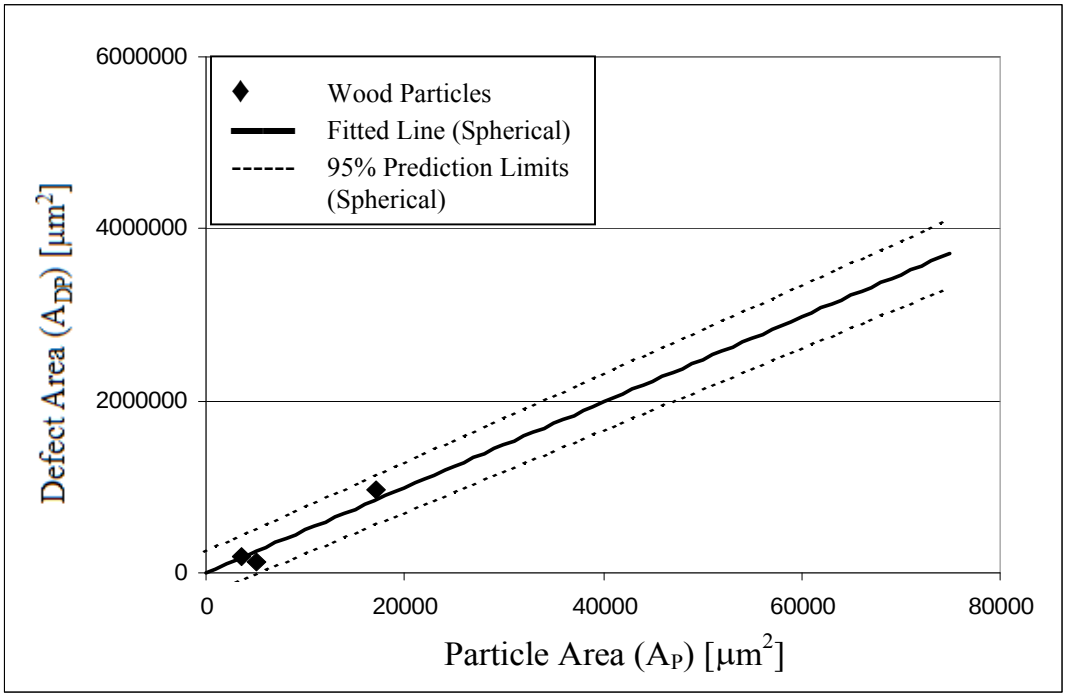


**Figure 4-VII-16:** Defect area ($A_{DP}$) versus particle area ($A_P$) for low average height defects caused by wood particles at 152.0 µm film thickness.

**Note:** The data does not contain any low average height defects caused by wood particles at 109.4 μm film thickness.

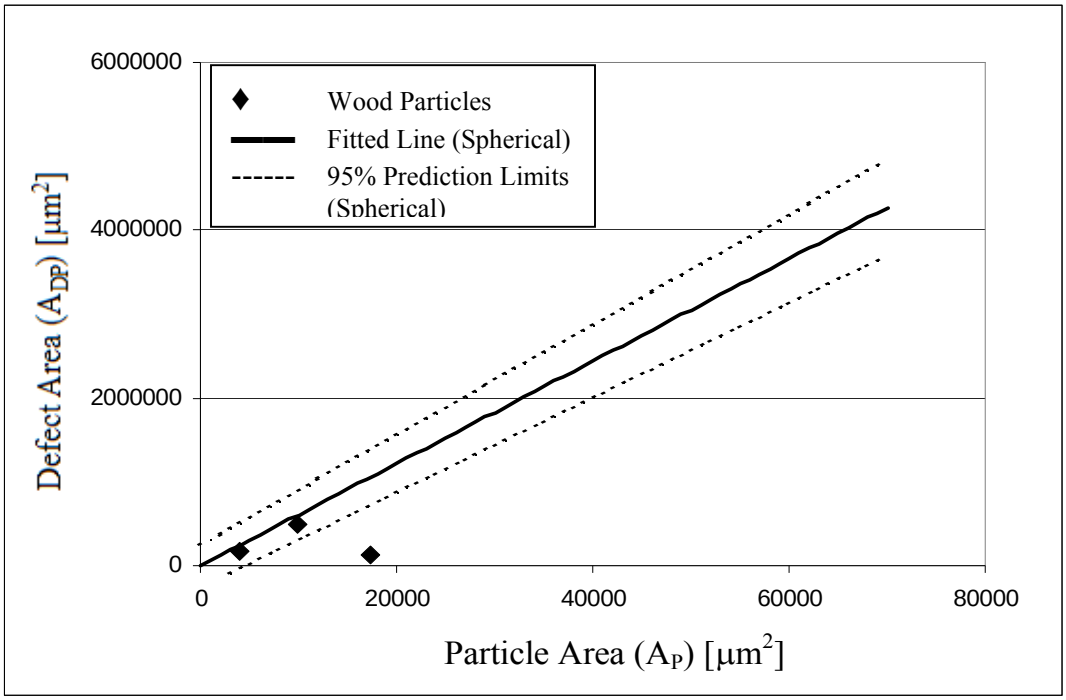


**Figure 4-VII-17:** Defect area ($A_{DP}$) versus particle area ($A_P$) for low average height defects caused by wood particles at 82.1 μm film thickness.

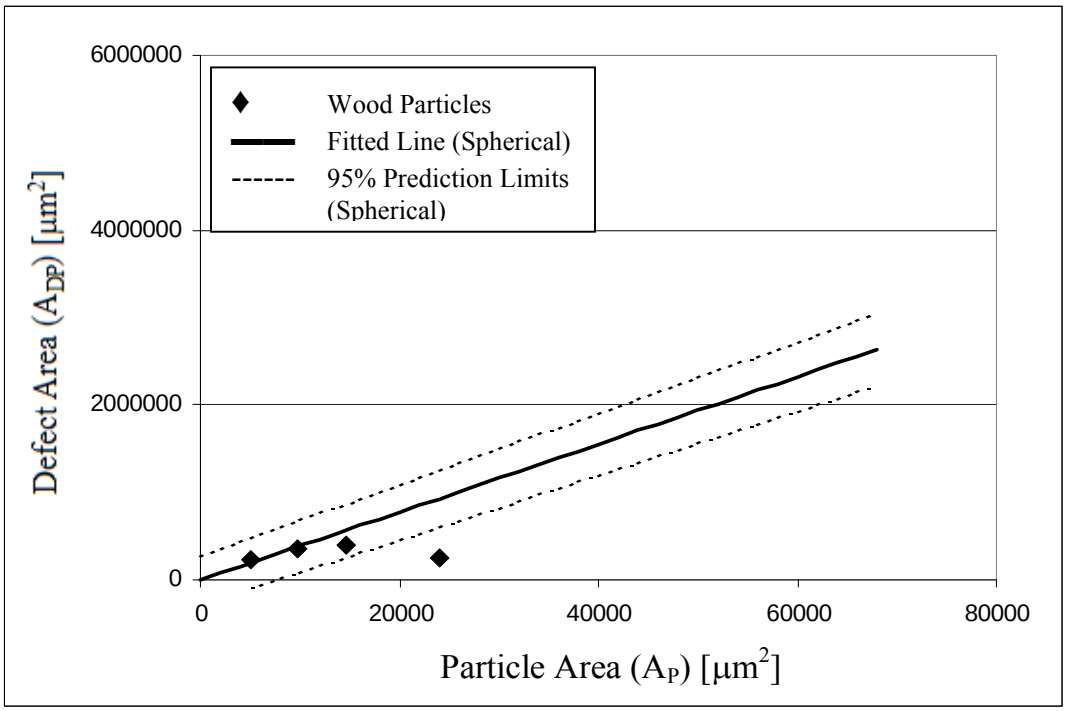


**Figure 4-VII-18:** Defect area ($A_{DP}$) versus particle area ($A_P$) for low average height defects caused by wood particles at 66.6 μm film thickness.

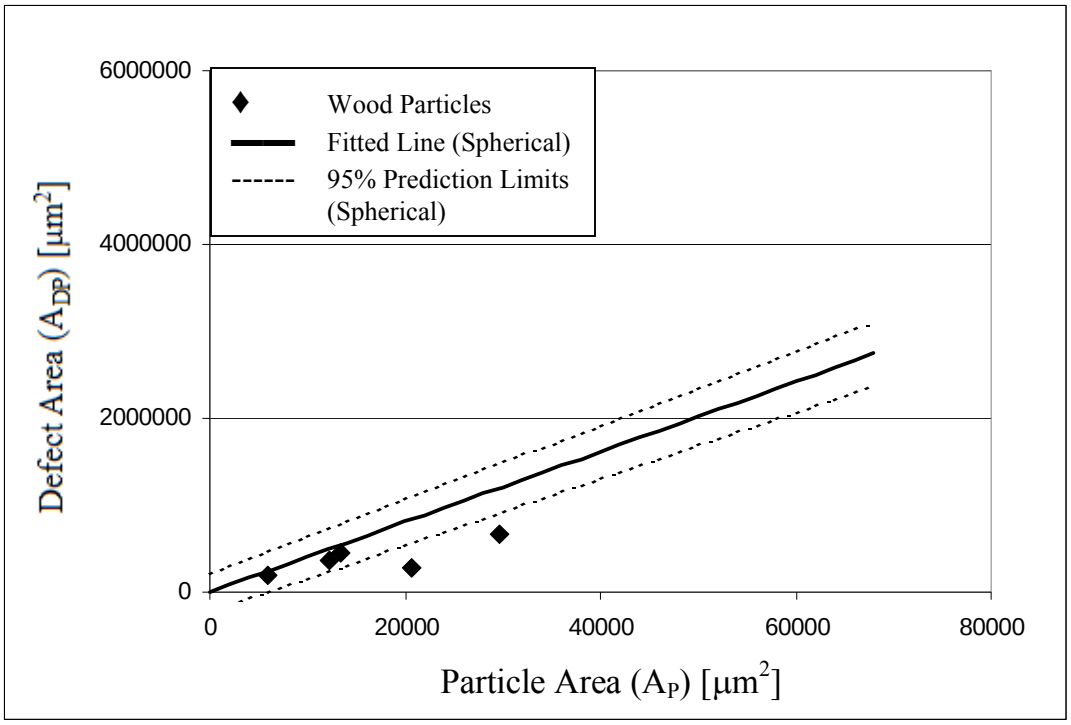


**Figure 4-VII-19:** Defect area ($A_{DP}$) versus particle area ($A_P$) for low average height defects caused by wood particles at 56.6 µm film thickness.

**APPENDIX 4-VIII:** Average Defect Height and Magnification for Cross-Linked Polymer Pieces

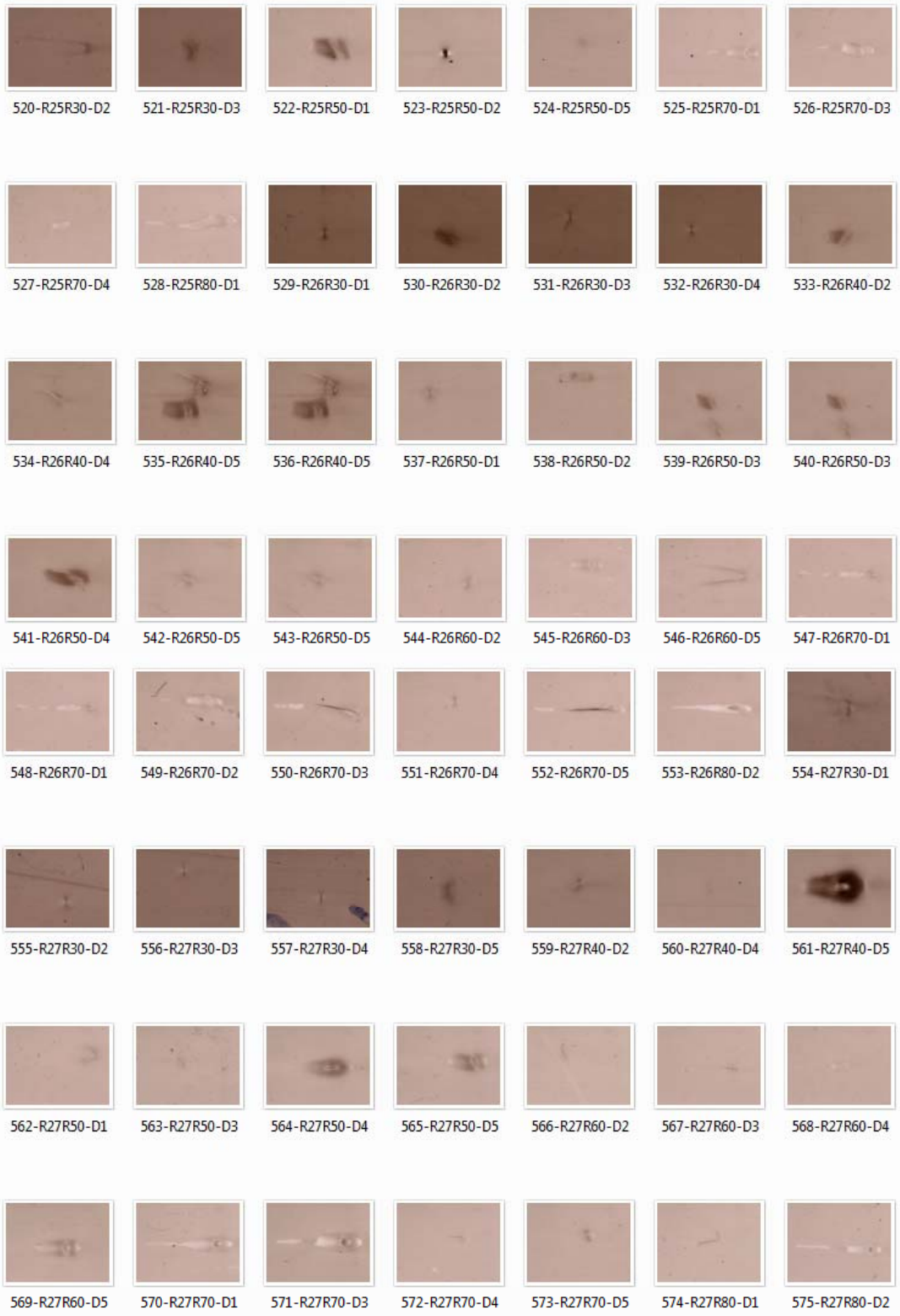


**Figure 4-VIII-1:** Polarized light images of defects caused by cross-linked polymer particles.

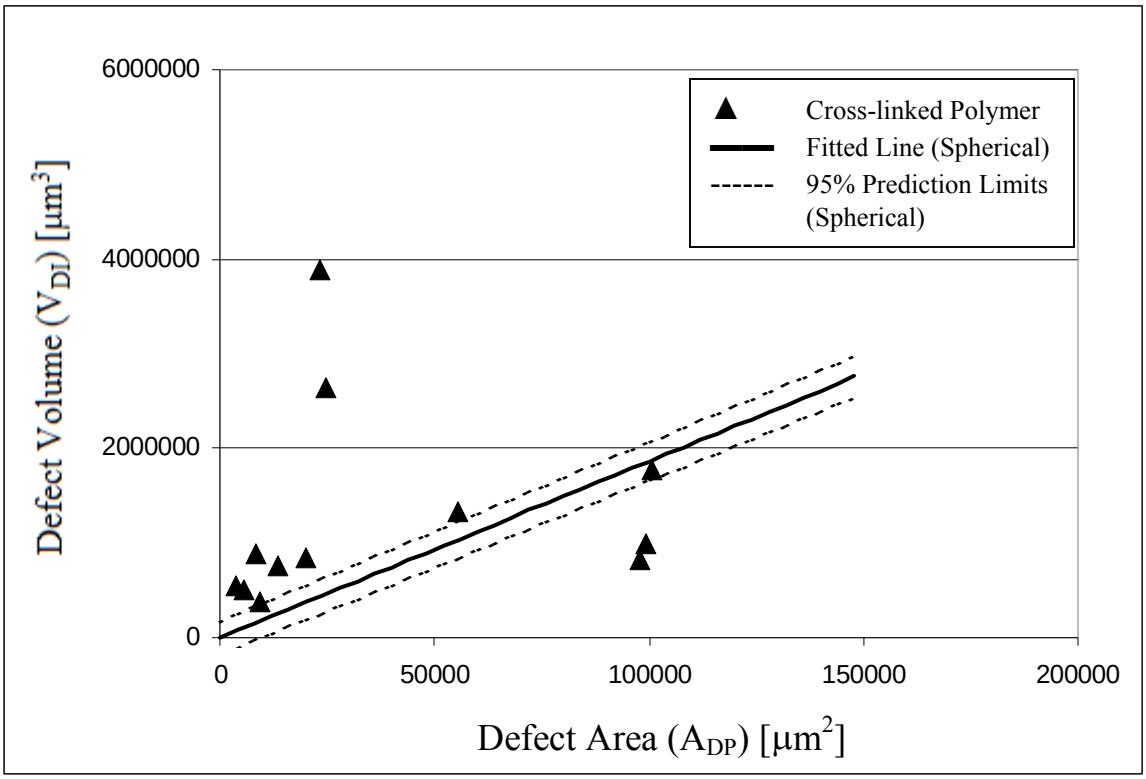


**Figure 4-VIII-2:** Defect volume ($V_{DI}$) versus defect area ($A_{DP}$) for high average height defects caused by cross-linked polymer particles at a film thickness of 240.7 µm. This graph shows that the scanned high average height defects caused by cross-linked polymer particles at this film thickness level do not follow the trend shown by the defects caused by spherical particles.

Symbols: (▲) Cross-Linked polymer particles, (—) The simple least squares line fitted to the spherical particle dataset at each film thickness. (---) 95% prediction limits for the dependent variable for a single future observation calculated from the spherical particle dataset at each film thickness.

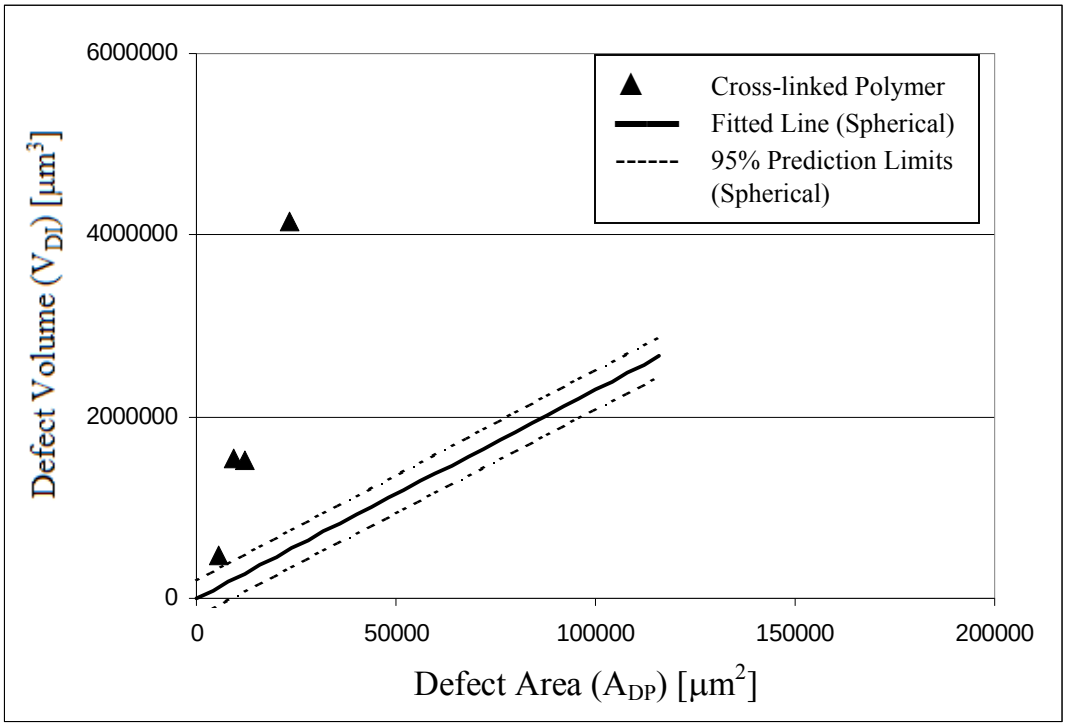


**Figure 4-VIII-3:** Defect volume ($V_{DI}$) versus defect area ($A_{DP}$) for high average height defects caused by cross-linked polymer particles at a film thickness of 152.0 µm.

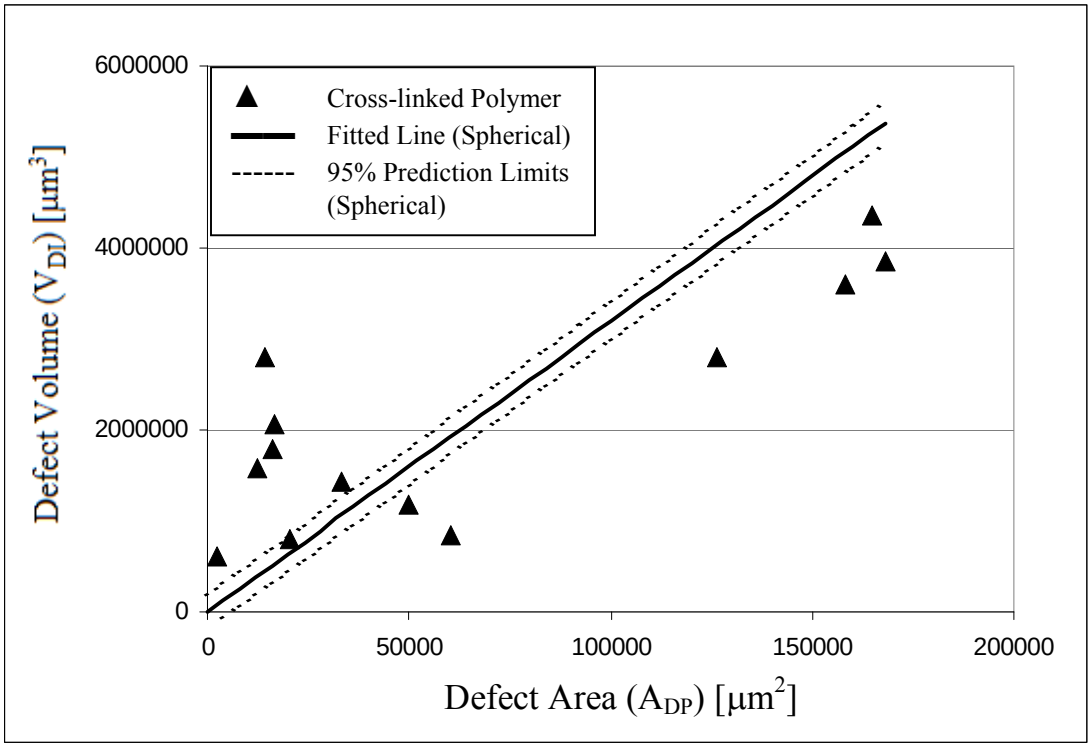


**Figure 4-VIII-4:** Defect volume ($V_{DI}$) versus defect area ($A_{DP}$) for high average height defects caused by cross-linked polymer particles at a film thickness of 109.4 µm.

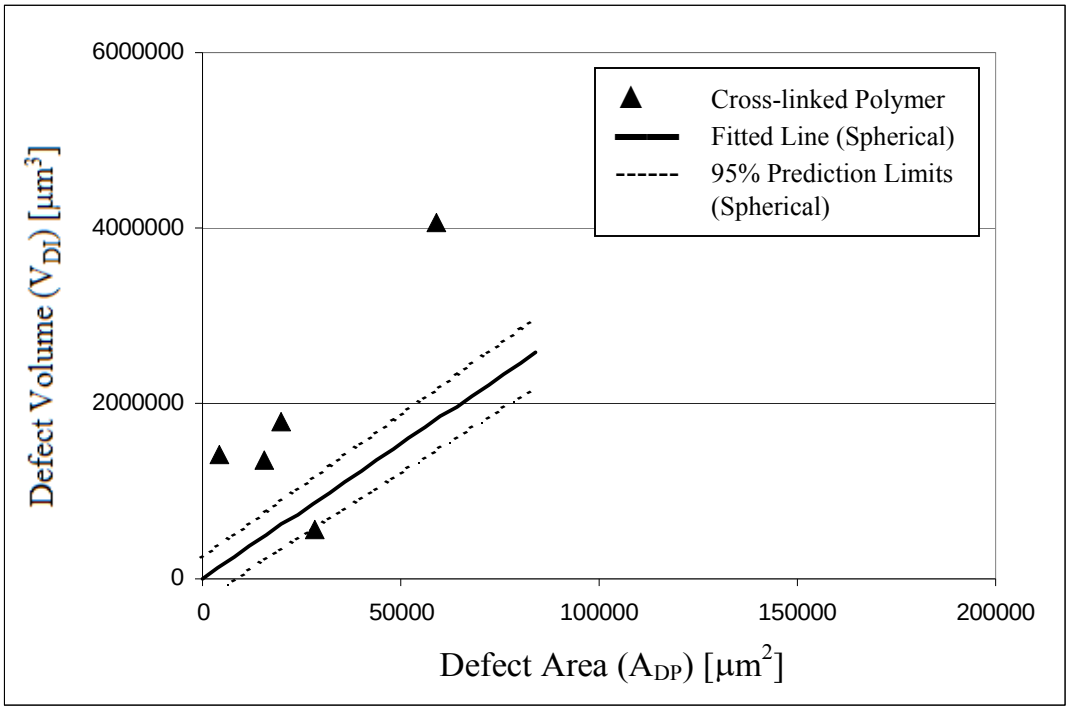


**Figure 4-VIII-5:** Defect volume ($V_{DI}$) versus defect area ($A_{DP}$) for high average height defects caused by cross-linked polymer particles at a film thickness of 82.1 µm.

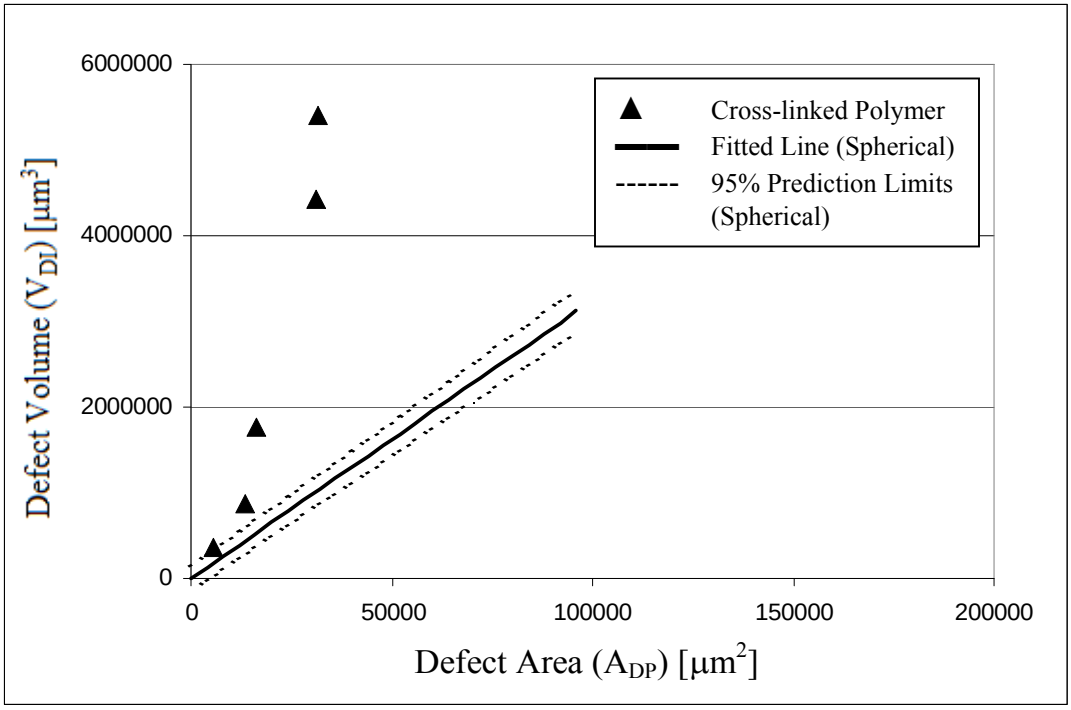


**Figure 4-VIII-6:** Defect volume ($V_{DI}$) versus defect area ($A_{DP}$) for high average height defects caused by cross-linked polymer particles at a film thickness of 66.6 µm.

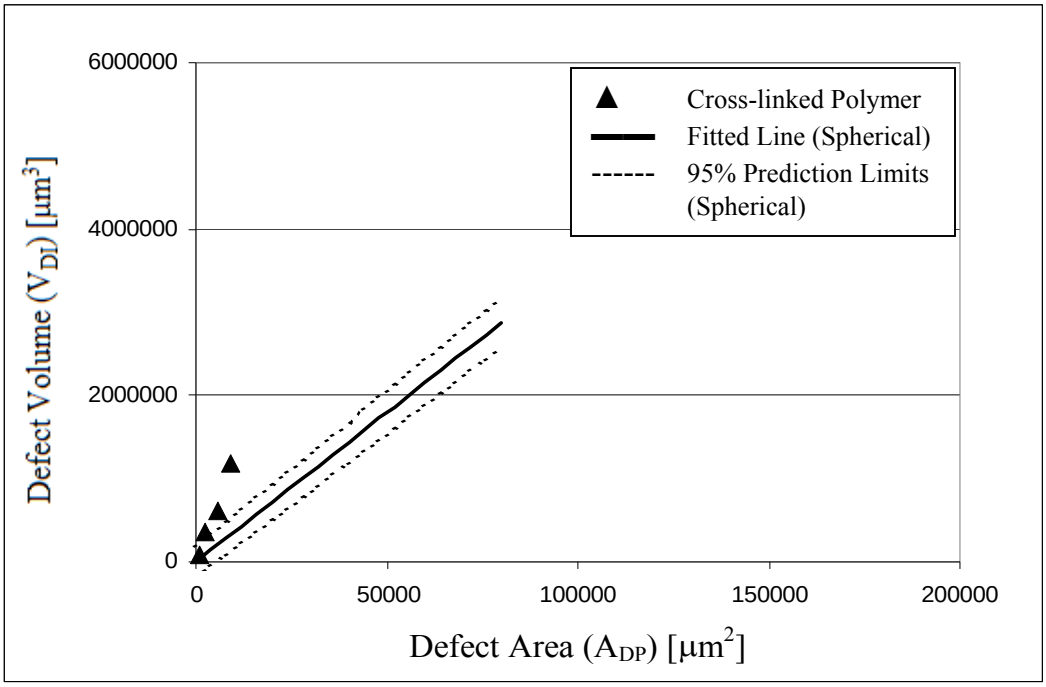


**Figure 4-VIII-7:** Defect volume ($V_{DI}$) versus defect area ($A_{DP}$) for high average height defects caused by cross-linked polymer particles at a film thickness of 56.6 µm.

**Note:** The dataset does not contain any low average height defects caused by a cross-linked particle at a thickness of 240.7 µm.

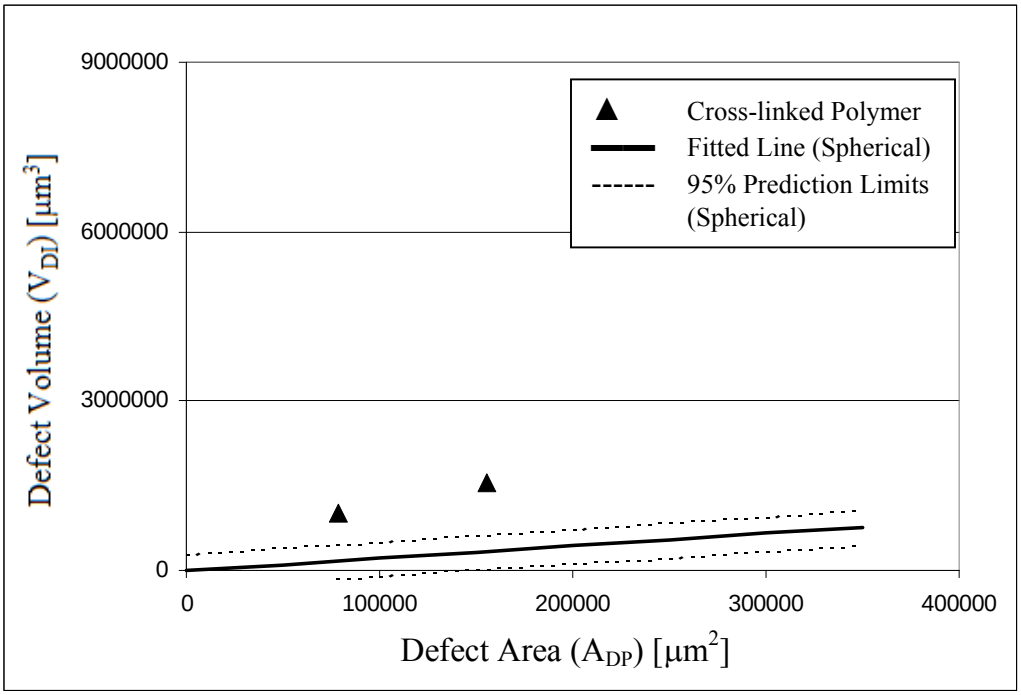


**Figure 4-VIII-8:** Defect volume ($V_{DI}$) versus defect area ($A_{DP}$) for low average height defects caused by cross-linked polymer particles at a film thickness of 152.0 µm.

**Note:** The dataset does not contain any low average height defects caused by a cross-linked particle at a thickness of 109.4μm.

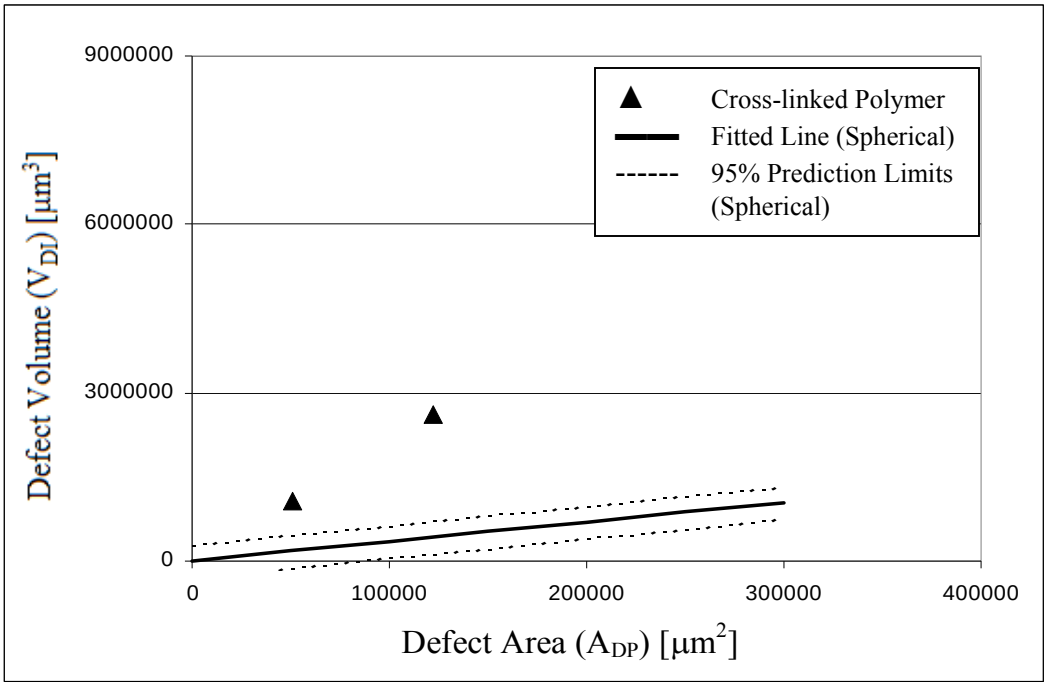


**Figure 4-VIII-9:** Defect volume ($V_{DI}$) versus defect area ($A_{DP}$) for low average height defects caused by cross-linked polymer particles at a film thickness of 82.1 μm.

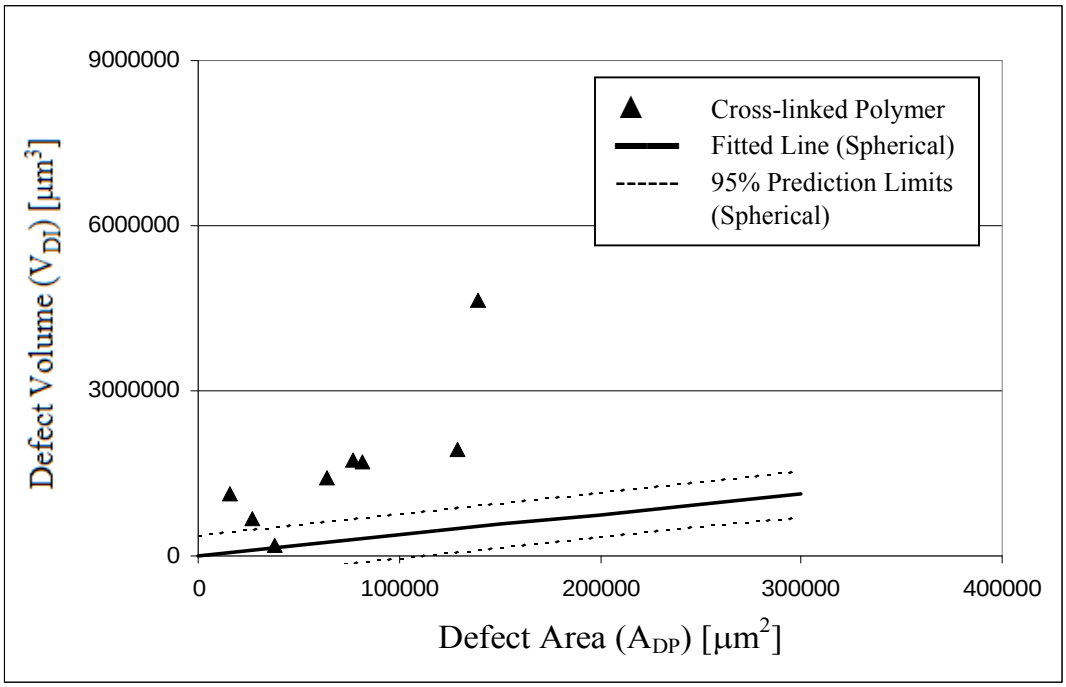


**Figure 4-VIII -10:** Defect volume ($V_{DI}$) versus defect area ($A_{DP}$) for low average height defects caused by cross-linked polymer particles at a film thickness of 66.6 μm.

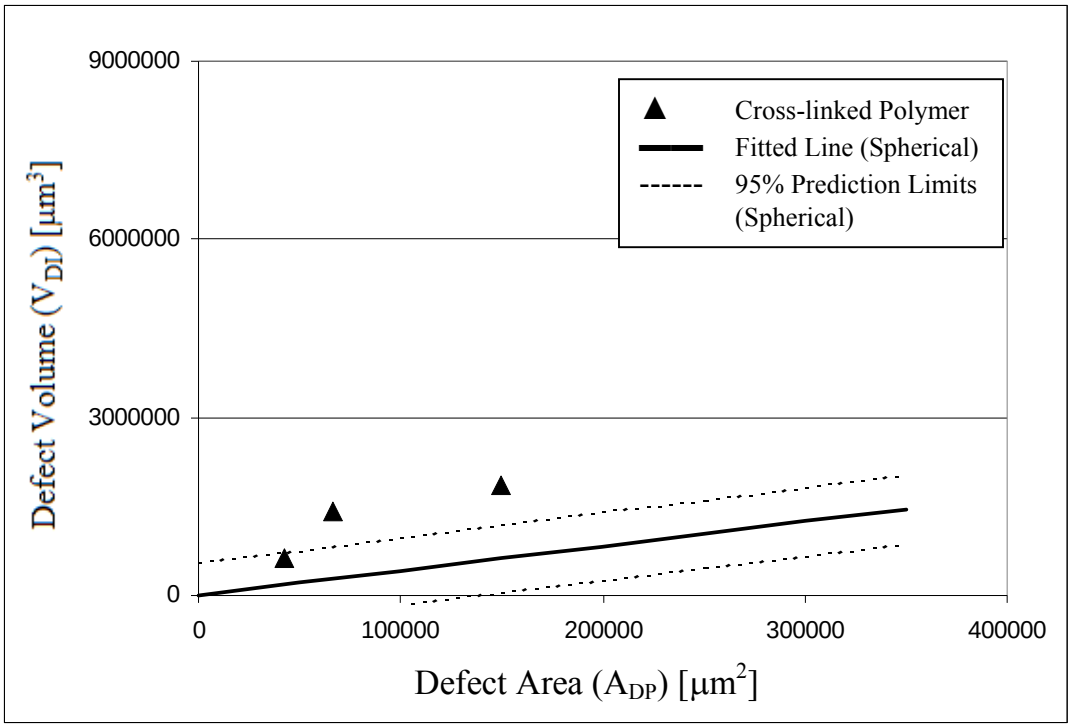


**Figure 4-VIII-11:** Defect volume ($V_{DI}$) versus defect area ($A_{DP}$) for low average height defects caused by cross-linked polymer particles at a film thickness of 56.6 µm.

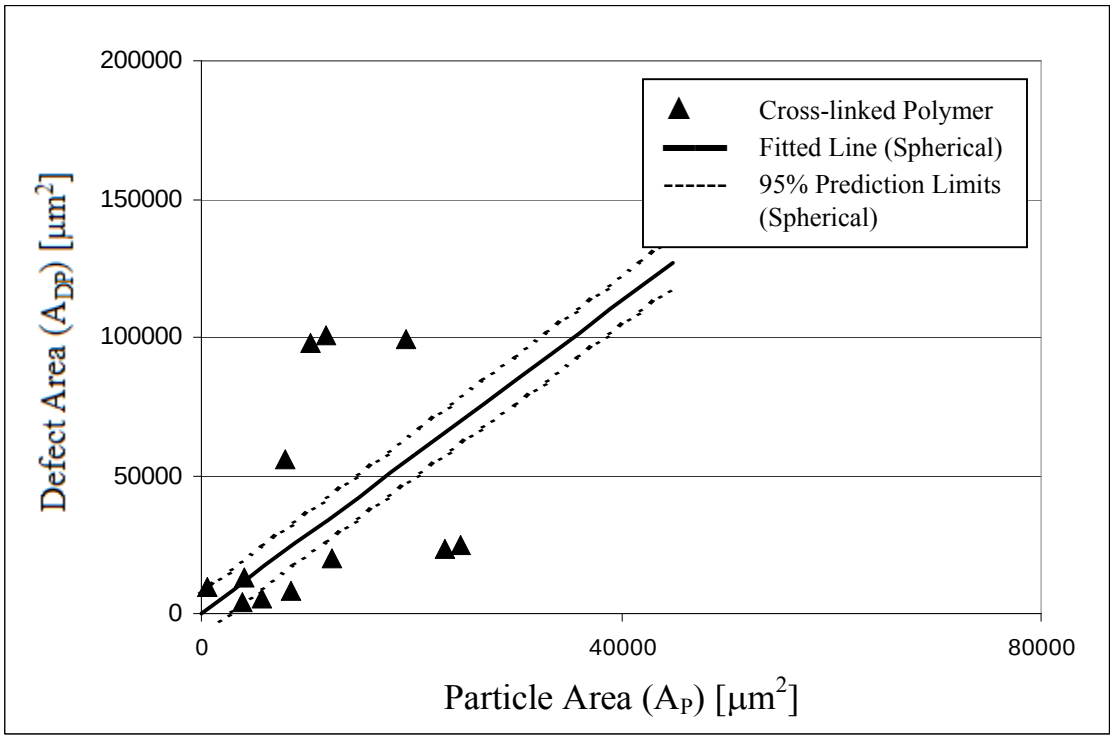


**Figure 4-VIII -12:** Defect area ($A_{DP}$) versus particle area ($A_P$) for high average height defects caused by cross-linked polymer particles at a film thickness of 240.7 µm.

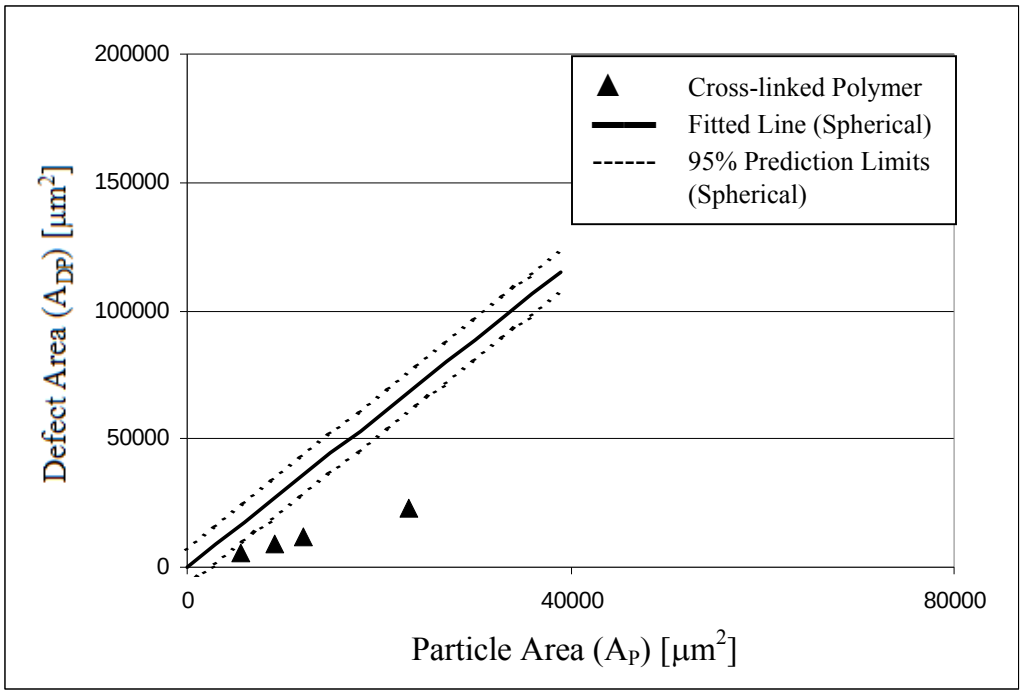


**Figure 4-VIII -13:** Defect area ($A_{DP}$) versus particle area ($A_P$) for high average height defects caused by cross-linked polymer particles at a film thickness of 152.0 µm.

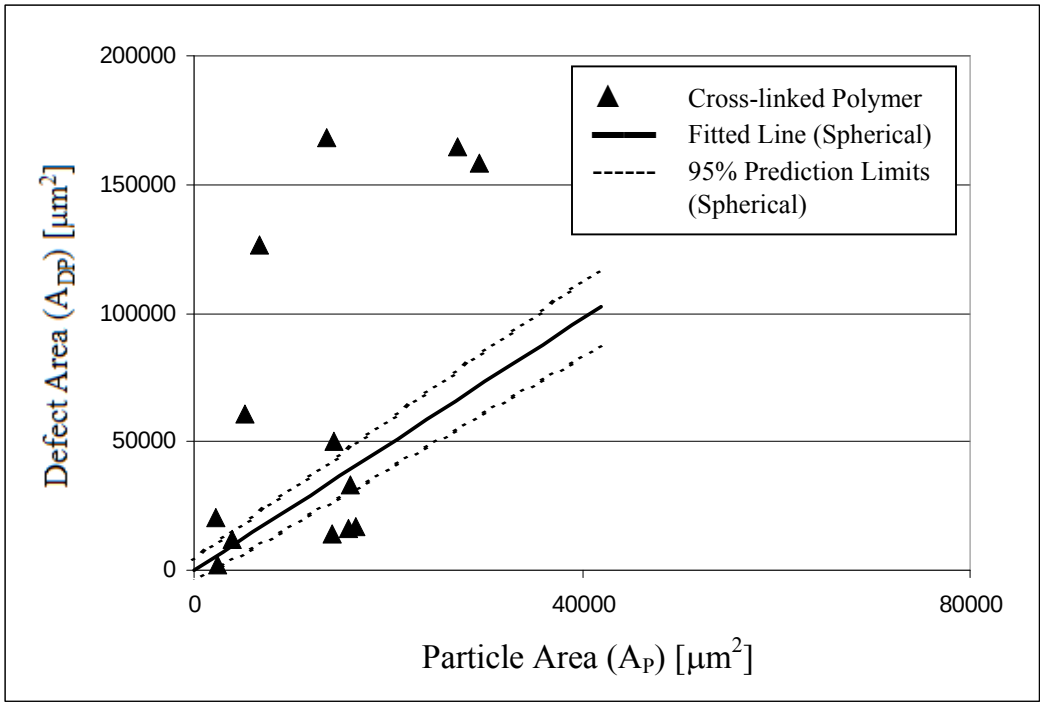


**Figure 4-VIII-14:** Defect area ($A_{DP}$) versus particle area ($A_P$) for high average height defects caused by cross-linked polymer particles at a film thickness of 109.4 µm.

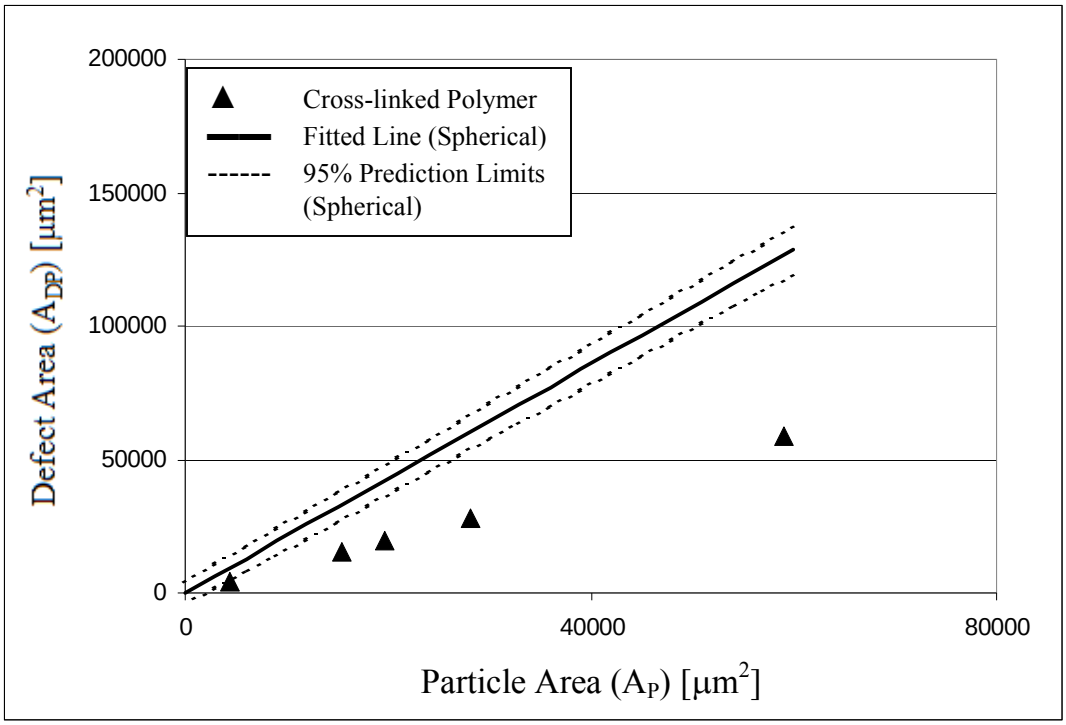


**Figure 4-VIII-15:** Defect area ($A_{DP}$) versus particle area ($A_P$) for high average height defects caused by cross-linked polymer particles at a film thickness of 82.1 µm.

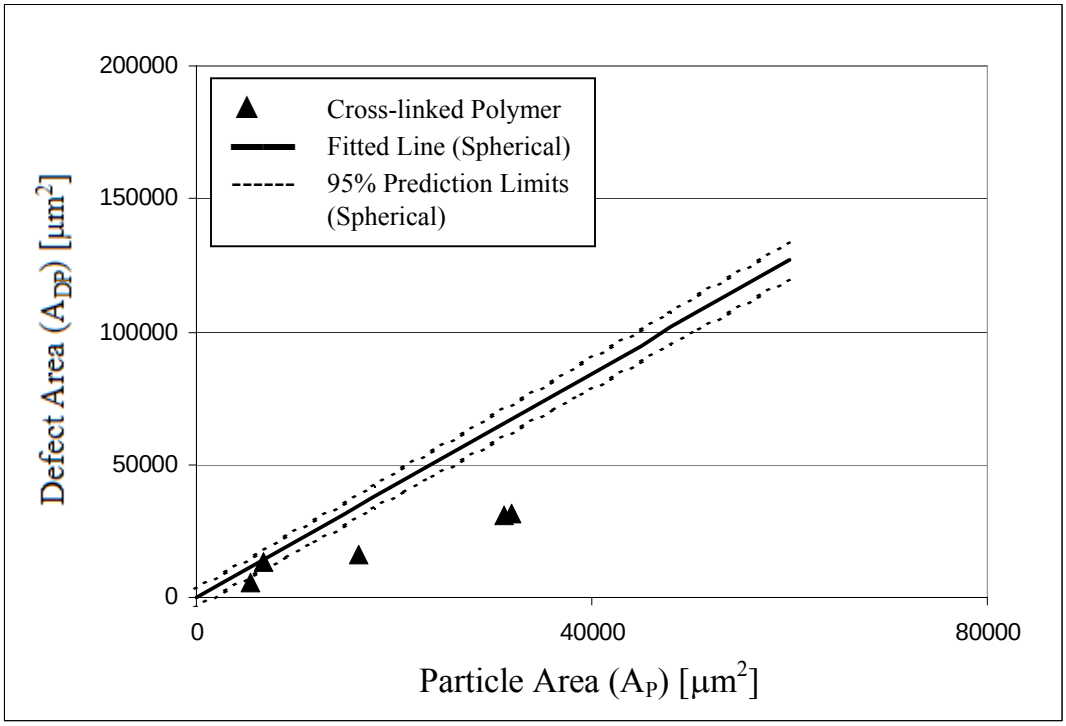


**Figure 4-VIII -16:** Defect area ($A_{DP}$) versus particle area ($A_P$) for high average height defects caused by cross-linked polymer particles at a film thickness of 66.6 µm.

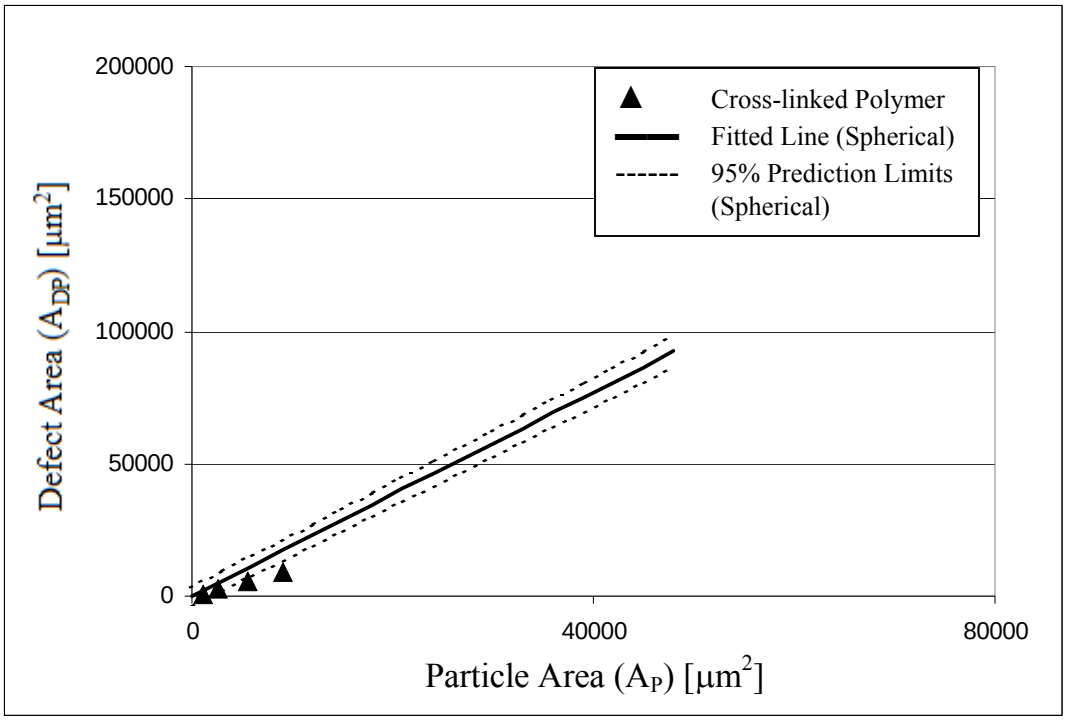


**Figure 4-VIII-17:** Defect area ($A_{DP}$) versus particle area ($A_P$) for high average height defects caused by cross-linked polymer particles at a film thickness of 56.6 μm.

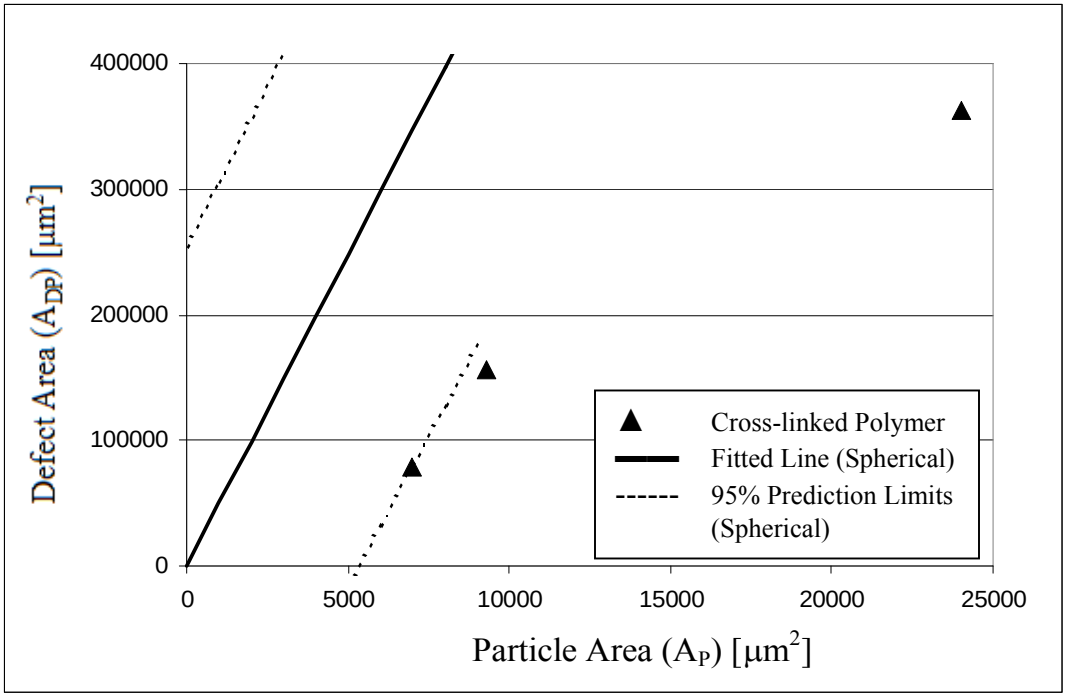


**Figure 4-VIII-18:** Defect area ($A_{DP}$) versus particle area ($A_P$) for low average height defects caused by cross-linked polymer particles at a film thickness of 152.0 μm.

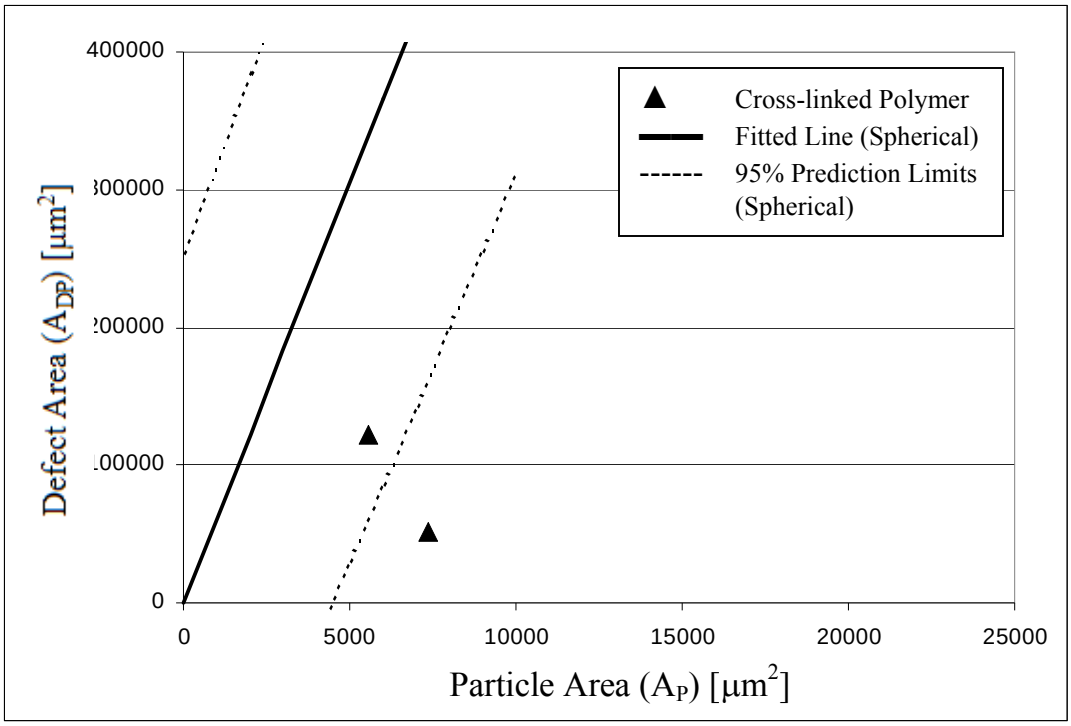


**Figure 4-VIII -19:** Defect area ($A_{DP}$) versus particle area ($A_P$) for low average height defects caused by cross-linked polymer particles at a film thickness of 82.1 µm.

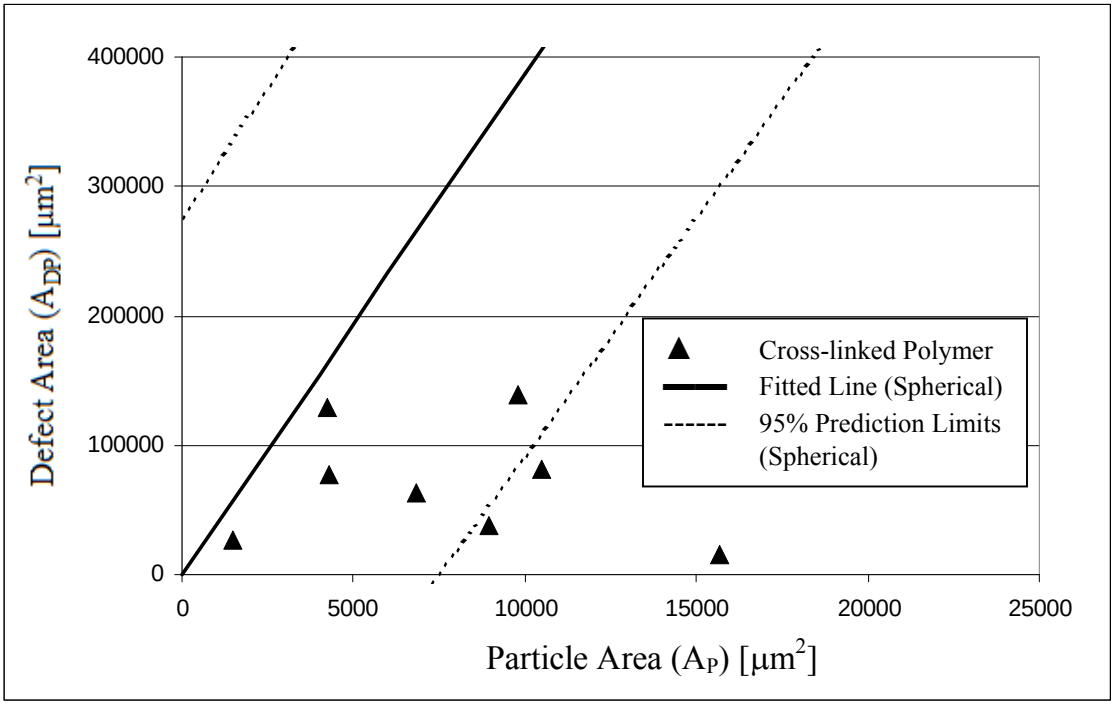


**Figure 4-VIII -20:** Defect area ($A_{DP}$) versus particle area ($A_P$) for low average height defects caused by cross-linked polymer particles at a film thickness of 66.6 µm.

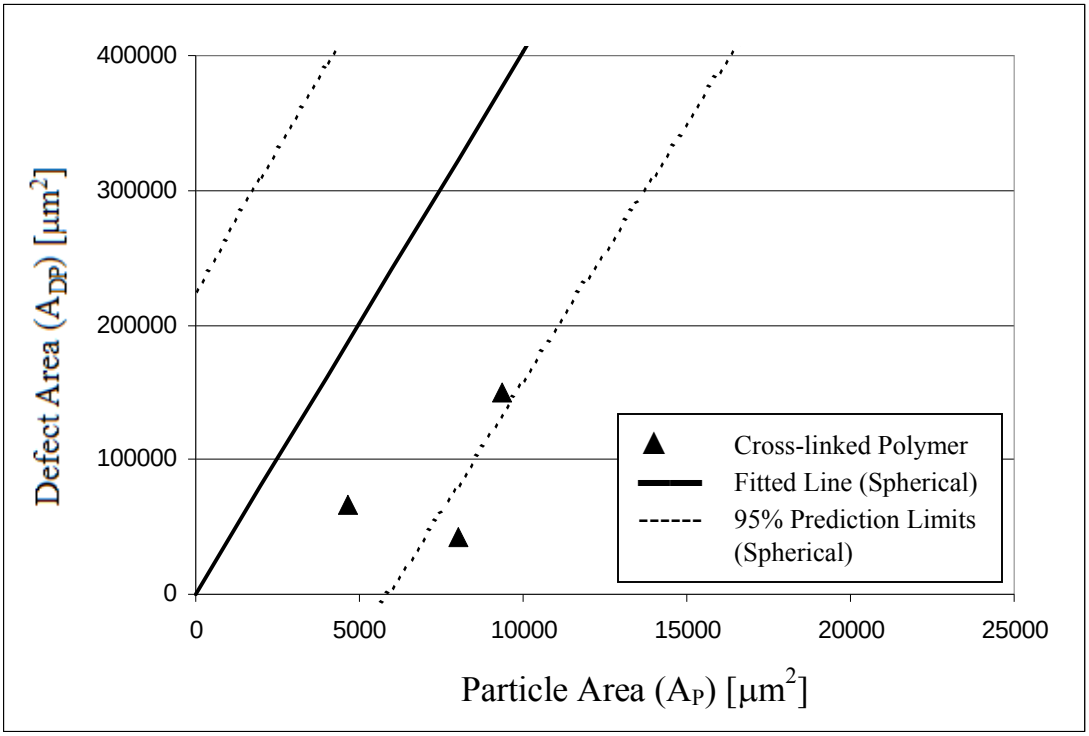


**Figure 4-VIII -21:** Defect area ($A_{DP}$) versus particle area ($A_P$) for low average height defects caused by cross-linked polymer particles at a film thickness of 56.6 μm.

## **Appendix 4-IX:** Possible Causes for Two Distinct Groups of Defects Being Observed

From the outset, the focus of this work was to obtain a mathematical model that would help processors to relate particle and processing properties to defect properties. The work emphasized experimentally causing the defects, creation of a suitable database and then finally, development of a model utilizing the database. The observation that only two distinct groups of defects occurred was a complete surprise and became evident only in the final modeling work after several very powerful data mining techniques had not provided the needed model. As described in other sections of this thesis, the model was readily obtained once these two groups of defects were identified. Even a "mechanistic" model based on constant defect volume was developed. However, although this model is useful, it does not provide any information on one fundamental question: "Why are only two groups of defects observed?" Obtaining a full, experimentally verified answer to this mechanistic question is beyond the scope of this thesis. It deserves additional experimental work, including techniques not used here, with that specific objective.

However, despite this situation, the limited data obtained in this work does at least permit an initial attempt to very tentatively answer this tantalizing question. In this Appendix, four major hypotheses are considered in turn to explain the creation of only two defect groups. These hypotheses are as follows:

**Hypothesis I:** The diameter of the particle relative to the size of thickness of the film provides the basis for two defect groups. For example, once the diameter of a particle exceeds the thickness of the film it belongs to a second group of defects.

**Hypothesis II:** The maximum height (rather than the average height) of a defect provides the basis for two defect groups. For example, a critical maximum height may exist that marks the boundary between defect groups.

**Hypothesis III:** Invalid pixels in the interferometer measurement causes an inaccuracy in the calculation of defect volume, which in turn, is reflected in an inaccuracy in average defect height. Those defects with interferograms of sufficient inaccuracy become members of the second defect group.

**Hypothesis IV:** Particle debonding from the polyethylene matrix occurs at a specific stress level: the two defect groups consist of those in which particle debonding has occurred and those in which it has not occurred.

Each of these hypotheses is examined in the following paragraphs.

## Hypothesis I: Critical Average Particle Diameter to Film Thickness Ratio ($D_P/h_{film}$)

The relationship between the ratio of average particle diameter ($D_P$) to film thickness ($h_{film}$) and defect type was investigated for the spherical particle dataset. There are a total of 154 low average height defects and 208 high average height defects in this dataset.

The $D_P/h_{film}$ ratio of the spherical particle dataset ranges from 0.092 to 2.43. Figure 4-IX-1 shows the number of defects versus $D_P/h_{film}$ as histograms for high average height defects (Figure 4-IX-1 (a)) and for low average height defects (Figure 4-IX-1 (b)). The

histograms differ in shape. Most of the high average height defects occurred at smaller values of $D_P/h_{film}$ (< 0.5) while the low average height defects tended to be in the middle range of $D_P/h_{film}$. For $D_P/h_{film}$ ratios greater than 1, about 65% of the scanned defects were low average height defects. However, the important point is that the histograms would show a large overlap if they were displayed on the same axes. Figure 4-IX-1 demonstrates that both high and low average height defects were created across the tested range of $D_P/h_{film}$.

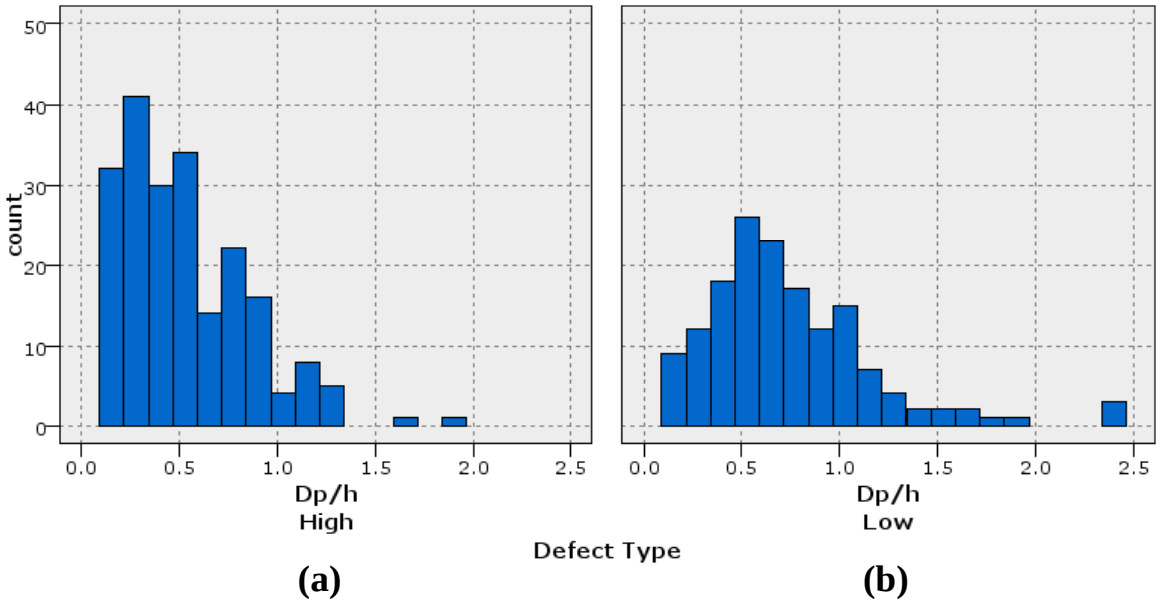


**Figure 4-IX-1:** Histogram of the ratio of average particle diameter to film thickness ($D_P/h_{film}$) **(a)** High average height defects, **(b)** Low average height defects.

Statistical analysis of the entire dataset shows no significant trend or correlation between $D_P/h_{film}$ and any of the defect attributes. The dataset was divided into two subsets based on defect type. In the high average height defect dataset, $D_P/h_{film}$ is not significantly correlated with any of the defect attributes either. However, in contrast, for the low average height defect dataset, and as shown in the least squares fit of the data, Figure 4-IX-2, a strong correlation ($R^2$ =0.91) was found between defect maximum height ($H_{max}$ ) and $D_P/h_{film}$.

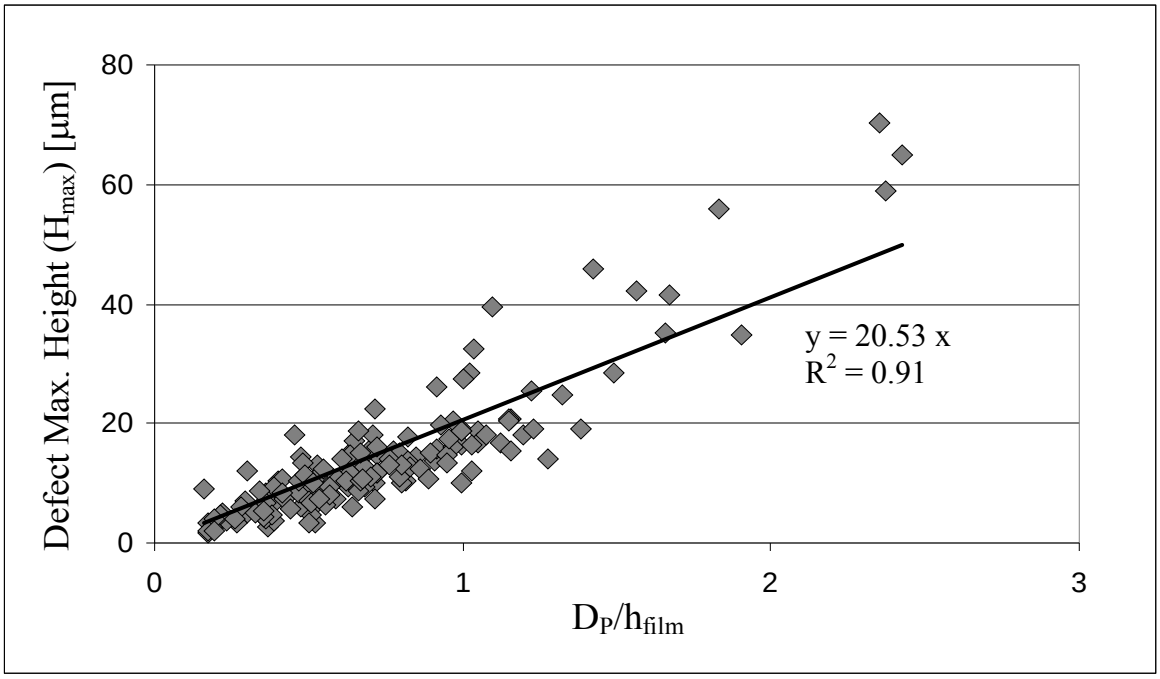


**Figure 4-IX-2:** Defect maximum height ($H_{max}$) is plotted against the ratio of average particle diameter to film thickness ($D_P/h_{film}$) for low average height defects in the spherical particle dataset. A straight line with no intercept was fit to the data points. This line and its equation are shown.

Thus, Hypothesis I, the hypothesis that $D_P/h_{film}$ ratio is the variable responsible for creating two groups of defects is not supported by the existing data. However, the maximum height ($H_{max}$) of a low average height defect is correlated with $D_P/h_{film}$: the larger $D_P/h_{film}$ the larger is the maximum height of a low average height defect.

### Hypothesis II: Critical Defect Maximum Height ($H_{max}$)

Defect maximum height ($H_{max}$) is the height of the peak of the protrusion caused by the particle on the top film surface. Its value was obtained from the interferometric image of each defect. Figures 4-IX-3 (a) and (b) show the histograms of this variable for high and low

average height defects. The histogram for the low average height defects shows that majority (~ 85%) of low average height defects have an $H_{max}$ value less than 20 μm. However, there are some low average height defects with maximum height as high as 70 μm. Thus, there is an overlap between the maximum height values of high and low average height defects.

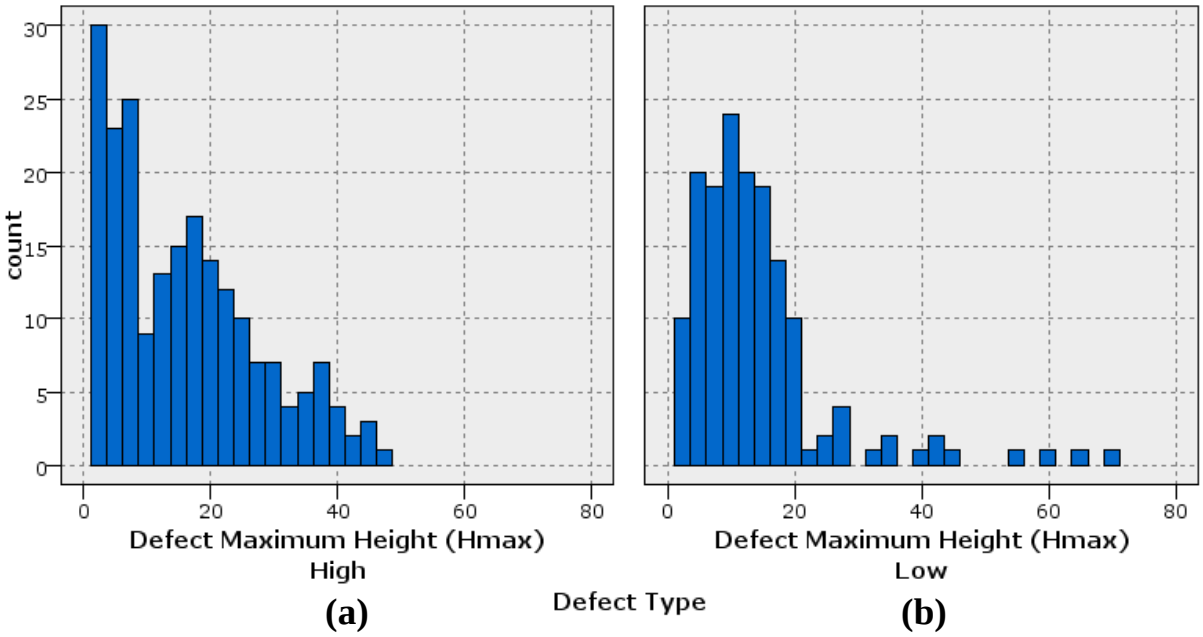


**Figure 4-IX-3:** Histogram of defect maximum height ($H_{max}$), **(a)** High average height defects, **(b)** Low average height defects.

In the following graphs, maximum defect height is plotted against particle area at each film thickness for the respective previously identified high and low average height defect groups.

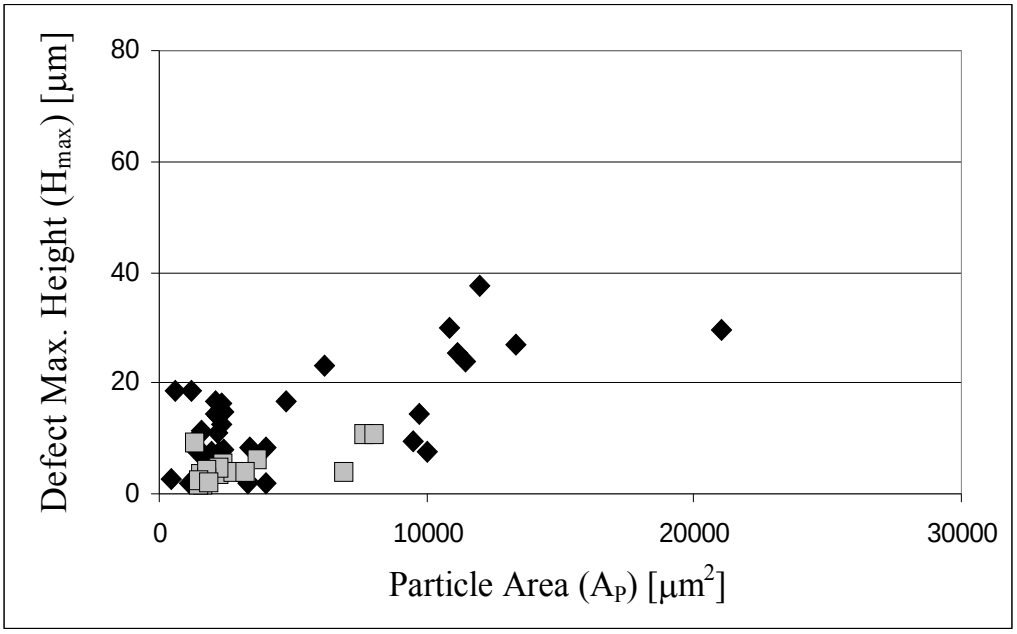


**Figure 4-IX-4:** Defect maximum height ($H_{max}$) versus particle area ($A_P$) for high and low average height defects caused by all spherical particles at 240.7 μm film thickness.

Symbols: ♦: High average height defects, ■: Low average height defects

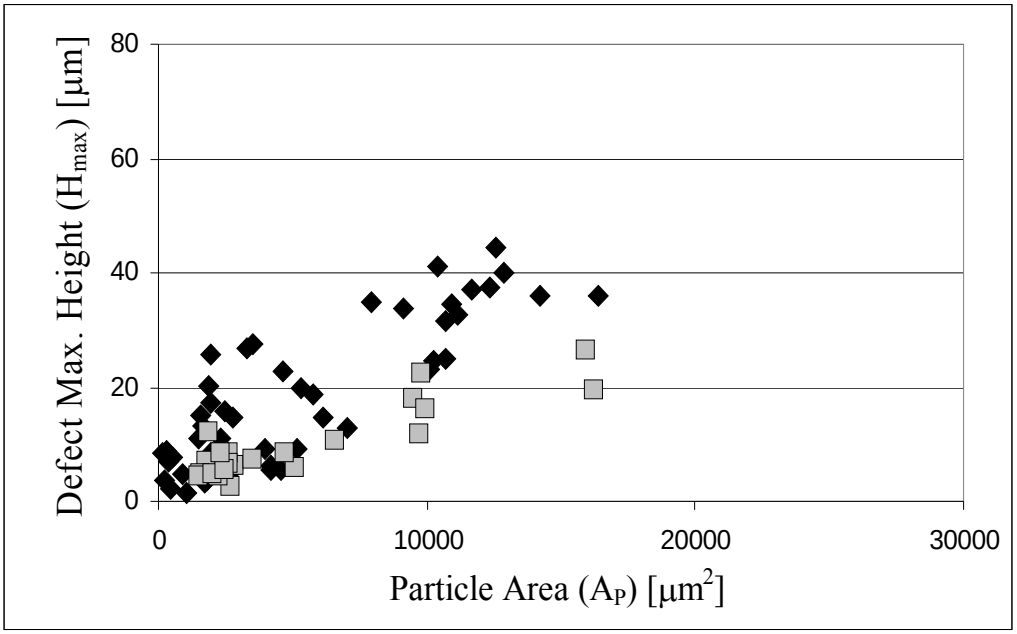


**Figure 4-IX-5:** Maximum defect height ($H_{max}$) versus particle area ($A_P$) for high and low average height defects caused by all spherical particles at 152.0 μm film thickness.

Symbols: ♦: High average height defects, ■: Low average height defects

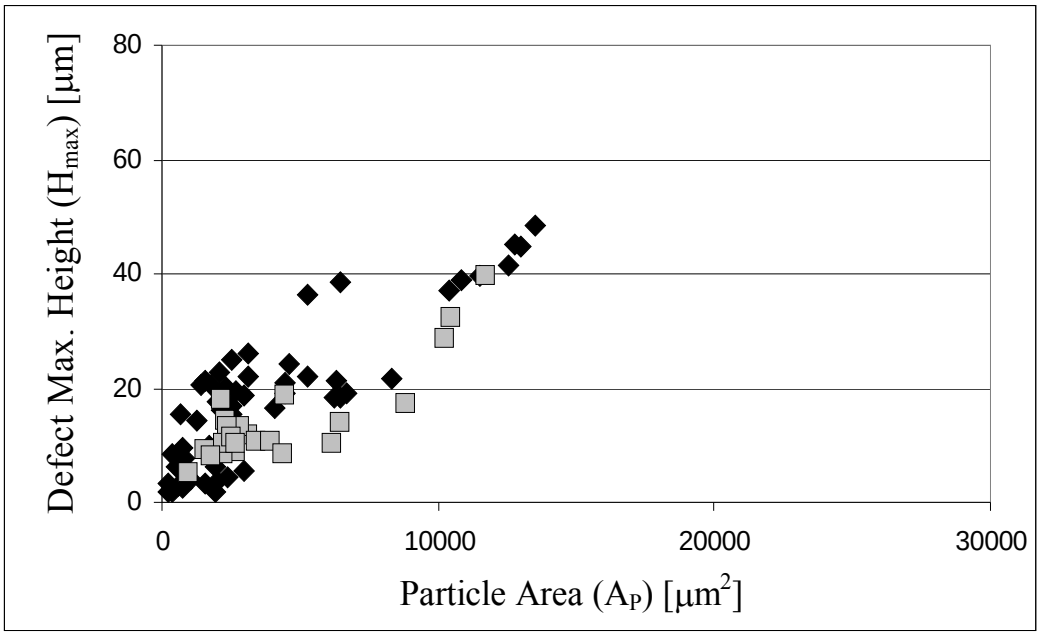


**Figure 4-IX-6:** Defect maximum height ($H_{max}$) versus particle area ($A_P$) for high and low average height defects caused by all spherical particles at 109.4 μm film thickness.

Symbols: ♦: High average height defects, ■: Low average height defects

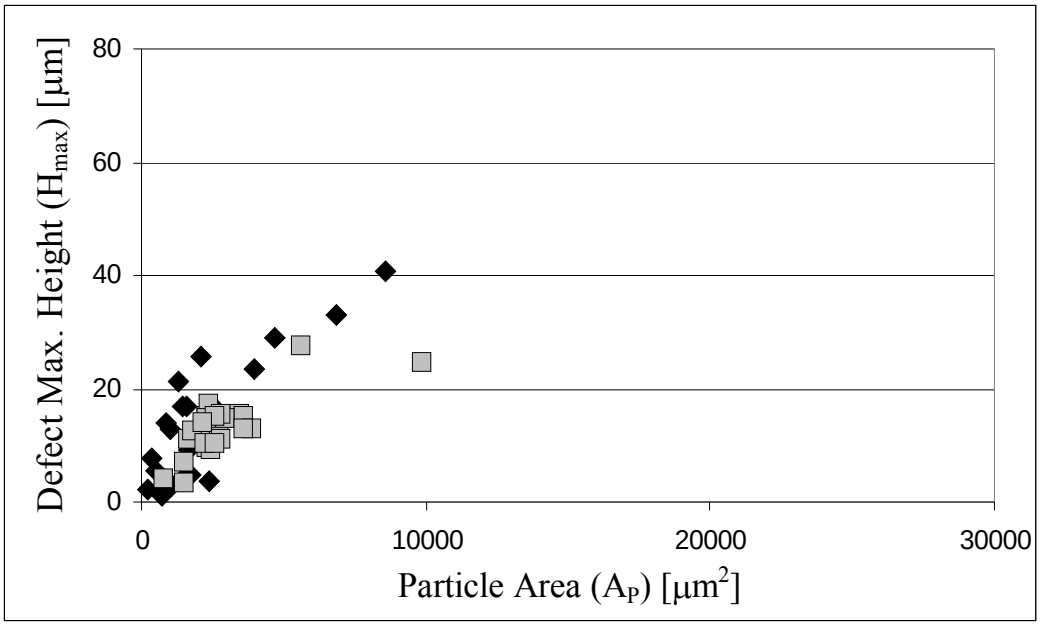


**Figure 4-IX-7:** Defect maximum height ($H_{max}$) versus particle area ($A_P$) for high and low average height defects caused by all spherical particles at 82.1 μm film thickness.

Symbols: ♦: High average height defects, ■: Low average height defects

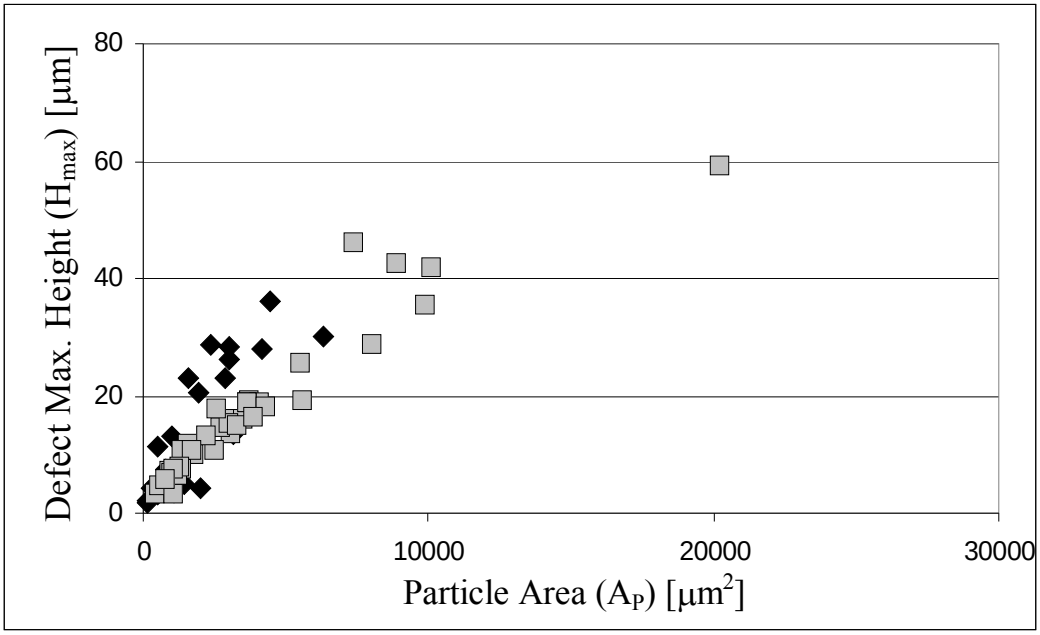


**Figure 4-IX-8:** Defect maximum height ($H_{max}$) versus particle area ($A_P$) for high and low average height defects caused by all spherical particles at 66.6 μm film thickness.

Symbols: ♦: High average height defects, ■: Low average height defects

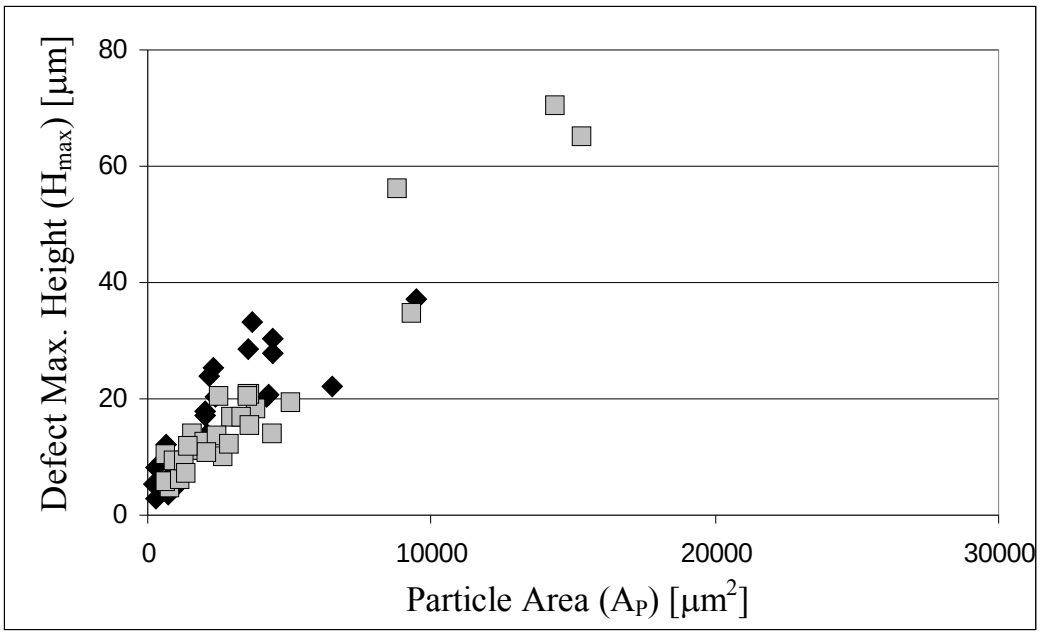


**Figure 4-IX-9:** Defect maximum height ($H_{max}$) versus particle area ($A_P$) for high and low average height defects caused by all spherical particles at 56.6 μm film thickness.

Symbols: ♦: High average height defects, ■: Low average height defects

The relationship between $H_{max}$ and other particle and defect attributes was also investigated. A significant relationship was the correlation between $H_{max}$ and $D_P/h_{film}$ for the low average height defect dataset as shown previously in Figure 4-IX-2.

Thus, Hypothesis II, the hypothesis that $H_{max}$ is an indicator of the defect group is not supported by the available data: $H_{max}$ values for high and low average height defects span a similar range. The data shows an increasing trend in the defect maximum height with particle area.

## Hypothesis III: Invalid Pixels in Interferometric Images

As explained in section 4.1.2.4, the raw surface profile images reported by the interferometer for some defects contained invalid pixels. The instrument was unable to record height data for these pixels. Wyko NT2000 technical reference manual lists three reasons as possible causes for invalid pixels: the surface is too steep for a suitable reflection, the surface is not reflective, or that the pixel value did not reach the modulation threshold. A restoration algorithm available in Wyko Vision32 software used by the interferometer estimates the values of the invalid pixels based on the neighboring pixels. (Veeco Instruments Corp., 1999) These values are then used by the image processing software to obtain various image attributes, notably defect volume. In this thesis, these defect volume data are combined with defect area data from the polarized light measurement to provide average defect height (H).

In a test, glass microspheres of approximately 50 μm in diameter were scattered on top of a solid piece of film and then the sample was scanned by the optical interferometer.

The raw and restored surface profiles are shown in Figure 4-IX-10. The raw surface profile shows that data was obtained for only a small area on top of the spheres. The pixel values for the remaining area of each sphere were invalid and are shown in white color. The diameter of the invalid region is approximately 50 μm, equal to the microsphere diameter.

For the defects produced in film extrusion, most of the high average height defects and some of the low average height defects where the particle was located close to the top surface or exposed contained a large number of invalid pixels in their interferometric images. Two examples are shown in Figures 4-IX-11 (a) and (b). Figure 4-IX-11 (a) shows the polarized light image and the interferometric image for a high average height defect. Figure 4-IX-11 (b) shows analogous images for a low average height defect. Invalid pixels are usually located at the outer edge of the particle and in the deformed region immediately surrounding the particle. For both defects in Figure 4-IX-11, the diameter of the invalid region is greater than the particle diameter. This shows that interferometric data could not be obtained for parts of the particle area and also for the steeply deformed area surrounding the particle. This agrees with the observations discussed in the previous paragraph when microspheres scattered on the surface were examined.

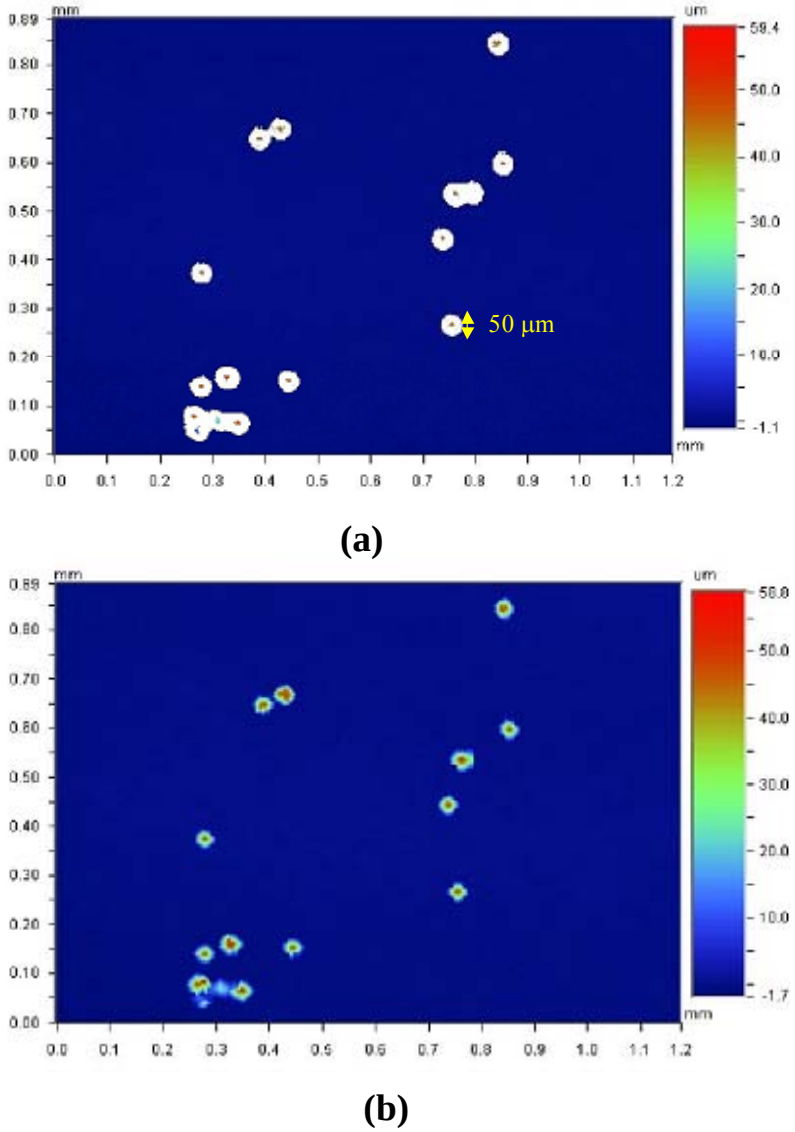


**Figure 4-IX-10:** Surface profile of 50 µm glass microspheres scattered on solid film surface **(a)** Original surface profile **(b)** Restored surface profile.

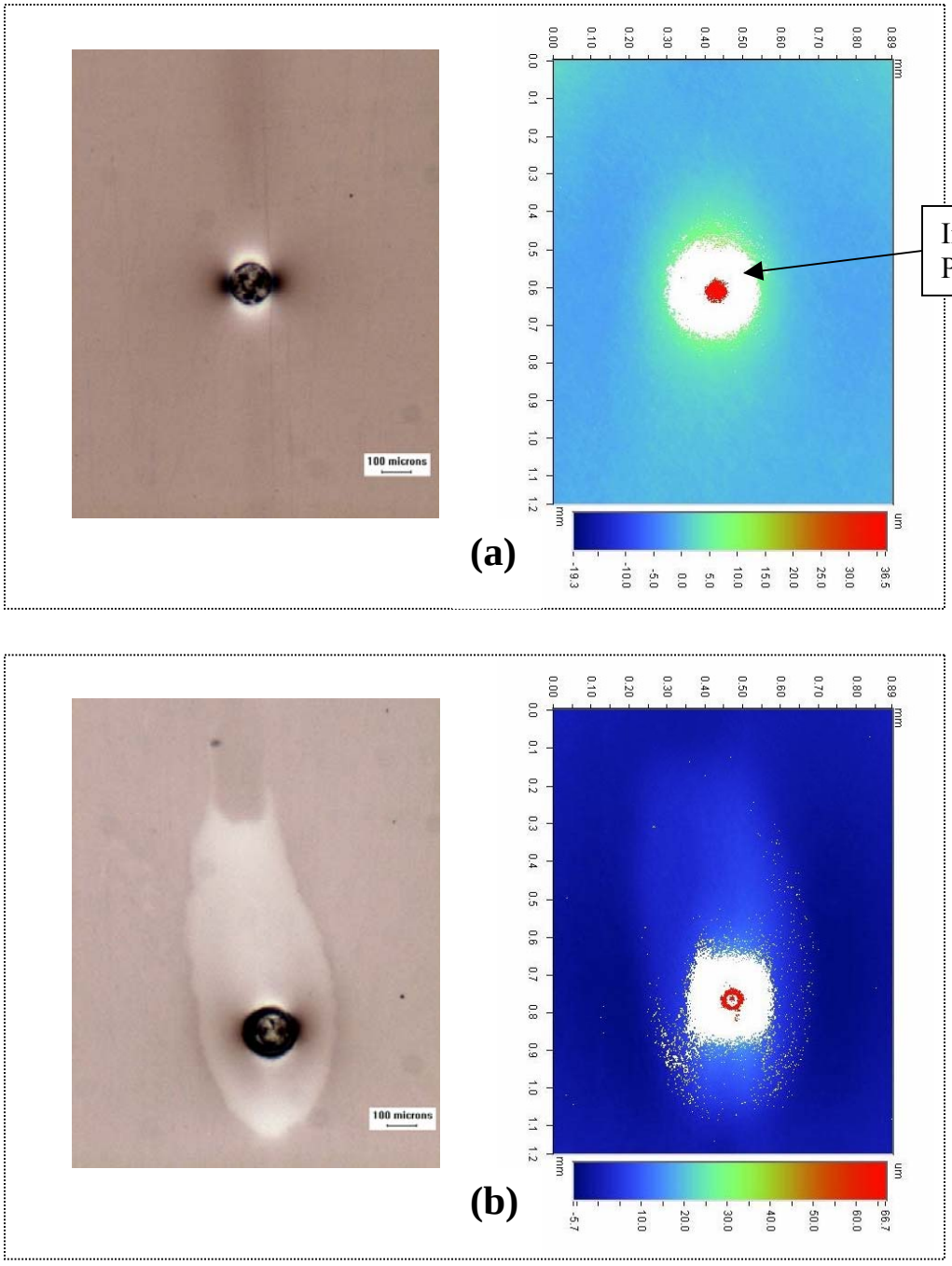


**Figure 4-IX-11:** High and low average height defects with invalid pixels in their interferometric images. **(a)** Polarized light image and original interferometric image of a high average height defect (R19R40-D7), ($D_P/h_{film}$ = 0.94, $H_{max}$ = 35.85 μm). **(b)** Polarized light image and original interferometric image of a low average height defect (R19R80-D9), ($D_P/h_{film}$ = 2.43, $H_{max}$ = 65 μm). The white regions in the surface profile images show the area for which interferometric data could not be obtained.

Two more examples are shown in Figures 4-IX-12 (a) and 4-IX-12 (b). Figure 4-IX-12 (a) shows the polarized light and interferometric images of a high average height defect with invalid pixels. The maximum height of this defect is 16.93 μm. This defect is similar to the defects in Figure 4-IX-11. Figure 4-IX-12 (b) shows the same images for a high average height defect created by a larger particle but without invalid pixels in its interferometric image. The maximum height of this defect is 7.54 μm. Both defects have a $D_P/h_{film}$ ratio of about 0.5. Particles similar to the one in the latter defect appear to be out of focus in polarized light images. Since in polarized light imaging the camera was focused on the top film surface, this could indicate that these particles were located deeper through the film. This would result in a more gradual and lower deformation on the top surface and therefore no invalid pixels in the corresponding interferometric images.

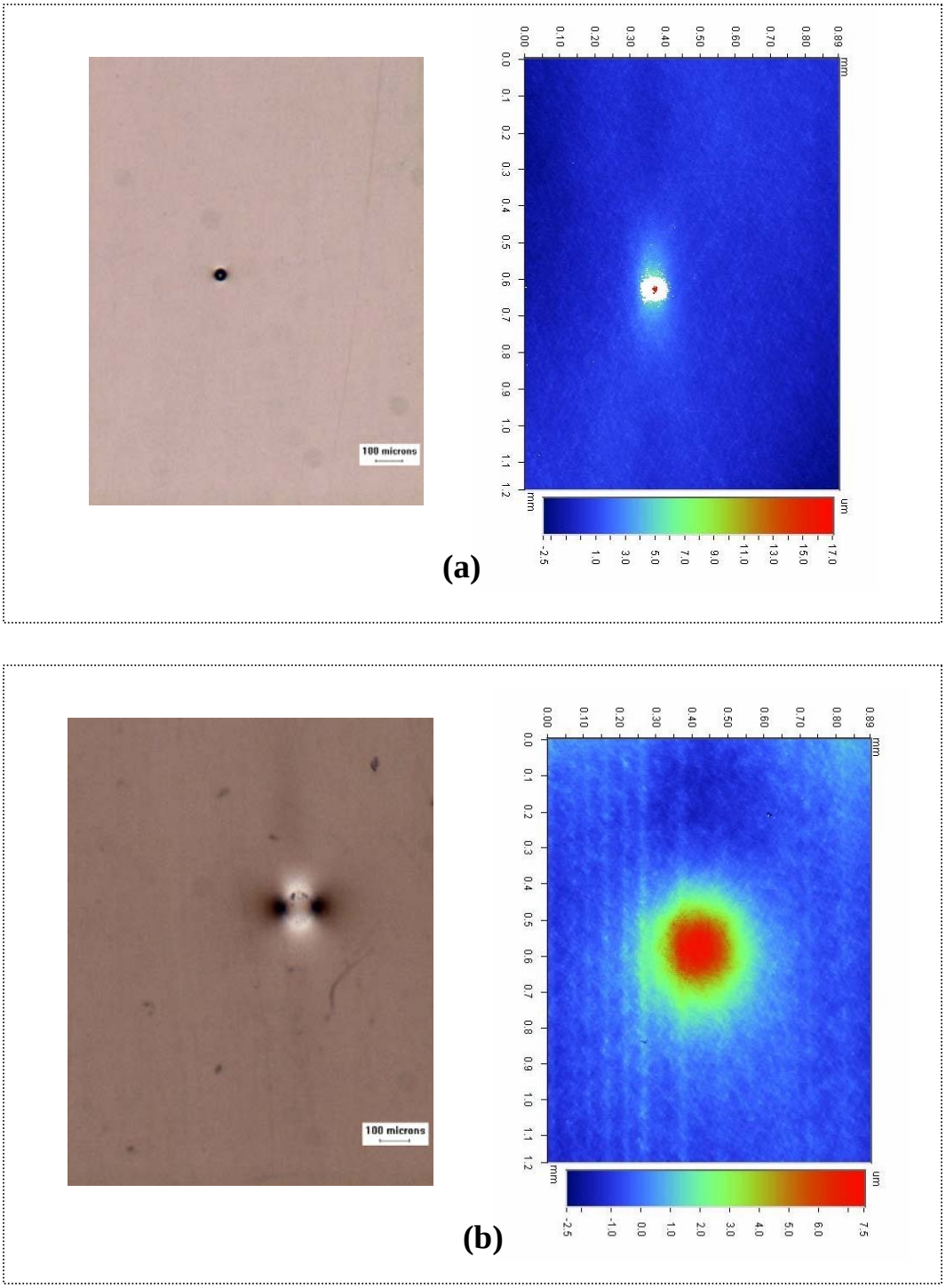


**Figure 4-IX-12: (a)** Polarized light and original interferometric images of a high average height defect with invalid pixels (R20R60-D1) ($D_P/h_{film}$ = 0.49, $H_{max}$ = 16.93 μm).
**(b)** Polarized light and original interferometric images of a high average height defect without invalid pixels (R18R30-D19) ($D_P/h_{film}$ = 0.46, $H_{max}$ = 7.54 μm).

Thus, Hypothesis III, that attributes the different defect groups to the presence or absence of invalid pixels is not supported by the available data: invalid pixels occurred in both low and high average height defects. It is possible that the interferometer's attempt to substitute correct values for invalid pixels could introduce inaccuracy to some data. However, data for both low and high average height defects would be affected.

### Hypothesis IV: Particle Debonding

Debonding is the separation of the particle from the polymer and the creation of two new interfaces: a particle-air interface and a polyethylene-air interface. There are two critical conditions for debonding to occur. First, the elastic energy released by forming the stress free particle surface is at least equal to the work of fracture. Second, the normal stress at the interface must exceed the threshold bond strength between particle and matrix. (Chen *et al.* 2003)

Bai *et al.* (2000) studied the effect of interfacial strength on the mechanical properties of glass bead filled high-density polyethylene. In their study, in situ tensile tests were carried out under a scanning electron microscope (SEM). Critical stress for debonding was measured at each case. SEM images of the debonding process showed that interfacial debonding started at the polar region of the particle. As the applied load increased, the interfacial crack developed into microvoids and elongated in the loading direction. Bai *et al.* (2001 and 2003) showed that interfacial adhesion strength had a strong influence on the strength and deformation mechanism of particulate filled polymer composites. The size and number of voids, and the critical stress for debonding depended on the particle-matrix interfacial

strength. In another study, Cho *et al.* (2006) reported that interfacial debonding initiated at one pole of the particle in the load direction and then the debonded region grew. Next, debonding initiated at the opposite particle pole and the debonded region grew similarly.

In this dataset, the polarized light images of high average height defects show the silhouette of the embedded particles surrounded by a high stressed region marked by very bright and very dark pixels. To illustrate this, approximate outline of the embedded particle and its surrounding stressed area for a typical high average height defect are shown in Figure 4-IX-13. In polarized light images of most high average height defects, the perimeter of the embedded particle especially in the machine direction is clearly visible. (Figure 4-IX-13 (a))

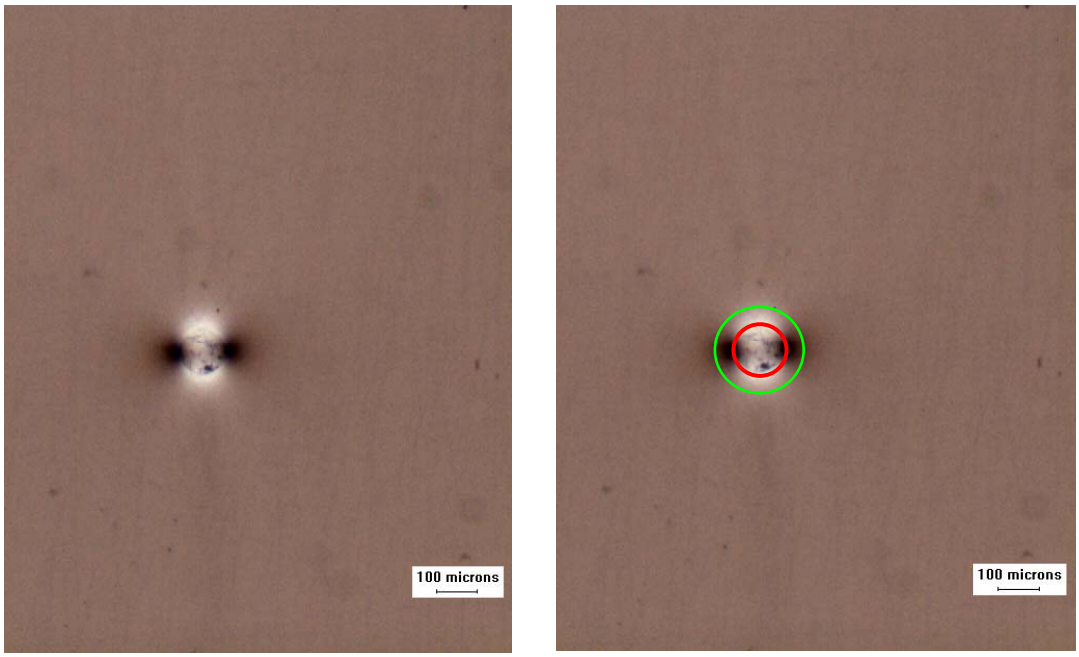


**Figure 4-IX-13: (a)** Polarized light image of a typical high average height defect (R18R40-D9) **(b)** This image shows the approximate outline of the particle (red) and the stressed region (green) for the defect shown in part (a).

However, low average height defects generally have a different appearance: the outline of the embedded particles in polarized light images appeared to be covered or surrounded by a dark ring or an arc. Schematic diagrams of the observed effects around the embedded particles are presented in Figure 4-IX-14. Polarized light images of three low average height defects with the corresponding particle outlines pictured in Figure 4-IX-14 are shown in Figure 4-IX-15. These kinds of changes in the intensity of the inclusion are similar to some of the results published in the literature. (Chen *et al.* 2003, Bai *et al.* 2000, Cho *et al.* 2006) The observed dark regions around the particles may be an indication that particles partially debonded or separated from the matrix.

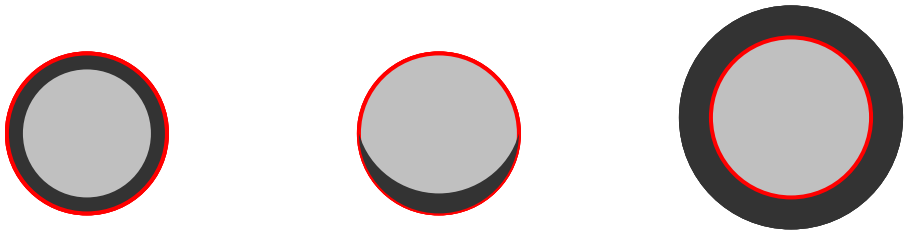

**Figure 4-IX-14:** Schematic diagrams of different dark patterns observed around the embedded particles in polarized light images. Particle outline is highlighted in red.

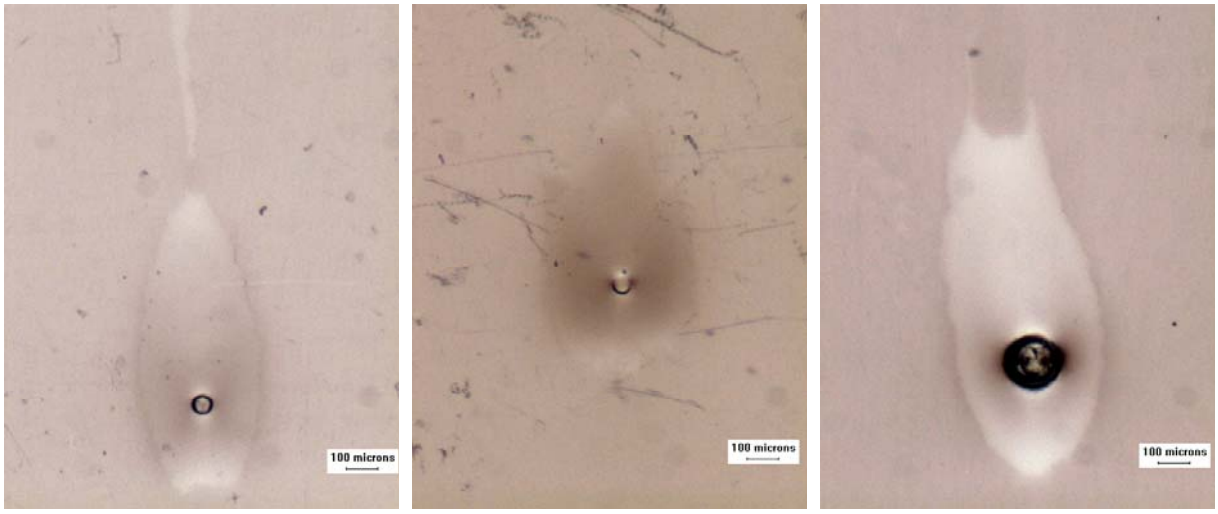


**Figure 4-IX-15:** Polarized light images of three low average height defects with dark outlines around the particles shown in the corresponding schematic diagrams of Figure 4-IX-14. (Defect names from left to right: R17R60-D9, R17R40-D12, and R19R80-D9)

Debonding leads to surface detachment, which could propagate over the surface of the whole particle. The load transfer between the particle and the matrix is weakened and this results in higher strain and deformation experienced by the matrix around the particle. The polymer matrix undergoes localized yielding. The area that experiences higher strain would have higher chain alignment and lower thickness. Both factors can change the amount of light passing through the polarizing filters and create the bright, deformed regions that are visible in all low average height defects.

Debonding results in release of stress around the embedded particles and lowers the residual stress levels. This is possibly why most low average height defects do not show dark and bright regions around the particles with the intensity as high as those observed for high average height defects.

Particles other than glass microspheres, notably ceramic and metal particles, were also examined for indications of debonding. However, those particles appeared black with the transmitted polarized light and no effect could be seen. However, recall that the correlations of defect volume versus defect area and defect area versus particle area were unaffected by the composition of the spherical particles used.

Thus, there is some experimental evidence that Hypothesis IV, particle debonding, may provide the reason for the presence of the two distinct groups of defects observed. This tentative conclusion is based upon an interpretation of the defect appearance and results shown in the related literature.